An All-Resolution Cumulant-Based Lattice Boltzmann Approach for Simulating High Reynolds Number Engineering Shear Flows

Vom Promotionsausschuss der
Technischen Universität Hamburg
zur Erlangung des akademischen Grades

Doktor-Ingenieur (Dr.-Ing.)

genehmigte Dissertation

von
Martin Gehrke

aus
Heide (Holstein)

2024

Gutachter:
1. Gutachter: Prof. Dr.-Ing. Thomas Rung
2. Gutachter: Prof. Dr.-Ing. habil. Gunther Brenner

Tag der mündlichen Prüfung:
20. November 2023

Vorsitzender des Prüfungsausschusses:
Prof. Dr.-Ing. habil. Alexander Düster

Digital Object Identifier (DOI): 10.15480/882.9154
Open Researcher & Contributor ID (ORCID): 0000-0002-5073-397X

Abstract

This dissertation covers the development of a universal lattice Boltzmann method (LBM) framework for accurately and efficiently simulating high Reynolds number flows. The LBM is prominently characterized by its suitability for parallelization, with the utilized solver's GPU acceleration furthermore supporting the explicit nature of the method. A focal area of LBM research relates to the development and investigation of collision operators, mainly accounting for modeling the underlying flow physics.

The research of the thesis is divided into two main topics, where the first one involves a state-of-the-art scrutinization of widely used collision operators, i.e., the well-known single-relaxation-time and a multiple-relaxation-time model, besides including the recent cumulant approach. The latter has variants distinguished by the linearized leading error with respect to the equivalent Navier-Stokes equations. The variants hold different sets of relaxation rates, where the parameterized option refers to the latest published enhancement constituting a promising approach for simulating turbulent flows at high Reynolds numbers based on few studies in the literature so far. The employed test cases of the underlying work are the elementary wall-bounded turbulent channel flow (TCF) and the free-shear Taylor-Green vortex, first considered at low Reynolds numbers. The baseline direct numerical simulation grids are successively coarsened to determine meaningful, i.e., related to both numerical stability and accuracy, resolution limits without utilizing any additional turbulence or wall model. In-depth investigations throughout rely on various turbulent quantities, ranging from mean flow profiles, two-point correlations, and spectral density distributions over turbulent kinetic energy evolutions to structure sizes. The quantitative comparison to published reference data is complemented by qualitative snapshots of the instantaneous velocity field or isosurfaces of the vorticity vector to visualize turbulent structures. Since the studies confirmed the advantageous suitability of the parameterized cumulant (C-P) model, it was chosen for all subsequent developments.

The second topic, signifying the main building block of this thesis research, involves advancements of the native C-P model. Extending the resolution limit toward engineering requirements makes further modeling indispensable. To this end, three contributions are evolved, referring to turbulence and wall modeling. The turbulence modeling features an implicit and explicit part. The former is confined to the upper-frequency part of the spectrum being incorporated through the C-P collision model itself by freely adjustable regularization. Since the implicit influence is bounded by $\Delta x^+ \approx 30$, substantiated by profound studies of the considered periodic hill flow test case, the limit is further augmented by adding an explicit turbulence model based on the algebraic Smagorinsky-Lilly large eddy simulation (LES) closure utilizing a dynamic parameter. Both the regularization approach and the adapted LES model are sensitized to the spatial and temporal resolution yielding a self-adaptive blend between resolving and modeling turbulence besides ensuring sufficient numerical stability in all cases. The resolutions enabled by the developed LES approach distinctly exceed the threshold of a wall-resolved LES for a uniform Cartesian grid layout, making the use of a wall function essential. The last component to complete the overall approach correlates to the adaption of the wall treatment by introducing a virtual shift of the wall position, whereby priorly deficient wall-near gradients are corrected.

Finally, the proposed framework is tested for TCF simulations up to $\mathrm{Re}_\tau = 50000$ ($\mathrm{Re}_B = 1.7 \cdot 10^6$) featuring an isotropic grid spacing of $\Delta x^+ \approx 2200$. A restriction refers to plain boundaries since the wall function is not generalized for arbitrarily formed geometries.

Acknowledgements

This dissertation summarizes the findings of my work as a research associate at the "Institute for Fluid Dynamics and Ship Theory" (FDS) at the Hamburg University of Technology (TUHH) between 2015 and 2023. During this time, I had the pleasure of collaborating with many inspiring and passionate individuals, some of whom I would like to thank here.

First and foremost, I would like to thank Prof. Dr.-Ing. Thomas Rung for the supervision and continuous support of my research and consulting work. Looking back on my Master's studies, it was him who sparked my initial interest in (computational) fluid mechanics in his various lectures. Later on, during my time at the FDS, his productive and trustful leadership and his continuous motivation gave me opportunities for personal and technical growth, which I am very grateful for. Under his supervision and guidance, I successfully worked on a broad range of challenging projects, ranging from research projects on ice-going ships and diverse industrial projects to large fluid mechanics lectures and exams.

I would like to thank Prof. Dr.-Ing. habil. Gunther Brenner for acting as second assessor of this thesis, and Prof. Dr.-Ing. habil. Alexander Düster for charing the examination board.

Next, I would like to thank Christian Janßen, who had a decisive influence on my career path. In his lecture "Application of Computational Fluid Dynamics in Naval Architecture", I had my first contact with the LBM. Thanks to his motivating character and a late-night conversation at the 2013 Naval Architects' "Ordensfest", I decided to write my Master's thesis under his and Prof. Rung's supervision, which then formed the basis of my subsequent employment at the FDS. His enthusiasm for building and leading the "ELBE" team resulted in a time of high collegiality and productivity. I want to thank him for all of this and his foresight in many aspects.

Many thanks to Dennis Mierke and Amir Banari for a superb time as office mates. We always had an open ear for each other and supported each other in a very constructive and motivating way. In particular, I would like to thank Dennis for his patient guidance in all matters of C++ and CUDA programming, in which he has excellent knowledge. I want to thank Amir for many valuable discussions concerning physical, modeling, and mathematical aspects, which frequently provoked new thought approaches to dead ends.

I would like to thank Philip Streckwall for our great time together at the institute. Mostly during our joint coffee breaks, his curiosity, his positive, critical and questioning nature, and his broad-based knowledge often provided new ideas.

I appreciate and thank Henrik Asmuth for detailed discussions regarding his LBM wall function approach and for the further exchange of LBM experiences. Moreover, I would like to thank Niklas Kühl for taking the time to carefully proofread this thesis.

I want to thank my family and friends for always believing in me and for encouraging me to keep going over the years. My parents' continuous support and our mutual reliance have always made me feel safe. They provided me with the recognition that I was on the right path, which has perpetually supplied me with motivation. Finally, I would like to thank my wonderful partner Yvonne for her endless patience and support. I have invested a lot of spare time in the completion of this thesis, including working on numerous evenings, weekends, and even on vacation days that were actually planned together, which was not always easy for either of us. With the defense and publication of this dissertation, these burdens of the past will fade and we look forward to a happy future with our lovely daughter Nela.

Contents

Nomenclature

Lower-case Latin

$\mathbf{f}$	Force density
$\boldsymbol{e}_\zeta$	Directional speed matrix/discrete particle velocity
$\boldsymbol{m}$	Multiple-relaxation-time moments (vector)
$\boldsymbol{x}$	Spatial vector/position
$\overline{u_\mathrm{i}' u_\mathrm{j}'}$	Reynolds stress tensor
$\tilde{o}$	Total order of a cumulant expression
a_ij	Nondimensional anisotropy tensor
c	Lattice speed
c_s	Speed of sound in the lattice
$c_{\alpha\beta\gamma}$	Cumulant expression
f	Frequency, particle distribution function
k	Turbulent kinetic energy
n	Empirical power law value
p	Pressure
q	Subgrid distance
s_m	Stages of vortex stretching
t	Time
t_FP	Flow-pass time
u	Streamwise/axial velocity component
u_η	Kolmogorov velocity scale
u_i	Velocity vector $u_\mathrm{i} = (u, v, w)^\intercal$
u_τ	Friction velocity
v	Wall-normal velocity component
w	Spanwise/lateral velocity component
w_ζ	Weight coefficients of the discrete velocity spaces
x, y, z	Cartesian coordinates
x_i	Spatial (Cartesian) position
x_B, y_B	Two-dimensional barycentric coordinates
y^+	Nondimensional wall distance

Upper-case Latin

$\boldsymbol{M}$	Linear transformation matrix of the multiple-relaxation-time model
$\boldsymbol{S}$	Relaxation rate (diagonal) matrix of the multiple-relaxation-time model
$\mathbf{C}_\epsilon$	Third-order cumulant related expression for C-P regularization
$\mathcal{C}_\mathrm{LES}$	Resolution-sensitive cumulant-based dynamic large eddy simulation parameterization
$\mathcal{C}_\omega$	Resolution-sensitive C-P regularization parameter
$\overline{Q}$	Tensor norm of the non-equilibrium stress tensor Q_ij

$\overline{S}$	Tensor norm/local intensity of the strain rate tensor S_{ij}
Re	(General) Reynolds number
$\mathrm{Re}_{B;\,\tau;\,C;\,\Delta x}$	Bulk; friction; centerline; (local) cell Reynolds number
A	Empirical power law value, C-P parameter
B	Boundary, C-P parameter
C	Center
C^{+}	Nondimensional log law (integration) constant
C_S	Smagorinsky constant
$C_{\alpha\beta\gamma}$	Cumulant expression (density-related, $C_{\alpha\beta\gamma} = c_{\alpha\beta\gamma}\rho$)
E, E_{ik}	Energy spectrum function
F	Fluid
G	Large eddy simulation convolution/filter kernel
H	Half-channel height (turbulent channel flow)
L	Length, integral length scale
L_{ii}	Turbulent length scale
L_2	L2 norm
N, N_H	Reference number of discrete lattice nodes, per height H
N_x, N_y, N_z	Number of discrete lattice nodes in (x, y, z) direction
P	Position/location (of a point probe)
P_k	Turbulence energy production
Q_{ij}	Non-equilibrium stress tensor
R	Molar gas constant
R_{ij}	Two-point correlation
S	Solid
S_{ij}	Strain rate tensor
T	(Absolute) Temperature
$T_{\{i;\,e\}}$	Initial (transient); extraction period
V	Volume
Kn	Knudsen number
Ma	Mach number

Lower-case Greek

$\boldsymbol{\xi}$	(Continuous) particle velocity vector $\boldsymbol{\xi} = (\xi, \upsilon, \theta)^{\intercal}$ in phase space
χ	Generic (instantaneous, unfiltered) field variable
δ	Delta dirac function, (density) fluctuation
δ_{ik}	Kronecker delta
ϵ	Infinitesimal positive value
ϵ_{ijk}	Levi-Civita symbol/epsilon
η	Kolmogorov length scale
κ	Wave number, von Kármán constant
$\kappa_{\alpha\beta\gamma}$	Central moments
λ	Wavelength, C-P regularization value
λ_T	Taylor microscale (length scale)
μ	Dynamic viscosity
ν, ν_D, ν_t, ν_e	Kinematic, numerical, turbulent, effective viscosity
ω	Angular frequency, specific dissipation rate of turbulent kinetic energy,

	relaxation rate (kinematic viscosity-related)
ω_{i}	Vorticity vector
$\omega_{\alpha\beta\gamma}$	Cumulant relaxation rates (order-dependent)
ϕ	Generic field variable
ψ	Generic field variable
ρ	Density
τ	Relaxation time (kinematic viscosity-related)
τ_η	Kolmogorov time scale
τ_{ij}	Viscous stress tensor
τ_W	Wall shear stress
ε	Turbulent dissipation rate
ϑ	Generic flow quantity
ζ	Directions/collocation points of discrete LBM velocity spaces

Upper-case Greek

$\boldsymbol{\Xi}$	(Continuous) particle velocity vector $\boldsymbol{\Xi} = (\Xi, \Upsilon, \Theta)^\intercal$ in frequency space
Δt	Time step/temporal increment
Δx, Δx^+	Dimensional, nondimensional regular (isotropic) Cartesian lattice spacing
Δ	Large eddy simulation filter width
Γ	Circulation
$\Lambda_{\{1,2,3\}}$	Eigenvalues of the nondimensional anisotropy tensor a_{ij}
$\Lambda_{\{x;\,u;\,t;\,\nu\}}$	Scaling factors (LB $\leftrightarrows$ SI) for space; velocity; time; viscosity
Ω	Domain, (continuous) BE collision operator
Ω_ζ	(Discrete) BE collision operator
Ψ	Predicted to required eddy viscosity estimate
Θ	Wall distance in outer scaling, i.e., $\Theta = y/H$

Superscripts

eq	Equilibrium part
neq	Non-equilibrium part
ref	Reference value

Subscripts

$\alpha\beta\gamma$	Triple order index (cumulant-related)
ζ	Direction of the discrete velocity space
B	Bulk-related quantity (velocity, Reynolds number), bottom (wall) related quantity
C	Centerline-related quantity (velocity, Reynolds number)
c	Cutoff (value)
E	Ensemble average
e	Effective (value)
P	Physical/SI quantity
S	Spatial average
T	Temporal average

T	Top (wall) related quantity
t	Turbulent
W	Wall-related quantity
0	Reference value
av	Averaged quantity
crit	Critical (value)
def	Default (value)
i, j, k	Cartesian coordinates
lin	Linear (relation)
max	Maximum (value)
mod	Modeled (part)
opt	Optimal (value)
ref	Reference (length, time, velocity)
rel	Relative (value)
res	Resolved (part)
tot	Total (value)
uni	Uniform
vis	Viscous (part)

Operations

$(\cdot)\prime$	Fluctuating part
$(\cdot)^*$	Post-collision state
$(\cdot)^+$	Nondimensionalization through inner scaling (u_τ)
$(\cdot)^\parallel$	Wall-tangential part/direction
$(\bar{\cdot})$	Mean value, opposite direction
$(\tilde{\cdot})$	Regularized relaxation rate (C-P related)
$\mathcal{O}(\cdot)^m$	m-th order/magnitude
$\mathrm{d}(\cdot)/\mathrm{d}t$	Substantial derivative
$\lim(\cdot)$	Limit (of a function)
$\ln(\cdot)$	Natural logarithm
$\max(\cdot)$, $\min(\cdot)$	Maximum, minimum value
$\mathscr{L}\{(\cdot)\}$	Laplace transform
$\overline{1} = -1$	Miller notation
$\partial(\cdot)/\partial x_\mathrm{i}$	Partial derivative
$\sigma^2_{(\cdot)}$	Variance

Abbreviations

(D)BE	(Discrete) Boltzmann Equation
(L)BGK	(Lattice) Bhatnagar, Gross and Krook (single-relaxation-time collision model)
(U)RANS	(Unsteady) Reynolds-Averaged Navier-Stokes (equations, solver)
1D, 2D and 3D	One-, Two- and Three-Dimensional
AIM	Anisotropy Invariant Map
BC	Boundary Condition
C-AO	Cumulant-*All-One* (relaxation rate set)

C-P	Cumulant-*Parameterized* (relaxation rate set)
CFD	Computational Fluid Dynamics
CUDA	Compute Unified Device Architecture
DES	Detached Eddy Simulation
DFT	Discrete Fourier Transform
DNS	Direct Numerical Simulation
ELBE	Efficient Lattice Boltzmann Environment (in-house lattice Boltzmann solver of the institute for fluid dynamics and ship theory)
ERCOFTAC	European Research Community on Flow, Turbulence And Combustion
EVM	Eddy Viscosity Model
FD, FDM	Finite Difference (approximation), Finite Difference Method
FDS	(Institute for) Fluid Dynamics and Ship theory (of the Hamburg University of Technology)
FP	Flow Pass
FV, FVM	Finite Volume (approximation), Finite Volume Method
GPU	Graphics Processing Unit
GS	Grid Scale
IBB	Interpolated Bounce-Back (scheme)
IMEM	Inverse Momentum Exchange Method
KBC	Karlin-Bösch-Chikatamarla (entropic LB model)
LBE, LBM	Lattice Boltzmann Equation/Method
LES	Large Eddy Simulation
LESOCC	Large Eddy Simulation On Curvilinear Coordinates (reference solution solver)
MEM	Momentum Exchange Method
MGLET	Multi Grid Large Eddy Turbulence (reference solution solver)
MKM-99	Reference data set of Moser et al. [1999]
MRT	Multiple-Relaxation-Time (model)
NS	Navier-Stokes
PDF	Particle Distribution Function
PHF	Periodic Hill Flow (test case)
PR	Polynomial Reconstruction
PSD	Power Spectral Density
RMS	Root Mean Square
RP	Reattachment Point
RSM	Reynolds Stress (transport) Model
RST	Reynolds Stress Tensor
SBB	Simple Bounce-Back (scheme)
SGS	Subgrid Scale
SI	International System of units (physical/dimensional quantities)
SL	Smagorinsky-Lilly
SRS	Scale-Resolving Simulations
SRT	Single-Relaxation-Time (model)
SST	Shear Stress Transport
TBL	Turbulent Boundary Layer
TCF	Turbulent Channel Flow (test case)
TGV	Taylor-Green Vortex (test case)

TKE	Turbulent Kinetic Energy
TPC	Two-Point Correlation
TRT	Two-Relaxation-Time (model)
TUHH	Hamburg University of Technology
VLES	Very Large Eddy Simulation
VOF	Volume Of Fluid (method)

1 Introduction

The introduction commences with an outline of the scientific background and the motivation of the research (cf. Sec. 1.1), followed by a depiction of the dissertation's starting point and goals (cf. Sec. 1.2). Section 1.3 is devoted to the scientific contributions, and the chapter closes by outlining the structure of the thesis (cf. Sec. 1.4).

1.1 Scientific Background and Motivation

The prime objective of engineering computational fluid dynamics (CFD) is the reliable simulation of single-/multi-phase flows affecting diverse industries. Most common applications include hydro- and aerodynamics, combustion, cooling of equipment, acoustics and chemical engineering. A frequent challenge is that almost all technically relevant flows are high Reynolds (Re) number turbulent flows, where Fig. 1.1 representatively displays the instantaneous vorticial structures of a flow over curved geometries at the bottom boundary. Such

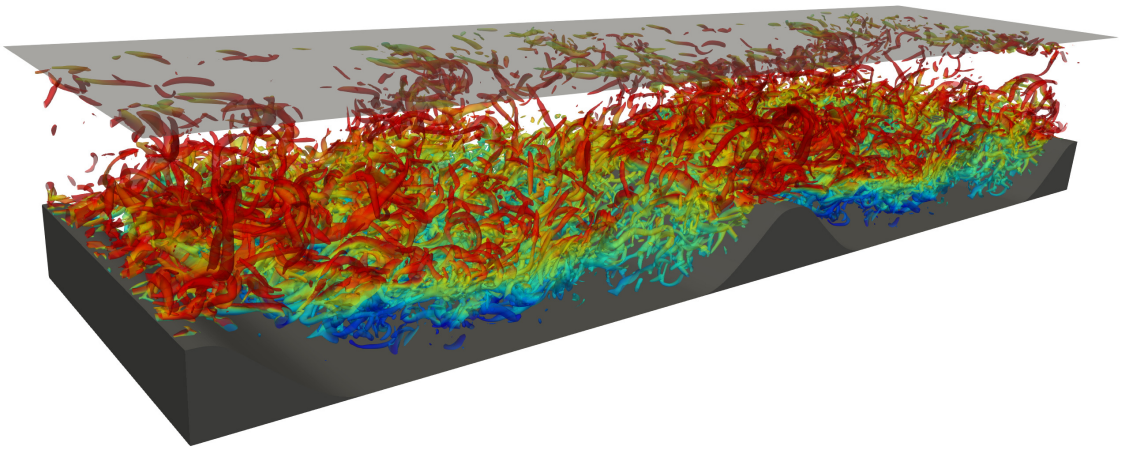

Figure 1.1: Turbulent structures of a separated and reattaching shear flow.

flows exhibit a broad spectrum of spatial and temporal scales, which must either be fully resolved down to the Kolmogorov microscales by the numerical grid or adequately modeled to obtain credible results. The spatial resolution requirements of these direct numerical simulations (DNS) scale with $\mathrm{Re}^{9/4}$. Therefore, typically the modeling route is pursued since, even today, computational resources are the limiting factor for DNS of complex industrial flows at high Reynolds numbers. Wide-spread approaches correspond to classical (unsteady) Reynolds-averaged Navier-Stokes (RANS) strategies, partially scale-resolving large eddy simulations (LES), or even hybrid RANS-LES models to meet engineering requirements claiming reasonable computational times and manageable amounts of data to assist the design process most effectively.

Alongside classical CFD approaches, the lattice Boltzmann method (LBM) is a promising alternative for transient simulations of scale-resolving turbulent flows, which is discussed in more detail below.

The **goal** of the thesis is to develop an *efficient, robust, and accurate* LBM framework for the simulation of high Reynolds number turbulent flows. The main effort is to fully decouple the turbulence modeling from any additional, heuristic user input, such that the model's parameterization solely depends on the chosen spatial and temporal discretization.

Lattice Boltzmann Method

Dissimilar to traditional continuum mechanics strategies, i.e., the finite volume method (FVM) or the finite difference method (FDM), which directly solve the conservation equations, i.e., for mass, momentum, and energy, of the macroscopic flow quantities, the LBM rests upon a set of particle distribution functions (PDF) of fictitious particles and, therefore, is classified as a mesoscopic method. The particles' evolution in space and time is used to reconstruct the macroscopic flow field. Among the most favorable properties of common LB approaches are their weak compressibility, explicit advancement in time, and (usually) the structured Cartesian grid discretization. Moreover, the crucial algorithmic benefit of the method is related to the strict separation of nonlocal and nonlinear terms, which provides excellent suitability for parallelization, specifically on high-performance shared and distributed memory CPU (central processing unit) and GPU (graphics processing unit) computing systems, e.g., as shown by Tölke and Krafczyk [2008], Feichtinger et al. [2011], Wang and Aoki [2012], Janßen et al. [2015] and Latt et al. [2021]. Hence, massively parallel LBM applications often reflect impressive scalability of up to ten thousand cores and short turnaround times due to large node update rates. Prominent distributed-memory CPU computations by Schornbaum and Rüde [2016], including up to $2.0 \cdot 10^{11}$ grid nodes or state-of-the-art GPU-based AI systems, e.g., NVIDIA DGX A100, with up to 640GB shared-memory and $\mathcal{O}(10^5)$ CUDA cores enabling computations with up to $\mathcal{O}(10^9)$ grid nodes in a single server setup, demonstrate a considerable reduction of hardware-related limitations to enable highly-resolved turbulent flow simulations at high Reynolds numbers. Furthermore, recent studies of Hasegawa et al. [2019] or Watanabe and Aoki [2021], executed on a distributed-memory HPC cluster, also involve up to $3.3 \cdot 10^9$ nodes processed by maximal 256 GPUs in parallel.

For these reasons, the LBM is perpetually gaining increased attention for the efficient simulation of challenging industrial flows, e.g., Kotapati et al. [2009], Noelting and Fares [2015], Pasquali et al. [2016], Niedermeier et al. [2018], Lenz et al. [2019], Sharma et al. [2019], Boudet et al. [2021] or Asmuth [2022]. The predictive success of LBM in simulating – mainly academic – turbulent flows has been addressed in several preceding studies, among many others by Geier et al. [2006], Abdel Kareem et al. [2009], Aidun and Clausen [2010], Chikatamarla et al. [2010], Jahanshaloo et al. [2013], Suga et al. [2015], Geier et al. [2017b] and Banari et al. [2020].

As indicated in literature, the accuracy of turbulent flow predictions is strongly intertwined with the employed collision model/operator, e.g., Nathen et al. [2018], Coreixas et al. [2020] or Geier et al. [2021], and modifications to the collision model are therefore a focal area of LBM research. Separating discretization aspects from flow physics modeling is more challenging in an LBM than in a conventional Navier-Stokes framework, since both

aspects are related to the collision model that relaxes the PDFs toward their equilibrium state. Published suggestions to increase the stability and accuracy of LBM in simulating turbulent flows (a) adopt two and more relaxation times, e.g., the two-relaxation-time (TRT) model by Ginzburg et al. [2008a,b] and multiple-relaxation-time (MRT) variants by d'Humières et al. [2002] or Tölke et al. [2006], (b) introduce improved Galilean invariance of the collision operator as suggested by the cascaded approach of Geier et al. [2006], (c) promote stability in addition to accuracy enhancements by a regularization, cf. Latt and Chopard [2006] or by a local adaptation of relaxation times using discrete entropy minimizing methods introduced by Karlin et al. [2014], Bösch et al. [2015] and Dorschner et al. [2016], or (d) transform and relax the distribution functions in cumulant space, cf. Geier et al. [2015, 2017a].

1.2 Starting Point and Goals

This dissertation builds on the initial works of Janßen [2010], Janßen and Krafczyk [2010, 2011] and Janßen et al. [2013] from which the GPU-accelerated ELBE – efficient lattice Boltzmann environment – research code development was initiated as documented by Janßen et al. [2015]. Initially focused on functionalities and modules for accurately simulating free-surface (FS) flows by the volume of fluid (VOF) method, a rudimentary class for single-phase flows, providing the BGK (Bhatnagar et al. [1954]), the MRT (Tölke et al. [2006]), and the cumulant (Geier et al. [2015]) collision model, was available at the start of this thesis. The main objectives of this dissertation, which is confined to single-phase shear flows, are:

- to scrutinize common LBM collision models (BGK, MRT, cumulant) for turbulent benchmark test cases.
- to develop an efficient and universal strategy for simulating turbulent shear flows at various Reynolds numbers employing almost arbitrary Cartesian grid resolutions.
- to access, analyze, and adapt different contributions to turbulence modeling.

1.3 Present Contributions

Regarding the aforementioned goals, the research scope is divided into two main topics:

I. The work commences with a state-of-the-art scrutinization of the three initial collision models (BGK, MRT, cumulant) employing standard turbulent shear flows including the following issues:
  - The predictive accuracy is assessed for DNS of turbulent channel flows (TCF), i.e., the most elementary wall-bounded flow type, at the lowest Reynolds number ensuring fully developed turbulent conditions, i.e., $\mathrm{Re}_\tau = 180$. Along with mean flow quantities, investigations involve a variety of turbulence statistics, among others two-point correlations, spectral density distributions and structure sizes, thoroughly compared to published reference data.

- Based on the numerical stability and accuracy, reasonable spatial resolution limits, i.e., $\Delta x^+ = \{3.5; 4; 6\}$ valid for BGK, MRT and a baseline cumulant model labeled C-AO, are determined for each model by bridging from DNS toward (slightly) under-resolved discretizations, when neither applying an explicit large eddy simulation (LES) closure nor explicit filtering. Hence, the wall-adjacent fluid node at $y^+ = \Delta x^+/2$ is still located within the viscous sublayer for the limiting resolutions.
- In addition to the spatial discretization study, influences of the temporal resolution and numerical approximation scheme are considered. Since the employed MRT model offers no benefits over the rather equally complex C-AO, the former is dropped hereafter, also to keep the underlying parameter space manageable.
- Subsequently, the dissipation of turbulent kinetic energy is studied for the BGK and C-AO based on the Taylor-Green vortex (TGV) test case at a low Reynolds number, i.e., $\mathrm{Re} = 1600$, involving free shear decaying turbulence. For the BGK model, the influence of the utilized velocity space discretization, i.e., the D3Q19 and the D3Q27 stencil, is investigated. Additionally, a second cumulant variant, i.e., the parameterized (C-P) model featuring an enhanced set of relaxation rates published by Geier et al. [2017a], is included in this study. The fundamental distinction of the C-AO and C-P involves the elimination of the linearized leading error by the C-P, whereby the diffusion term of the equivalent NS equations is fourth order accurate. So far, the C-P noticeably provides the best agreement with reference data when the resolution coarsens.
- Derived from the TGV findings, the C-P capabilities are further investigated for the TCF ($\mathrm{Re}_\tau = 180$) under coarsening up to $\Delta x^+ = 18$. Thus, the first fluid node is located in the lower buffer layer for the limit case. Since the accuracy of the C-P is beneficially resolution-independent, besides being inherently stable within the given range without employing any explicit turbulence model, this model's selection is substantiated as the origin for further developments.

All results related to this basic research building block of the thesis are published in the first two peer-reviewed articles:

(P-1) Gehrke et al. [2017a]: M. Gehrke, C.F. Janßen, and T. Rung. Scrutinizing lattice Boltzmann methods for direct numerical simulations of turbulent channel flows. *Computers & Fluids*, Elsevier, 156:247–263, 2017.

(P-2) Gehrke et al. [2020]: M. Gehrke, A. Banari, and T. Rung. Performance of Under-Resolved, Model-Free LBM Simulations in Turbulent Shear Flows. In Y. Hoarau, S.-H. Peng, D. Schwamborn, A. Revell, and C. Mockett, *Progress in Hybrid RANS-LES Modelling*, *Notes on Numerical Fluid Mechanics and Multidisciplinary Design*, Springer International Publishing, Cham, 143:3–18, 2020.

II. The second main objective involves investigations and developments addressing turbulence modeling. Essentially, the contributions are based on three aspects corresponding to consecutive stages, each of which permits coarsening the limiting grid resolution. To this end, the stages are added successively in the subsequent order, where the most extensive and final proposed modeling strategy comprises all of the three following enhancements and developments:

(i) **Collision** model

- Firstly, the C-P model's *implicit* LES capabilities and their limits are assessed. To this end, the periodic hill flow (PHF), which offers a rich basis of numerical and experimental data, is considered particularly suitable for benchmarking as this test case includes flow separation and reattachment. Therefore, it is distinctly more complex than the previously consulted TCF, imposing higher demands on the model, and findings are thus regarded as more far-reaching.
- The C-P model's eponymous parameterization, enabling fourth-order accurate diffusion, employs a free regularization value (λ) also referred to as limiter. It preserves sufficient numerical stability in the low-viscosity limit by introducing numerical damping. The literature reported default value is assigned to $\lambda_{\text{def}} = 10^{-2}$. Initial grid coarsening studies of the PHF revealed that the choice of increased λ notably affects the method's accuracy on under-resolved grids. Preceding publications apply the default, cf. Geier et al. [2017a,b], or lack in-depth analyses of increased resp. specifically tuned λ-values, cf. Asmuth et al. [2020] or Pasquali et al. [2020], constituting the motivation for the thorough research presented in Sec. 6.1 of this thesis.
- The outcomes of the accomplished PHF parameter study, including variations of the spatial and temporal discretizations for (bulk) Reynolds numbers within $700 \leq \text{Re}_B \leq 37000$, are employed to deduce an empirical alternate formulation of the initial limiter. The proposed regularization is linked to the cell Reynolds number, i.e., $\text{Re}_{\Delta x} = u\,\Delta x/\nu$, and Mach number which serve to embed resolution sensitivity to the approach. The latter entails the advantageous self-adaptive tuning of optimal regularized expressions without needing any additional user input for a wide range of scale-resolving discretizations.
- The implicit LES capability of the C-P, employing the self-adaptive regularization, solely acts in the upper-frequency regime of the turbulent energy spectrum containing small-scale structures. A smooth transition exists between the energy-containing large-scale motion and the energy-dissipating modeled scales. Compared to the primary C-P simulations of the TCF (cf. last bullet point under **I.**), where the native regularization with its constant default λ-value is applied, the proposed formulation almost doubles the resolution limit to $\Delta x^+ \approx 30$, rigorously supported by the evaluation of various turbulent quantities.

(ii) **Subgrid scale** model

- Adding an *explicit* subgrid scale model is indispensable to extend the resolution limit further. The developed approach originates from the well-known algebraic Smagorinsky-Lilly LES closure, which stands out due to the simplicity of the underlying Boussinesq viscosity concept and the straightforward local availability of the strain rate tensor in the context of LBM. The modification is characterized by substituting the Smagorinsky constant by a dynamic parameter in terms of Germano et al. [1991]. The derivation is in

accordance with the previously discussed regularization, and a resolution-sensitive expression is proposed, again incorporating the cell Reynolds and Mach number. The model's contributions seamlessly vanish for direct numerical simulations.

- Since the enabled resolution distinctly exceeds the threshold of a wall-resolved LES under the condition of a uniform Cartesian grid layout, where $y^+ = \Delta x^+/2$ applies, the use of a wall function is essential. For this, the wall function of Asmuth et al. [2021] is employed in a slightly amended way.
- The C-P enhanced by the dynamic subgrid scale model is scrutinized by TCF simulations for friction Reynolds numbers up to $\mathrm{Re}_\tau = 5200$. Analyses of the mean flow field, resolved and modeled second moments, two-point correlations, as well as spectral data and correlation lengths reveal sufficient accuracy for $\Delta x^+ \approx 400$, where the wall location is exactly between the solid and first fluid node of the domain, i.e., associated with $y^+ \approx 200$.
- A remaining deficit, i.e., the so-called overshoot phenomenon related to near-wall gradients, refers to the interaction between the dynamic SGS model and the wall function, where the dynamic character of the SGS model suffers from the missing dynamics of the wall function in coarse resolutions, i.e., $\Delta x^+ > 30$. Nevertheless, the defect is localized and does not affect the outer flow field at all. The following incorporation of a turbulent wall model in (*iii*) addresses its remedy.

(*iii*) **Wall** model

- The last segment to complete the overall approach refers to the adaption of the wall treatment. To this end, an all-resolution (universal) wall function is constituted by virtually shifting the wall position, whereby the deficient overshoot phenomenon is completely resolved. The shift is incorporated through the y^+ value entering the wall function to iterate the targeted wall shear stress linked to the present Reynolds number of the simulation. The implementation is parameterized by employing the full lattice spacing, i.e., $y^+ = y^+(\Delta x^+)$.
- The final approach utilizing all three contributions, i.e., (*i*) – (*iii*), is tested for a variety of TCF simulations for (friction) Reynolds numbers up to $\mathrm{Re}_\tau = 50000$ associated with nondimensional inner lattice spacings of $\Delta x^+ = 2200$ featuring shifted $y^+(\Delta x^+) = 330$ for the coarsest consulted discretization. The developed framework provides accurate results and proves the fundamental suitability for bridging toward industrially relevant high Reynolds number flows.

The related analyses and developments of (*i*) and (*ii*) are published in the subsequent two refereed journal articles of the author:

(P-3) Gehrke and Rung [2022a]: M. Gehrke and T. Rung. Periodic hill flow simulations with a parameterized cumulant lattice Boltzmann method. *International Journal for Numerical Methods in Fluids*, John Wiley & Sons, Inc., 94(8):1111-1154, 2022.

(P-4) Gehrke and Rung [2022b]: M. Gehrke and T. Rung. Scale-resolving turbulent channel flow simulations using a dynamic cumulant lattice Boltzmann method. *Physics of Fluids*, AIP Publishing, 34(7):075129, 2022.

The outcome of (*iii*) is published in a peer-reviewed technical note:

(P-5) Gehrke and Rung [2022c]: M. Gehrke and T. Rung. Scrutinizing Dynamic Cumulant Lattice Boltzmann Large Eddy Simulations for Turbulent Channel Flows. *Computation*, MDPI, 10(10):171, 2022.

Related Publications

During the author's time at the institute for *Fluid Dynamics and Ship theory* (FDS) at Hamburg University of Technology (TUHH), several publications beyond the reported scope of this thesis belong to the research outcome. These are all off-topic, i.e., related to studying the onset of transition, free-surface flows and even inhere complex fluid-structure interaction of ice-going ships:

(R-1) Banari et al. [2020]: A. Banari, M. Gehrke, C.F. Janßen, and T. Rung. Numerical simulation of nonlinear interactions in a naturally transitional flat plate boundary layer. *Computers & Fluids*, 203:104502, 2020.

(R-2) Gehrke et al. [2019]: M. Gehrke, D. Mierke, T. Rung, and Hauer, P. Validation of a GPU Accelerated LBM Based Numerical Ice Tank for a Voith Schneider Propulsion System (Presentation), In *VIII International Conference on Computational Methods in Marine Engineering, May 13–15, Gothenburg*, 2019.

(R-3) Mierke et al. [2019]: D. Mierke, M. Gehrke, T. Rung, and Hisette, Q. Validation of a GPU-Accelerated Fully Viscous Numerical Ice Tank Using Lattice Boltzmann Method (Presentation), In *VIII International Conference on Computational Methods in Marine Engineering, May 13–15, Gothenburg*, 2019.

(R-4) Gehrke et al. [2017b]: M. Gehrke, D. Mierke, C.F. Janßen, and T. Rung. GPU-accelerated LBM-VOF two-phase flow simulations with grid refinement (Presentation), In *VII International Conference on Computational Methods in Marine Engineering, May 15–17, Nantes*, 2017.

(R-5) Gehrke et al. [2016]: M. Gehrke, C.F. Janßen, and T. Rung. Three-dimensional applications of a GPU-accelerated numerical wind tunnel (Poster), In *XIII International Conference for Mesoscopic Methods in Engineering and Science, July 18–22, Hamburg*, 2016.

1.4 Outline of the Thesis

The remainder of the dissertation is organized into six chapters, where the two following chapters outline the phenomenological, theoretical, and numerical background. To this end, Chap. 2 is devoted to flow turbulence and its statistical approach, besides addressing commonly employed simulation approaches for turbulent flows. Subsequently, Chap. 3 summarizes the LBM principles, including numerical approximations, discrete collision

operators, and in addition, LBM-specific boundary, wall, and turbulence treatments are discussed. Focus is given to the cumulant model and its variants since these form the origin of the suggested approach. The fourth chapter depicts the test cases on which the benchmarks, verifications and validations are based. The presentation of the results is divided into two chapters. Firstly, established collision models are scrutinized for DNS to slightly under-resolved resolutions in Chap. 5, leading to the cumulant operator's preferred suitability. Subsequently, the most comprehensive Chap. 6 presents the developed cumulant model advancements concerning universality for simulating turbulent shear flows and involves thorough parameter studies. Lastly, Chap. 7 concludes the presented work and potential future research.

Some additional theoretical details and results not necessarily required in the main part are considered in the appendix A to C for completeness. The underlying thesis uses Einstein's summation convention for lower-case (normal font) Latin subscripts. Moreover, the tensorial notation relates to Cartesian coordinates.

2 Flow Turbulence

The central dimensionless quantity to classify and compare flows, cf. dimensional analysis of Buckingham [1914], is given by the Reynolds number

$$\mathrm{Re} = \frac{u_{\mathrm{ref}}\, L_{\mathrm{ref}}}{\nu} = \frac{\rho\, u_{\mathrm{ref}}\, L_{\mathrm{ref}}}{\mu}\,, \tag{2.1}$$

which describes the ratio between inertial and viscous forces acting in a fluid. The definition relates to a reference (ref) velocity (u) and length (L) and the viscosity of the underlying, i.e., the kinematic ν or dynamic μ viscosity linked by the fluid's density $\rho = \mu/\nu$. Even if the designation is based on Reynolds [1883], the initial concept traces back to Stokes [1851]. Depending on specific consideration, general references are, e.g., the bulk, centerline or friction velocity or, moreover, fluctuations can be related.

At low Reynolds numbers, viscous damping forces dominate, and the motion is stated laminar. This flow type is characterized by its stationarity and layered order. Upon reaching a critical (crit) Reynolds number, instabilities occur, implying through irregular turbulent bursts, cf. blue circle in Fig. 2.1 illustrating exemplary temporal velocity signals of the three flow types. Flows at $\mathrm{Re} \approx \mathrm{Re}_{\mathrm{crit}}$ are termed transitional. It is to be noted that the critical Reynolds number is not a constant but depends on the specific boundary conditions for a flow problem under consideration, e.g., internal/external flow, adverse/zero/favorable pressure gradient, geometry complexity, et cetera. After exceeding the range of $\mathrm{Re}_{\mathrm{crit}}$ the flow becomes (fully) turbulent, which is apparent by the strong fluctuations (u') around the mean ($\overline{u}$) of the signal depicted in c.

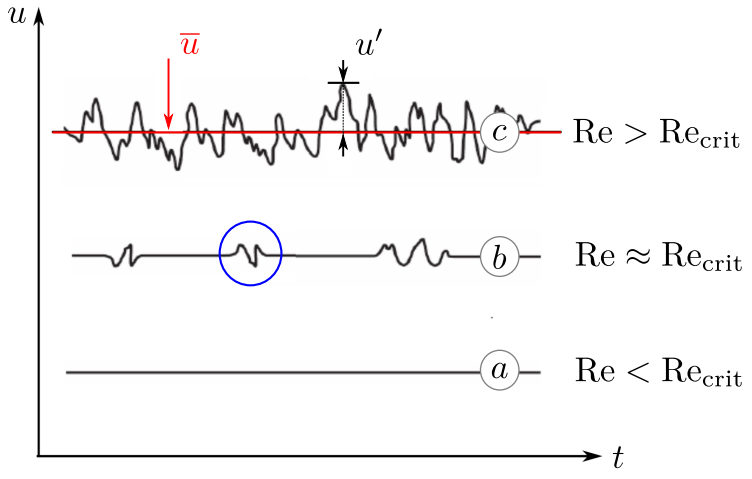

Figure 2.1: Characteristic temporal scalar velocity signals of a) laminar, b) transitional and c) turbulent flows at a fixed location within the field.

The following sections are devoted to summarize and outline the phenomenology (cf. Sec. 2.1), the statistical approach (cf. Sec. 2.2), and common simulation strategies (cf. Sec. 2.3) of turbulent flows.

2.1 Phenomenology

Since almost all flows of technical interest are turbulent, their understanding is indispensable. Subsequently, the properties of turbulent flows are succinctly listed based on the elaborations of Hinze [1959], Rotta [1972] and Wilcox [1993]. According to these, turbulent flows are:

- *irregular*
  The turbulent motion exhibits random variations of field quantities (pressure, velocity and temperature) in both space and time and is, therefore, an inherently unsteady and stochastic 3D process.

- *vorticial*
  The illustration of turbulence relies on the presence of a wide range of scales in terms of a superposition of commonly named turbulent eddies. These are ascribed to a swirling motion defined by the vorticity vector $\omega_\mathrm{i} = \varepsilon_\mathrm{ijk}\,\partial\,u_\mathrm{k}/\partial\,x_\mathrm{j}$ with the Levi-Civita symbol, as the curl of the velocity vector implying the distinct rotational characteristic of turbulence. Likewise, the vorticity can be locally intense and display strong temporal fluctuations.

  The vorticity transport equation assuming incompressible, barotropic and viscous flows with conservative body forces reads

  $$\frac{\mathrm{d}\omega_\mathrm{i}}{\mathrm{d}t} = \underbrace{\omega_\mathrm{k}\,\frac{\partial u_\mathrm{i}}{\partial x_\mathrm{k}}}_{\text{vortex stretching}} + \underbrace{\nu\,\frac{\partial^2 \omega_\mathrm{i}}{\partial x_\mathrm{k}^2}}_{\text{viscous dissipation}} \quad . \tag{2.2}$$

  This simplified equation constitutes the central concept of the hierarchical energy transfer between turbulent scales. The so-called energy cascade, detailed in Sec. 2.1.1, traces back to Richardson [1922], and phenomenology involves the generation of large eddies, subsequently transferring their energy to successively smaller ones due to vortex stretching. The latter mechanism is crucial for maintaining the fluctuating vorticity over a variety of co-existing scales.

- *nonlinear*
  The instability-generating processes causing the laminar flow to transition and the fully turbulent flow dynamics are highly nonlinear.

- *three-dimensional*
  Turbulence is always three-dimensional which directly associates with the *vorticical* nature of turbulence. Since $\omega_\mathrm{i} \perp u_\mathrm{i}$ applies, vortex stretching is lacking in 2D by definition entailing vortex lines are intrinsically nonparallel.

- *diffusive*
  An essential property of turbulent flows relates to their mixing intensity. This increases the overall flow homogeneity away from boundaries, enhances the transfer of all flow quantities, e.g., mass, momentum and energy, and boosts stresses by orders of magnitude compared to laminar flows.

- *dissipative*
  The smallest scales dissipate their mechanical (kinetic) into thermal internal (heat) energy via molecular viscosity. Like all viscous flows, turbulent flows are, therefore, per se diffusive, requiring a continuous supply of energy to compensate for viscous losses.

- *continuous*
  The largest turbulent scales are common $\mathcal{O}(L_{\mathrm{ref}})$, whereas the smallest scales are plenty of orders of magnitude lower. Nevertheless, these, in turn, are still orders of magnitude larger than the molecular length scale, wherefore turbulence is deemed as a *continuum* phenomenon according to Tennekes and Lumley [1972].

2.1.1 Spectral Conception

The most fundamental conception of turbulence founds on the turbulent energy spectrum, which comprises the spectral distribution of turbulent energy as a function of continuous scales. This primal description of turbulent flow physics prevailingly goes back to the findings and hypotheses of Richardson [1922], Taylor [1935a,b] and Kolmogorov et al. [1991a,b] that are briefly outlined below. The subsequent synoptic remarks of this section are mainly based on the works of Bradshaw [1971], Wilcox [1993] and Pope [2000].

The total turbulent kinetic energy (TKE), $k\,[\mathrm{m^2 s^{-2}}]$, and dissipation rate $\varepsilon\,[\mathrm{m^2 s^{-3}}]$ – each related to unit mass – of the fluctuating flow motion are defined via

$$k = \int_0^\infty E(\kappa)\,\mathrm{d}\kappa \quad \text{and} \tag{2.3}$$

$$\varepsilon = 2\nu \int_0^\infty \kappa^2 E(\kappa)\,\mathrm{d}\kappa\,, \tag{2.4}$$

where $E(\kappa)$ is the energy spectrum function, $\kappa\,[\mathrm{m^{-1}}]$ represents the length of the wave number vector κ_{i}, i.e., $\kappa = (\kappa_{\mathrm{i}}\kappa_{\mathrm{i}})^{1/2}$, and ν is the kinematic viscosity. The reciprocal of κ relates to a specific eddy size, since the wavelength (λ) is linked via $\lambda = 2\pi/\kappa\,[\mathrm{m}]$. Hence, the smallest turbulent eddies appear in the rightmost part of the spectrum. Figure 2.2 schematically depicts the spectral representation of $E(\kappa)$ as a Fourier decomposition into wave numbers. The energy spectrum is divided into three ranges, each of which is assigned a representative length scale that relates to the various contributions to the turbulence energy budget, i.e., the supply, transfer and dissipation. The attributes of the ranges are:

- *production range*
  This range includes the large-scale energy-bearing eddies that contain approximately 90% of the TKE. Its characteristic length, given by the spectral maximum, is termed the integral length scale (L) and corresponds to the largest eddy size of the flow. This scale equals the order of magnitude of the characteristic (geometric) flow dimensions, whereby L similarly corresponds to the Reynolds number reference length. Depending on the quantities defined by equations (2.3) and (2.4), $L \sim k^{3/2}/\varepsilon$ applies. The energy spectrum function relates to L and an appropriate velocity scale u_L via $E \sim L\,u_L^2$.

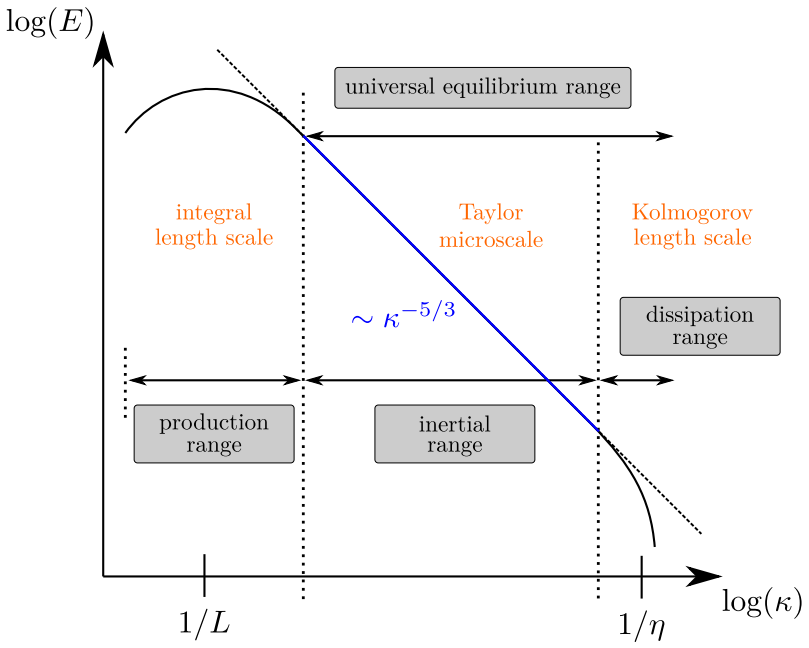

Figure 2.2: Schematic energy spectrum function $E(\kappa)$ in double logarithmic Fourier space representation.

- *dissipation range*
  The right end of the spectrum matches the dissipation range where the smallest turbulent scales occur. For sufficiently high Reynolds number flows their motions are assumed to be locally isotropic, cf. Kolmogorov et al. [1991a]. According to Kolmogorov's *first* similarity hypothesis the statistics of the small-scale eddies uniquely depend on ν and ε. Through dimensional analysis, employing ν [m^2/s] and ε [m^2/s^3], the so-called Kolmogorov microscales (of length, time and velocity) are obtained, i.e.,

$$\eta = \left(\nu^3/\varepsilon\right)^{1/4} \text{[m]}\,, \quad \tau_\eta = (\nu/\varepsilon)^{1/2} \text{[s]} \quad \text{and} \quad u_\eta = (\nu\varepsilon)^{1/4} \text{[m/s]}\,. \tag{2.5}$$

  By definition, the related Reynolds number is $\mathrm{Re}_\eta = \eta\, u_\eta/\nu \equiv 1$, implying the dominating viscous forces at these scales, where any velocity gradients are quickly smoothed by viscous damping. Relating macroscopic (L, t and u) large-scale quantities to the microscales, yields $L/\eta \sim \mathrm{Re}^{3/4}$, $t/\tau_\eta \sim \mathrm{Re}^{1/2}$ and $u/u_\eta \sim \mathrm{Re}^{1/4}$, implying the prevalent Reynolds number influence on the length scale ratio. At the highest wave numbers of the spectrum all kinetic energy dissipates via molecular viscosity into heat as displayed by the rapid decay, alias roll-off, close to $\kappa = 1/\eta$. The energy spectrum function of the dissipation range follows the proportionality $E \sim \eta\, u_\eta^2 = \varepsilon^{1/4}\,\nu^{5/4}$.

- *inertial range*
  This range fills the gap between the production and dissipation ranges. Its overall extent $\Delta\kappa$ is determined by the Reynolds number by relating the size of the largest to the smallest scales. The corresponding length scale is the Taylor microscale (λ_T). It is based on Kolmogorov's *second* similarity hypothesis that states the existence of a distinct separation of scales, i.e., $\eta \ll \lambda_T \ll L$, for high Reynolds number flows. Since the spectral energy transfer rate, i.e., the net directional energy transfer from

lower to higher wave numbers, is assumed to be constant within the inertial range, neither production mechanisms nor viscous effects are of importance. Thus, unlike the previously mentioned scales, the Taylor microscale is regarded as a hybrid scale obtained by the adjacent large- and small-scale eddy properties. Thus, the energy spectrum function of this range is given by the eminent *Kolmogorov -5/3 law*, i.e., $E \sim \lambda_T \, u_{\lambda_T}^2 = \varepsilon^{2/3} \, \kappa^{-5/3}$, using $\lambda_T = 1/\kappa$ and $u_{\lambda_T} = (\lambda_T \, \varepsilon)^{1/3}$, where $u \sim k^{1/2}$ and $k \sim (\lambda_T \, \varepsilon)^{2/3}$.

The combination of both similarity hypotheses constitutes Kolmogorov's *universal equilibrium theory* that states a universal form of the inertial and dissipation range, which holds for every high Reynolds number flow. The energy transfer rate of larger to smaller eddies is in the order of the dissipation rate of the smallest eddies since, otherwise, energy will accumulate or lapse at high wave numbers.

2.1.2 Energy Cascade

In general, the cascade involves the production and transfer of turbulent energy up to and including dissipation as a hierarchical process.

The mechanism of the energy cascade is based on vortex-stretching. Its starting point resembles the stretching of large diameter vortex lines through the main flow's velocity gradient, whereby energy is initially injected to the fluctuating motion. This is assigned to the production range of the energy spectrum. The largest and, moreover, energy-bearing eddies are characterized by anisotropy as well as instability and depend on the boundary conditions of a specific flow. The large-scale motion is virtually inviscid and therefore independent of the Reynolds number.

Neglecting viscous effects, Helmholtz's first theorem (conservation of angular momentum) involves the strength of a vortex tube, i.e, the circulation

$$\Gamma = \int_A \omega_\mathrm{i} \, \mathrm{d}A_\mathrm{i} \, , \tag{2.6}$$

where A_i is the cross section of the tube, to be constant along its pathway. Thus, stretching resp. a decrease of A leads to an augmented vorticity ω_i within the narrowed cross section. Associated with the stretching in one direction (e.g., x is the generating direction), the velocity components in y and z increase, while the length scale of the planar motion, i.e., the eddy size, decreases at each stage. Hence, the intensified motion in y and z with larger gradients, again, introduce smaller-scale vortex stretching in these directions. This continuable hierarchical mechanism, where energy is passed to successively smaller turbulent eddies, corresponds to the inertial range of the energy spectrum. Only turbulent scales of the same order of magnitude interact, which correlates to Kolmogorov's wide separation of scales. The *hypothesis of local isotropy states* that, after many stages of vortex stretching, the energy is equally distributed in three directions among the small-scale eddies, where the most vorticity resides. These dissipative scales are in a state of statistical equilibrium, cf. Kolmogorov et al. [1991b] and Bradshaw [1971].

Figure 2.3 depicts the vortex-stretching mechanism exemplarily shown for four ($m = 4$) stages (s_m), whereby $s \sim L/\eta \sim Re^{3/4}$ implied by the dotted interception at the right side of the transfer range. The number of generating directions (colored coordinates) at each stage equals 2^m, such that, e.g., 25 stages already possess $\mathcal{O}(10^7)$ generating directions.

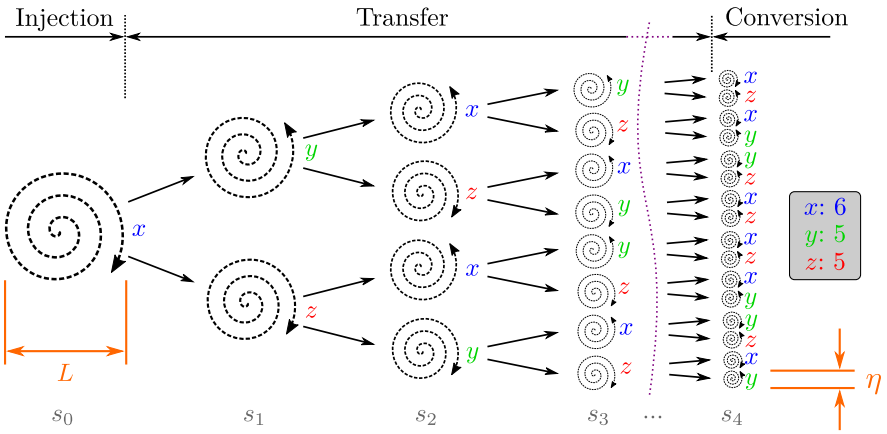

Figure 2.3: Illustration of the vortex-stretching mechanism where the colored coordinates mark the specific generating direction at each stage s. The largest eddy size is labeled with L and the smallest scale with η, respectively.

2.2 Statistical Approach

Since turbulent flows are characterized by random fluctuations of flow quantities, statistical approaches are required for the analysis. The principal cornerstone is the Reynolds decomposition of an instantaneous random variable ϕ , i.e., velocity, pressure or temperature,

$$\phi\left(\boldsymbol{x},t\right)=\overline{\phi}\left(\boldsymbol{x},t\right)+\phi'\left(\boldsymbol{x},t\right), \tag{2.7}$$

in a mean (bar) and fluctuation (prime) value, cf. Reynolds [1895]. Universally the mean value is assigned to the ensemble (E) average

$$\overline{\phi}_E\left(\boldsymbol{x},t\right)=\lim_{N\to\infty}\frac{1}{N}\sum_{n=1}^{N}\phi_n\left(\boldsymbol{x},t\right), \tag{2.8}$$

where n depicts the n-th realization (e.g., of an experiment or a simulation). Based on the ergodic hypothesis (Jacobs [1960]), the ensemble average equals the temporal (T)/spatial (S) mean for steady/homogeneous flows through

$$\overline{\phi}_T\left(\boldsymbol{x}\right)=\lim_{T\to\infty}\frac{1}{T}\int_{t}^{t+T}\phi\left(\boldsymbol{x},t\right)\mathrm{d}t\quad\text{resp.}\quad\overline{\phi}_S\left(t\right)=\lim_{V\to\infty}\frac{1}{V}\iiint_{V}\phi\left(\boldsymbol{x},t\right)\mathrm{d}V\,. \tag{2.9}$$

Furthermore, the decomposition includes

$$\overline{\overline{\phi}}=\overline{\phi},\quad\overline{\phi'}=0\quad\text{and}\quad\overline{\phi'\psi'}\neq0\,, \tag{2.10}$$

which implies vanishing first (one fluctuation included) statistical moments, i.e., $\overline{\overline{\phi}\,\psi'}=0$, whereas higher moments are not necessarily zero.

By substituting the Reynolds decomposition of the velocity $u_\mathrm{i}=\overline{u_\mathrm{i}}+u_\mathrm{i}'$ (short notation without spatial and temporal dependencies) into the left-hand side of the Navier-Stokes

(NS) momentum equation, subsequent temporal $\overline{(\cdot)}$ averaging leads to

$$\begin{aligned}\overline{\rho\,\frac{\mathrm{D}\,(\overline{u_\mathrm{i}}+u_\mathrm{i}')}{\mathrm{D}t}} &= \overline{\rho\,\frac{\partial\,(\overline{u_\mathrm{i}}+u_\mathrm{i}')}{\partial t}+\rho\left(\overline{u_\mathrm{j}}+u_\mathrm{j}'\right)\frac{\partial\,(\overline{u_\mathrm{i}}+u_\mathrm{i}')}{\partial x_\mathrm{j}}}\\ &= \rho\,\frac{\partial\overline{u_\mathrm{i}}}{\partial t}+\rho\overline{u_\mathrm{j}}\,\frac{\partial\overline{u_\mathrm{i}}}{\partial x_\mathrm{j}}+\rho\,\frac{\partial\overline{u_\mathrm{i}'u_\mathrm{j}'}}{\partial x_\mathrm{j}}\,.\end{aligned} \tag{2.11}$$

Arising from the nonlinear convective term, the second-order tensor containing velocity covariances associated with the fluid's density $\rho\,\overline{u_\mathrm{i}'u_\mathrm{j}'}$ [$\mathrm{kgm^{-1}s^{-2}}$] is termed Reynolds stress tensor (RST). Despite the denotation, it does not represent a constitutive relation. Rather, it is due to the fact that the RST has the dimension of a stress and, therefore, can be harmonized with the viscous stress tensor of Newtonian fluids

$$\overline{\tau_\mathrm{ij}} = 2\mu S_\mathrm{ij}-\frac{2}{3}\,\mu\,\frac{\partial\overline{u_\mathrm{k}}}{\partial x_\mathrm{k}}\,\delta_\mathrm{ij}\,, \tag{2.12}$$

with the Kronecker delta (δ_ij) and the symmetrical strain rate tensor

$$S_\mathrm{ij} = \frac{1}{2}\left(\frac{\partial\overline{u_\mathrm{i}}}{\partial x_\mathrm{j}}+\frac{\partial\overline{u_\mathrm{j}}}{\partial x_\mathrm{i}}\right)\,, \tag{2.13}$$

at the r.h.s. of the (*compressible*) Reynolds-averaged Navier-Stokes (RANS) momentum equation

$$\rho\,\frac{\partial\overline{u_\mathrm{i}}}{\partial t}+\rho\overline{u_\mathrm{j}}\,\frac{\partial\overline{u_\mathrm{i}}}{\partial x_\mathrm{j}} = -\frac{\partial\overline{p}}{\partial x_\mathrm{i}}+\frac{\partial}{\partial x_\mathrm{j}}\left(\overline{\tau_\mathrm{ij}}-\rho\,\overline{u_\mathrm{i}'u_\mathrm{j}'}\right)+\overline{f_\mathrm{i}}\,, \tag{2.14}$$

where $\overline{p}$ denotes the pressure and $\overline{f_\mathrm{i}}$ [$\mathrm{kgm^{-2}s^{-2}}$] is a force density, each given as mean values. The RST is a symmetric 3×3 tensor ($\overline{u_\mathrm{i}'u_\mathrm{j}'}=\overline{u_\mathrm{j}'u_\mathrm{i}'}$) with totally six unknowns. Furthermore, the trace is linked to the TKE (2.3) via $k=\overline{u_\mathrm{i}'u_\mathrm{i}'}/2$.

Assuming incompressible ($\rho=$ const.) flows, where $\partial\,\overline{u_\mathrm{k}}/\partial\,x_\mathrm{k}=0$ (divergence-free velocity field) follows from the mass continuity equation, the *incompressible* RANS momentum equation reads

$$\begin{aligned}\frac{\partial\overline{u_\mathrm{i}}}{\partial t}+\overline{u_\mathrm{j}}\,\frac{\partial\overline{u_\mathrm{i}}}{\partial x_\mathrm{j}} &= -\frac{\partial\overline{P}}{\partial x_\mathrm{i}}+\frac{\partial}{\partial x_\mathrm{j}}\left(2\nu\,S_\mathrm{ij}-\overline{u_\mathrm{i}'u_\mathrm{j}'}\right)+\overline{F_\mathrm{i}}\\ &= -\frac{\partial\overline{P}}{\partial x_\mathrm{i}}+\nu\,\frac{\partial^2\overline{u_\mathrm{i}}}{\partial x_\mathrm{j}^2}-\frac{\partial\overline{u_\mathrm{i}'u_\mathrm{j}'}}{\partial x_\mathrm{j}}+\overline{F_\mathrm{i}}\,,\end{aligned} \tag{2.15}$$

with $\overline{P}=\overline{p}/\rho$ and $\overline{F_\mathrm{i}}=\overline{f_\mathrm{i}}/\rho$. In this case, $\overline{u_\mathrm{i}'u_\mathrm{j}'}$ [$\mathrm{m^2s^{-2}}$] is called specific RST.

2.2.1 Correlations

As outlined before, averaged nonlinear fluctuating quantities can be non-zero. In this case they are considered correlated, otherwise uncorrelated. There are two fundamental definitions of correlations which are important for the statistical evaluation of turbulent flows. These are the *two-point correlation* (TPC) tensor

$$R_\mathrm{ij}(\boldsymbol{x},t,\boldsymbol{r}) = \overline{u_\mathrm{i}'(\boldsymbol{x},t)\,u_\mathrm{j}'(\boldsymbol{x}+\boldsymbol{r},t)}\,, \tag{2.16}$$

incorporating the product of fluctuations at the same time instant, spatially separated by the displacement $\boldsymbol{r}$. The *autocorrelation* tensor

$$R_{\mathrm{ij}}(\boldsymbol{x}, t, t^*) = \overline{u_{\mathrm{i}}'(\boldsymbol{x}, t)\, u_{\mathrm{j}}'(\boldsymbol{x}, t + t^*)}\,, \tag{2.17}$$

is defined at a single point at different time instants, where t^* denotes the time increment. This expression is valid for statistically stationary flows, where the temporal difference and no explicit instants are of relevance. Subsequently, the abbreviated notations $R_{\mathrm{ij}}(\boldsymbol{r})$ and $R_{\mathrm{ij}}(t^*)$ are used. The tensors' traces relate to the TKE through

$$k = \frac{R_{\mathrm{ii}}(\boldsymbol{r} = \boldsymbol{0})}{2} = \frac{R_{\mathrm{ii}}(t^* = 0)}{2}\,. \tag{2.18}$$

An important measure to quantify length scales of turbulent structures – related to the main directions (ii) – results from

$$L_{\mathrm{ii}} = \frac{1}{R_{\mathrm{ii}}(\boldsymbol{r} = \boldsymbol{0})} \int_a^b R_{\mathrm{ii}}(\boldsymbol{r})\, \mathrm{d}\boldsymbol{r}\,. \tag{2.19}$$

There exist several different length scales depending on the integration limits a and b. The most common refers to $a = 0$ and b corresponding to the first zero-passage of $R_{\mathrm{ii}}(\boldsymbol{r})$, which is the integral length scale of the largest turbulent eddies.

The wave number (spatial) and frequency (temporal) energy spectra E_{ij} are linked to the correlation tensors via Fourier transform, i.e., E_{ij} and R_{ij} form a Fourier transform pair. Within the scope of this work, the evaluation of one-dimensional energy spectra is convenient defined by (e.g., depicted for κ_1 in x direction, where $\boldsymbol{r} = \boldsymbol{e}_1\, r_1$)

$$E_{\mathrm{ij}}(\kappa_1) = \frac{1}{\pi} \int_{-\infty}^{\infty} R_{\mathrm{ij}}(\boldsymbol{e}_1\, r_1)\, e^{-i\,\kappa_1\, r_1} \mathrm{d}r_1 \tag{2.20}$$

in wave number space. The inversion reads

$$R_{\mathrm{ij}}(\boldsymbol{e}_1\, r_1) = \frac{1}{2} \int_{-\infty}^{\infty} E_{\mathrm{ij}}(\kappa_1)\, e^{i\,\kappa_1\, r_1} \mathrm{d}\kappa_1\,. \tag{2.21}$$

For the subsequent evaluations, the short notation $[E/R]^{x_{\mathrm{i}}}_{u_{\mathrm{i}}' u_{\mathrm{j}}'}$ or $[E/R]^{x_{\mathrm{i}}}_{u_{\mathrm{i}} u_{\mathrm{j}}}$ is used for wave number spectra resp. TPCs, where the superscript specifies the Cartesian direction into which a fluctuating quantity is considered as denoted by the double subscript.

Likewise, the Fourier pair in (ordinary) frequency $f = \omega/(2\pi)\,[\mathrm{s}^{-1}]$ space is given as

$$E_{\mathrm{ij}}(f) = \frac{1}{\pi} \int_{-\infty}^{\infty} R_{\mathrm{ij}}(t^*)\, e^{-i\,2\pi\, f\, t^*} \mathrm{d}t^* \quad \text{and} \quad R_{\mathrm{ij}}(t^*) = \frac{1}{2} \int_{-\infty}^{\infty} E_{\mathrm{ij}}(f)\, e^{i\,2\pi\, f\, t^*} \mathrm{d}t^*\,, \tag{2.22}$$

based on the autocorrelation $R_{\mathrm{ii}}(t^*)$, where the one-dimensional spectral function $E_{\mathrm{ij}}(f)$ is commonly referred to as the *power spectral density* (PSD).

2.2.2 Turbulent Boundary Layer

Since the influence of solid boundaries determines the majority of industrial relevant flows, i.e., wall-bounded shear flows, a key significance is attributed to the characteristics of the turbulent boundary layer (TBL). Relatively simple, non-complex geometries include, e.g., channel, pipe, or flat plate flows. Considering an incompressible ($\rho = \text{const.}$), stationary ($\partial/\partial t = 0$) turbulent flow bounded by two infinite, i.e., periodically extended, axis-parallel plates located in the x-z plane with a distance of $2H$ in wall-normal (y) direction, driven by an axial (x) pressure gradient without mean acceleration $\overline{F_i} = \mathbf{0}$. This flow is commonly known as turbulent channel flow (TCF), cf. Fig. 2.4.

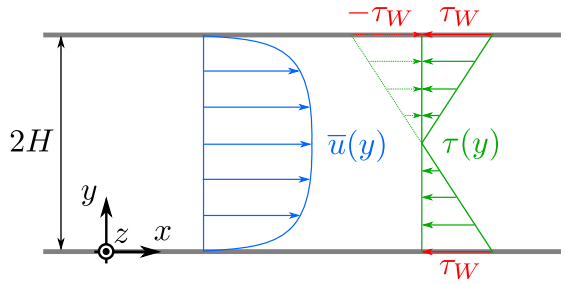

Figure 2.4: Sketch of a turbulent channel flow illustrating the mean axial velocity $\overline{u}(y)$ and the mean shear stress profile $\tau(y)$.

Subsequently, the (mean) velocity variables $\overline{u}$, $\overline{v}$ and $\overline{w}$ relate to the Cartesian coordinates in x, y and z. Assuming an incompressible fully developed ($\partial\overline{u}_\mathrm{i}/\partial x = 0$) and two-dimensional flow, i.e., the latter implies homogeneity ($\overline{w} = 0$) in lateral (z) direction, the continuity equation gives $\overline{v} \equiv 0$, whereby $\overline{u} = u(y)$ and $\partial/\partial y \to \mathrm{d}/\mathrm{d}y$ apply.

To this end, the integration of the mean momentum equation (2.15) in wall-normal direction yields

$$\frac{\overline{p}}{\rho} + \overline{v'v'}(y) = \frac{p_W(x)}{\rho} \quad \Leftrightarrow \quad \frac{\partial\overline{p}}{\partial x} = \frac{\mathrm{d}p_W}{\mathrm{d}x}\,, \tag{2.23}$$

where p_W denotes the mean pressure on the channel's walls. The right equation reveals the axial pressure gradient to be uniform across the flow. Furthermore, the simplified axial mean momentum equation reads

$$0 = -\frac{1}{\rho}\frac{\partial\overline{p}}{\partial x} + \frac{\mathrm{d}}{\mathrm{d}y}\left(\nu\frac{\mathrm{d}\overline{u}}{\mathrm{d}y} - \overline{u'v'}\right)\,. \tag{2.24}$$

Utilizing (2.23) and supposing a linear total shear stress, cf. Fig. 2.4,

$$\tau(y) = \tau_W\left(1 - \frac{y}{H}\right)\,, \tag{2.25}$$

with the *wall shear stress* τ_W, which is the prominent quantity to judge the skin friction of an object in a flow, gives

$$\frac{\partial\overline{p}}{\partial x} = \frac{\mathrm{d}p_W}{\mathrm{d}x} = \frac{\mathrm{d}\tau}{\mathrm{d}y} = -\frac{\tau_W}{H}\,. \tag{2.26}$$

This involves the balance of the axial pressure gradient by the wall-normal total shear stress gradient. Substituting (2.26) in (2.24), the subsequent integration results in

$$\tau(y) = \nu\rho\frac{\mathrm{d}\overline{u}}{\mathrm{d}y} - \rho\overline{u'v'} \qquad [\rightarrow \tau_{\mathrm{tot}} = \tau_{\mathrm{vis}} + \tau_{\mathrm{R}_{xy}}]\,, \tag{2.27}$$

which contains the partition of the total shear stress into a viscous and Reynolds stress contribution. The notation of $\tau(y)$ omits the bar, since from an engineering perspective generally the mean friction is of focal interest.

Due to the no-slip boundary condition at the surface, i.e., $u_{\mathrm{i}}(y = 0) = \mathbf{0}$, Reynolds stresses are zero per definition, cf. (2.7). Hence, the wall shear stress is entirely composed of the viscous contribution, i.e., $\tau_W = \tau_{\mathrm{vis}}$. Based on τ_W, the *friction velocity*

$$u_\tau = \sqrt{|\tau_W|/\rho} \tag{2.28}$$

corresponds to the (viscous) velocity scale of the near-wall region, which is the major quantity for normalization. Likewise as for τ_W, the bar is omitted since the friction velocity ordinary refers to an averaged value. Furthermore, the *friction Reynolds number* involves u_τ via

$$\mathrm{Re}_\tau = \frac{u_\tau\, H}{\nu}\,. \tag{2.29}$$

Based on the derivation related to the TCF, the reference length H complies with the half-channel height. Replacing the latter constant by the variable y leads to

$$y^+ = \frac{u_\tau\, y}{\nu}\,, \tag{2.30}$$

i.e., a local (friction) Reynolds number termed nondimensional wall distance, also referred to as wall units. The belonging nondimensional velocity is $u^+ = \overline{u}/u_\tau$. In the context of H or y/H and y^+, the terms outer and inner variables (coordinates)/scaling are used. The outer (bulk) and inner (friction) Reynolds number are intertwined by Dean's empirical correlation (cf. Dean [1978]) which reads

$$\mathrm{Re}_B = \frac{u_B\, H}{\nu} \approx \left(\frac{8}{0.073}\right)^{4/7} \frac{\mathrm{Re}_\tau^{8/7}}{2}\,, \tag{2.31}$$

$$\approx 7.32\,\mathrm{Re}_\tau^{8/7} \qquad \Leftrightarrow \qquad \mathrm{Re}_\tau \approx 0.175\mathrm{Re}_B^{7/8}\,. \tag{2.32}$$

The bulk (u_B) and centerline (u_C) velocity (each averaged) related Reynolds numbers are empirically linked by

$$\mathrm{Re}_C \approx 1.16\,\mathrm{Re}_B \quad \Leftrightarrow \quad u_C \approx 1.16\,u_B\,, \tag{2.33}$$

e.g., compliant with Moser et al. [1999].

According to the fundamental work of Prandtl [1925], the so-called inner layer of the mean velocity profile – of a flow at sufficiently high Reynolds number – is linked to the law of the wall through

$$u^+ = f(y^+) \tag{2.34}$$

only depending on viscous scales (u_τ and y^+). The dimensionless function $f(y^+)$ is explicitly defined for two distinct regions. Among these is the *viscous sublayer* ($y^+ < 5$), where

$$u^+ = y^+ \tag{2.35}$$

applies when neglecting turbulent contributions of $\mathcal{O}(y^{+4})$ and a vanishing pressure gradient contribution of $\mathcal{O}(y^{+2}/\mathrm{Re}_\tau)$. The significant contribution of $\tau_{\mathrm{vis}}/\tau_{\mathrm{tot}}(y^+ = 5) \approx 0.9$ emphasizes governing viscous effects within the immediate vicinity of the wall with $y/H \lll 1$.

Moreover, a logarithmic relation is found for $y^+ > 30$ through the mixing length hypothesis and by neglecting viscous contributions, i.e.,

$$u^+ = \frac{\ln(y^+)}{\kappa} + C^+ \,, \tag{2.36}$$

where κ denotes the von Kármán constant and C^+ is a nondimensional (integration) constant. Equation (2.36) is referred to as the logarithmic law of the wall or short *log law*, which retains valid up to $y/H \approx 0.3$. Within the stated interval the Reynolds shear stress contribution increases from $\tau_{\mathrm{R}_{xy}}/\tau_{\mathrm{tot}}(y^+ = 30) \approx 0.85$ to $\tau_{\mathrm{R}_{xy}}/\tau_{\mathrm{tot}}(y/H = 0.3) \approx 0.95$. The empirically well-determined constants are

$$\kappa = 0.41 \ [\pm 5\%] \quad \text{and} \quad C^+ = 5 \ [\pm 5\%] \,, \tag{2.37}$$

as per, e.g., Schlichting et al. [1955] or Kline et al. [1969] among many succeeding others, with minor variations depending on the specific flow under consideration, e.g., on the surface roughness or the Reynolds number.

Figure 2.5 illustrates the characteristic mean velocity profile of a TBL. The example specifically relates to a TCF at $\mathrm{Re}_\tau = 2000$ which has implications for the explicitly statet values of y^+ and y/H. Besides the regions introduced above, there are several others, whose following representation is based on Pope [2000]. The figure features two abscissae, with the lower one in inner and the upper one in outer scaling, respectively, to take account for assorted definitions based on y^+ and/or y/H. The viscous sublayer and the log law are linked through the *buffer layer* ($5 < y^+ < 30$). Both the viscous sublayer and the buffer layer are assigned to the *viscous wall region*. The latter extents up to $y^+ = 50$, where, although $\tau_{\mathrm{vis}}/\tau_{\mathrm{tot}} \approx 0.1$, the viscous stress contribution is still considered as influential. At a further distance from the wall, i.e., $y/H > 0.3$ (equivalent to $y^+ = 600$ for the TCF at $\mathrm{Re}_\tau = 2000$), the profile clearly deviates from the log law showing an augmented mean velocity. This region is termed *wake region*, also known as velocity defect law, cf. Coles [1956].

The inner and outer layer have an *overlap region*, as indicated by the bicolored curved line in the Figure. The lower bound is $y^+ = 50$ ($y/H = 1/40$ equiv.) and the upper one is indicated in outer scaling with $y/H = 0.1$, which equals $y^+ = 200$ as part of the example. Despite its description based on the TCF, as outlined here, the TBL characteristic generally applies for various wall-bounded turbulent flows.

An alternative to the log law goes back to Prandtl, i.e., the power law

$$u^+ = A\,(y^+)^{1/n} \tag{2.38}$$

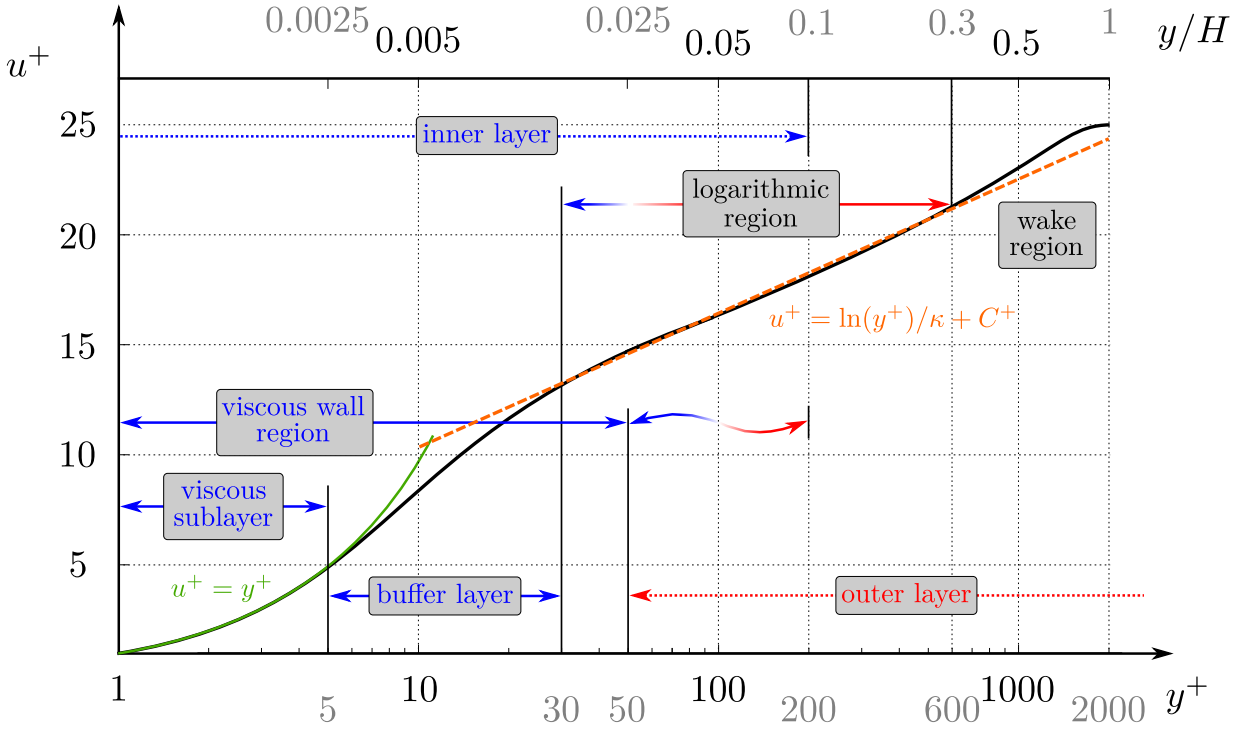

Figure 2.5: Characteristic mean velocity profile of a turbulent boundary layer. The depicted example refers to a fully developed turbulent channel flow at $\mathrm{Re}_\tau = 2000$. The classification is in accordance with Pope [2000].

relation, where A and n are empirically dependent values. Prandtl initially stated $n = 7$, whilst comprehensive experiments yield $n \in [6, 8]$, to incorporate the Reynolds number dependency. The switch from $u^+ = y^+$ to the power law occurs at y_S^+, located within the buffer layer. For instance, Werner and Wengle [1993] employed $A = 8.3$ and $n = 7$

$$u^+ = \begin{cases} y^+ & y_\mathrm{S}^+ \leq A^{n/(n-1)} \approx 11.8 \\ 8.3\,(y^+)^{1/7} & \text{otherwise} \end{cases} . \tag{2.39}$$

The rationale for the power law is given by the improved agreement with experimental data for specific configurations, e.g., pipe flows.

To overcome the issue of piecewise-defined functions, Spalding [1961] introduced an *universal law of the wall* based on a u^+ power series expansion, viz.

$$y^+ = u^+ + \exp^{-\kappa C^+} \left[\exp^{\kappa u^+} - \left(1 + \kappa\, u^+ + (\kappa\, u^+)^2/2! + \mathcal{O}((u^+)^3)\right) \right] , \tag{2.40}$$

shown up to second order. This single formula is advantageous for practical reasons and matches the buffer layer essentially better. Another established option is the compound wall treatment introduced by Popovac and Hanjalic [2007]. Nevertheless, e.g., George [2007] outlined that an overall and exact universality does not hold since wall-bounded flows (boundary layers, channel, or pipe flows) possess fundamentally different properties whereby formulas can only be adopted and exploited for specific flows.

2.3 Numerical Approaches

Several fundamental approaches exist to simulate turbulent flows, distinguished by their computational cost, resolution properties and complexity. The classification is based on the ratio of the resolved to the modeled scales as outlined by the schematic decomposition of the energy spectrum in Figure 2.6. The direct numerical simulation (DNS) resolves all scales without a model and thus implies the highest computational cost. In contrast, the whole spectrum is modeled in a RANS simulation, and the conditions are inverted. The highest modeling requirements accompany the lowest expense of computational resources. The (very) large eddy simulation ((V)LES) is an intermediate approach where a part of the spectrum is resolved. At the best, an LES aims to resolve $\geq 80\%$ of the spectrum, and a VLES down to 50%, ensuring the large anisotropic scales being captured by the grid. To this end, the spatial grid discretization typically serves as a filter, where the unresolved subgrid scales (SGS) need to be modeled. Hence, (V)LES and DNS are summarized under scale-resolving simulations (SRS).

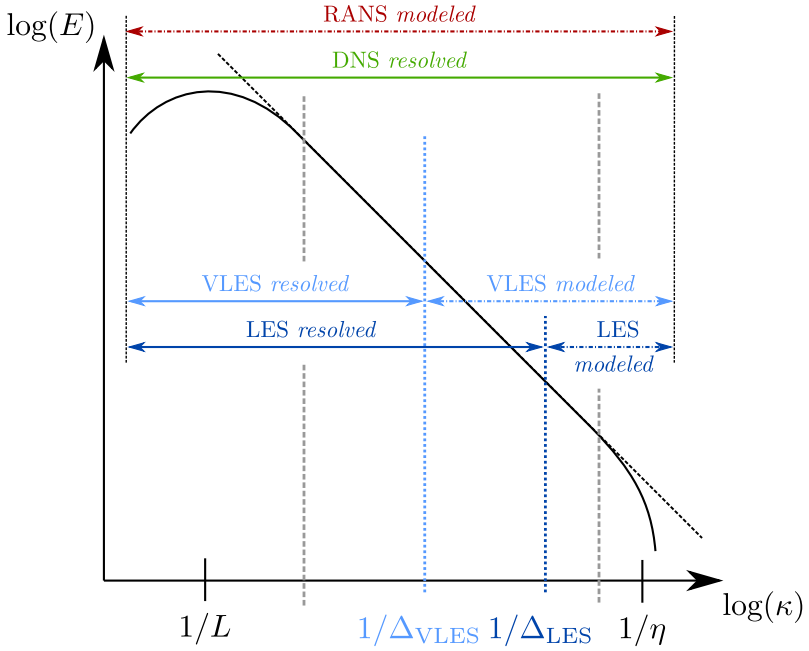

Figure 2.6: Schematic decomposition of the turbulent energy spectrum for various simulation approaches.

The subsequent sections, depicting the approaches mentioned above, do not claim to be complete and should be regarded as a brief overview instead.

2.3.1 Direct Numerical Simulation

A direct numerical simulation, the term was introduced by Orszag [1970], conforms the exact and time-dependent solution of the Navier-Stokes continuity and momentum equations in three dimensions without using any sort of turbulence model. To demonstrate its computational effort, Wilcox [1993] estimated the required number of discrete nodes to spatially resolve the Kolmogorov length scale for a 3D turbulent channel flow on a uniform

(uni) grid at

$$N_{\text{uni}} \approx (110\,\text{Re}_\tau)^{9/4}\,, \tag{2.41}$$

with Re_τ related to the half-channel height H. Employing a non-uniform discretization in wall-normal direction, featuring refined (ref) zones in the vicinity of the solid boundary where the smallest eddies reside, the DNS evaluations of Kim et al. [1987] lead to a decrease by a factor of ≈ 3300 in this case, i.e.,

$$N_{\text{ref}} \approx (3\,\text{Re}_\tau)^{9/4}\,. \tag{2.42}$$

Assuming the explicit time step (Δt) of the DNS to match the Kolmogorov time scale (τ_η) gives

$$\Delta t = \tau_\eta \approx 0.006\,\frac{\delta}{u_\tau}\,\text{Re}_\tau^{-1/2}\,. \tag{2.43}$$

To insure a statistically steady (S) state as the basis for evaluations, a period of $T_\text{S} \approx 10H/u_\tau\,[\approx 200H/u_B]$ is required for averaging, which equals a total of $T_\text{S}/(\Delta t) \approx 1700\,\text{Re}_\tau^{1/2}$ discrete time steps. Additionally, the transient phase extends the computational effort, until the flow is fully developed from the initial conditions. From experience the overhead can amount up to 25% of the total runtime. Considering a high but industrially realistic Reynolds number of $\text{Re}_\tau = 10^5$ requires $\mathcal{O}(10^{11})$ nodes and $\mathcal{O}(10^5)$ time steps, yielding $\mathcal{O}(10^{16})$ node updates in total. This insistently displays the unfeasible computational effort.

Eddy Viscosity Concept

Once the DNS resolution requirements are no longer met by the discretization, turbulence modeling strategies are essential. The prominent approach to model unresolved scales of the turbulent energy spectrum is given by the eddy viscosity concept. Phenomenologically, it is based on the hypothesis, that turbulent fluctuations effect the mean flow by dissipating energy, which is considered by introducing an additional turbulent viscosity ν_t. There exist a variety of so-called *eddy viscosity models* (EVM) ranging from simple isotropic to substantially more complex anisotropic approaches. Their application depends on the extent of the unresolved part of the spectrum. To this end, high-fidelity models are crucial for RANS simulations, where the entire spectrum requires modeling. Furthermore, these approaches assume ν_t independent of the resolution since an increase in the latter improves the approximation quality of gradients but must not be associated with vanishing eddy viscosity. For LES, the modeling properties and efforts are fundamentally different since most of the spectrum is resolved, and the model only addresses the isotropic small-scales, cf. right stages in Fig. 2.3. Moreover, the model is directly linked to the resolution by a filter, hence ν_t vanishes in the fine resolution limit.

The most common EVM refers to the Boussinesq viscosity model, i.e., an isotropic approach containing a link between the mean strain and the Reynolds stresses via

$$\overline{u_\text{i}' u_\text{j}'} \sim -2\nu_t\,S_\text{ij}\,, \tag{2.44}$$

which is analogous to the stress tensor caused by molecular viscosity, though the eddy viscosity usually varies in space and time.

2.3.2 Reynolds-Averaged Navier-Stokes Simulation

The RANS momentum equation is not directly solvable due to the occurrence of the RST ($\overline{u_\mathrm{i}' u_\mathrm{j}'}$), which contains the influence of the fluctuating part on the mean flow. As the number of unknowns exceeds the number of equations by 6 this is known as the closure problem. There are two main approaches to this problem, i.e., *Reynolds stress* (transport) *models* (RSM) and eddy viscosity models (EVM).

The former rest upon a differential transport equation $\mathrm{D}\overline{u_\mathrm{i}' u_\mathrm{j}'}/\mathrm{D}t$ for the RST, providing 6 equations for the 6 unknown individual Reynolds stress components. The distinct shortcoming is the intricate form of the equations' right-hand sides, which are, in addition, mainly not closed again as they are composed of unknown double correlations or even third statistical moments ($\overline{u_\mathrm{i}' u_\mathrm{j}' u_\mathrm{k}'}$) occur. RSM closures involve mathematics of increased complexity and the development is usually aborted at this point, requiring modeling strategies. Thus, the RSM merely represents an approximation of the exact Reynolds stress transport. Nevertheless, the RSM is regarded as the classical and most complete turbulence modeling approach as it considers non-local and history effects by concept.

Moreover, there exists a variety of EVMs ranging from zero-(algebraic), over one-(e.g., Spalart and Allmaras [1992]) to two-equation models for determining ν_t. The involvement of transport equations of turbulent properties enables history effects to be taken into account, where the most widely used ones are the k-ε of Launder and Spalding [1974] and the shear stress transport (SST) k-ω model by Menter [1993], comprising transport equations for the TKE and dissipation (ε) or specific dissipation (ω) rate of TKE. All these RANS closures inhere a variety of semi-empirical model coefficients.

2.3.3 Large Eddy Simulation

This section intends to provide a concise overview of the gist and common practices of LES. For further details, the reader is referred to the comprehensive works of, e.g., Sagaut [2001] and Fröhlich [2006], from which the subsequent part is analogously adopted.

The LES approach rests upon separating the flow-dependent large scales from the universal small scales through a wave number related low-pass filter of the exact solution. The most common and primordial (Leonard [1975]) approach is given by employing a homogeneous spatial filter

$$\overline{\chi}(x_\mathrm{i}) = \int_\Omega G(x_\mathrm{i} - \xi_\mathrm{i})\, \chi(\xi_\mathrm{i})\, \mathrm{d}\xi_\mathrm{i}, \tag{2.45}$$

via the domain-spanning (Ω) three dimensional integration of a so-called convolution product, where G is the convolution or filter kernel and $\chi(\xi_\mathrm{i})$ denotes an instantaneous, unfiltered generic flow quantity. As a result, the filtered quantity resolved by the grid is denoted by the bar. The kernel, localized within $|x_\mathrm{i} - \xi_\mathrm{i}| = \mathcal{O}(\Delta)$, where a Δ is the filter width or spatial cutoff length, satisfies

$$\int_\Omega G(x_\mathrm{i} - \xi_\mathrm{i})\, \mathrm{d}\xi_\mathrm{i} = 1\,, \quad \overline{\phi + \psi} = \overline{\phi} + \overline{\psi} \quad \text{and} \quad \frac{\overline{\partial \psi}}{\partial x_\mathrm{i}} = \frac{\partial \overline{\psi}}{\partial x_\mathrm{i}} \quad \left[\frac{\overline{\partial \psi}}{\partial t} = \frac{\partial \overline{\psi}}{\partial t}\right], \tag{2.46}$$

denoting the conservation of constants, linearity, and commutation with derivatives. The standard filters are a Gaussian, a box, or a sharp cutoff. Applying the filter (2.45) to the

incompressible NS equations results in

$$\frac{\partial \overline{u}_\mathrm{i}}{\partial x_\mathrm{i}} = 0 \tag{2.47}$$

$$\frac{\partial \overline{u}_\mathrm{i}}{\partial t} + \frac{\partial \overline{u}_\mathrm{i}\overline{u}_\mathrm{j}}{\partial x_\mathrm{j}} = -\frac{\partial \overline{P}}{\partial x_\mathrm{i}} + \nu \frac{\partial^2 \overline{u_\mathrm{i}}}{\partial x_\mathrm{j}^2} - \frac{\partial \tau_\mathrm{ij}}{\partial x_\mathrm{j}}\,, \tag{2.48}$$

the filtered Navier-Stokes equations, where τ_ij [$\mathrm{m^2 s^{-2}}$] is the (specific) subgrid scale (SGS) tensor defined by

$$\tau_\mathrm{ij} = \overline{u_\mathrm{i} u_\mathrm{j}} - \overline{u}_\mathrm{i}\overline{u}_\mathrm{j} \tag{2.49}$$

$$\begin{aligned}[&= \overline{\left(\overline{u}_\mathrm{i} + u'_\mathrm{i}\right)\left(\overline{u}_\mathrm{j} + u'_\mathrm{j}\right)} - \overline{u}_\mathrm{i}\overline{u}_\mathrm{j} \\ &= \overline{\overline{u}_\mathrm{i}\overline{u}_\mathrm{j}} + \overline{\overline{u}_\mathrm{i} u'_\mathrm{j}} + \overline{u'_\mathrm{i}\overline{u}_\mathrm{j}} + \overline{u'_\mathrm{i} u'_\mathrm{j}} - \overline{u}_\mathrm{i}\overline{u}_\mathrm{j} \,]\,,\end{aligned} \tag{2.50}$$

which determines the influence of the unresolved on the resolved scales. To this end, the nonlinear term $\overline{u_\mathrm{i} u_\mathrm{j}}$ in (2.49) is formally decomposed via

$$u_\mathrm{i} = \overline{u}_\mathrm{i} + u'_\mathrm{i}\,, \tag{2.51}$$

into a filtered (bar) and unfiltered (prime) part. The filtered quantities are the grid scales (GS) and the unfiltered ones are the subgrid scales, respectively. This decomposition is not to be confounded with the Reynolds averaging decomposition (2.7) since they possess fundamentally different properties.

Equation (2.48) has the same form as the incompressible RANS equation (2.15) likewise entailing the demand for a closure of the SGS tensor. The most simple and widely used approximation is the Smagorinsky-Lilly (SL) subgrid scale model, which is based on the Boussinesq hypothesis, and joins a gradient-diffusion model (cf. Smagorinsky [1963]) with a one-equation model (cf. Lilly [1966]). It is to be noted, that all terms of (2.50) are lumped in this model, despite their various physical equivalents and scales. The SL approach is based on

$$\tau^d_\mathrm{ij} = -2\nu_t\,\overline{S_\mathrm{ij}}\,, \tag{2.52}$$

where ν_t [$\mathrm{m^2 s^{-1}}$] denotes the turbulent/eddy viscosity and $\overline{S_\mathrm{ij}}$ [$\mathrm{s^{-1}}$] is the filtered strain rate tensor. The superscript (d) indicates the relation to the deviatoric, i.e., anisotropic, part of the SGS tensor $\tau^d_\mathrm{ij} = \tau_\mathrm{ij} - \tau_\mathrm{kk}/3\,\delta_\mathrm{ij}$. The latter is attributed to the traceless strain rate tensor, $\overline{S}_\mathrm{ii} = 0$, due to $\partial\,\overline{u}_\mathrm{i}/\partial x_\mathrm{i} = 0$, cf. (2.47). For compensation the pressure term is impinged by a trace-related pseudo pressure through $\overline{P} = \overline{P} + \tau_\mathrm{kk}/3\,\delta_\mathrm{ij}$. The assumption of an appropriate length (L_t) and velocity (u_t) scale ($\nu_t \sim L_t\,u_t$) yields the expression for the turbulent viscosity

$$\nu_t = (C_S\,\Delta)^2\sqrt{2\,\overline{S}_\mathrm{ij}\,\overline{S}_\mathrm{ij}}\,, \tag{2.53}$$

where C_S is the Smagorinsky constant, or better coefficient, which is usually within a relatively wide range, 0.1 (cf. Deardorff [1970]) $\leq C_S \leq 0.23$ (cf. Lilly [1966]), adjusted to match/optimize the flow under consideration. Assuming an infinite Reynolds number ($\nu \to 0$), an inertial range spectrum and a sharp cutoff filter (at $k_F = \pi/\Delta$), Meyers and

Sagaut [2006] indicate a theoretical value of $C_{S\infty} = 0.173$. Moreover, Δ is the filter width, usually set to $\Delta = (\Delta_1\Delta_2\Delta_3)^{1/3}$, i.e., the average cell length of the computational grid, and the square root expression defines a norm of the strain rate tensor. Among the drawbacks of the SL SGS model are the flow dependent nature of the Smagorinsky coefficient, where even an adoption is not able to capture local and temporal variations, the non-vanishing turbulent viscosity for laminar flows and the prevention of energy backscatter. Germano et al. [1991] introduced an advanced model featuring a dynamic eddy viscosity depending on the flow characteristics in space and time to eradicate these issues. A further development by Piomelli and Liu [1995] satisfies mathematical consistency and improves the numerical stability of the model.

There are considerably more proposed SGS models of rising complexity for LES in literature, e.g., closely resembling those of the RANS EVM context. However, these are far beyond the scope of the underlying work.

Owing to the filtering, an LES has restrictive resolution requirements, e.g., Piomelli and Chasnov [1996], Baggett et al. [1997] or Choi and Moin [2012], near solid boundaries to confine the modeled part of the spectrum. To this end, the options of either wall-resolved, e.g., Fröhlich et al. [2005], Uzun and Malik [2017], Li et al. [2021] and Rizzetta and Garmann [2022] or, more frequently, wall-modeled LES, e.g., Piomelli et al. [1989], Cabot and Moin [2000], Piomelli and Balaras [2002], Chung and Pullin [2009], Kawai and Larsson [2012], Malaspinas and Sagaut [2014] or Gao et al. [2019] exist. The former approach implies non-uniform grids featuring refined cells near the wall, whereas the latter maps the influence of the wall on the (uniform) grid through wall functions.

Another class of LES is given by so-called implicit LES approaches, where the model is implicitly included through the truncation error of the convective terms' discretization, cf. Hickel et al. [2006] or Adams and Hickel [2009] for further details.

2.3.4 Very Large Eddy Simulation

The class of very large eddy simulations aims at reducing the computational effort even further. A VLES is a combination of RANS and LES harnessing the advantageous accuracy of LES and the substantial lower effort of RANS, cf. Speziale [1998] or Ruprecht et al. [2004]. The LES is applied to the outer flow and the RANS formulation is used to model the turbulent boundary layer. There are many derivatives or synonyms, among others termed hybrid RANS-LES, e.g., Girimaji et al. [2015] and Hoarau et al. [2018] or non-zonal, e.g., Spalart et al. [1997, 2006] and Shur et al. [2008], and zonal, e.g., Deck [2005], detached eddy simulation (DES) techniques. Generally, these differ by the type of smooth blending or abrupt switching between the models, i.e., based on the grid discretization or wall distance.

3 Numerical Background

This chapter outlines the fundamentals of the employed lattice Boltzmann method, including details of discrete collision operators (cf. Sec. 3.1.1), boundary conditions (cf. Sec. 3.1.2), the incorporation of body forces (cf. Sec. 3.1.3) and constant Smagorinsky-Lilly SGS modeling (cf. Sec. 3.1.4). Section 3.2 is devoted to the cumulant collision operator, which is of central research interest.

3.1 Lattice Boltzmann Method

The present work is based on a lattice Boltzmann implementation for the simulation of incompressible fluid flows, cf. Qian et al. [1992], Wolf-Gladrow [2000] and Yu et al. [2003a] among many others.

The Boltzmann equation (BE) governs the evolution of particle distribution functions (PDF), i.e., $f(\boldsymbol{x}, t, \boldsymbol{\xi})$, through

$$\frac{\mathrm{D}f(\boldsymbol{x}, t, \boldsymbol{\xi})}{\mathrm{D}t} = \frac{\partial f(\boldsymbol{x}, t, \boldsymbol{\xi})}{\partial t} + \boldsymbol{\xi}\frac{\partial f(\boldsymbol{x}, t, \boldsymbol{\xi})}{\partial \boldsymbol{x}} + \boldsymbol{F}\frac{\partial f(\boldsymbol{x}, t, \boldsymbol{\xi})}{\partial \boldsymbol{\xi}} = \Omega(f(\boldsymbol{x}, t, \boldsymbol{\xi}))\,. \tag{3.1}$$

A PDF describes the probability of encountering a particle at a position $\boldsymbol{x}$ moving with the velocity $\boldsymbol{\xi}$ at the time t. While the left-hand side of the BE (3.1) is of advection type, the right-hand side contains the so-called collision operator Ω, which covers the interaction of particles. The third term of the left-hand side incorporates surface or body forces ($\boldsymbol{F}$). For the sake of simplicity, the term is neglected for the discretization outlined below, and its consideration is explicitly mentioned when applied.

In the framework of a numerical approximation, the BE is solved for a set of discrete particle distribution functions described by a lattice of grid points. The present work employs two common three-dimensional (D3) regular lattices, viz. D3Q19 and D3Q27. Accordingly, a set of 19 (27) discrete velocities is introduced, oriented in characteristic directions of the underlying grid, cf. Fig. 3.1. The D3Q19 stencil includes the center (C), alias rest, of the cube ($|\boldsymbol{e}_1| = 0$), the principal axes ($|\boldsymbol{e}_{2\ldots7}| = 1$) and the edges' medians ($|\boldsymbol{e}_{8\ldots19}| = \sqrt{2}$). The D3Q27 stencil additionally includes the vertices ($|\boldsymbol{e}_{20\ldots27}| = \sqrt{3}$). Deploying these assumptions, equation (3.1) transforms into the discrete Boltzmann equation (DBE), viz.

$$\frac{\partial f_\zeta(\boldsymbol{x}, t)}{\partial t} + \boldsymbol{e}_\zeta \cdot \frac{\partial f_\zeta(\boldsymbol{x}, t)}{\partial \boldsymbol{x}} = \Omega_\zeta(f_\zeta(\boldsymbol{x}, t))\,, \tag{3.2}$$

where $\boldsymbol{e}_\zeta = c\,(i, j, k)^\intercal_\zeta$ refers to a directional speed matrix with $\zeta = \{1, \ldots, 19(27)\}$. The indices i, j, k are each $\{\bar{1}, 0, 1\}$ and employ the Miller notation ($-1 \equiv \bar{1}$, $0 \equiv 0$, $1 \equiv 1$).

This yields

$$\boldsymbol{e}_\zeta = c \begin{bmatrix} i \\ j \\ k \end{bmatrix}_\zeta = c \underbrace{\left[\begin{array}{c|cccccc|cccccccc|cccccccc} 0 & 1 & \bar{1} & 0 & 0 & 0 & 0 & 1 & \bar{1} & 1 & \bar{1} & 1 & \bar{1} & 1 & \bar{1} & 0 & 0 & 0 & 0 & 1 & 1 & 1 & 1 & \bar{1} & \bar{1} & \bar{1} & \bar{1} \\ 0 & 0 & 0 & 1 & \bar{1} & 0 & 0 & 1 & \bar{1} & \bar{1} & 1 & 0 & 0 & 0 & 0 & 1 & \bar{1} & 1 & \bar{1} & 1 & \bar{1} & 1 & \bar{1} & 1 & \bar{1} & 1 & \bar{1} \\ 0 & 0 & 0 & 0 & 0 & 1 & \bar{1} & 0 & 0 & 0 & 0 & 1 & \bar{1} & \bar{1} & 1 & 1 & \bar{1} & \bar{1} & 1 & 1 & \bar{1} & \bar{1} & 1 & 1 & \bar{1} & \bar{1} \end{array}\right]}_{\text{C}\quad\text{Principal Axes}\qquad\qquad\text{Medians}\qquad\qquad\qquad\text{Vertices}} . \tag{3.3}$$

The lattice speed is defined as $c = \Delta x/\Delta t$, where Δx represents the regular isotropic lattice spacing, i.e., $\Delta x = \Delta x_\mathrm{i}\,[= \Delta x = \Delta y = \Delta z]$, and Δt refers to the time step. Usually, and in the scope of the underlying work, spatial and temporal unit spacings are assumed, i.e., $\Delta x = 1$ and $\Delta t = 1$. Thus, c is also assigned to unity implying the particles are restricted to stay (at C) or move only to one of their 18(26) next neighbor nodes within a discrete time step. The numerical solution of the DBE (3.2) is obtained from a finite difference

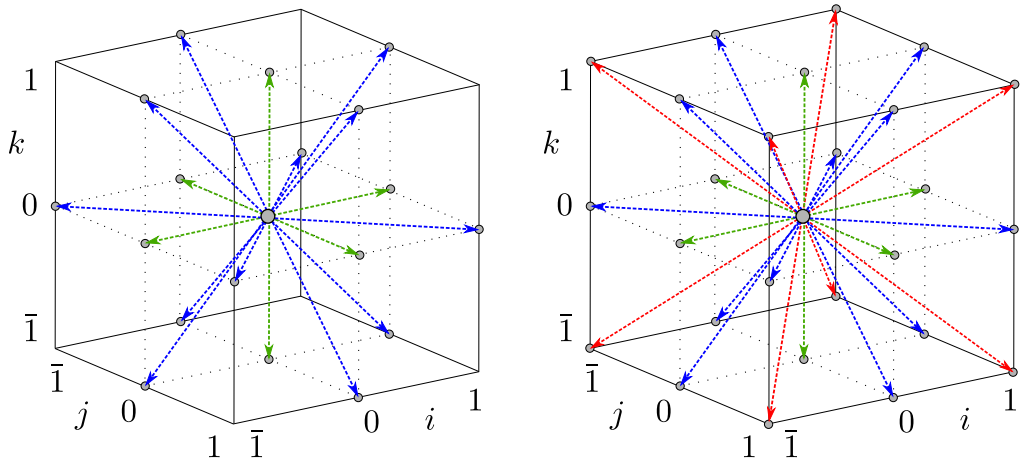

Figure 3.1: D3Q19 (left) and D3Q27 (right) lattice models, where the arrows indicate the possible discrete velocity vectors. The so-called collocation points are marked in gray.

(FD) approximation over a grid cell yielding the lattice Boltzmann equation (LBE), i.e.,

$$f_\zeta(\boldsymbol{x} + \boldsymbol{e}_\zeta \Delta t, t + \Delta t) = f_\zeta(\boldsymbol{x}, t) + \Delta t \Omega_\zeta(\boldsymbol{x}, t)\,, \tag{3.4}$$

where the FD method initially corresponds to a fully explicit forward Euler scheme of first-order in space and time. Appropriate definitions of the collision operator and its inherent primary relaxation rate, cf. (3.18), provide second-order in space and time on the considered regular grid.

The macroscopic flow quantities of pressure and velocity are extracted from the PDF space, viz.

$$p = c_s^2\,\rho = c_s^2 \sum_\zeta f_\zeta \quad \text{and} \quad \boldsymbol{u} = u_\mathrm{i} = (u, v, w)^\intercal = \frac{1}{\rho} \sum_\zeta f_\zeta\, \boldsymbol{e}_\zeta\,, \tag{3.5}$$

where $c_s = c/\sqrt{3}$ matches the speed of sound in the lattice. The implementation is usually divided into two parts, i.e.,

$$f^*_\zeta(\boldsymbol{x}, t) = f_\zeta(\boldsymbol{x}, t) + \Delta t \Omega_\zeta(\boldsymbol{x}, t) \qquad \text{the collision step}\,, \tag{3.6}$$

$$f_\zeta(\boldsymbol{x} + \boldsymbol{e}_\zeta \Delta t, t + \Delta t) = f^*_\zeta(\boldsymbol{x}, t) \qquad \text{and the propagation step}\,, \tag{3.7}$$

as depicted in Fig. 3.2. Since the 2D illustration is much clearer, the regular D2Q9 lattice is employed for illustration purposes, whereby the scheme is equivalently applicable in 3D. The first part, i.e., (3.6), contains the collision step, where the initial (incoming pre-collision, colored red) PDFs $f_\zeta(\boldsymbol{x}, t)$ deviate from equilibrium state. The asterisk notation f_ζ^* represents post-collision PDFs (green). Vividly, the collision causes a redistribution of the PDFs, represented by the changed length of vectors in Fig. 3.2. Mind that macroscopic quantities (ρ and u_i) are inherently conserved during the collision, which complies with the conservation constraints of fluid mass and momentum. Furthermore, the collision operator has to fulfill the conservation law of energy. The second part, i.e., (3.7), simply shifts the

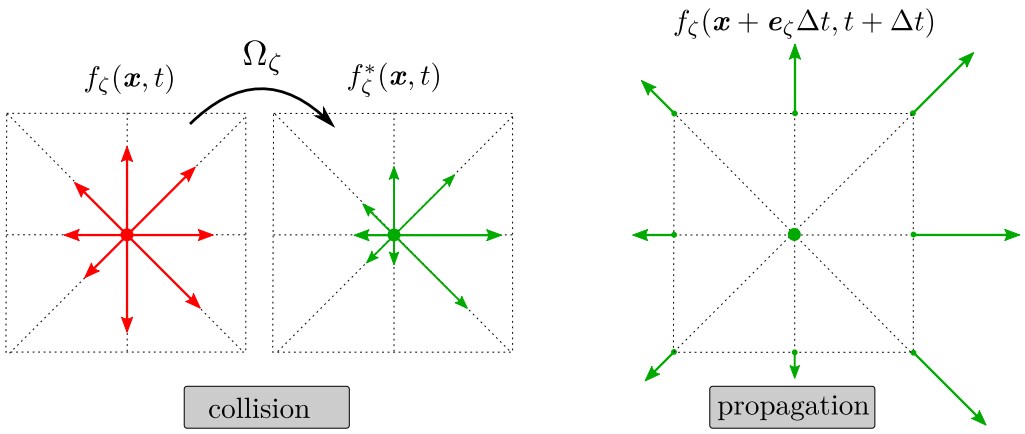

Figure 3.2: Sketch of the collision and propagation step on the D2Q9 lattice.

evolved particle distribution functions to their respective neighboring nodes and is termed the propagation or streaming step. The prevalent strict locality of the LBM collision step allows exploiting the advantage of GPUs for high-performance computing, e.g., cf. Tölke [2008], Wang and Aoki [2012], Wang et al. [2014], Schornbaum and Rüde [2016], Niedermeier et al. [2018] or Latt et al. [2021].

3.1.1 Discrete Collision Operators

Since the propagation step is straightforward on a regular grid, the major effort of most fundamental LBM research is put into developing discrete collision operators Ω_ζ, cf. (3.6). To this end, the three collision models employed within the thesis's scope are introduced below.

Single-Relaxation-Time Model

The single-relaxation-time (SRT) model is the original discrete LBM collision operator, where the particle distribution functions are driven to an equilibrium state with a single, constant relaxation time τ. Omitting $(\boldsymbol{x}, t)$ in the notation, the SRT operator reads

$$\Omega_\zeta = \frac{1}{\tau}\left(f_\zeta^\mathrm{eq} - f_\zeta\right) = -\frac{1}{\tau}\underbrace{\left(f_\zeta - f_\zeta^\mathrm{eq}\right)}_{f_\zeta^\mathrm{neq}} = -\omega\, f_\zeta^\mathrm{neq}\,. \tag{3.8}$$

The reciprocal of τ is the relaxation rate/frequency ω. The approach is, to some extent, based on a continuous relaxation operator first published by Bhatnagar et al. [1954],

i.e., frequently called BGK or lattice BGK (LBGK) model. The continuous Maxwell-Boltzmann distribution in three spatial dimensions reads

$$f^{\mathrm{eq}}(\rho, T, \boldsymbol{u}, \boldsymbol{\xi}) = \frac{\rho}{(2\pi RT)^{3/2}} \exp\left(\frac{-\left(\boldsymbol{\xi}-\boldsymbol{u}\right)^2}{2RT}\right), \tag{3.9}$$

with $RT = c_s^2$ matching the speed of sound in the underlying fluid, where R depicts the molar gas constant and T is the absolute temperature. The speed of sound is also proportional to a microscopic velocity scale to be thought of as an approximation of the collision time. A low Mach number approximation, i.e., accomplished by a small velocity truncation of a series expansion of (3.9), leads to

$$f^{\mathrm{eq}}(\rho, T, \boldsymbol{u}, \boldsymbol{\xi}) = \frac{\rho}{(2\pi c_s^2)^{3/2}} \exp\left(\frac{-\boldsymbol{\xi}^2}{2c_s^2}\right)\left(1 + \frac{\boldsymbol{\xi}\cdot\boldsymbol{u}}{c_s^2} + \frac{1}{2}\frac{\left(\boldsymbol{\xi}\cdot\boldsymbol{u}\right)^2}{c_s^4} - \frac{1}{2}\frac{\boldsymbol{u}\cdot\boldsymbol{u}}{c_s^2}\right) + \mathcal{O}(\boldsymbol{u}^3), \tag{3.10}$$

e.g., cf. He and Luo [1997] or Chen and Doolen [1998]. The corresponding set of discrete equilibrium PDFs reads

$$f_\zeta^{\mathrm{eq}} = w_\zeta\,\rho\left[1 + \frac{\boldsymbol{e}_\zeta\cdot\boldsymbol{u}}{c_s^2} + \frac{1}{2}\frac{\left(\boldsymbol{e}_\zeta\cdot\boldsymbol{u}\right)^2}{c_s^4} - \frac{1}{2}\frac{\boldsymbol{u}\cdot\boldsymbol{u}}{c_s^2}\right]. \tag{3.11}$$

Here, c_s refers to an *artificial* speed of sound linked to the (estimated) maximum flow velocity $u_{\max}$, i.e., $\mathrm{Ma} = u_{\max}/c_s \leq 0.1$ to comply with the weak compressibility requirement of the LBM. For the nondimensional LB context $c_s = c/\sqrt{3}$ applies with the lattice velocity $c = 1$, whereby (3.11) alters to

$$f_\zeta^{\mathrm{eq}} = w_\zeta\,\rho\left[1 + 3\left(\boldsymbol{e}_\zeta\cdot\boldsymbol{u} + \frac{3}{2}\left(\boldsymbol{e}_\zeta\cdot\boldsymbol{u}\right)^2 - \frac{1}{2}\boldsymbol{u}\cdot\boldsymbol{u}\right)\right]. \tag{3.12}$$

Assuming the fluid is at rest, i.e., $\boldsymbol{u} = \boldsymbol{0}$, the occurring weight coefficients w_ζ have to preserve the constraints

$$\rho = \sum_\zeta f_\zeta^{\mathrm{eq}} = \sum_\zeta w_\zeta\rho \rightarrow \sum_\zeta w_\zeta = 1, \tag{3.13}$$

$$\rho\boldsymbol{u} = 0 = \sum_\zeta f_\zeta^{\mathrm{eq}}\,\boldsymbol{e}_\zeta = \sum_\zeta w_\zeta\rho\boldsymbol{e}_\zeta \rightarrow \sum_\zeta w_\zeta\boldsymbol{e}_\zeta = 0. \tag{3.14}$$

Depending on the employed stencil, the weights are

$$w_\zeta^{\mathrm{D3Q19}} = \begin{cases} \frac{1}{3} & \zeta = 1 \\ \frac{1}{18} & \zeta = \{2,\ldots,7\} \\ \frac{1}{36} & \zeta = \{8,\ldots,19\} \end{cases} \quad \text{and} \quad w_\zeta^{\mathrm{D3Q17}} = \begin{cases} \frac{8}{27} & \zeta = 1 \\ \frac{2}{27} & \zeta = \{2,\ldots,7\} \\ \frac{1}{54} & \zeta = \{8,\ldots,19\} \\ \frac{1}{216} & \zeta = \{20,\ldots,27\} \end{cases}, \tag{3.15}$$

cf. He and Luo [1997] and Shan et al. [2006].

For setting the relaxation time τ in (3.8), the ansatz is $\tau = \nu^*/c_s^2$, where $\nu^* = \nu + \nu_{\mathrm{D}}$ is the effective viscosity composed of the kinematic viscosity and the numerical viscosity. The

latter determines the numerical diffusion of the method on the underlying regular grid and a leading error analysis of the expanded, i.e., the result of the Taylor series and Chapman-Enskog procedure, e.g., cf. Chen and Doolen [1998], LBE reveals $\nu_\mathrm{D} = \Delta x\, c_s/2 = \Delta t\, c_s^2/2$ from which follows

$$\tau = \frac{\nu^*}{c_s^2} = \frac{\nu + \nu_\mathrm{D}}{c_s^2} = \frac{\nu + \Delta t\, c_s^2/2}{c_s^2} = \frac{\nu}{c_s^2} + \frac{\Delta t}{2}\,, \tag{3.16}$$

$$\overset{\mathrm{LB}}{=} 3\nu + \frac{1}{2} \quad \Leftrightarrow \quad \nu = \frac{1}{3}\left(\tau - \frac{1}{2}\right). \tag{3.17}$$

Though (3.4) employs first-order discretizations, the LBE inheres second-order numerical accuracy in the lattice spacing and discrete time step by applying $\tau - 1/2$ in (3.17). The latter involves physics consistent with the incompressible NS equations, e.g., cf. Sterling and Chen [1996], Chen and Doolen [1998] or Junk [2001].

The expression involves $\tau > 1/2$ ($\omega < 2$) to adhere positive viscosity, which serves as a numerical stability requirement. Thus, $\mathrm{Re} \to \infty$ constitutes the stability limit of the method since $\nu \to 0$ yields $\tau \to 1/2$. The viscosity-related dimensionless LB relaxation rate follows from

$$\omega = \frac{2}{6\nu + 1}\,. \tag{3.18}$$

The BGK model is perhaps the most widely used approach. While its implementation is rather trivial, the model is deemed to provide unsatisfactory numerical stability for engineering relevant high Reynolds number applications. However, several theoretical and numerical works, e.g., by Freitas et al. [2011] or Geier et al. [2015], demonstrated that the SRT might also perform more stable and accurately than some sophisticated models.

The equivalent macroscopic PDEs are recovered from the LBE (3.4) conjunct with the SRT collision operator (3.8) by means of an asymptotic analysis, i.e., the combination of a Taylor and Chapman-Enskog expansion, cf. Chapman and Cowling [1970] or He and Luo [1997]. Hence, the LBE converges to the incompresible Navier-Stokes equations through

$$\frac{\partial u_\mathrm{i}}{\partial x_\mathrm{i}} = 0 + \mathcal{O}(\Delta t^2) + \mathcal{O}(\mathrm{Ma}^2)\,, \tag{3.19}$$

$$\frac{\partial u_\mathrm{i}}{\partial t} + u_\mathrm{j}\frac{\partial u_\mathrm{i}}{\partial x_\mathrm{j}} = -\frac{1}{\rho}\frac{\partial p}{\partial x_\mathrm{i}} + \nu\frac{\partial^2 u_\mathrm{i}}{\partial x_\mathrm{j}^2} + \mathcal{O}(\mathrm{Kn}^2) + \mathcal{O}(\Delta t^2) + \mathcal{O}(\mathrm{Ma}^2)\,, \tag{3.20}$$

for sufficiently small temporal step sizes (Δt), adequately small Mach (Ma) and Knudsen (Kn) numbers. The latter relates the mean free path to a characteristic reference length and represents the expansion parameter of the analysis. The Knudsen number has to be small enough to satisfy the continuum regime.

Multiple-Relaxation-Time Model

In response to the stability issues of the BGK model, multiple-relaxation-time (MRT) models have been suggested. These are based on transforming from particle distribution to moment space, where the relaxation proceeds. Linear combinations of PDFs span the moment space ($\boldsymbol{m}$), offering the advantage of assigning single moments to physical equivalents and separating conserved (hydrodynamic, i.e., linear combinations of mass and

momentum) and non-conserved (kinetic) moments, e.g., cf. Lallemand and Luo [2000] or d'Humières et al. [2002]. The general form of the employed D3Q19 MRT collision operator reads

$$\Omega_\zeta(\boldsymbol{x},t) = \underbrace{\boldsymbol{M}^{-1}\,\underbrace{\boldsymbol{S}\,\underbrace{\underbrace{\left(\underbrace{(\boldsymbol{M}\,f_\zeta(\boldsymbol{x},t))}_{\mathrm{PDF}\rightarrow\boldsymbol{m}_\zeta(\boldsymbol{x},t)} - m_\zeta^{\mathrm{eq}}(\boldsymbol{x},t)\right)}_{\boldsymbol{m}^{\mathrm{neq}(\boldsymbol{x},t)}}}_{\text{Relaxation}}}_{\boldsymbol{m}_\zeta(\boldsymbol{x},t)\rightarrow\mathrm{PDF}}. \tag{3.21}$$

Here $\boldsymbol{S}$ is a diagonal matrix containing the particular relaxation rates, and $\boldsymbol{M}$ is a linear transformation matrix, cf. Appendix A for details. The relaxation of hydrodynamic moments within the MRT model is physically motivated and similar to the BGK model. The non-hydrodynamic moments can be relaxed individually and adjusted with regard to specific flow conditions. Their relaxation does not affect the convergence to the Navier-Stokes equations on the leading order. However, it influences higher-order contributions that either yield diffusive or dispersive errors and aims to increase the method's accuracy and stability distinctly. The transformation into moment space is invariable and linear. Hence, no complex matrix-vector operations are required. The computational effort of MRT and SRT models is, therefore, almost comparable.

Several different MRT formulations exist, distinguished by the definition of the transformation matrix, i.e., $\boldsymbol{M}$, and the choice of the collision rates. The model applied for the present thesis refers to the one of Tölke et al. [2006]. Opposite to the original MRT of d'Humières et al. [2002], the basis vectors adhere to a weighted rather than unweighted orthogonality, cf. Dellar [2002] or Asinari [2008] for details on this. The model has been successfully applied to high Reynolds number and free surface flows in an LES framework, e.g., see Tölke et al. [2006], Stiebler et al. [2011], Janßen and Krafczyk [2011], Janßen et al. [2015], Mierke et al. [2018] and Janßen et al. [2017]. Different values are reported in the literature for the choice of collision parameters related to non-hydrodynamic moments. In the present work, all (five) independent relaxation rates are assigned to negative unity to limit the parameter space to be processed.

Even though MRT models show an increase in stability for most practical applications and, consequently, are widely used, several drawbacks are identified. First, the choice of moments is somewhat arbitrary. Thus, no unique moment space and no unique MRT model exist. Second, the choice of relaxation rates is ambiguous, and several optimization strategies exist. Third, some analyzes revealed severe stability issues, at least for some essential benchmark problems, see, e.g., Freitas et al. [2011] or Geier et al. [2015].

Cumulant Model

Recently, more advanced, high-fidelity collision operators were suggested. They are motivated by the lack of a unique procedure to identify optimal collision parameters, the almost arbitrary choice of the moment space, and formal deficiencies, e.g., a lack of Galilean invariance. The cumulant model of Geier et al. [2015], from which the following outline closely follows under adjustments of the notation, is an example of a more elaborate alternative. The use of cumulants in conjunction with LBM simulations was initially suggested

by Seeger and Hoffmann [2000]. While this initial publication refers to the equations of motion in cumulant space, the subsequent developments, cf. Geier et al. [2015, 2017a], restrict the use of cumulants to the collision step.

Per se, the cumulant model also corresponds to an MRT since it is fundamentally characterized by the distinction of statistical moments, which are assigned different relaxation rates during the collision. Nevertheless, the cumulant ansatz is considered a standalone model pursuing a more profound statistical approach featuring substantially intricate transformations. First benchmarks, e.g., of Krafczyk et al. [2015], Pasquali et al. [2016], Pasquali [2016], Far et al. [2016], Asmuth et al. [2019] and Banari et al. [2020] showed very promising results, in terms of stability and accuracy, compared to existing alternatives.

The starting point is the conversion from the discrete (ζ subscript) to a continuous ($\boldsymbol{\xi} = (\xi, \upsilon, \theta)^\intercal$ is the microscopic velocity vector) PDF space via

$$f(\boldsymbol{\xi}) = \sum_{\zeta} \delta(i_\zeta c - \xi)\, \delta(j_\zeta c - \upsilon)\, \delta(k_\zeta c - \theta)\, f_\zeta \,, \tag{3.22}$$

where δ is the Dirac delta function, c is the lattice speed and i, j, k, each depending on ζ, refer to the discrete velocity space, cf. Fig. 3.1. Aiming at a Galilean invariant factorization of the continuous PDF, a transformation from spatial ($\boldsymbol{\xi}$) to frequency space $\boldsymbol{\Xi} = (\Xi, \Upsilon, \Theta)^\intercal$ is required, i.e., a two-sided Laplace transform

$$F(\boldsymbol{\Xi}) = \mathscr{L}\{f(\xi, \upsilon, \theta)\} = \int_{-\infty}^{+\infty} f(\boldsymbol{\xi}) \exp(-\boldsymbol{\xi} \cdot \boldsymbol{\Xi})\, \mathrm{d}\boldsymbol{\xi} \tag{3.23}$$

$$= \sum_{\zeta} f_\zeta \exp(-\Xi i_\zeta c)\, \exp(-\Upsilon j_\zeta c)\, \exp(-\Theta k_\zeta c) \,, \tag{3.24}$$

yielding the continuous PDF $F(\boldsymbol{\Xi})$. Supposing statistically independence and Galilean invariance of observable quantities c_χ, the resulting joint probability density function reads

$$F(\boldsymbol{\Xi}) = \prod_{\chi} F_\chi(x_\chi) \quad \overset{\ln}{\Leftrightarrow} \quad \ln(F(\boldsymbol{\Xi})) = \sum_{\Xi} \ln(F_\chi(x_\chi)) \,. \tag{3.25}$$

Applying the natural logarithm to both sides of the left equation, a subsequent Taylor expansion of the summation (right) yields the Taylor coefficients

$$c_{\alpha\beta\gamma} = \frac{1}{c^{\alpha+\beta+\gamma}} \frac{\partial^\alpha \partial^\beta \partial^\gamma}{\partial \Xi^\alpha \partial \Upsilon^\beta \partial \Theta^\gamma} \ln(F(\boldsymbol{\Xi}))|_{\boldsymbol{\Xi}=0} \,, \tag{3.26}$$

evaluated at the origin, i.e., $\boldsymbol{\Xi} = 0$. This is the definition of the eponymous (countable) cumulants of the model, where (powers of) c are formally enclosed for nondimensionalization. Herein the triple Greek subscript includes the order, i.e.,

$$\tilde{o} = \alpha + \beta + \gamma \,, \tag{3.27}$$

of each cumulant, and, since α, β, γ are each $\{0, 1, 2\}$, there is a total of $3! = 27$ cumulants with the highest order of $\tilde{o} = 6$. Thus, the present cumulant LBM inherently links to the D3Q27 velocity space by definition. The collision is executed in the cumulant space, viz.

$$c^*_{\alpha\beta\gamma} = c_{\alpha\beta\gamma} + \omega_{\alpha\beta\gamma}(c^{\mathrm{eq}}_{\alpha\beta\gamma} - c_{\alpha\beta\gamma}) = c_{\alpha\beta\gamma} - \omega_{\alpha\beta\gamma} c^{\mathrm{neq}}_{\alpha\beta\gamma} \,, \tag{3.28}$$

$$[\, = \omega_{\alpha\beta\gamma} c^{\mathrm{eq}}_{\alpha\beta\gamma} + (1 - \omega_{\alpha\beta\gamma})\, c_{\alpha\beta\gamma}]$$

where the asterisk expresses the post collision states, $\omega_{\alpha\beta\gamma}$ represents the order-dependent relaxation rates and the short notation $c^{(\cdot)}_{\alpha\beta\gamma} = c^{(\cdot)}_{\alpha\beta\gamma}(\boldsymbol{x}, t)$ applies. Since the relaxation rates constitute the crucial parameters of the collision step, they are referred to in detail in Sec. 3.2. While $c_{\alpha\beta\gamma}$ are pre-collision cumulant states, $c^{\mathrm{eq}}_{\alpha\beta\gamma}$ denotes their equilibria, based on

$$\ln(F^{\mathrm{eq}}(\Xi)) = \ln\left(\frac{\rho}{\rho_0}\right) - \Xi u - \Upsilon v - \Theta w + \frac{c_s^2}{2}\left(\Xi^2 + \Upsilon^2 + \Theta^2\right). \tag{3.29}$$

From this equation, the countable equilibria are analogously obtained through a Taylor expansion, cf. from (3.25) to (3.26). The beneficial stability and accuracy of the cumulant model come at the expense of an increased computational effort, e.g., the number of arithmetic operations per discrete time steps due to transformations augments by a factor of $\mathcal{O}(10^3)$ compared to the SRT model. This order of magnitude is not to be compared to the computational time since the latter strongly depends on the parallel efficiency determined by the (GPU) load preset by the employed grid size. The computational times of the models merely differ by approximately 5-15% based on the total grid size. Since the cumulant LBM is the focal point of the present thesis research, a detailed description of the cumulant LBM, its variants, and stages of development will be given in Sec. 3.2 and thoroughly addressed in Chap. 6.

The fundamental advantage of the cumulant LBM is given by its Galilean invariance, i.e., the decoupling from the frame of reference, and the statistical independence of the cumulants. The latter property enables the separate relaxation of cumulants without passing information between independent orders. For theoretical derivations to their full extent, the statistical rationale and the recovery of the incompressible Navier-Stokes equations up to leading orders through asymptotic analyses, it is referred to various Ph.D. theses as the research outcome of the "Institute for Computational Modelling in Civil Engineering" of the TU Braunschweig, e.g., Uphoff [2013], Schönherr [2015], Goraki Fard [2015] and Pasquali [2016], and to the seminal cumulant LBM publication of Geier et al. [2015].

Others

There exist numerous other discrete collision operators and variants in literature. Since this thesis is restricted to the SRT, MRT, and cumulant model, a detailed review of further operators and their rationale is beyond the scope of the underlying work. A recent publication of Coreixas et al. [2020] can serve as a good and comprehensive overview.

Further well-known published suggestions are the cascaded approach of Geier et al. [2006], the two-relaxation-time (TRT) model of Ginzburg et al. [2008a,b] and the class of entropic (E)LBM introduced by Karlin et al. [1999], where the most popular extension is the Karlin-Bösch-Chikatamarla (KBC) model, e.g., see Karlin et al. [2014], Bösch et al. [2015] and Dorschner et al. [2016].

3.1.2 Boundary Conditions

Fig. 3.3 depicts two cutouts through the Cartesian grid where the continuous boundary (B) separates the solid (S) nodes of the discretized geometry from the fluid ($F_{(i)}$) nodes. Both examples are shown in two dimensions, where the left sketch refers to an arbitrarily

curved shape and the right to a planar boundary. However, the boundary conditions (BC) can be equivalently applied in 3D.

The illustrated vectors correspond to the particle distributions (PDF) of the discrete velocity space. Here the subscript α refers to a specific direction, i.e., the opposite of the wall-normal direction $\overline{\alpha}$. The PDFs moving outwards of the solid wall into the direction of the first fluid (F_1) node are unknown, i.e., $f_{\bar{\alpha}}(F_1)$. The corresponding directions are illustrated in red, and the subgrid distance, cf. Mierke et al. [2020], defining the distance in $\boldsymbol{e}_\alpha$ direction between the continuous solid boundary (wall) and the first fluid node, is depicted by the scalar value $q \in [0, 1]$. The PDF directions marked in green are known properties since they constitute valid post-streaming states received from their nearest wetted neighbor nodes. It is noted that all PDFs are accessed at the same discrete time step, which is why its explicit indication is omitted. The employed BC for arbitrarily shaped geometries

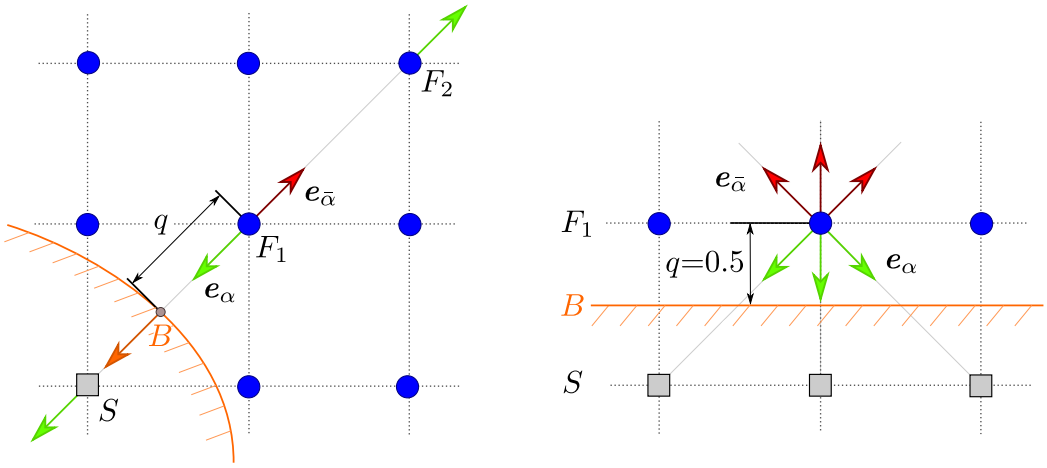

Figure 3.3: Illustration of the no-slip wall boundary implementations for curved boundaries with arbitrary $q \in [0, 1]$ (left) and for planar surfaces with fixed $q = 0.5$ (right).

(left) complies with the unified boundary treatment proposed by Yu et al. [2003b] as a modification of a BC introduced by Bouzidi et al. [2001], and has also been applied in an amended version by Geier et al. [2015]. The latter BC is solely based on using post-collision PDFs of the local node bypassing the need to access neighboring node information.

The sequence of the applied BC starts from a linear interpolation of the PDF located at the wall in α-direction (orange vector) via

$$f_\alpha(B) = f_\alpha(F_1) + q\,[f_\alpha(S) - f_\alpha(F_1)]\ , \tag{3.30}$$

using the information of the first fluid (F_1) node and the corresponding solid (S) node. To satisfy the momentum balance in the direction of α and at the same time fulfill the no-slip boundary condition on the surface of the geometry, requiring zero velocity on the wall, the inverse ($\bar{\alpha}$) value is set to $f_{\bar{\alpha}}(B) = f_\alpha(B)$ and the unknown PDF value follows from

$$f_{\bar{\alpha}}(F_1) = \frac{1}{1+q} f_{\bar{\alpha}}(B) + \frac{q}{1+q} f_{\bar{\alpha}}(F_2)\,. \tag{3.31}$$

Subsequently, this BC is denoted by the interpolated bounce-back (IBB) scheme.

In the case of planar walls and a wall location exactly in the middle of the solid and first fluid layer, i.e., $q = 0.5$ (right sketch), the simple bounce-back (SBB) scheme

$$f_{\bar{\alpha}}(F_1) = f_\alpha(F_1)\,, \tag{3.32}$$

is applied, which includes a straightforward point-mirroring along each $\boldsymbol{e}_\alpha$ direction, cf. Ziegler [1993] or Ginzburg and Adler [1994] .

3.1.3 Body Forces

According to Guo et al. [2002], the LBE (3.4) under consideration of body forces reads

$$f_\zeta(\boldsymbol{x} + \boldsymbol{e}_\zeta \Delta t, t + \Delta t) = f_\zeta(\boldsymbol{x}, t) + \Omega_\zeta + \Delta t \mathrm{f}_\zeta\,, \tag{3.33}$$

where f_ζ is the discrete forcing term related to a macroscopic (body) force density $\mathbf{f} = (\mathrm{f}_x, \mathrm{f}_y, \mathrm{f}_z)^\intercal\,[\mathrm{kgm^{-2}s^{-2}}]$. A variety of methods can be found in the literature regarding the discrete incorporation of $\mathbf{f}$. Hereinafter, only the two methods employed in the underlying work are presented. For the SRT, an explicit term is added to the collision, e.g., cf. He et al. [1997] or Buick and Greated [2000], i.e.,

$$\mathrm{f}_\zeta = \frac{w_\zeta}{c_s^2}\,(\boldsymbol{e}_\zeta \cdot \mathbf{f}) \quad \overset{c_s^2=1/3,\Delta t=1}{\rightarrow} \quad f_\zeta^*(\boldsymbol{x}, t) = f_\zeta(\boldsymbol{x}, t) + \Omega_\zeta + 3 w_\zeta\,(\boldsymbol{e}_\zeta \cdot \mathbf{f})\,, \tag{3.34}$$

which applies for body forces being constant in both space and time.

For the MRT and cumulant model, the modified equilibrium velocity approach is followed. It is based on the definition of an average ($\tilde{\boldsymbol{u}}$ with $\rho = \text{const.}$) macroscopic fluid momentum before ($\rho\boldsymbol{u}$) and after ($\rho\boldsymbol{u} + \Delta t\mathbf{f}$) collision through

$$\rho\tilde{\boldsymbol{u}} = \frac{(\rho\boldsymbol{u}) + (\rho\boldsymbol{u} + \Delta t\mathbf{f})}{2} = \rho\boldsymbol{u} + \frac{\Delta t\mathbf{f}}{2} = \sum_\zeta f_\zeta\,\boldsymbol{e}_\zeta + \frac{\Delta t\mathbf{f}}{2}\,. \tag{3.35}$$

Subsequently, the altered velocity $\tilde{\boldsymbol{u}}$ enters the computation of equilibrium MRT moments ($\boldsymbol{m}^{\mathrm{eq}}(\rho, \tilde{\boldsymbol{u}})$) or cumulants ($c^{\mathrm{eq}}_{\alpha\beta\gamma}(\rho, \tilde{\boldsymbol{u}})$), whereby the body force is implicitly applied and (3.6) formally turns into

$$f_\zeta^*(\boldsymbol{x}, t) = f_\zeta(\boldsymbol{x}, t) + \Omega_\zeta(\rho, \tilde{\boldsymbol{u}})\,. \tag{3.36}$$

3.1.4 Subgrid Scale Modeling

For modeling unresolved subgrid scales on coarse grids, the present simulations utilize the Smagorinsky [1963] - Lilly [1966] LES model which links an additional eddy viscosity (ν_t) with the filtered, i.e., resolved, local norm of the strain rate tensor (S_{ij})

$$\nu_t = (C_S\,\Delta)^2 \sqrt{2\,\overline{S}_{\mathrm{ij}}\,\overline{S}_{\mathrm{ij}}} = (C_S\,\Delta)^2\,\overline{S}\,. \tag{3.37}$$

Here $\overline{S}$ is a scalar strain rate measure (norm). The adaption of this classical modeling concept for the LBM has its origins from Hou et al. [1996] and Krafczyk et al. [2003]. Moreover, Dong et al. [2008] and Malaspinas and Sagaut [2012] might serve as further

copious references. The approach alters the relaxation time (3.16) related to the shear viscosity (ν) by a modification of the considered viscosity, viz.

$$\tau_e = \frac{\nu_e}{c_s^2} + \frac{\Delta t}{2} \quad [\mathrm{s}] \quad \text{with} \quad \nu_e = \nu + \nu_t \,, \tag{3.38}$$

where the subscript (e) refers to an effective relaxation time resp. an effective viscosity that includes an eddy viscosity contribution (ν_t) to mimic the influence of SGS stresses, cf. Teixeira [1998]. The LBM implementation is based on the relation

$$\overline{S}_{\mathrm{ij}} = -\frac{1}{2\rho_0 c_s^2 \tau_e} \overline{Q}_{\mathrm{ij}} \tag{3.39}$$

between the (filtered) strain rate tensor and the local non-equilibrium stress tensor defined as

$$\overline{Q}_{\mathrm{ij}} = \sum_{\zeta} \boldsymbol{e}_{\zeta,\mathrm{i}} \boldsymbol{e}_{\zeta,\mathrm{j}} f_{\zeta}^{\mathrm{neq}} = \sum_{\zeta} \boldsymbol{e}_{\zeta,\mathrm{i}} \boldsymbol{e}_{\zeta,\mathrm{j}} \left(f_{\zeta} - f_{\zeta}^{\mathrm{eq}} \right) \quad [\mathrm{kgm^{-1}s^{-2}}] \,. \tag{3.40}$$

Thus, the scalar strain rate measure follows from

$$\overline{S} = \frac{\overline{Q}}{2\rho_0 c_s^2 \tau_e} \quad [\mathrm{s^{-1}}] \quad \text{with} \quad \overline{Q} = \sqrt{2\,\overline{Q}_{\mathrm{ij}}\,\overline{Q}_{\mathrm{ij}}} \quad [\mathrm{kgm^{-1}s^{-2}}] \,. \tag{3.41}$$

Since $\overline{S}$ and $\overline{Q}$ represent tensor norms, the definition's negative sign of (3.39) is omitted. Substituting (3.41) in (3.37) and ensuing into (3.38) with $\nu = (\tau - \Delta t/2) c_s^2$ yields

$$\begin{aligned} \tau_e &= \frac{1}{c_s^2} \left(\left(\tau - \frac{\Delta t}{2} \right) c_s^2 + (C_S\,\Delta)^2 \frac{\overline{Q}}{2\rho_0 c_s^2 \tau_e} \right) + \frac{\Delta t}{2} \\ &= \tau + (C_S\,\Delta)^2 \frac{\overline{Q}}{2\rho_0 c_s^4 \tau_e} \\ \Leftrightarrow \quad 0 &= \tau_e^2 - \tau\tau_e - (C_S\,\Delta)^2 \frac{\overline{Q}}{2\rho_0 c_s^4} \,. \end{aligned} \tag{3.42}$$

The solution of the resulting quadratic equation of τ_e reads

$$\tau_e = \frac{\tau}{2} \left(1 + \sqrt{1 + \frac{2(C_S\,\Delta)^2 \overline{Q}}{\rho_0 c_s^4 \tau^2}} \right) \,. \tag{3.43}$$

Note that only one root is considered since the second root of (3.42) harms the stability criterion by introducing negative eddy viscosity. Employing the LBM assumptions for $\Delta = \Delta x = 1$ (equidistant Cartesian grid layout), $\rho_0 = 1$, and $c_s = c/\sqrt{3}$, with $c = 1$, a simplified expression for the effective relaxation time

$$\tau_e = \frac{\tau}{2} \left(1 + \sqrt{1 + \frac{18\, C_S^2\, \overline{Q}}{\tau^2}} \right) \tag{3.44}$$

is obtained. Though eddy viscosity models of turbulence are somewhat debatable in the context of LBM, e.g., Girimaji [2007] or Sagaut [2010], they are commonly employed in practical simulations with cumulant, e.g., Niedermeier et al. [2018] or Asmuth et al. [2020, 2021], or various other collision operators, e.g., Hou et al. [1996], Krafczyk et al. [2003], Yu et al. [2006], Onodera and Aoki [2014], Han et al. [2019], Haussmann et al. [2020] and Feng et al. [2021].

3.1.5 Wall Modeling

Since the regular Cartesian grid layout of the ELBE implementation only permits wall-resolved LES for fairly low Reynolds numbers, the use of a wall function is indispensable. Different variants of wall modeling approaches are used in conjunction with the LBM, e.g., Maeyama et al. [2020, 2021a,b], Han et al. [2021b] and Degrigny et al. [2021]. The presently employed wall function refers to a recent publication of Asmuth et al. [2021], i.e., the so-called inverse momentum exchange method (IMEM). This approach reconstructs a wall velocity vector $\boldsymbol{u}_W$ that induces the desired wall shear stress τ_W obtained from a classical wall function. The merits of the method refer to its robustness and the compatibility with universal *all-resolution* wall function strategies that bridge the viscous sublayer with the buffer layer and the logarithmic region. Hence, it is readily applied to investigate a range of resolutions.

The modeling relies on a piecewise reconstruction of nondimensional $u^+(y^+)$ velocity profiles. Within the scope of the present studies three reference profiles are consulted, i.e., communicated by Moser et al. [1999] for a lower Reynolds number of $\mathrm{Re}_\tau = 180$ and Bernardini et al. [2014] for $\mathrm{Re}_\tau = 550$ and $\mathrm{Re}_\tau = 2000$. The friction Reynolds number follows from $\mathrm{Re}_\tau = u_\tau H/\nu$, where H denotes half the channel height, and $u_\tau = |\tau_W|/\rho$ refers to the friction velocity which is computed from the magnitude of the wall shear stress and the density. To this end, the reference data is approximated by third-order polynomials, cf. Fig. 3.4 and Appendix B. Each of these is composed of five consecutive segments, which support continuous functions and gradients. The employed reconstruction of $u^+(y^+)$ extracted from DNS data can be readily replaced by any similar and more general method, such as wall function approaches by Spalding [1961], Musker [1979], Werner and Wengle [1993], Shih et al. [1999, 2002] or Rung et al. [2001], which all reconstruct the shear stress from a modeled $u^+(y^+)$ relation using the wall distance and tangential velocity at a wall-adjacent node, and usually agree with the present data, cf. Fig. 3.4. Though the wall

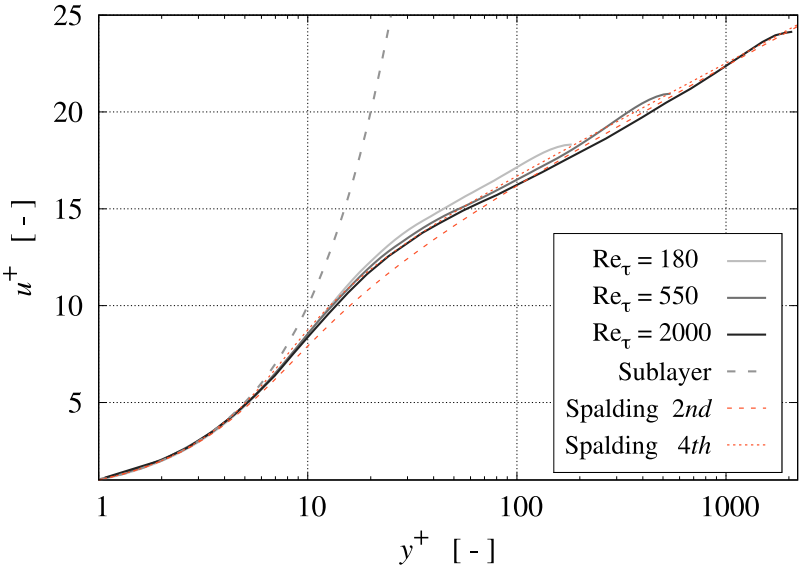

Figure 3.4: Illustration of the employed wall functions obtained from piecewise polynomial reconstructions of data reported by Moser et al. [1999] ($\mathrm{Re}_\tau = 180$) and Bernardini et al. [2014] for $\mathrm{Re}_\tau = \{550; 2000\}$, supplemented by a second- and fourth-order Spalding [1961] law using $\kappa = 0.39$ and $C^+ = 4.7$.

function approach originates from an averaged framework, the solid boundary treatment is performed for the local instantaneous velocities, which is an alternative to spatial (cf. Schumann [1975]) or temporal (cf. Yang et al. [2017]) averaging of entry values, and is often used in more complex flows, e.g., cf. Moeng [1984], Albertson and Parlange [1999] or Maronga et al. [2020]. It is noted that the temporal exponential filtering proposed by Yang et al. [2017] does not indicate substantial result changes to the conducted TCF studies and is, thus, discarded for the sake of brevity. Figure 3.5 summarizes the behavior of the instantaneous wall function approach for a fine ($\Delta x^+ \approx 4$) and a coarse ($\Delta x^+ \approx 170$) grid TCF example and indeed indicates negligible to minor temporal fluctuations of the nondimensional streamwise wall velocity component.

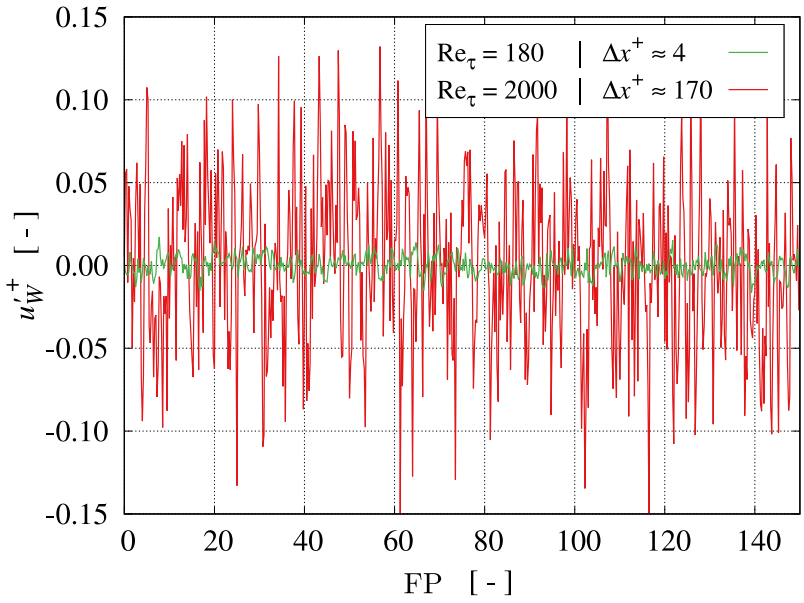

Figure 3.5: Illustration of the spatially averaged instantaneous wall function behavior for a fine grid with $y_1^+ = \Delta x^+/2 \approx 2$ [green] and a coarse grid featuring $y_1^+ = \Delta x^+/2 \approx 85$ [red] simulation of a turbulent channel flow for 150 flow passes (FP).

The implementation of the wall modeling strategy involves the following algorithmic sequence:

(i) Apply the boundary condition of Yu et al. [2003b] to receive the unknown PDFs reflected from the wall to the *first* fluid layer, cf. Sec. 3.1.2.

(ii) Compute the momentum exchange force $\boldsymbol{F}^{\mathrm{MEM}\parallel}$ [kgms^{-2}] between the solid and *first* fluid node in wall-tangential ($\parallel$) direction from the method of Bouzidi et al. [2001].

(iii) Extract the wall-tangential magnitude of the (instantaneous) velocity vector $u_2^{\parallel} = |\boldsymbol{u}_{\boldsymbol{2}}^{\parallel}|$ at the *second* fluid layer, i.e., the wall function reference location.

(iv) Initialize the friction velocity u_τ, e.g., based on the explicit power law of Wilhelm et al. [2018] and compute u_τ based on the averaged, nondimensional $u_2^+(y_2^+, u_2^{\parallel})$ wall function, cf. Fig. 3.4). The involved iteration embraces:

- Compute $y_2^+ = (u_\tau\, y_2)/\nu$ at the reference location with $y_2 = (1+q)\Delta x$,

- Update friction velocity via $u_\tau = u_2^{\parallel}/u_2^+(y_2^+)$,
- Proceed until convergence criterion $|y_{2,n+1}^+ - y_{2,n}^+| < 1/200$ is fulfilled.

(v) Assign the wall shear stress to $\tau_W = u_\tau^2\,\rho$ and compute related shear force $\boldsymbol{F}^{\parallel} = \tau_W\,\Delta x^2(\boldsymbol{u}_{\boldsymbol{1}}^{\parallel}/u_1^{\parallel})$ considering the sign of the tangential velocity $\boldsymbol{u}_{\boldsymbol{1}}^{\parallel}$ at the *first* node.

(vi) Assign the difference $\boldsymbol{F}^{\parallel} - \boldsymbol{F}^{\mathrm{MEM}\parallel}$ to the force $\boldsymbol{F}^{\boldsymbol{u}_W}$ contribution to be applied via a wall velocity $\boldsymbol{u}_W$. For a y-aligned plane wall-normal direction this reads

$$\boldsymbol{u}_W = -\frac{9c_s^2}{\rho}\frac{\Delta t^3}{\Delta x^5}\,\boldsymbol{F}^{\boldsymbol{u}_W}\,(1, 1/3, 1)^{\intercal}\,. \tag{3.45}$$

(vii) Introduce wall velocity $\boldsymbol{u}_W$ into the *first* fluid layer PDFs (i), e.g., via $f_\zeta(\boldsymbol{u})$ relation given in Chen et al. [2013].

It is noted that the described approach is valid only for planar boundaries, i.e., the turbulent channel flow test case for the underlying studies. An open issue concerns the generalization of arbitrarily shaped boundaries.

3.1.6 Physical Units and Scaling

The considered flows are uniquely determined by the physical (subscript P) quantities of kinematic viscosity (ν_P) and a reference length (l_P), supplemented by the spatial LB discretization (N), i.e., discrete number of lattice nodes per reference length, as well as two dimensionless similarity parameters, i.e., the Reynolds (Re) and Mach (Ma) number. Subsequently, LB-related quantities are not indexed (N, u and ν). There are three links between the physical and LB unit space. Firstly, the discretization is defined via

$$\Lambda_x = \frac{l_P}{N}\;[\mathrm{m}]\,, \tag{3.46}$$

where Λ_x is the spatial scaling factor. The second link rests upon the Mach number

$$\mathrm{Ma} = \left(\frac{u}{c_s}\right)_P\;[-] \quad\Leftrightarrow\quad u_P = \mathrm{Ma}\,c_{s,P}\;[\mathrm{m/s}]\,, \tag{3.47}$$

which relates a user-defined reference velocity (u_P) to the speed of sound ($c_{s,P}$) within the considered fluid. Applying the relation $c_s = c/\sqrt{3}$, where the grid velocity $c = \Delta x/\Delta t$ equals unity, of the weakly compressible LB model yields $u = \mathrm{Ma}/\sqrt{3}$. To this end, the velocity scaling factor results from $\Lambda_u = u_P/u = \sqrt{3}\,c_{s,P}$. Substituting the velocity in the Reynolds number definition by (3.47) constitutes the third link, and gives the unknown physical speed of sound

$$\mathrm{Re} = \frac{u_P\,l_P}{\nu_P} = \frac{\mathrm{Ma}\,c_{s,P}\,l_P}{\nu_P}\;[-] \quad\Leftrightarrow\quad c_{s,P} = \frac{\mathrm{Re}}{\mathrm{Ma}}\,\frac{\nu_P}{l_P}\;[\mathrm{m/s}]\,. \tag{3.48}$$

Thus, assuming Re and Ma similarity between the physical and LB space, the velocity scaling factor reads

$$\Lambda_u = \frac{u_P}{u} = \sqrt{3}\,c_{s,P} = \sqrt{3}\,\frac{\mathrm{Re}}{\mathrm{Ma}}\,\frac{\nu_P}{l_P}\;[\mathrm{m/s}]\,, \tag{3.49}$$

from which follows directly

$$\Lambda_\nu = \Lambda_x\,\Lambda_u = \sqrt{3}\,\frac{\mathrm{Re}}{\mathrm{Ma}}\,\frac{\nu_P}{N}\;\;[\mathrm{m}^2/\mathrm{s}] \quad \text{and} \quad \Lambda_t = \frac{\Lambda_x}{\Lambda_u} = \frac{1}{\sqrt{3}}\,\frac{\mathrm{Ma}}{\mathrm{Re}}\,\frac{l_P^2}{\nu_P\,N}\;\;[\mathrm{s}]\,, \tag{3.50}$$

i.e., the viscosity and temporal scaling factors. Hence, the LBM collision-determining shear viscosity (3.18) is obtained via

$$\nu = \frac{\nu_P}{\Lambda_\nu} = \frac{1}{\sqrt{3}}\frac{\mathrm{Ma}}{\mathrm{Re}}\,N\;\;[-]\,. \tag{3.51}$$

Additionally, the convective flow-pass (FP) time provides a temporal measure to judge both the phases and the statistical convergence of a flow, viz.

$$t_{\mathrm{FP},P} = \frac{l_P}{u_P} = \frac{N\,\Lambda_x}{u\,\Lambda_u} = \frac{N}{u}\,\Lambda_t\;\;[\mathrm{s}]\,, \tag{3.52}$$

relating a reference length, i.e., generally the domain's extend in main flow direction, and a reference velocity, ordinarily based on the averaged bulk flow. Several synonyms can be found in literature, i.e., flow-transit/through or turnover time. In the LB context, the equation above converts to

$$t_{\mathrm{FP}} = \frac{N_x}{u_B} \;= \begin{cases} \sqrt{3}\,N_x/\mathrm{Ma} & \mathrm{Ma} = \sqrt{3}\,u_B \\ 1.16\cdot\sqrt{3}\,N_x/\mathrm{Ma} & \mathrm{Ma} = \sqrt{3}\,u_C \quad \text{with} \quad (2.33) \end{cases} \tag{3.53}$$

involving linear proportionality from the resolution and the reciprocal Mach number. N_x denotes the total number of nodes in streamwise direction. Data processing usually employs the normalized value, i.e., $\mathrm{FP} = t/t_{\mathrm{FP}}$.

The underlying Reynolds number definitions based on LB quantities read

$$\mathrm{Re}_B = \frac{u_B\,N}{\nu} \qquad [\text{bulk Reynolds number}]\,, \tag{3.54}$$

$$\mathrm{Re}_C = \frac{u_C\,N}{\nu} \approx \frac{1.16 u_B\,N}{\nu} \qquad [\text{centerline Reynolds number}]\,, \tag{3.55}$$

$$\mathrm{Re}_\tau = \frac{u_\tau\,N}{\nu} \qquad [\text{friction Reynolds number}]\,. \tag{3.56}$$

Further, to judge the resolution characteristics, the dimensionless grid spacing Δx^+ and the (local) cell Reynolds number are utilized. Using LB spatial unity ($\Delta x = 1$) these inner and outer measures read

$$\Delta x^+ = \left(\frac{u_\tau\,\Delta x}{\nu}\right) = u_\tau/\nu \;\equiv \mathrm{Re}_\tau/N\,, \tag{3.57}$$

$$\mathrm{Re}_{\Delta x} = \left(\frac{u_B\,\Delta x}{\nu}\right) = u_B/\nu \equiv \mathrm{Re}_B/N\,. \tag{3.58}$$

3.2 Cumulant Collision Operator Implementation

This section outlines the explicit implementation of the cumulant collision operator in the ELBE framework. Since a prescribed summation of the PDFs is beneficial for recovering

the macroscopic flow (ρ and $\boldsymbol{u}$) variables, which enter both transformations and cumulant equilibria definitions, their computation is addressed in Sec. 3.2.1. Subsequently to the implementation of the collision step depicted in Sec. 3.2.2, the following Sec. 3.2.3 refers to the employed cumulant variants, building the foundation of the benchmark and development contributions of the present work.

3.2.1 Conditioning and Transformations

To improve the numerical accuracy of the cumulant LBM implementation, Geier et al. [2015] (cf. Appendix J therein) suggested two modifications referring to conditioning. The first modification addresses the minimization of rounding errors. These can significantly impair the predictive quality for both single and double precision simulations in low-velocity regimes. To reduce rounding errors, which originate from the weakly compressible nature of the cumulant approach, the so-called *well-conditioned* PDFs are obtained by subtracting the weights w_ζ (3.15), i.e., the constant reference part, from the "compressible" (c) PDF definition based on $\rho = \rho_0 + \delta\rho$ with $\rho_0 = 1$, i.e.,

$$f_\zeta = f_\zeta^{\mathrm{c}} - w_{ijk}\,. \tag{3.59}$$

Recalling (3.5) the PDF summation order is arbitrary and follows the numbering of the stencil's collocation points. Hence, the second modification constitutes an explicit prescription for computing macroscopic quantities. This essentially involves a favorable pairwise summation and subtraction of inverse ($\zeta \leftrightarrow \overline{\zeta}$) PDF directions as well as a separation of the different cube contributions (vertices, medians, principal axes, and center), cf. Fig. 3.1. To this end, the density fluctuation is given by

$$\begin{aligned}\delta\rho = [\ &\underbrace{(\,((f_{111}+f_{\bar1\bar1\bar1})+(f_{1\bar11}+f_{\bar11\bar1}))+((f_{11\bar1}+f_{\bar1\bar11})+(f_{1\bar1\bar1}+f_{\bar111}))\,)}_{\text{Vertices}}\\
&+\underbrace{(\,((f_{011}+f_{0\bar1\bar1})+(f_{01\bar1}+f_{0\bar11}))+((f_{101}+f_{\bar10\bar1})+(f_{10\bar1}+f_{\bar101}))}_{\text{Medians}}\\
&+\underbrace{\ ((f_{110}+f_{\bar1\bar10})+(f_{1\bar10}+f_{\bar110}))\,)}_{\text{Medians}}\\
&+\underbrace{\ ((f_{100}+f_{\bar100})+(f_{010}+f_{0\bar10})\ +\ (f_{001}+f_{00\bar1}))}_{\text{Principal Axes}}\,]+\underbrace{f_{000}}_{\text{Center}}\,,\end{aligned} \tag{3.60}$$

and the three velocity components follow from

$$\begin{aligned}u = [\,&(\,((f_{111}-f_{\bar1\bar1\bar1})+(f_{1\bar11}-f_{\bar11\bar1}))+((f_{11\bar1}-f_{\bar1\bar11})+(f_{1\bar1\bar1}-f_{\bar111}))\,)\\
&+(\,((f_{101}-f_{\bar10\bar1})+(f_{10\bar1}-f_{\bar101}))+((f_{110}-f_{\bar1\bar10})+(f_{1\bar10}-f_{\bar110}))\,)\\
&+\ (f_{100}-f_{\bar100})\,]/\rho\,,\end{aligned} \tag{3.61}$$

$$\begin{aligned}v = [\,&(\,((f_{111}-f_{\bar1\bar1\bar1})+(f_{\bar111}-f_{1\bar1\bar1}))+((f_{11\bar1}-f_{\bar1\bar11})+(f_{\bar11\bar1}-f_{1\bar11}))\,)\\
&+(\,((f_{011}-f_{0\bar1\bar1})+(f_{01\bar1}-f_{0\bar11}))+((f_{110}-f_{\bar1\bar10})+(f_{\bar110}-f_{1\bar10}))\,)\\
&+\ (f_{010}-f_{0\bar10})\,]/\rho\,,\end{aligned} \tag{3.62}$$

$$
\begin{aligned}
w = [\,(\,((f_{111} - f_{\bar{1}\bar{1}\bar{1}}) + (f_{\bar{1}11} - f_{1\bar{1}\bar{1}})) + ((f_{1\bar{1}1} - f_{\bar{1}1\bar{1}}) + (f_{\bar{1}\bar{1}1} - f_{11\bar{1}}))\,) \\
+(\,((f_{011} - f_{0\bar{1}\bar{1}}) + (f_{0\bar{1}1} - f_{01\bar{1}})) + ((f_{101} - f_{\bar{1}0\bar{1}}) + (f_{\bar{1}01} - f_{10\bar{1}}))\,) \\
+ \quad (f_{001} - f_{00\bar{1}})\,]/\rho\,.
\end{aligned} \tag{3.63}
$$

Due to the expression's complexity, the direct computation of cumulants based on (3.26) is costly. Therefore, a detour via the central moments ($k_{\alpha\beta\gamma}$) is involved, i.e.,

$$
f_\zeta \quad \rightleftarrows \quad \kappa_{\alpha\beta\gamma}(f_\zeta, (i,j,k)_\zeta, w_\zeta, \delta\rho, \boldsymbol{u}, c) \quad \rightleftarrows \quad C_{\alpha\beta\gamma}(k_{\alpha\beta\gamma}, \rho, \delta\rho) \quad [= c_{\alpha\beta\gamma}\rho]\,, \tag{3.64}
$$

that reduces the number of operations by a factor of three. Since the straightforward implementation exactly corresponds to the explicit representation in Geier et al. [2017a] (cf. Sec. 3.1/3.2: forward transformation and Sec. 3.4/3.5: backward transformation) their repetitive itemization is omitted here to safe space. Mind that capitalized cumulants relate to those of the definition (3.26) through the density, i.e., $C_{\alpha\beta\gamma} = c_{\alpha\beta\gamma}\rho$.

Additional body forces are considered by augmenting the velocity preliminary to the forward transformation $f_\zeta \to \kappa_{\alpha\beta\gamma} = \kappa_{\alpha\beta\gamma}(\boldsymbol{u} + \boldsymbol{F}/(2\rho))$. Moreover, the three first-order central moments ($\kappa_{\tilde{o}=1}$) have to change sign prior to the back transformation in this case.

3.2.2 Explicit Collision Step in Cumulant Space

The following equations (3.67) to (3.91) depict the entire explicit implementation of the collision step in a general sense, i.e., it includes variables enabling to switch between different cumulant variants that are discussed below. The presentation aims at showing the straightforward implemented version of the collision step in ELBE by omitting the use of linear combinations within some expressions as compared to the fundamental works of Geier et al. [2015, 2017a].

Subsequently, the relaxation rate's triple Greek index of (3.28) is replaced by a single index

$$
\omega_{\alpha\beta\gamma} \quad \to \quad \omega_C\,, \tag{3.65}
$$

where C denotes the assignment to specific cumulants resp. combinations of these. As a result, the primary total of 27 relaxation rates can be reduced to 10 independent rates, i.e., $C = \{1, \ldots, 10\}$, where the first relaxation rate is linked to the shear viscosity of the underlying fluid, i.e.,

$$
\omega_1 = \omega = \frac{2}{6\nu + 1}\,, \tag{3.66}
$$

defined by (3.18). Furthermore, ω_2 is (theoretically) related to the bulk viscosity and the other eight, i.e., $\omega_{C\geq 3}$, inhere no physical attribution. For $C \geq 2$, the relaxation rates can be chosen freely within the interval $[0, 2]$. The choice's influence on both the accuracy and numerical stability is discussed in Sec. 3.2.3 and an in-depth analysis is given in Chap. 5 and 6.

The zeroth-order and the three second-order cumulants are conserved quantities during collision, viz.

$$
C^*_{000} = C_{000}\,, \tag{3.67}
$$

$$
C^*_{100} = C_{100}\,, \quad C^*_{010} = C_{010}\,, \quad C^*_{001} = C_{001}\,. \tag{3.68}
$$

Half of the six second-order cumulants display a fairly simple relaxation

$$C^*_{110} = (1-\omega_1)C_{110}\,, \quad C^*_{101} = (1-\omega_1)C_{101}\,, \quad C^*_{011} = (1-\omega_1)C_{011}\,, \tag{3.69}$$

whereas the three remaining expressions are essentially more complex, i.e.,

$$\begin{aligned} C^*_{200} = {} & [(1-\omega_1)(C_{200}-C_{020}) - 3\rho(1-\omega_1/2)(u^2\partial_x u - v^2\partial_y v) \\ & + (1-\omega_1)(C_{200}-C_{002}) - 3\rho(1-\omega_1/2)(u^2\partial_x u - w^2\partial_z w) + \kappa_{000}\omega_2 \\ & + (1-\omega_2)(C_{200}+C_{020}+C_{002}) - 3\rho(1-\omega_2/2)(u^2\partial_x u + v^2\partial_y v + w^2\partial_z w)]/3\,, \end{aligned} \tag{3.70}$$

$$\begin{aligned} C^*_{020} = {} & [-2(1-\omega_1)(C_{200}-C_{020}) + 6\rho(1-\omega_1/2)(u^2\partial_x u - v^2\partial_y v) \\ & + (1-\omega_1)(C_{200}-C_{002}) - 3\rho(1-\omega_1/2)(u^2\partial_x u - w^2\partial_z w) + \kappa_{000}\omega_2 \\ & + (1-\omega_2)(C_{200}+C_{020}+C_{002}) - 3\rho(1-\omega_2/2)(u^2\partial_x u + v^2\partial_y v + w^2\partial_z w)]/3\,, \end{aligned} \tag{3.71}$$

$$\begin{aligned} C^*_{002} = {} & [\,(1-\omega_1)(C_{200}-C_{020}) - 3\rho(1-\omega_1/2)(u^2\partial_x u - v^2\partial_y v) \\ & - 2(1-\omega_1)(C_{200}-C_{002}) + 6\rho(1-\omega_1/2)(u^2\partial_x u - w^2\partial_z w) + \kappa_{000}\omega_2 \\ & + \;\; (1-\omega_2)(C_{200}+C_{020}+C_{002}) - 3\rho(1-\omega_2/2)(u^2\partial_x u + v^2\partial_y v + w^2\partial_z w)]/3\,. \end{aligned} \tag{3.72}$$

Herein $\kappa_{000}\,[=\delta\rho\;(3.60)]$ is the zeroth central moment and partial derivatives are introduced by

$$\partial_x u = [\omega_1(-2C_{200}+C_{020}+C_{002}) - \omega_2(C_{200}+C_{020}+C_{002}-\kappa_{000})]\,/(2\rho)\,, \tag{3.73}$$

$$\partial_y v = [\omega_1(+C_{200}-2C_{020}+C_{002}) - \omega_2(C_{200}+C_{020}+C_{002}-\kappa_{000})]\,/(2\rho)\,, \tag{3.74}$$

$$\partial_z w = [\omega_1(+C_{200}+C_{020}-2C_{002}) - \omega_2(C_{200}+C_{020}+C_{002}-\kappa_{000})]\,/(2\rho)\,, \tag{3.75}$$

which refer to approximated second-order cumulant expressions. These modified equilibria are traced to repair the anisotropy arising from the underlying velocity stencil and, therefore, to reduce aliasing effects. The seven third-order collisions read

$$C^*_{102} = [(1-\tilde{\omega}_{3,1})(C_{120}+C_{102}) - (1-\tilde{\omega}_{4,1})(C_{120}-C_{102})]/2\,, \tag{3.76}$$

$$C^*_{120} = [(1-\tilde{\omega}_{3,1})(C_{120}+C_{102}) + (1-\tilde{\omega}_{4,1})(C_{120}-C_{102})]/2\,, \tag{3.77}$$

$$C^*_{012} = [(1-\tilde{\omega}_{3,2})(C_{210}+C_{012}) - (1-\tilde{\omega}_{4,2})(C_{210}-C_{012})]/2\,, \tag{3.78}$$

$$C^*_{210} = [(1-\tilde{\omega}_{3,2})(C_{210}+C_{012}) + (1-\tilde{\omega}_{4,2})(C_{210}-C_{012})]/2\,, \tag{3.79}$$

$$C^*_{021} = [(1-\tilde{\omega}_{3,3})(C_{201}+C_{021}) - (1-\tilde{\omega}_{4,3})(C_{201}-C_{021})]/2\,, \tag{3.80}$$

$$C^*_{201} = [(1-\tilde{\omega}_{3,3})(C_{201}+C_{021}) + (1-\tilde{\omega}_{4,3})(C_{201}-C_{021})]/2\,, \tag{3.81}$$

$$C^*_{111} = (1-\tilde{\omega}_5)C_{111}\,. \tag{3.82}$$

The second subscript and the tilde refer to a case distinction to be addressed in detail below. Furthermore, the six fourth-order collisions are given by

$$\begin{aligned} C^*_{220} = {} & [2/3(1/\omega_1-1/2)A\rho(\partial_x u - 2\partial_y v + \partial_z w) + (1-\omega_6)(C_{220}-2C_{202}+C_{022}) \\ & + 2/3(1/\omega_1-1/2)A\rho(\partial_x u + \partial_y v - 2\partial_z w) + (1-\omega_6)(C_{220}+C_{202}-2C_{022}) \\ & - 4/3(1/\omega_1-1/2)A\rho(\partial_x u + \partial_y v + \partial_z w) + (1-\omega_7)(C_{220}+C_{202}+C_{022})]/3\,, \end{aligned} \tag{3.83}$$

$$\begin{aligned} C^*_{202} = {} & [-2/3(1/\omega_1-1/2)A\rho(\partial_x u - 2\partial_y v + \partial_z w) - (1-\omega_6)(C_{220}-2C_{202}+C_{022}) \\ & - 4/3(1/\omega_1-1/2)A\rho(\partial_x u + \partial_y v + \partial_z w) + (1-\omega_7)(C_{220}+C_{202}+C_{022})]/3\,, \end{aligned} \tag{3.84}$$

$$\begin{aligned} C^*_{022} = {} & [-2/3(1/\omega_1-1/2)A\rho(\partial_x u + \partial_y v - 2\partial_z w) - (1-\omega_6)(C_{220}+C_{202}-2C_{022}) \\ & - 4/3(1/\omega_1-1/2)A\rho(\partial_x u + \partial_y v + \partial_z w) + (1-\omega_7)(C_{220}+C_{202}+C_{022})]/3\,, \end{aligned} \tag{3.85}$$

$$C^*_{211} = -1/3(\omega_1/2-1)\omega_8 B\rho(\partial_y w + \partial_z v) + (1-\omega_8)C_{211}\,, \tag{3.86}$$
$$C^*_{121} = -1/3(\omega_1/2-1)\omega_8 B\rho(\partial_x w + \partial_z u) + (1-\omega_8)C_{121}\,, \tag{3.87}$$
$$C^*_{112} = -1/3(\omega_1/2-1)\omega_8 B\rho(\partial_x v + \partial_y u) + (1-\omega_8)C_{112}\,. \tag{3.88}$$

The partial derivatives in (3.86) to (3.88) are approximately obtained from second-order cumulants via

$$\partial_y w + \partial_z v = -3\omega_1/\rho C_{110}\,,\;\; \partial_x w + \partial_z u = -3\omega_1/\rho C_{101}\,,\;\; \partial_x v + \partial_y u = -3\omega_1/\rho C_{011}. \tag{3.89}$$

Again the equilibria definitions incorporate partial derivatives and two empirical scalar parameters A and B that aim at correcting aliasing effects. Last, the fifth- and sixth-order collisions are defined by

$$C^*_{221} = (1-\omega_9)C_{221}\,, \quad C^*_{212} = (1-\omega_9)C_{212}\,, \quad C^*_{122} = (1-\omega_9)C_{122}\,, \tag{3.90}$$
$$C^*_{222} = (1-\omega_{10})C_{222}\,. \tag{3.91}$$

3.2.3 Employed Cumulant Variants

The present thesis is based on two variants of the discrete cumulant collision operator. Both have in common that the second relaxation rate ω_2 is set to unity. This rate is linked to the bulk viscosity of the underlying fluid, cf. Geier et al. [2015, 2017a], and the choice of unity is accompanied by the introduction of numerical damping. Beyond, decoupling the shear and bulk viscosity is beneficial for the stability of simulating high Reynolds number flows.

All-One

The first variant, which matches initial recommendations of Geier et al. [2015], assigns all free rates to unity

$$\omega_{C\geq 2} = 1\,, \qquad \omega_1 = \omega = \frac{2}{6\nu+1}\,, \tag{3.92}$$

and $A = B = 0$. As a result, the explicit collision step distinctly simplifies to

$$C^*_{000} = C_{000}\,, \tag{3.93}$$
$$C^*_{100} = C_{100}, \quad C^*_{010} = C_{010}, \quad C^*_{001} = C_{001}\,, \tag{3.94}$$
$$C^*_{110} = (1-\omega)C_{110}, \quad C^*_{101} = (1-\omega)C_{101}, \quad C^*_{011} = (1-\omega)C_{011}\,, \tag{3.95}$$

$$\begin{aligned} C^*_{200} = {} & [(1-\omega)(2C_{200} - C_{020} - C_{002}) - 3\rho(1-\omega/2)(2u^2\partial_x u - v^2\partial_y v - w^2\partial_z w) \\ & + \kappa_{000} - 3/2\rho(u^2\partial_x u + v^2\partial_y v + w^2\partial_z w)]/3\,, \end{aligned} \tag{3.96}$$
$$\begin{aligned} C^*_{020} = {} & [(1-\omega)(-C_{200} + 2C_{020} - C_{002}) - 3\rho(1-\omega/2)(-u^2\partial_x u + 2v^2\partial_y v - w^2\partial_z w) \\ & + \kappa_{000} - 3/2\rho(u^2\partial_x u + v^2\partial_y v + w^2\partial_z w)]/3\,, \end{aligned} \tag{3.97}$$
$$\begin{aligned} C^*_{002} = {} & [(1-\omega)(-C_{200} - 2C_{020} + 2C_{002}) - 3\rho(1-\omega/2)(-u^2\partial_x u - v^2\partial_y v + 2w^2\partial_z w) \\ & + \kappa_{000} - 3/2\rho(u^2\partial_x u + v^2\partial_y v + w^2\partial_z w)]/3\,, \end{aligned} \tag{3.98}$$

with

$$\partial_x u = \left[\omega(-2C_{200} + C_{020} + C_{002}) - (C_{200} + C_{020} + C_{002} - \kappa_{000})\right]/(2\rho)\,, \tag{3.99}$$
$$\partial_y v = \left[\omega(\ \ C_{200} - 2C_{020} + C_{002}) - (C_{200} + C_{020} + C_{002} - \kappa_{000})\right]/(2\rho)\,, \tag{3.100}$$
$$\partial_z w = \left[\omega(\ \ C_{200} + C_{020} - 2C_{002}) - (C_{200} + C_{020} + C_{002} - \kappa_{000})\right]/(2\rho)\,. \tag{3.101}$$

All post-collision states of cumulants higher than order two are reset to zero, i.e.,

$$C^*_{\tilde{o}>2} = 0\,. \tag{3.102}$$

Subsequently, this approach is referred to as the *All-One* (C-AO) variant, which greatly supports the method's stability ascribed to obliterating the third- to sixth-order cumulants in the collision step. The C-AO was tested for a few benchmark cases, e.g, by Geier et al. [2015] or Far et al. [2016], including the Taylor-Green vortex for moderate Reynolds numbers and the flow around a sphere for Reynolds numbers in the range of $\mathcal{O}(10^2)$ to $\mathcal{O}(10^5)$. In addition, Asmuth et al. [2019] have successfully applied the C-AO approach to study more complex wind turbine flows at higher Reynolds numbers $\mathrm{Re} \approx \mathcal{O}(10^7)$ on relatively coarse grids.

Parameterized

Another cumulant operator suggested by Geier et al. [2017a] addresses the enhancement of the model's order yielding fourth-order accuracy with respect to the equivalent Navier-Stokes diffusion term. As a result of a leading error analysis, the three second-order relaxation rates read

$$\omega_3 = \frac{8(\omega-2)((3\omega-1)-5\omega)}{8(5-2\omega)\omega + (8+\omega(9\omega-26))} = \frac{8\,(2\omega^2-3\omega-2)}{7\omega^2-14\omega-8}\,, \tag{3.103}$$
$$\omega_4 = \frac{8(\omega-2)(\omega+(3\omega-7))}{(56-42\omega+9\omega^2)-8\omega} = \frac{8\,(4\omega^2-15\omega+14)}{9\omega^2-50\omega+56}\,, \tag{3.104}$$
$$\begin{aligned}\omega_5 &= \frac{24(\omega-2)(4\omega^2+\omega(18-13\omega)+(2+\omega(6\omega-11)))}{16\omega^2(\omega-6)-2\omega(216+5\omega(9\omega-46))+(\omega(3\omega-10)(15\omega-28)-48)} \\ &= \frac{24\,(3\omega^3-13\omega^2+12\omega+4)}{29\omega^3-130\omega^2+152\omega+48}\,.\end{aligned} \tag{3.105}$$

Moreover, the two scalar parameters are assigned to

$$A = \frac{4\omega^2+2\omega(\omega-6)+(\omega(10-3\omega)-4)}{(\omega-1)((2+3\omega)-8\omega)} = \frac{3\omega^2-2\omega-4}{-5\omega^2+7\omega-2}\,, \tag{3.106}$$
$$B = \frac{4\omega(9\omega-16)-4\omega^2-2(2+9\omega(\omega-2))}{3(\omega-1)((2+3\omega)-8\omega)} = \frac{14\omega^2-28\omega-4}{-15\omega^2+21\omega-6}\,. \tag{3.107}$$

Compared to the derivation of Geier et al. [2017a] based on $\omega_{\{3;4;5\}} = \omega_{\{3;4;5\}}(\omega_1,\omega_2)$ and $A[B] = A[B](\omega_1,\omega_2)$, here the substitutions $\omega_1 = \omega$ and $\omega_2 = 1$ are already used. The parameters A and B, occurring in conjunction with partial derivatives in the fourth-order collision, cf. (3.83) to (3.88), are, in turn, introduced to correct the anisotropy of the discretization. Hereinafter, this variant is labeled *Parameterized* (C-P) cumulant. The decisive value shrinking the initial interval of $\omega \in (0,2)$ resembles the parameterized $\omega_4(\omega)$

value, cf. (3.104), which becomes negative for $\omega < 7/4$ harming $\omega_{C\geq 2} \in [0, 2]$. Mind that this lower bound, $\omega = 7/4$, already matches (very) low Reynolds numbers laminar flows, such that a consideration is anyhow irrelevant for the scope of this work. Moreover, all singularities of (3.103) to (3.107) are uncritical since these are outside of $7/4 < \omega < 2$.

In the low viscosity (high Reynolds number) limit $\omega \to 2$ results from (3.18), whereby

$$\lim_{\nu \to 0} \omega_{\{3;4;5\}}(\omega) \to 0 \tag{3.108}$$

applies, cf. (3.103) to (3.105). Hence, the corresponding third-order cumulant expressions are fully conserved during collision

$$C^*_{102} \to C_{102}\,, \quad C^*_{120} \to C_{120}\,, \quad C^*_{012} \to C_{012}\,, \tag{3.109}$$

$$C^*_{210} \to C_{210}\,, \quad C^*_{021} \to C_{021}\,, \quad C^*_{201} \to C_{201}\,, \quad C^*_{111} \to C_{111}\,, \tag{3.110}$$

which has a detrimental effect on the numerical stability. To regularize these expressions at low viscosities, Geier et al. [2017a] suggested a limiter defined as

$$\tilde{\omega}_{3,1} = \omega_3 + \frac{(1-\omega_3)|C_{120}+C_{102}|}{\rho\lambda_3 + |C_{120}+C_{102}|}, \quad \tilde{\omega}_{4,1} = \omega_4 + \frac{(1-\omega_4)|C_{120}-C_{102}|}{\rho\lambda_4 + |C_{120}-C_{102}|}, \tag{3.111}$$

$$\tilde{\omega}_{3,2} = \omega_3 + \frac{(1-\omega_3)|C_{210}+C_{012}|}{\rho\lambda_3 + |C_{210}+C_{012}|}, \quad \tilde{\omega}_{4,2} = \omega_4 + \frac{(1-\omega_4)|C_{210}-C_{012}|}{\rho\lambda_4 + |C_{210}-C_{012}|}, \tag{3.112}$$

$$\tilde{\omega}_{3,3} = \omega_3 + \frac{(1-\omega_3)|C_{201}+C_{021}|}{\rho\lambda_3 + |C_{201}+C_{021}|}, \quad \tilde{\omega}_{4,3} = \omega_4 + \frac{(1-\omega_4)|C_{201}-C_{021}|}{\rho\lambda_4 + |C_{201}-C_{021}|}, \tag{3.113}$$

$$\tilde{\omega}_5 = \omega_5 + \frac{(1-\omega_5)|C_{111}|}{\rho\lambda_5 + |C_{111}|}, \tag{3.114}$$

where $\lambda_{\{3;4;5\}}$ refer to adjustable free parameters dimensionalized by the density. In line with Geier et al. [2017a], the present studies, which employ the standard limiter, are restricted to the same value applied to all cumulants, i.e.,

$$\lambda_{\{3;4;5\}} = \lambda\,, \tag{3.115}$$

and the default value is assigned to $\lambda_{\text{def}} = 10^{-2}$. For small products of $\rho\lambda$, the optimized relaxation rates converge to unity and, thus, to the C-AO variant. For large values, the limiter has virtually no effect, i.e., $\tilde{\omega}_{\{3;4;5\},\{1;2\}} = \omega_{\{3;4;5\}}$.

For the present work, the remaining higher-order ($\tilde{o} > 3$) relaxation rates are set to unity, i.e., $\omega_{C>5} = 1$, whereby the collision step, in addition to the C-AO relaxation, .i.e., (3.93)−(3.98), and the third-order relaxation, i.e., (3.76)−(3.82), includes

$$C^*_{220} = (1-2/\omega)A\rho(\partial_y v + \partial_z w)/3\,, \tag{3.116}$$

$$C^*_{202} = (1-2/\omega)A\rho(\partial_x u + \partial_z w)/3\,, \tag{3.117}$$

$$C^*_{022} = (1-2/\omega)A\rho(\partial_x u + \partial_y v)/3\,, \tag{3.118}$$

$$C^*_{211} = (\omega/2-1)B\omega C_{110}\,, \tag{3.119}$$

$$C^*_{121} = (\omega/2-1)B\omega C_{010}\,, \tag{3.120}$$

$$C^*_{112} = (\omega/2-1)B\omega C_{011}\,, \tag{3.121}$$

which again vanish in the low viscosity limit, i.e., $C^*_{\tilde{o}=4}(\omega \to 2) \to 0$, emphasizing the modifications' predominant impact on the third-order collision for high Reynolds number flows.

The regularization interacts with the turbulence treatment by suppressing the small-scale motion of the upper-frequency end of the energy spectra as discussed later herein, also observed by Asmuth et al. [2020] for wind turbine simulations. The latter study compares results of an LES ($\lambda = 10^{-6}$) that incorporates an algebraic SGS closure model, with results obtained by increasing the regularization parameter from the default value to $\lambda = 10^{-1}$ and $\lambda = 10^{0}$ without the use of an explicit SGS turbulence model. The study indicates significant flow changes in the turbulent wake downstream of the wind turbine, whereby results obtained from $\lambda = 10^{-2}$ to some extent resembled SGS results. Moreover, Pasquali et al. [2020] also researched the influence of increased or specifically tuned λ-values for TCF simulations at $\mathrm{Re}_\tau = \{950; 2000; 16000\}$. Since these contributions note a clear impact of the regularization parameter's choice on the quality of results, they serve as a basis and motivation for further in-depth research on the turbulence modeling capabilities by tuning the λ-value (3.115). Specifically, the following work, cf. Chap. 6, focuses on the limits of use, the extent of modeling parts of the TKE spectrum for different shear flow types, cf. Chap. 4, and the potential for improvement of results on computationally low-expense coarse grids.

4 Considered Test Cases

This chapter presents the three test cases consulted for benchmarking and verification. Among these is the free shear Taylor-Green vortex (TGV) test case to analyze the TKE dissipation for decaying turbulence and two wall-bounded shear flows, i.e., the plane turbulent channel flow (TCF) and the more complex periodic hill flow (PHF), which includes flow separation and reattachment. The description includes the primary test case specifics, such as domain sizes, initial and boundary conditions. Moreover, major results of related previous publications are briefly summarized, and the employed computational strategy of the present studies, referring to runtime and postprocessing implementations, is outlined for each case.

4.1 Taylor-Green Vortex

The Taylor-Green vortex (TGV) is a free shear flow test case that assumes a divergence-free velocity field, viz.

$$u = a_1 \cos(a_2 x) \sin(b_2 y)\ \sin(c_2 z)\,, \tag{4.1}$$
$$v = b_1 \sin(a_2 x) \cos(b_2 y)\ \sin(c_2 z)\,, \tag{4.2}$$
$$w = c_1 \sin(a_2 x)\ \sin(b_2 y) \cos(c_2 z)\,, \tag{4.3}$$

intruduced by Taylor and Green [1937] with eligible coefficients (a_ζ, b_ζ and c_ζ), where an exact analytical solution of the three-dimensional incompressible Navier-Stokes equations exists. In line with others, e.g., Wang et al. [2013], Fauconnier et al. [2013], Marié and Gloerfelt [2017] or Geier et al. [2021], this study employs the solenoidal initialization

$$u(x,y,z,t=0) = \quad u_0 \sin(x/L) \cos(y/L) \cos(z/L)\,, \tag{4.4}$$
$$v(x,y,z,t=0) = -u_0 \cos(x/L) \sin(y/L) \cos(z/L)\,, \tag{4.5}$$
$$w(x,y,z,t=0) = \quad 0\,, \tag{4.6}$$

within the 2π-periodic box domain $-\pi L \leq x_\mathrm{i} \leq \pi L$, where L is an arbitrary reference length. The initial density field is given by

$$\rho(x,y,z,t=0) = \rho_0 + \frac{\rho_0\, u_0^2}{16\, c_s^2} \left(\cos(2x/L) + \cos(2y/L)\right) \left(\cos(2z/L) + 2\right)\,, \tag{4.7}$$

cf. Fauconnier et al. [2013], applying the LBM pressure-density relation $\rho = p/c_s^2$, and ρ_0 displays an averaged reference density.

Figure 4.1 illustrates the flow's three distinct phases. The initial phase involves the transition to turbulence, where large-scale structures are formed, followed by a second phase, where the vortices are stretched and break into increasingly smaller scales. Shortly afterward, the flow becomes fully turbulent, and the kinetic energy dissipation maximizes.

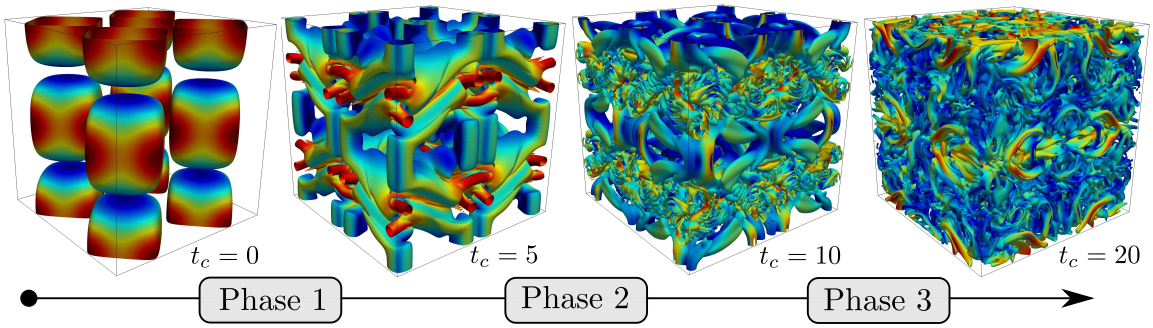

Figure 4.1: Transient evolution of vorticial structures displayed by the Q-criterion (Dubief and Delcayre [2000]) colored by the velocity magnitude, during the three subsequent phases for the TGV at $\mathrm{Re} = 1600$.

Finally, a third phase governed by the decay of turbulence is observed. The Reynolds number is defined by $\mathrm{Re} = (u_0\, L)/\nu$ and the Mach number relates to u_0.

The TGV test case is often used to verify the dissipation of numerical schemes, e.g., cf. Fauconnier et al. [2013], derive selective/adaptive LES filtering strategies, e.g., Aubard et al. [2013]; Marié and Gloerfelt [2017]) or to assess the overall performance of LBM implementations, e.g., cf. Nathen et al. [2018] or Geier et al. [2021].

Computational Strategy

The total simulation time covers $20t_c$ based on the characteristic convective time $t_c = L/u_0$. During runtime, the scalar TKE is computed from the instantaneous velocity vector in every discrete time and at each node. The output time series $k(t)$ contains the integrated values for the entire domain, i.e., the total instantaneous TKE per time step. The assessment starts immediately at the beginning of the simulation, as $\overline{u}_\mathrm{i} = 0$ applies, whereby each velocity component equals a fluctuation, viz. $u_\mathrm{i} = u'_\mathrm{i}$.

Since the test case involves neither turbulent production from a mean flow nor convection, the temporal evolution of the TKE dissipation rate reduces to $\varepsilon = -\mathrm{d}k/\mathrm{d}t$. The minus takes the continuous negative gradient into account, such that $\varepsilon(t)$ is always positive for plotting. The postprocessing involves a second-order finite difference scheme for the two outermost time steps (t_1 & t_2 and t_{n-1} & t_n) and a fourth-order finite difference scheme in between these bounds. Results are displayed in non-dimensional form through $\varepsilon\,[\,\cdot\, L/u_0^3]$ and $t\,[\,/t_c \equiv \cdot\, u_0/L]$ and the emloyed reference data relates to spectral simulations of Brachet et al. [1983] and Marié and Gloerfelt [2017].

4.2 Turbulent Channel Flow

The plane turbulent channel flow is a fundamental wall-bounded shear flow test case implying relevant engineering physics which can be thoroughly studied without compromising the domain's resolution and extent. The latter depends on the specific flow under consideration and requires an augmentation to cover large-scale eddies at high Reynolds numbers, where an insufficiently small domain size might affect the credibility of turbulence statistics due to the large correlation lengths, e.g., example demonstrated by Moser et al. [1999]. The lowest friction Reynolds number ensuring fully developed turbulent flow conditions

is $\mathrm{Re}_\tau = 180$, where the benchmark results of a DNS study go back to Kim et al. [1987] accomplished by a classical Navier-Stokes based solver. The flow geometry and the coordinate system are illustrated in Fig. 4.2, with periodic boundaries applied in the x and z direction for an infinite continuation. In line with the description in Sec. 2.2.2, the height of the domain matches $2H$ and the wall-normal direction complies with the y coordinate bounded by no-slip plane walls. Moreover, the exent is $4\pi H$ in the streamwise (x) and $2\pi H$ in the spanwise (z) direction. Vreman and Kuerten [2014] provide a comprehensive overview of available DNS results for the TCF at $\mathrm{Re}_\tau = 180$.

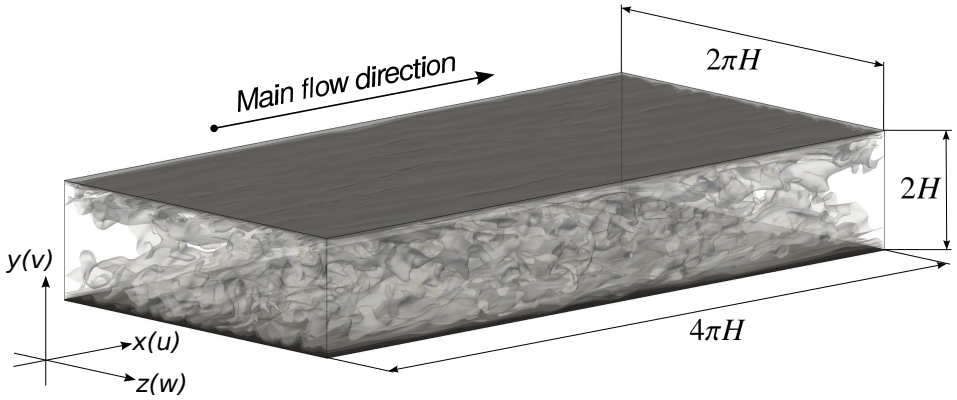

Figure 4.2: Illustration of the turbulent channel flow domain.

Initial LES of the TCF were, for instance, conducted by Deardorff [1970] for $\mathrm{Re}_\tau = 2400$ or Moin and Kim [1982] for $\mathrm{Re}_\tau = 650$. Subsequent DNS studies including higher Reynolds numbers are reported by, e.g., Moser et al. [1999] up to $\mathrm{Re}_\tau = 590$, Bernardini et al. [2014] including $\mathrm{Re}_\tau = 4000$ or Lee and Moser [2015] through $\mathrm{Re}_\tau = 5200$ among numerous others. LBM related TCF studies at various Reynolds numbers, i.e., between $\mathrm{Re}_\tau = 180$ and $\mathrm{Re}_\tau = 16000$, and employing different collision models are published by, e.g., Amati et al. [1997], Lammers et al. [2006], Wang et al. [2014], Nathen et al. [2018], Pasquali et al. [2020] and Maeyama et al. [2021a].

Computational Strategy

The TCF is computationally driven by a steady, homogeneous axial pressure gradient ($\partial p/\partial x$) which is imposed as a force density acting on every fluid node via

$$\mathrm{f}_{x,P} = \left(\frac{\partial p}{\partial x}\right)_P \quad [\mathrm{kgm^{-2}s^{-2}}]\,. \tag{4.8}$$

The pressure gradient is supposed to balance the mean shear load, which, in turn, is assumed to display a linear variation along the vertical coordinate, viz.

$$\left(\frac{\partial p}{\partial x}\right)_P = \left(\frac{\partial \tau}{\partial y}\right)_P = \left(\frac{|\tau_W|}{H}\right)_P = \mathrm{Re}_\tau^2 \left(\frac{\nu^2 \rho}{H^3}\right)_P . \tag{4.9}$$

Hence, the employed body force is rigidly linked to the prescribed friction Reynolds number. Substituting $\rho = \rho_0 = 1$, the nondimensional axial LB body force density is defined by

$$\mathrm{f}_x = \frac{\mathrm{Re}_\tau^2\, \nu^2}{N_H^3}\,, \tag{4.10}$$

with N_H denoting the number of discrete lattice nodes per half-channel height.

The no-slip solid wall BC refers to the SBB method, cf. (3.32), for $\mathrm{Re}_\tau = 180$, whereas the IBB scheme, outlined in detail in Sec. 3.1.2, is applied for all higher Reynolds numbers. For all TCF simulations, the preset Mach number relates to the centerline velocity, i.e.,

$$\mathrm{Ma} = \frac{u_C}{c_s^2} \quad \rightarrow \quad u_C = \frac{\mathrm{Ma}}{\sqrt{3}} \quad \Leftrightarrow \quad u_B = \frac{\mathrm{Ma}}{1.16\sqrt{3}} \approx \frac{\mathrm{Ma}}{2} \quad \Leftrightarrow \quad u_\tau \overset{(2.32)}{\approx} 0.096\mathrm{Ma}^{7/8} \,. \tag{4.11}$$

Two-Point Correlations and Energy Spectra

To analyze the results in greater detail and verify the adequacy of the considered domain size, one-dimensional two-point correlations $R_\vartheta^{x[z]}$ $[\mathrm{m}^2/\mathrm{s}^2]$ are compiled in streamwise (superscript x), and spanwise (superscript z) direction for selected wall-normal distances (labeled Θ) employing spatial-temporal averaged line probes. Attention is confined to normal stress components, i.e., $\vartheta = \{\overline{u'u'}; \overline{v'v'}; \overline{w'w'}\}$. The TPCs are computed in the entire x-z planes of the domain. However, evaluations rest upon axially parallel lines in stream- and spanwise direction controlled by a running index $\varepsilon = \{0; N_{x[z]} - 1\}$, viz.

$$R^x_{\overline{u'u'}}(x, z_\epsilon, \Theta) = \overline{u'(x = 0, z_\epsilon, \Theta)\, u'(x, z_\epsilon, \Theta)} \,, \tag{4.12}$$

$$R^z_{\overline{u'u'}}(x_\epsilon, z, \Theta) = \overline{u'(x_\epsilon, z = 0, \Theta)\, u'(x_\epsilon, z, \Theta)} \,, \tag{4.13}$$

exemplary depicted for the $\overline{u'u'}$ component here. The displayed one-dimensional TPCs follow from in-plane spatial averages, viz.

$$R_\vartheta^{x[z]}(x[z], \Theta) = 1/N_{z[x]} \sum_{\epsilon=0}^{N_{z[x]}-1} R_\vartheta^{x[z]}(x[x_\epsilon], z_\epsilon[z], \Theta) \,. \tag{4.14}$$

Related one-dimensional energy spectra $E_\vartheta^{x[z]}(k_{x[z]})$ $[\mathrm{m}^3\mathrm{s}^{-2}]$ computed from the averaged TPCs are used to assess the energy distribution along the resolved scales. Here, $\kappa_{x[z]}$ $[\mathrm{m}^{-1}]$ denotes the wave number, whereby low values correspond to large scales. The energy spectra are obtained from discrete Fourier transformation (DFT), cf. Cooley and Tukey [1965], which requires an adequate processing of the averaged TPCs (4.14), particularly demanding a symmetric input. Figure 4.3 illustrates the adopted four-step symmetrization approach for a straightforward example with five (left) and four (right) input points, respectively.

Firstly, the global maximum (zeroth) element ($x = 0$) is assigned to the mid value (0), which remains unchanged. Subsequently, an unweighted mean is computed for $x[z] > 0$ via

$$R(x[z]) = \frac{R(x[z] + R(N_{x[z]} - x[z])}{2} \qquad x[z] = \{1; ...; \varsigma\} \,, \tag{4.15}$$

with $\varsigma = (N_{x[z]} - 1)/2$ [odd] and $\varsigma = N_{x[z]}/2 - 1$ [even] as indicated by *2)* in Fig. 4.3 (R sub- and superscript omitted here for clarity). Averaging eliminates (numerical) deviations of the actually symmetrical R shape, which should not occur due to the assumed stream- and spanwise periodicity. Subsequently, the values are shifted *3)* to the right-hand side of the center. The intended symmetric correlations follow from the final data mirroring *4)*.

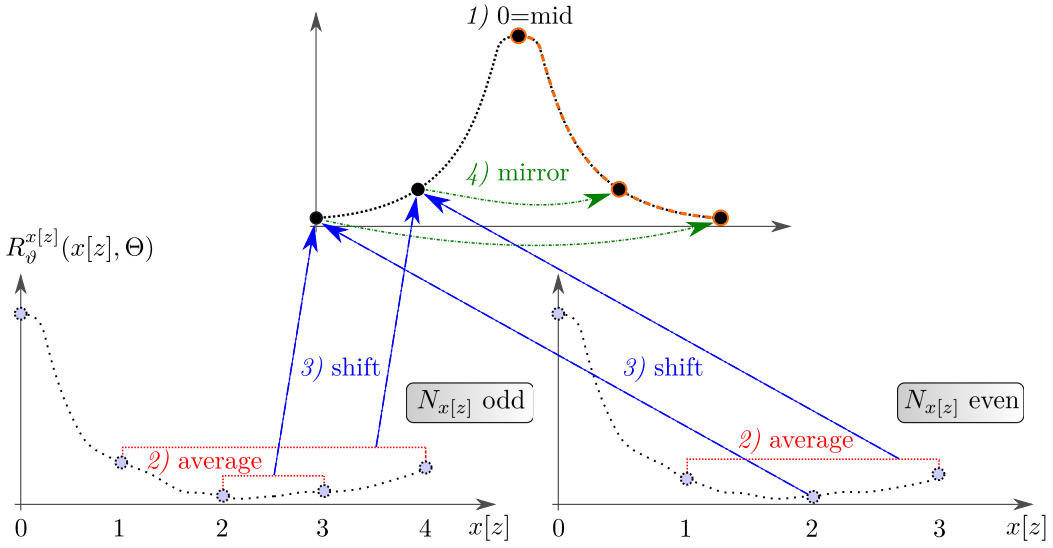

Figure 4.3: Employed $R_\vartheta^{x[z]}$ symmetrization algorithm for an even [odd] number of input data points. Points along dotted lines in the bottom figures represent 1D TPCs defined by (4.14). The resulting DFT input is illustrated by the closed black circles in the top figure.

Thus, the length ($N_{x[z]}$) of $R_\vartheta^{x[z]}$ is incremented by one for even input elements. The orange dashed line in Fig. 4.3, covering the half pathway starting from the global maximum, exemplary represents the two-point correlation data shown in the results section, where the trajectories are additionally normalized using their maxima.

The discrete energy contributions $E_\vartheta^{x[z]}(k_{x[z]})$ per wave number $\kappa_{x[z]} = 2\pi\, x[z]/N_{x[z]}$ correspond to the magnitude of the computed Fourier coefficients. In order to reduce oscillations, the symmetric DFT input (R) is filtered using a von Hann window ($1/2 - \cos(2\pi\, x[z]/N_{x[z]})/2$), cf. Harris [1978]. Due to the odd number of real input elements in the present study, $N_B = (N_{x[z]} + 1)/2$ [bin indexing: $[0 : (N_{x[z]} - 1)/2]$ DFT bins are obtained, attributed to conjugate (Hermitia) symmetry.

The representation is nondimensionalized by means of $E^{x[z],+} = E^{x[z]}/(u_\tau^2\,\Theta)$ [-] plotted over $\kappa_{x[z]}\,\Theta$ [-]. The first bin with the zero wave number contribution is not displayed and a cutoff $k_c = 0.9\,N_B$ is applied to all spectra. To suppress strong oscillations in the high wave number regime the streamwise spectra are additionally truncated according to the following conditions: *(i)* $k_c > 0.4\,N_B$, *(ii)* positive E gradient, and *(iii)* $E(k)/E(k-1) > 3/2$ to avoid excessive sharp cutting for minor gradients.

Moreover, integral lengths scales are computed from the TPCs via

$$\lambda^+_{x[z]}(y_\Theta) = \frac{1}{u_\tau\,\nu}\int_0^{\mathrm{r}} R_\vartheta^{x[z]}\mathrm{d}x[\mathrm{d}z] \overset{y_\Theta = y^+}{=} \int_0^{\mathrm{r}} R_\vartheta^{x[z],+}\mathrm{d}x^+[\mathrm{d}z^+] \tag{4.16}$$

to assess the computed structures and the sensitivity to resolution aspects. To avoid cancellation of positive and negative values, the integral lengths are evaluated from their (positive) origin to the first root (r) of their argument.

Shear Stress Computation

For the subsequent cumulant model developments, cf. Sec. 6.2 and Sec. 6.3, the particular contributions to the total shear stress are investigated in detail. To this end, according to Geier et al. [2017a] and Pasquali et al. [2020], a second-order representation of the shear stress in a plane channel flow reads

$$\tau_{xy} = \mu \left(\frac{\partial u}{\partial y} + \frac{\partial v}{\partial x} \right) = \mu \left(-\frac{3}{\rho} \omega \, C_{101} \right) = -3\nu \, \omega \, C_{101} \, , \tag{4.17}$$

where ω is given by (3.66) and the cumulant subscripts refer to $i[x] = 1$, $j[z] = 0$ and $k[y] = 1$, owing to the orientation of the wall-normal and the primal flow direction in the present case, cf. Fig. 3.1 and Fig. 4.2. To enable an in-depth analysis of distinct contributions, the total shear stress (tot) along the x-y plane is partitioned through

$$\begin{aligned} \tau_{\mathrm{tot}} &= \tau_{\mathrm{res}} + \tau_{\mathrm{vis}} + \tau_{\mathrm{mod}} \\ &= - \left(\rho \, \overline{u'v'} + 3 \left(\nu + \nu_t \right) \omega_e \, C_{101} \right) , \end{aligned} \tag{4.18}$$

where the prior subscript xy to mark the in-plane orientation is omitted in the remainder for the sake of brevity. The contributions correspond to the resolved (res) stresses and a combination of viscous (vis) and modeled (mod) stresses. The latter two involve an effective relaxation rate ω_e due to the employed Boussinesq viscosity concept, cf. (3.38).

4.3 Periodic Hill Flow

The periodic hill flow (PHF) test case was initially the subject of experimental investigations for a periodic arrangement of analytically described hills in a straight channel. The two dimensional geometry was initially published by Almeida et al. [1993]. Its piecewise definition via six polynomials $s_i(x)$ is given in a nondimensional representation rounded to three decimal places as

$$s_i(x)/H^* = \begin{cases} \min\left(1, 1.000 + 0.190\,x^2 - 1.666\,x^3\right) & x \in [0, 0.321] \; H^* \\ 0.896 + 0.975\,x - 2.845\,x^2 + 1.482\,x^3 & x \in \,]0.321, 0.500] \; H^* \\ 0.921 + 0.821\,x - 2.536\,x^2 + 1.275\,x^3 & x \in \,]0.500, 0.714] \; H^* \\ 1.445 - 1.380\,x + 0.545\,x^2 - 0.162\,x^3 & x \in \,]0.714, 1.071] \; H^* \\ 0.640 + 0.874\,x - 1.559\,x^2 + 0.492\,x^3 & x \in \,]1.071, 1.429] \; H^* \\ \max\left(0, 2.014 - 2.011\,x + 0.461\,x^2 + 0.021\,x^3\right) & x \in \,]1.429, 1.929] \; H^* \end{cases} \tag{4.19}$$

where the hill height H^* is equal to unity within this notation. The resulting contour of the hill is shown in Fig. 4.4 [solid red]. The geometry is homogeneous in the lateral (z) direction, and the flow is deemed periodic in the longitudinal (x) and lateral direction, cf. Fig. 4.5.

The case features separation from a curved surface and accelerated and decelerated mean shear. Due to the more complex physics, the test case represents a natural candidate to scrutinize simulation capabilities subsequent to assessing simple unidirectional channel flows. The PHF is part of prominent benchmark databases, e.g., ERCOFTAC (Rapp et al.

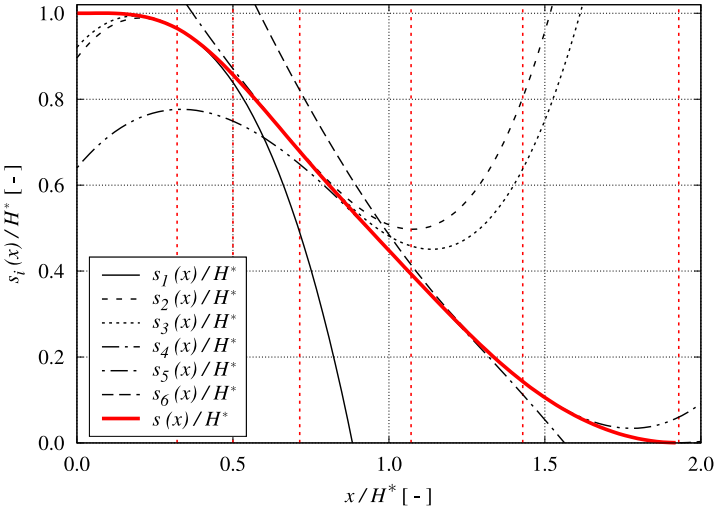

Figure 4.4: Hill geometry piecewisely defined via six polynomials $s_i(x)$ normalized by the hill height H^*.

[2009]), featuring reference data from various simulations of Breuer and Rodi [1996] or Manhart et al. [2001] and experiments by Rapp and Manhart [2011].

To reduce the influence of lateral walls and improve the periodicity in the lateral direction, the initial geometry of Almeida et al. [1993], firstly numerically analyzed by Rodi et al. [1995], was revised by Mellen et al. [2000]. The revised setup also served as a basis for extensive experimental studies, e.g., Rapp and Manhart [2007, 2011]. In comparison to the initial geometry, the revised geometry increases the ratio of the horizontal to vertical dimension L_x/L_y to π, which avoids an undesired longitudinal correlation as proven by Fröhlich et al. [2005]. Experimental data for the revised geometry were reported for four Reynolds numbers, i.e. $\mathrm{Re} = \{5600; 10600; 19000; 37000\}$ by Rapp and Manhart [2011] and two further Reynolds numbers, i.e. $\mathrm{Re} = \{8000; 33000\}$ by Kähler et al. [2016], whereas numerical studies, cf. Temmerman and Leschziner [2001], Fröhlich et al. [2005], Breuer et al. [2006, 2009], Xia et al. [2013], Gloerfelt and Cinnella [2019], Gao et al. [2020] and Xiao et al. [2020], refer to a wider range of Reynolds numbers between $\mathrm{Re} = 10^2$ and $\mathrm{Re} = 10^5$, i.e., laminar as well as highly turbulent conditions. Similar to the majority of investigations, the present study employs the revised geometry in a domain that spans $L_x \times L_y \times L_z = 9H \times 3.035H \times 4.5H$. Here H refers to the height of the hill, L_x denotes the horizontal distance between the hill crests, and L_y denotes the maximum vertical distance between the plane bottom wall and the straight top wall, cf. Fig. 4.5. The definition of the Reynolds number employs H and the bulk velocity u_B at the entrance plane ($x = 0$), which is spatially averaged in lateral (z) and vertical (y) direction, viz.

$$\mathrm{Re} = \left(\frac{u_B\, H}{\nu} \right)_P \quad \text{with} \quad u_{B,P} = \frac{1}{2.035H \cdot L_z} \int_{L_z} \int_{H}^{3.035H} u\,(x = 0, y, z)\, \mathrm{d}y\, \mathrm{d}z\,, \tag{4.20}$$

where $\mathrm{d}y\, \mathrm{d}z = \Lambda_x^2$, cf. (3.46). Numerical simulations are performed with periodic boundary conditions along the longitudinal (x) and lateral (z) end planes. The Mach number also relates to the bulk velocity, i.e., $\mathrm{Ma} = u_B/c_s$ and the required SI quantities are set constant to $\nu_P = 1.01 \cdot 10^{-6}\,\mathrm{m}^2/\mathrm{s}$ and $H = 0.05\,\mathrm{m}$ for all PHF parameter studies.

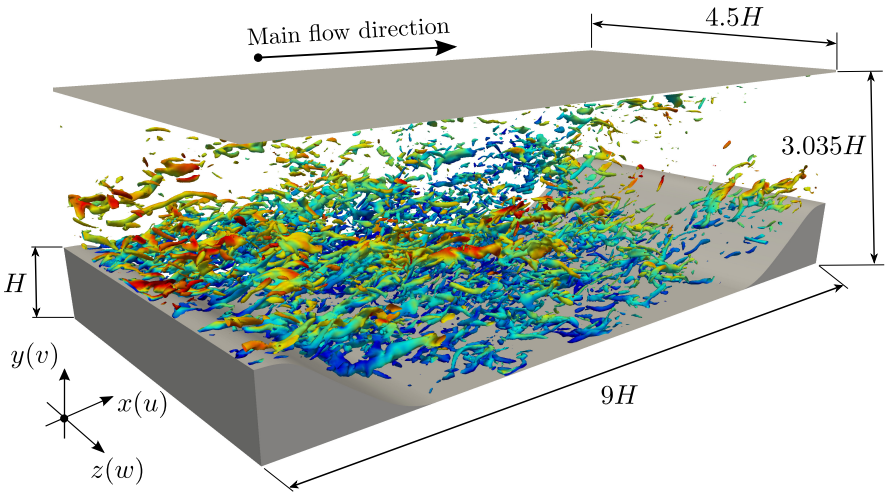

Figure 4.5: Illustration of the physical domain supplemented by isosurfaces of the longitudinal vorticity component $\omega_x = \partial w/\partial y - \partial v/\partial z$ (20% of the maximum value) colored by the velocity magnitude.

Computational Strategy

The investigated flow is driven by a pressure gradient $\partial p/\partial x$ acting in the longitudinal direction. The pressure gradient is imposed as an homogeneous axial body force f_x, cf. Sec. 3.1.3, which is adjusted during runtime to comply with the targeted bulk Reynolds number. To this end, an initial value is iteratively found during the preceding initial transient phase of the simulation. Subsequently, a reconciliation between the current and targeted Reynolds number is carried out ten times per flow pass t_{FP}. The latter employs the computation of a spatially averaged instantaneous inlet-plane velocity as described in (4.20). If the deviation (dev) of the Reynolds numbers, i.e., $\mathrm{Re}_{\mathrm{dev}} = 1 - \mathrm{Re}_{\mathrm{actual}}/\mathrm{Re}_{\mathrm{target}}$ is outside of $-0.015 < \mathrm{Re}_{\mathrm{dev}} < 0.015$, the body force is scaled by $\mathrm{f}_x = \mathrm{f}_x(1 - 0.1\mathrm{Re}_{\mathrm{dev}})$. This approach was found to be both robust and accurate enough to limit the Reynolds number deviations to $\mathcal{O}(10^{-3})$.

The flow-pass time (3.52) corresponds to $t_{\mathrm{FP},P} = L_x/u_{B,P}$ and, hereafter, the spatial discretization is referred to by specifying the nondimensional number of discrete nodes per hill height, i.e., $N_H = H/\Lambda_x\,[-]$, whereby $t_{\mathrm{FP}} = 9N_H/u_B$ applies due to $L_x = 9H$.

Data Recording

The simulation process includes an initial transient period of 50 FP. This is followed by another 50 FP to converge the temporally averaged velocity vector $\overline{u}_i$. Subsequently, the computation of the Reynolds stresses is performed for approximately 100 FP. Thus, each simulation covers around 200 FP. In accordance with reference data sets sourced from ERCOFTAC, cf. Rapp et al. [2009], mean velocity and Reynolds stress profiles are evaluated at ten different axial locations, see Fig. 4.6. The profiles are obtained from the temporally averaged flow field, which is also spatially averaged in the homogeneous lateral (z) direction to accelerate convergence. Results are compared with experiments and data reported from two different Navier-Stokes procedures, namely *LESOCC* by Breuer and Rodi [1996] based on curvilinear grids and *MGLET* developed by Manhart et al. [2001] for non-equidistant Cartesian grids, cf. Tab. 4.1. LES reference solutions employ

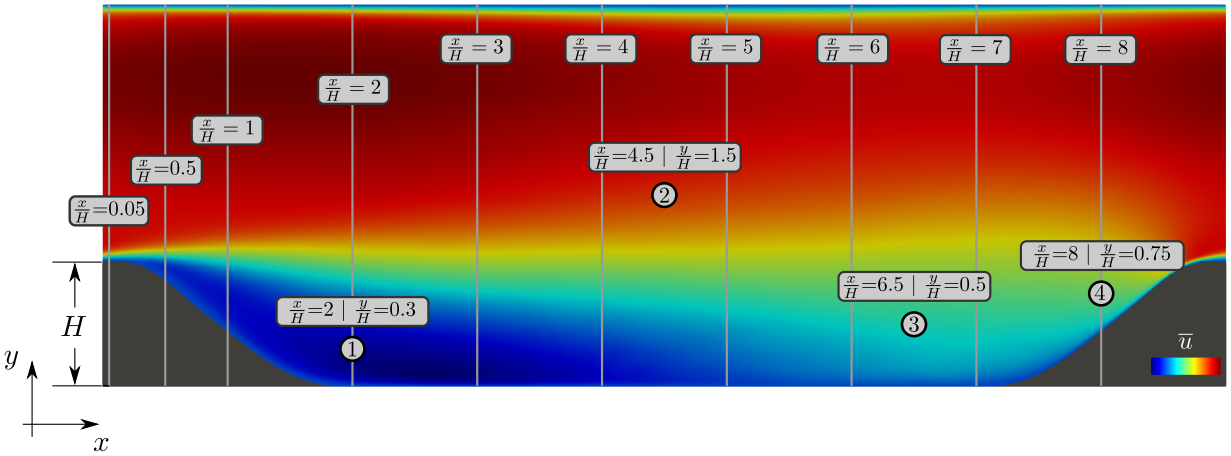

Figure 4.6: Locations of averaged profiles (lines) and instantaneous quantities (points) in the central x-y plane of the domain.

the well-known (dynamic) Smagorinsky model complemented by the van Driest [1956] damping function near solid walls. Additionally, instantaneous velocity data is recorded

Table 4.1: Utilized reference data sets with a classification of turbulence treatment and grid size.

Re	Solver	Classification	$\sum_{i=\{x;y;z\}} N_i$ [$\times 10^6$]
700	*LESOCC*	DNS	13.1
2800	*LESOCC* & *MGLET*	DNS	13.1 & 48.0
10600	*MGLET*	LES	4.1
37000	*MGLET*	LES	4.1

at four different characteristic points of the flow field over 150 FP to compute the PSD, cf. Tab. 4.2 accompanied by Fig. 4.6.

Table 4.2: Point probe positions for the instantaneous velocity recordings in the x-y center plane.

Identifier	Position $[(x, y)/H]$	Flow Characteristics
P-1	(2 , 0.3)	Recirculating Flow
P-2	(4.5 , 1.5)	Core Flow
P-3	(6.5 , 0.5)	Reattached Flow
P-4	(8 , 0.75)	Accelerated Flow

Energy Spectra and Filtering

The PSD follows from a discrete Fourier transform (DFT) of the instantaneous time series of the velocity components (u, v and w) recorded at four different locations in the numerical domain, cf. Tab. 4.2. For the underlying study, this is equivalent to considering only the main diagonal elements of the autocorrelation tensor (2.17). No comparison is performed with other research efforts as the related spectral data is non-available. In order to enable comparisons of different configurations, the displayed data is nondimensionalized with H and u_B, viz. $PSD\,[\mathrm{m}^2/\mathrm{s}]/(u_B\,H)$ resp. $f\,[1/\mathrm{s}]\cdot H/u_B$.

Figure 4.7 (left) depicts the exemplary raw data $PSD(f)$ for all three velocity components extracted at location P-2 (core flow). Due to distinct oscillations, the visual comparison

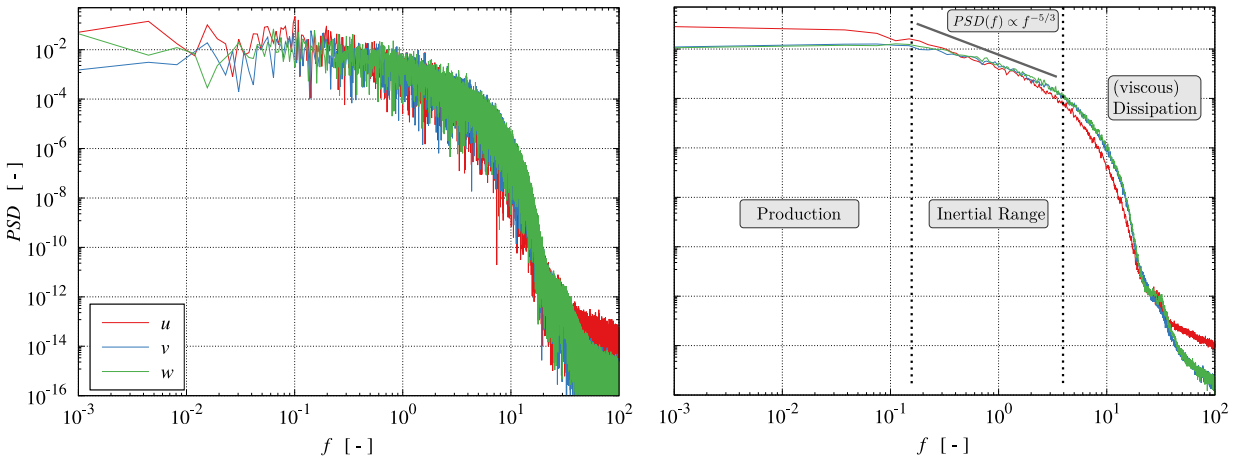

Figure 4.7: Exemplary power spectral density $PSD(f)$ the three velocity components, i.e., u [red], v [blue] and w [green], at P-2 (core flow) of the PHF. Raw (left) and filtered (right) data sets.

between the graphs is hampered, and a moving average filter is applied to the underlying DFT raw data. The filter width spans 100 discrete frequency contributions and the filtered $PSD(f)$ graphs are depicted in Fig. 4.7 (right).

Reynolds Stress Invariant Maps

A widespread approach to analyze turbulent structures is the visual evaluation using the Q-criterion introduced by Dubief and Delcayre [2000]. Due to its qualitative nature, not all details can be revealed, and the present study opts to observe the tensor of the (resolved) Reynolds stresses using anisotropy invariant maps (AIM). The starting point is the nondimensional anisotropy tensor, cf. Lumley and Newman [1977] or Choi and Lumley [2001],

$$a_{\mathrm{ij}} = \frac{\overline{u'_{\mathrm{i}}u'_{\mathrm{j}}}}{2k} - \frac{\delta_{\mathrm{ij}}}{3}\,, \tag{4.21}$$

with $k = \overline{u'_{\mathrm{i}}u'_{\mathrm{i}}}/2$ representing the turbulent kinetic energy and δ_{ij} being the Kronecker delta. The graphical evaluation, exemplarily depicted in Fig. 4.8, of the flow anisotropy introduced by Banerjee et al. [2007] refers to plotting the invariants of a_{ij} in a two-dimensional

space, viz.

$$x_B = \Lambda_1 - \Lambda_2 + \frac{3}{2}\Lambda_3 + \frac{1}{2} \quad \text{and} \quad y_B = \frac{\sqrt{27}}{2}\Lambda_3 + \frac{\sqrt{3}}{2}\,. \tag{4.22}$$

Herein x_B and y_B denote barycentric (B) coordinates and Λ_i are the eigenvalues of a_{ij}, sorted in descending order, i.e., $\Lambda_1 \geq \Lambda_2 \geq \Lambda_3$. All possible points are bounded by

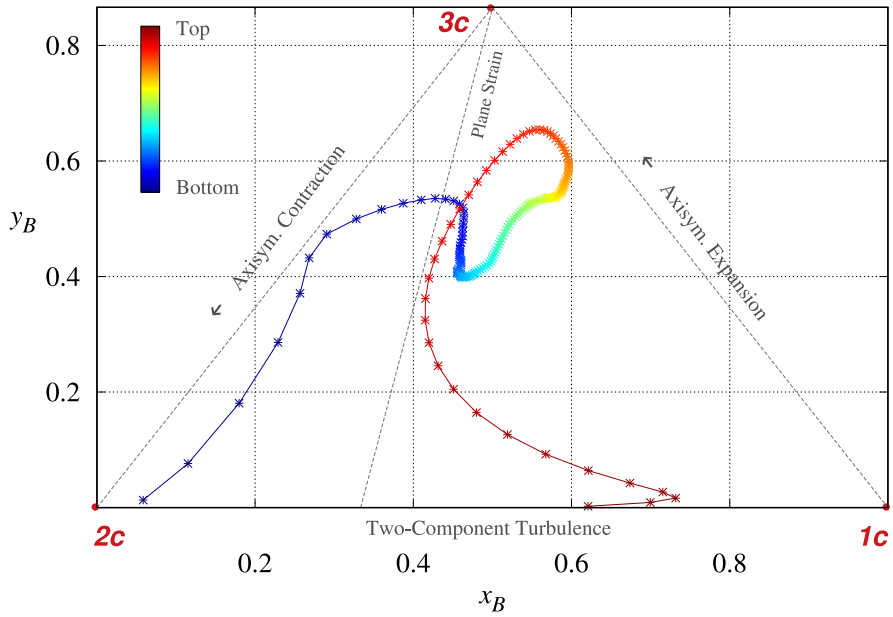

Figure 4.8: Exemplary AIM at $x/H = 3$, cf. Fig. 4.6, of a fine grid simulation for the baseline bulk Reynolds number of Re = 2800.

an isosceles triangle whose vertices state one-component turbulence ($1c$ at [1,0]), isotropic two-component turbulence ($2c$ at [0,0]) and isotropic 3D turbulence ($3c$ at [1/2,$\sqrt{3}$/2]). The triangle edges indicate two-component turbulence ($\overline{2c-1c}$) and axisymmetric contraction ($\overline{3c-2c}$) or axisymmetric expansion ($\overline{1c-2c}$). The advantage of the barycentric map rests upon equal weighting of the vertex points, i.e., $1c$, $2c$, and $3c$ turbulence, whereby important details are crucially magnified.

Error Quantification

To allow for a code-to-code-verification of the predicted velocity and Reynolds stress profiles and assess the global flow field, a relative L_2 error norm of a specific flow quantity (ϑ) is introduced by

$$L^{\mathrm{ref}}_{2,\mathrm{rel}}(\vartheta)\big|_{x/H} = \frac{\sum\limits_{n=1}^{N_y}\left(\vartheta_{x/H}\,(n) - \vartheta^{\mathrm{ref}}_{x/H}\,(n)\right)^2}{\sum\limits_{n=1}^{N_y}\left(\vartheta^{\mathrm{ref}}_{x/H}\,(n)\right)^2}\,. \tag{4.23}$$

To this end, a cubic spline interpolation of the available reference (ref) ERCOFTAC data sets, cf. Rapp et al. [2009], is taken as the ground truth, which is evaluated at each (n) discrete lattice node. As a result, each one-dimensional profile featuring N_y nodes is reduced

to a single scalar. L2-Graphs displayed in Sec. 6.1.2 include these ten (verification) "error" measures, one for each assessed x/H location, as well as their respective (unweighted) mean value to characterize the overall accuracy of the flow field prediction.

Nondimensional Wall Distance

The classification of the grid resolution rests upon the nondimensional wall distance y^+, cf. (2.30). Its computation is based on the velocity gradient obtained at the first wall-adjacent fluid nodes using the averaged velocity vector components $\overline{u}$ and $\overline{v}$ in the centered x-y plane. The tangential part $\overline{u}_\parallel$ is obtained by subtracting the projection of the two-dimensional components in the direction of the wall normal. The velocity gradient follows from $u_\parallel/q$ with q being the subgrid distance, cf. Fig. 3.3. The corresponding wall shear stress $\tau_W = \nu\,\overline{u}_\parallel/q$, the friction velocity (2.28), and the nondimensional wall distance are defined from linear relations and, thus, get inaccurate beyond $y^+ \geq 12$. Visualized data is smoothed by a centered unweighted moving average involving five sampling points to account for the Cartesian discretization of the hill geometry. Mind that the y^+ distribution is generally smooth along the top wall and the plain center section of the bottom wall, where $q = 0.5$ is imposed. A rougher distribution is experienced alongside the curved segments of the lower wall, i.e., $x/H \leq 1.93$ and $x/H \geq 7.07$, where q varies. For $q = 0.5$, the evaluated y^+ distribution quantifies the resolution of the isotropic, homogeneous Cartesian grid by means of $\Delta x^+ = 2y^+$.

5 Collision Model Benchmark

This chapter includes a comprehensive preliminary benchmark of the employed LBM collision operators. Based on a division in two parts, Sec. 5.1 addresses TCF studies employing fully-resolved to slightly under-resolved grids ($\Delta x^+ = 12$) in the DNS, LES or VLES regime, while coarser grids up to $\Delta x^+ = 18$ are covered in Sec. 5.2.

5.1 (Highly) Resolved Turbulent Channel Flow

The initial collision model benchmark is grounded on the turbulent channel flow at $\mathrm{Re}_\tau = u_\tau\, H/\nu = 180$, i.e., the lowest Reynolds number to ensure fully resolved turbulence. Equally, this enables the finest discretizations down to and including the Kolmogorov scale. This preliminary scrutinization aims at assessing the performance of three common collision models, i.e., BGK, MRT and cumulant (C-AO) for simulating fully- to slightly under-resolved grids. The latters refers to discretizations featuring $\Delta x^+ \leq 10$.

5.1.1 Specifications

Table 5.1 summarizes the test case specifics of the employed TCF studies. The domain size spans $4\pi H$ in streamwise (x), $2\pi H$ in spanwise (z) and $2H$ in wall-normal (y) direction. The baseline Mach number, related to the mean centerline velocity, is set to $\mathrm{Ma} = 1/20$, whereby the LB viscosity is of order $\mathcal{O}(10^{-4})$. Employing $\mathrm{Re} = \mathrm{Re}_C$, from (3.51) follows $\nu = \{1.3, \ldots, 8.2\} \cdot 10^{-4}$ for $\mathrm{Ma} = 1/20$, where the highest viscosity value relates to the finest discretization of $\Delta x^+ = 2$. The fine grid definition is based on the requirement to resolve the Kolmogorov scale. According to Kim et al. [1987] and Moser et al. [1999], a lattice spacing of roughly two wall units is needed, i.e., $H/\Lambda_x = N_H \geq 90$, where N_H is the number of discrete lattice nodes per half-channel height and $\Lambda_x = 2H/(N_y - 2)$ is the spatial scaling factor, hence $N_H = N_y/2 - 1$. The employed homogeneous isotropic DNS grid consists of $N_y = 184$ nodes in normal, $N_x = 1120$ nodes in streamwise and $N_z = 562$ nodes in spanwise direction. As opposed to the reference studies, the present discretization is significantly finer in the streamwise and the spanwise direction, where homogeneous lattice distances of $\Delta x^+ = 10$ and $\Delta z^+ = 5$ are often deemed sufficient. The wall-normal resolution of alternative methods is usually realized with inhomogeneous grids that stretch from near-wall spacings around $\Delta y^+ = 0.1$ to $\Delta y^+ = 5$ at the horizontal midplane.

Following the fine-grid studies, successively coarser meshes using $N_y = 111$ ($\Delta x^+ \approx 3.3$), $N_y = 62$ ($\Delta x^+ \approx 6$), $N_y = 47$ ($\Delta x^+ \approx 8$), $N_y = 38$ ($\Delta x^+ \approx 10$) and $N_y = 31$ ($\Delta x^+ \approx 12$) were investigated to assess the sensitivity of diffusive scaling, cf. Tab. 5.2. As some of the collision models are unstable under coarsening, intermediate grids were used to assess their limits. The flow-pass time (3.53) is defined through $t_{\mathrm{FP}} = N_x/u_B \approx 25.2 N_H/\mathrm{Ma}$. Mind that the near-wall distance of the first fluid node adjacent to the solid boundary always

Table 5.1: Test case specifications for the initial collision model benchmark.

	Specification
Test case	TCF at $\mathrm{Re}_\tau = 180$
	$\rightarrow \mathrm{Re}_B \approx 2750$, $\mathrm{Re}_C \approx 3200$
Reference data	Moser et al. [1999] (MKM-99)
Collision Models	BGK, MRT, C-AO
Turbulence Modeling	none/implicit
Wall Modeling	none
Wall BC	SBB (with $q \equiv 0.5$)
Physical quantities	$\nu_P = 1.5 \cdot 10^{-5}\,\mathrm{m^2 s^{-1}}$, $H = 0.05\,\mathrm{m}$
Domain size	$4\pi H(x) \times 2\pi H(z) \times 2H(y)$
Δx^+	$\{2, \ldots, 10\}$
Ma	$\{1/40, 1/20, 1/10\}$

refers to half the respective lattice spacing, i.e. $y^+ = \Delta x^+/2$. Due to this grid layout and the relatively fine discretizations, the SBB solid boundary condition is applied, cf. Fig. 3.3 (right) and (3.32).

Table 5.2: Grid number, spatial resolution, LB viscosity (for Ma = 1/20), total amount of grid points, flow-pass time and employed collision models.

No.	Δx^+	ν $[\cdot 10^{-4}]$	$N_x \times N_y \times N_z$	N_{tot}	t_{FP}	Models
1	2	8.2	$1120 \times 184 \times 562$	115 816 960	45900	BGK, MRT, C-AO
2	3.3	4.9	$690 \times 111 \times 346$	26 500 140	27500	BGK, MRT, C-AO
3	6	2.7	$382 \times 62 \times 192$	4 547 328	15100	BGK, MRT, C-AO
4a	7	2.3	$330 \times 53 \times 166$	2 903 340	12900	BGK
4b	8	2.0	$290 \times 47 \times 146$	1 989 980	11300	MRT, C-AO
5	10	1.6	$232 \times 38 \times 118$	1 040 288	9100	C-AO
6	12	1.3	$192 \times 31 \times 98$	583 296	7300	C-AO

For each computation, the initial forcing f_x resulting from (4.10) is iteratively adjusted until stable compliance with the target Reynolds number $\mathrm{Re}_\tau = 180$ is approximately achieved, i.e. $(u_\tau - \overline{u}_\tau)/\overline{u}_\tau \leq 5\%$, where u_τ refers to the instantaneous planar averaged value and $\overline{u}_\tau$ resembles the spatially and temporally averaged quantity. The iteration requires about 10 FP.

Subsequent to the adjustment of the forcing, an initial transient period of $T_i \approx 45\,\mathrm{FP}$, i.e., $2 \cdot 10^6$ discrete time steps, is included to ensure fully developed turbulence, before time averaged data and statistics are compiled from a data extraction period of again $T_e \approx 45\,\mathrm{FP}$ for the baseline Mach number. Hence, the DNS grid includes about 100 flow passes in total. This cycle was not altered when the grid was coarsened, which implies a longer averaging and extraction period at the root of the coarse grid results and was

probably lavish in terms of computational efforts. Thus, the medium grid No. 3 already covers about 250 FP in total, and grid No. 5 involves 440 FP. Statistical convergence has been verified by comparing the respective time averaged and statistical quantities for $\{1/5; 2/5; 3/5; 4/5; 1\}T_e$. In this regard, no substantial changes were observed beyond $3T_e/5$ for any grid. For consistency reasons, identical initial transient and averaging periods have been used for the other two Mach numbers, which therefore refer to double (Ma = 1/40) and half (Ma = 1/10) the amount of time steps, respectively. Subsequently displayed normalized quantities refer to:

- two-point correlations $R^{x|z}_{\overline{u'_\mathrm{i}u'_\mathrm{i}}}\left[= R^{x|z}_{u_\mathrm{i}u_\mathrm{i}}\right]$ by their maxima at $[x|z]^+ = 0$,
- one-dimensional energy spectra $E^{x|z}_{\overline{u'_\mathrm{i}u'_\mathrm{i}}}\left[= E^{x|z}_{u_\mathrm{i}u_\mathrm{i}}\right]$ by means of u_τ and H,
- wave numbers $\kappa_{x|z}$ by H,
- root mean square (RMS) values by u_τ, i.e., $\overline{u'_\mathrm{i}u'^{+}_\mathrm{i}}_{\mathrm{RMS}}\left[= u'_\mathrm{i}u'^{+}_{\mathrm{iRMS}}\right] = \frac{\sqrt{\overline{u'_\mathrm{i}u'_\mathrm{i}}}}{u_\tau}$.

5.1.2 Results and Discussion

Adequacy of the Domain Size and Resolution

The adequacy of the employed DNS discretization of the finest grids and the considered domain size is indicated by the two-point correlations and energy spectra displayed in Fig. 5.1 to Fig. 5.3. The figures compare MKM-99 data with exemplary results obtained from the BGK model in conjunction with the two finest grids declared in Tab. 5.2. The predicted normalized two-point correlations $R^{x/z}_{uu|vv}$ on the left side and corresponding 1D energy spectra on the right side were extracted in streamwise (top) and spanwise (bottom) direction at fixed wall distances, i.e., $y^+ = 5$ and $y^+ = 79$, respectively. The correlations decline to small values well away from the domain boundaries, and the energy density drops by approximately four orders of magnitude between the low and the high wave numbers. The energy spectra indicate no energy accumulation in the high wave number region. Moreover, the results do not differ significantly when the resolution is slightly coarsened to $\Delta x^+ = 3.3$ and display a fair agreement level with the reference data. Mind that displayed spectra were filtered with a third-order Savitzky-Golay filter using 11 base points for the sake of clarity. The filtering procedure does not change the result in streamwise direction but removes minor high wave number oscillations occurring in the spanwise direction, as indicated by a comparison between the raw and the filtered data in Fig. 5.3.

Mean Flow

Table 5.3 outlines the predicted mean flow and log law parameters for the fine-grid results. Moreover, Fig. 5.4 displays the mean velocity profile in comparison with reference data reported by Moser et al. [1999]. The predictive discrepancy between the different collision models is small and the BGK model provides a surprisingly fair agreement with the reference data. The parameter $\overline{u}/\overline{u}_m$ shows an almost perfect agreement between the considered data sets. All collision models display a fairly moderate variation of the von Kármán parameter κ, where the biggest deviation from the reference value $\kappa = 0.38$ is around 4.2% for the C-AO model.

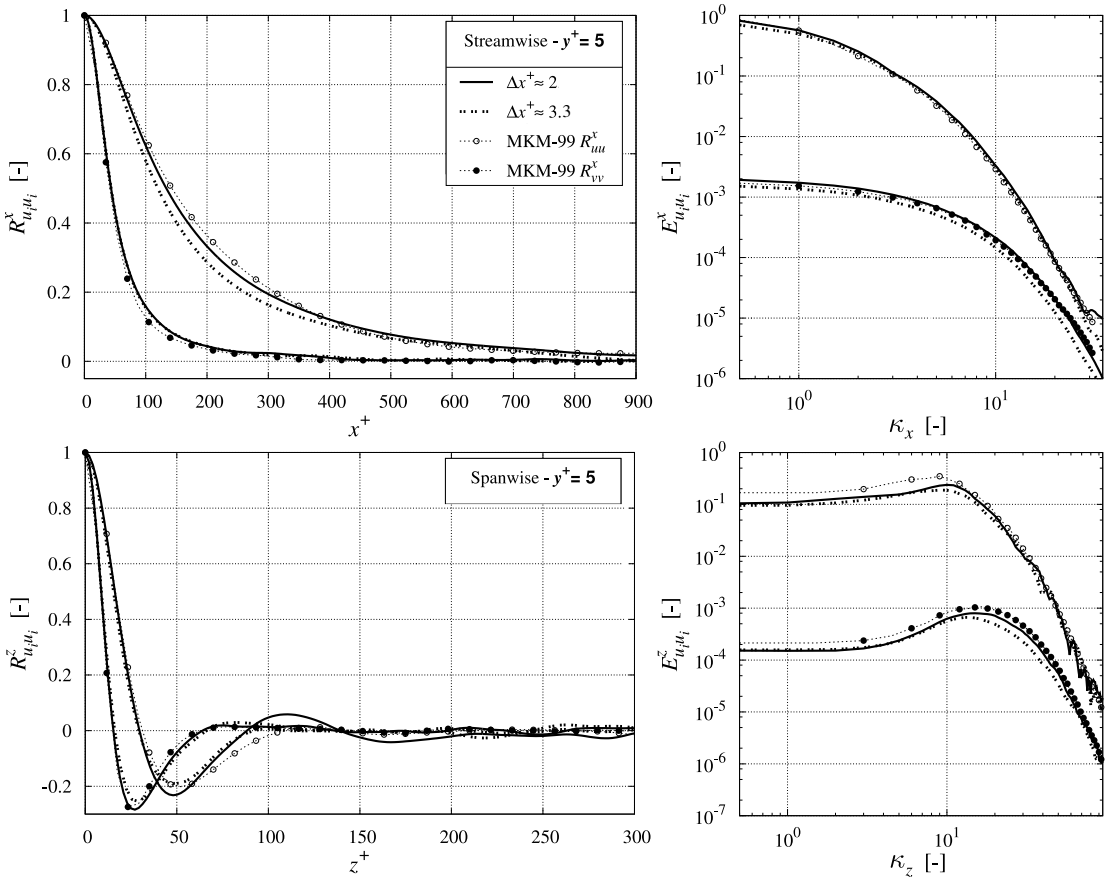

Figure 5.1: TPCs $R^{x/z}_{uu|vv}$ (left) returned by the BKG model for two different resolutions, i.e., $\Delta x^+ = 2$ [solid], $\Delta x^+ = 3.3$ [dashed], and related 1D energy spectra $E^{x/z}_{uu|vv}$ (right) in streamwise (top) and spanwise (bottom) direction at a near-wall position of $y^+ = 5$ in comparison to MKM-99 reference data.

Table 5.3: Computed mean values of the bulk (u_B), centerline (u_C) and friction (u_τ) velocity besides parameters of the log law $u^+ = \ln(y^+)/\kappa + C^+$ for the fine grid ($\Delta x^+ = 2$) alongside with the MKM-99 reference data.

Model	BGK	MRT	C-AO	MKM-99
u_B/u_τ	15.72	16.07	16.23	15.73
u_C/u_τ	18.28	18.68	18.89	18.30
u_C/u_B	1.16	1.16	1.16	1.16
κ	0.390	0.385	0.396	0.380
C^+	5.13	5.43	5.94	5.03

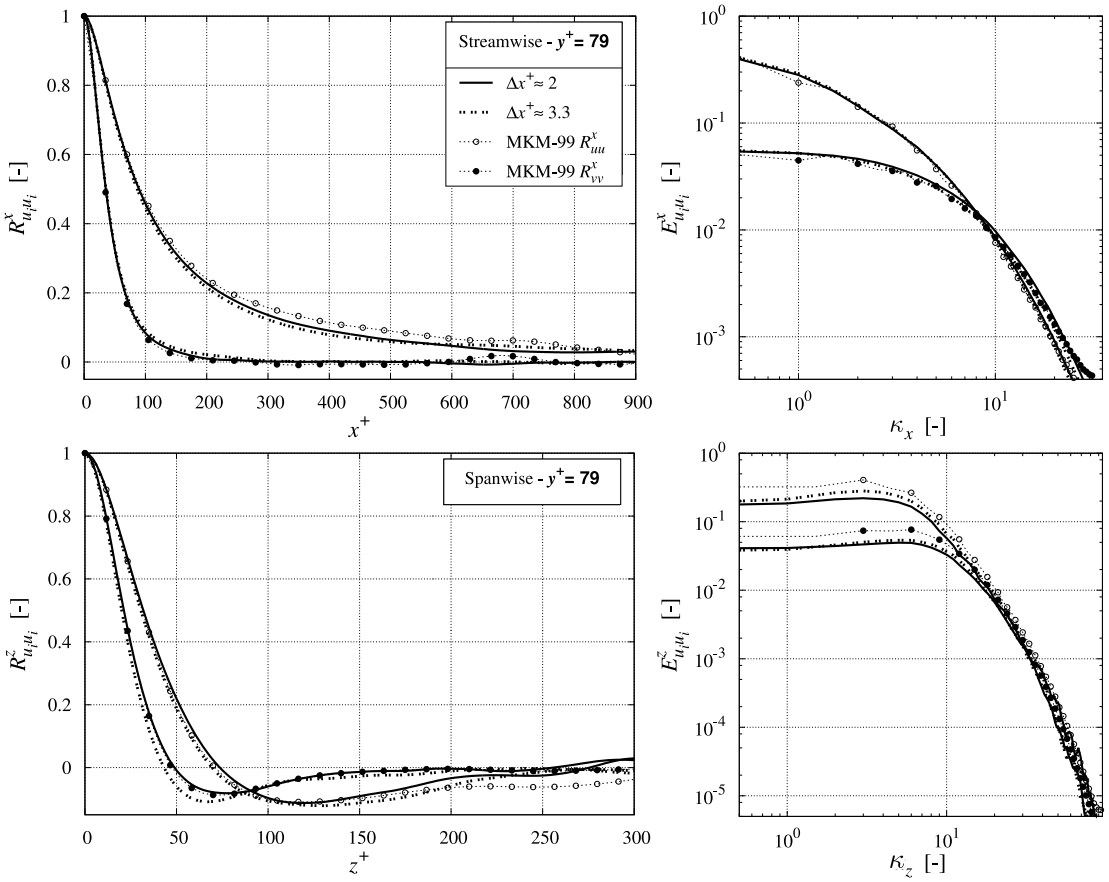

Figure 5.2: Two-point correlations $R^{x/z}_{uu}$ and $R^{x/z}_{vv}$ (left) returned by the BKG predictions for two different resolutions, i.e., $\Delta x^+ = 2$ [solid], $\Delta x^+ = 3.3$ (dashed), and related 1D energy spectra $E^{x/z}_{uu}$ and $E^{x/z}_{vv}$ (right) in streamwise (top) and spanwise (bottom) direction at $y^+ = 79$ in comparison to MKM-99 reference data.

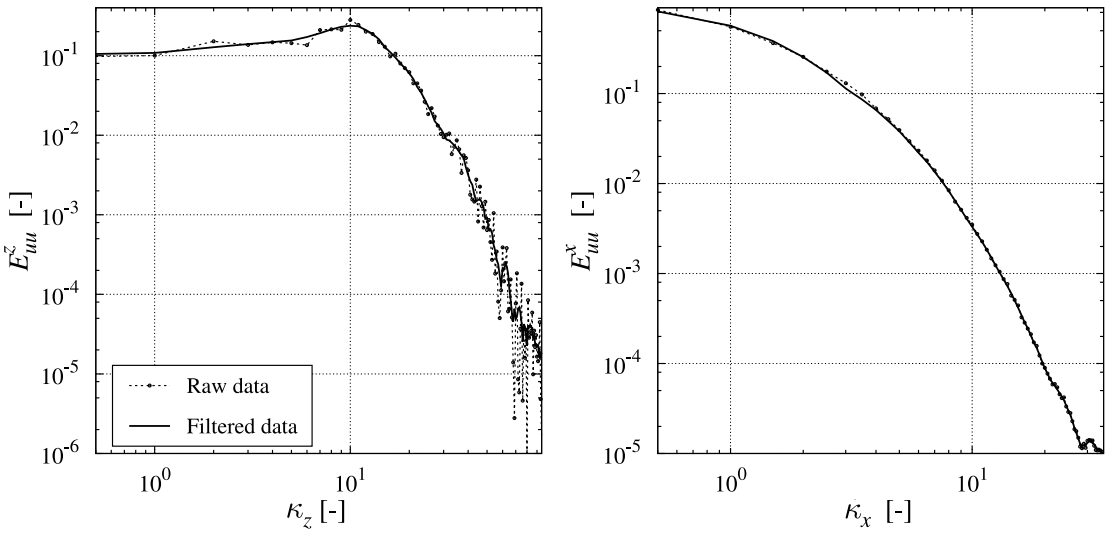

Figure 5.3: Comparison of raw data [dashed] and filtered data [solid] for span- (left) and streamwise (right) 1D energy spectra computed on the fine grid at $y^+ = 5$.

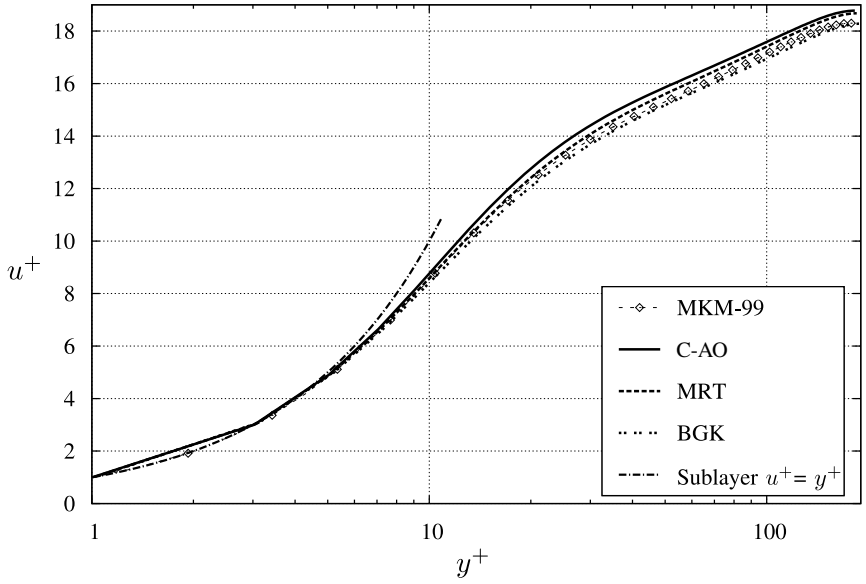

Figure 5.4: Predicted nondimensional mean velocity for the DNS grid.

The onset of the turbulent regime displays more variations to each other, and the reference data, where the maximum difference between the LBM-predicted C^+-parameters is slightly more than 16% and the value returned by the C-AO model exceeds the reference value $C^+ = 5.03$ by approximately 18%. This can be attributed to an enhanced ratio between the centerline velocity and the friction velocity u_c/u_τ for the MRT and, particularly, the C-AO model. It appears that the predicted shear stress falls below the MKM-99 reference value by more than 3.5% [2%] for the C-AO [MRT] model. For the MRT model, an increase of 2% for u_c^+ matches the observed increase of almost 8% of the C^+-parameter fairly accurate.

The data also compares favorably with an experimental study of Zanoun et al. [2003] which suggests $\kappa = 1/e$ and $C^+ = 10/e$ in conjunction with a parameter value of $e \approx 2.7$ for large enough Reynolds numbers $\mathrm{Re}_\tau \geq 2000$, i.e., $\kappa = 0.37$ and $C^+ = 3.7$. Similar to the findings of Lammers et al. [2006] and Moser et al. [1999], a slightly different relation is found due to the low Reynolds number ($e \approx 2.6, C^+ \approx 13.2/e$) for the present LBM DNS results.

The reason for a lower wall shear stress displayed by the MRT and the C-AO model is accessed by the single- and two-point turbulence statistics, where the C-AO model appears to return a higher correlation length in the streamwise direction and a more pronounced near-wall damping as outlined below. On the contrary, the BGK model displays less wall damping and an earlier increase of turbulent motion when leaving the near-wall regime.

Turbulence Intensities and Reynolds Stresses

The different near-wall behavior of the three investigated collision models is appraised by the turbulence intensities. All intensities shown in Fig. 5.5 reveal very similar general characteristics and closely follow the reference data. The BGK model provides peak and log law intensities which are slightly higher than the C-AO results. Values returned by the MRT model are located in between the results of the other two models, usually closer to the C-AO model. While an increase of peak and log law intensities is of minor importance

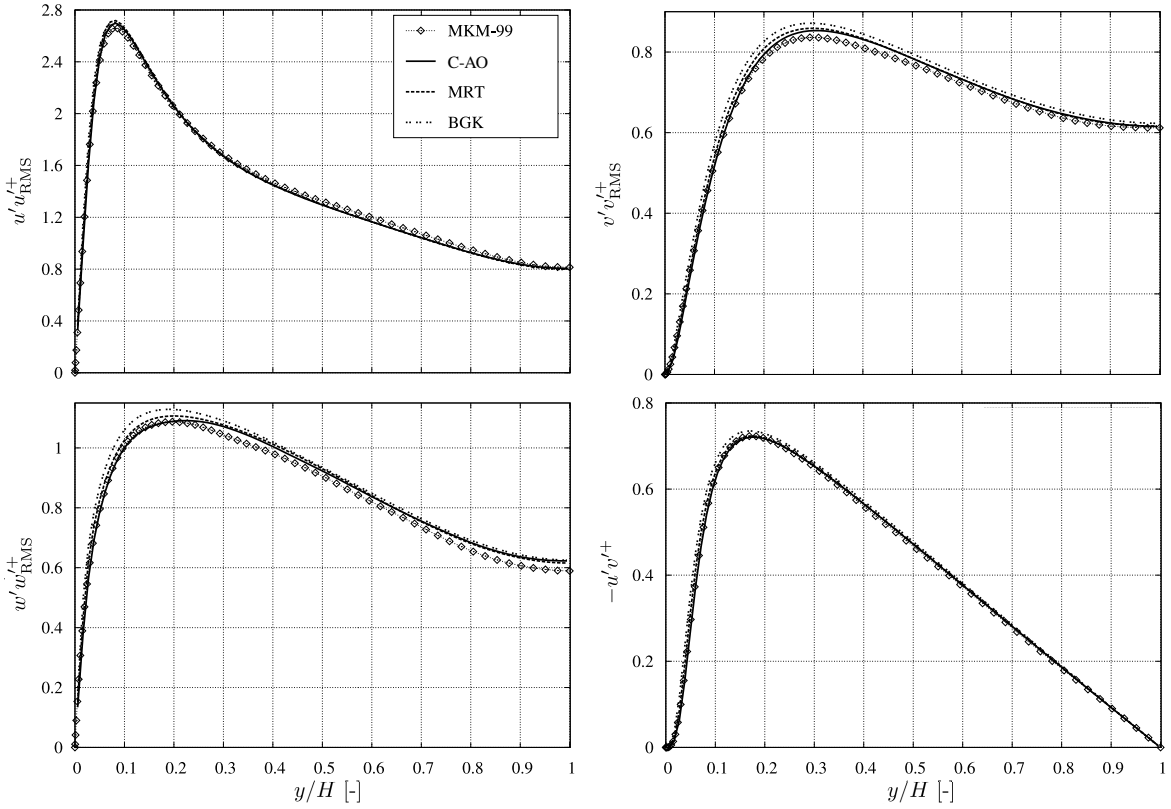

Figure 5.5: Predicted nondimensional turbulence intensities and turbulent shear stresses.

for the mean flow, a closer look at the near-wall situation illustrated by Fig. 5.6 manifests much larger differences which comply with the findings for the mean velocities. Here, the C-AO model predictions of near-wall intensities for the streamwise RMS values are around $10 - 15\%$ lower than the BGK predictions, and the correlating difference for the wall-normal component is more than 30%. In accordance with the significant difference in wall-normal direction, the predicted turbulent shear stress is significantly lower for the C-AO model than the BGK result. Also, it reflects a much smaller shear-exerting gradient near the wall. It is noted that the near-wall agreement of the intensities and the shear stress with the MKM-99 data is not necessarily the best for the BGK model, but the LBM results are consistent with each other.

Two-point Correlations and Turbulent Structures

An elementary aspect is the behavior of the predicted two-point correlations. Emphasis is given to normalized streamwise and spanwise correlations $R^{x|y|z}_{u_i u_i}$ for a sequence of fixed nondimensional wall distances $y^+ = \{5; 19; 40\}$. The occurrence and location of the $R^z_{u_i u_i}$ minima support identifying structures and estimating their size. Similar to the reference data, both spanwise correlations $R^z_{uu|vv}$ outlined in Fig. 5.7 display local minima below wall distance values of $y^+ < 80$. All spanwise correlation minima reach negative values between -0.2 and -0.3, in line with findings of previous researchers, e.g., cf. Moser et al. [1999] and Bespalko et al. [2012]. The detected R^z_{vv} minima reveal the occurrence of streamwise vortices. Their location between $z^+ \approx 25$ near the wall and $z^+ \approx 50$ at $y^+ = 40$ gives an estimate of their diameter.

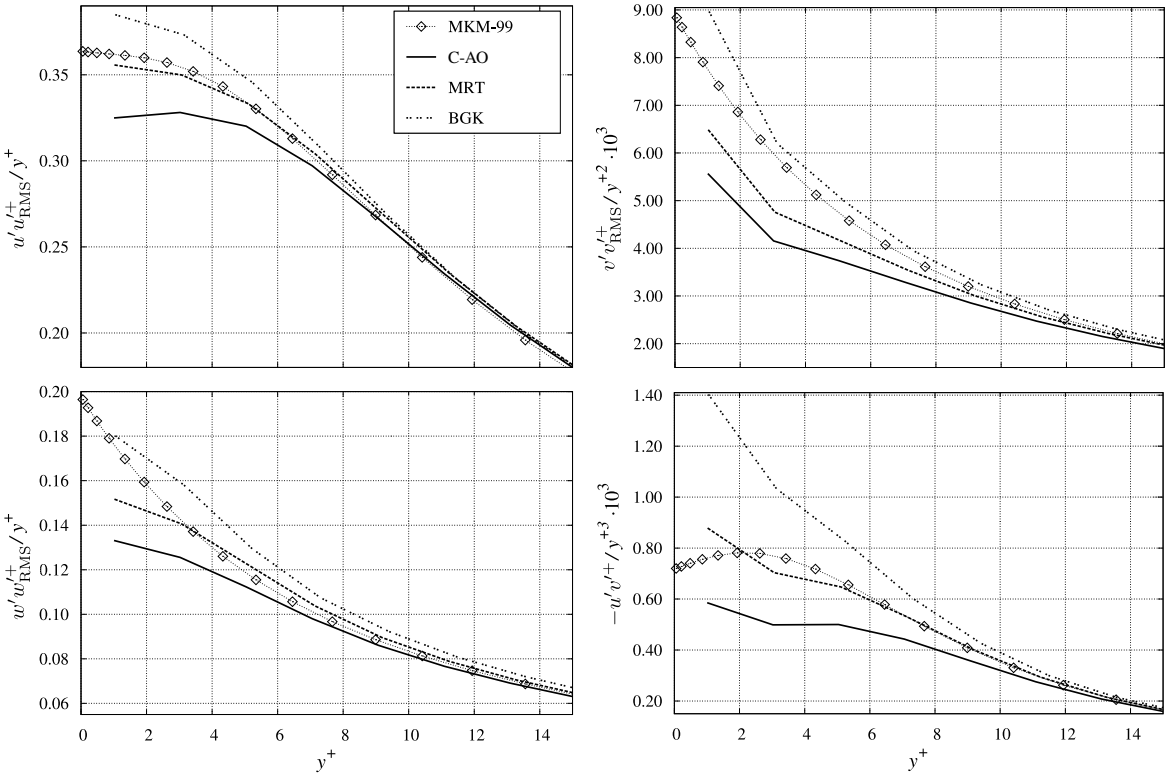

Figure 5.6: Near-wall behavior of the predicted nondimensional intensities and turbulent shear stresses for the DNS grid ($\Delta x^+ = 2$).

Consistent with formerly reported results, the spanwise R^z_{vv}-minimum occurs closer to the wall than the R^z_{uu}-minimum. The latter marks the separation between the high-speed and the low-speed fluid at approximately half the mean streak spacing. Furthermore, the spanwise R^z_{ww}-minimum is restricted to regions within $y^+ < 30$, which does not support the existence of counter-rotating vortex pairs, cf. Moser and Moin [1984]. The shape of the streamwise correlations is much simpler and shows a fair agreement, as indicated by the exemplary results outlined by Fig. 5.8. Identifying predictive differences from the data displayed in Fig. 5.7 and Fig. 5.8 is quite ambiguous. Hence, integral values might support distinguishing the individual collision model behavior. Former analyses, e.g., cf. Tritton [1967], revealed that the normalized streamwise correlation length of the streamwise velocity peaks at the upper end of the buffer layer, where the respective values significantly exceed the y^+ values and subsequently drops in the log layer. Similar behavior is found for all other correlations in the streamwise direction.

Figure 5.9 compares the integral length scales for the R^x_{uu} and the R^x_{vv} components obtained from the present study with the reference data reported by Moser et al. [1999]. The comparison indicates that the BGK model delivers length scales that follow the MKM-99 results very closely for the primary component (R^x_{uu}) and also display a lower peak for the wall-normal component (R^x_{vv}) that agrees better with the MKM-99 results.

On the contrary, the MRT model and, in particular, the C-AO model display significantly larger peak values, which are approximate 15% higher than the BGK result for the C-AO model. The generally lower correlation-length values predicted by the BGK model increase the turbulence energy levels and support smaller scales. The latter is visible from the

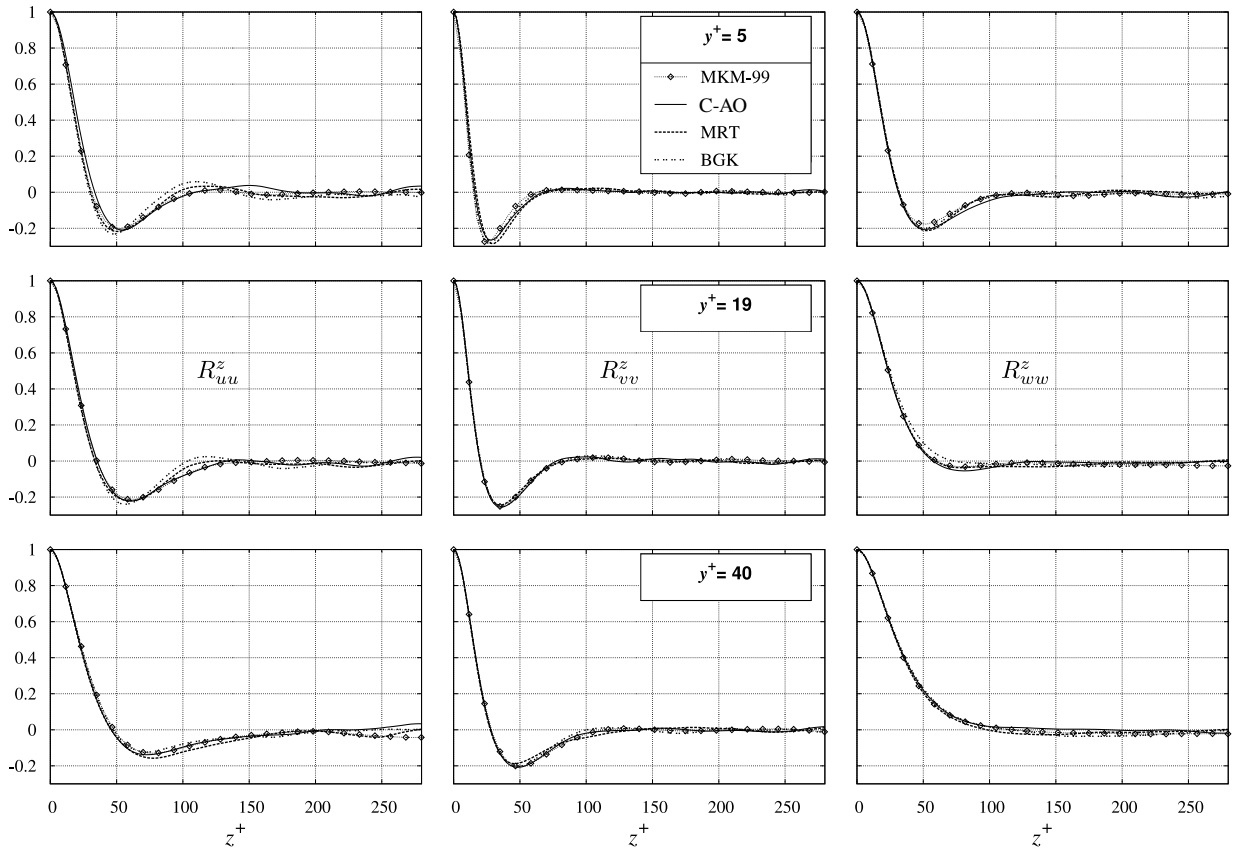

Figure 5.7: Predicted spanwise normalized two-point correlations R^z_{uu} (left), R^z_{vv} (center) and R^z_{ww} (right) at $y^+ = 5$ (top), $y^+ = 19$ (center) and $y^+ = 40$ (bottom).

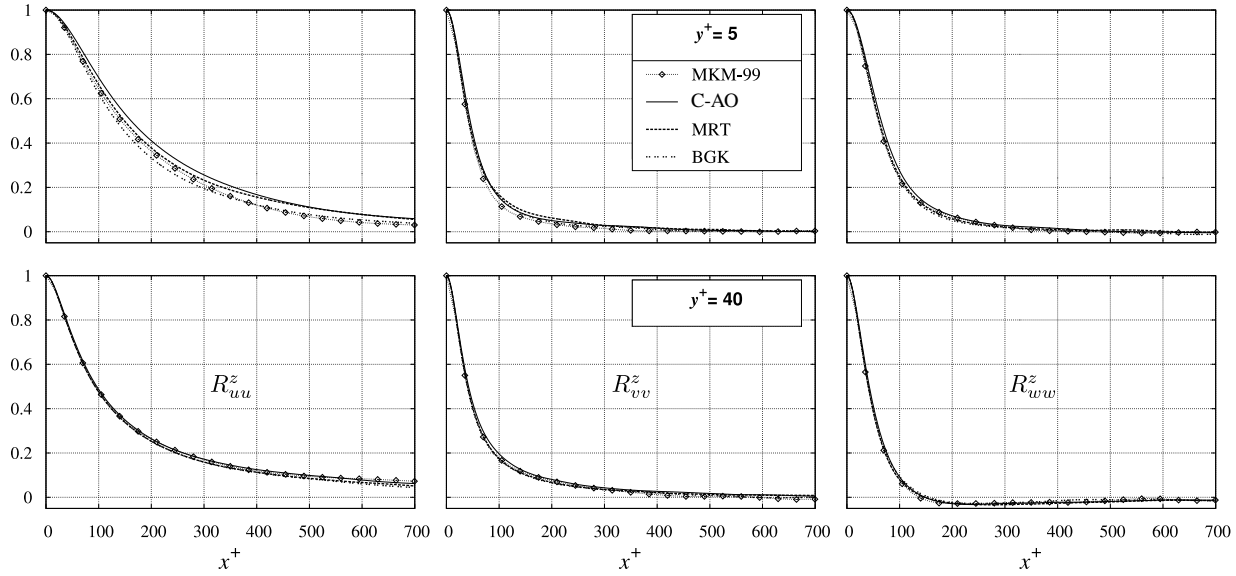

Figure 5.8: Predicted streamwise normalized two-point correlations R^x_{uu} (left), R^x_{vv} (center) and R^x_{ww} (right) at $y^+ = 5$ (top) and $y^+ = 40$ (bottom).

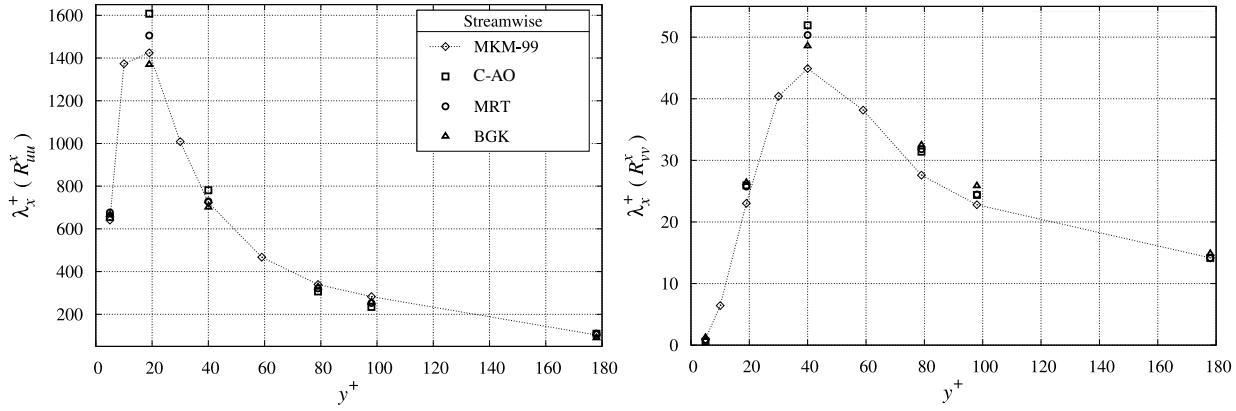

Figure 5.9: Predicted streamwise turbulent length scales for the normalized two-point correlations R_{uu}^x (left) and R_{vv}^x (right).

smaller decline of the spectral energy at higher wave numbers displayed in Fig. 5.10.

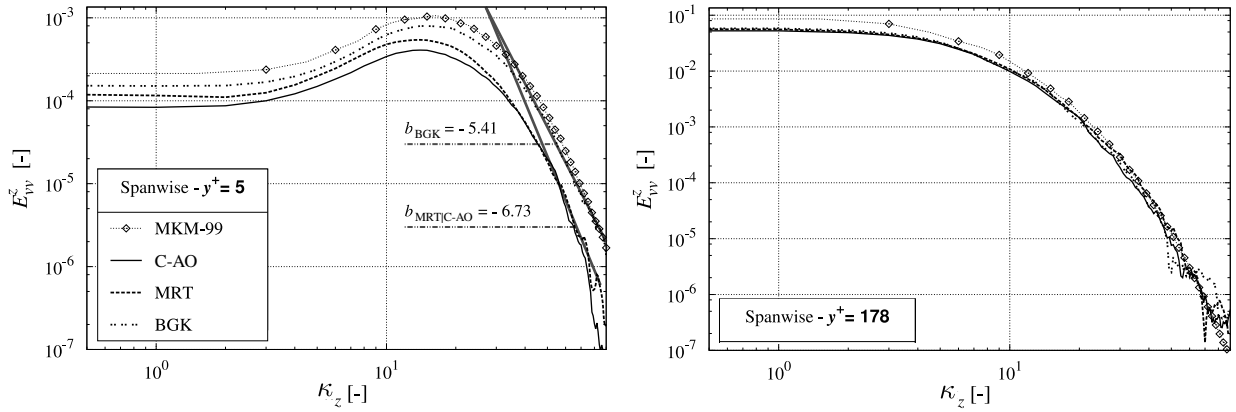

Figure 5.10: Spanwise 1D energy spectra E_{vv}^z at wall distances $y^+ = 5$ (left) and $y^+ = 178$ (right) obtained by the DNS grid.

In line with the more pronounced wall damping reflected by the MRT and the C-AO results, the E_{vv}^z spectra of the BGK model shown in Fig. 5.10 are above the data of the other two collision models in the near-wall regime, where the MRT and particularly the C-AO model seems to indicate some hyperviscous contributions as displayed by the steep decline (left). However, the differences vanish in the core flow (right). Mind that Geier et al. [2015] found a negative hyperviscosity contribution during their analysis of another MRT model variant, which would explain potential instabilities in the core flow regime as outlined below.

Mach Number and Discretization Influences

For verifying the reliability of the results, Mach number influences have been studied for the BGK model on grid No. 2 featuring $\Delta x^+ = 3.3$. In general, the individual differences obtained from halving or doubling the baseline Mach number of Ma = 1/20 virtually do not alter the predictive response. Figure 5.11 outlines the differences for the normalized

mean velocity through

$$u^+_{\text{norm}}(y^+) = \frac{|u^+_{\text{MKM-99}}(y^+) - u^+(y^+, \{\text{Ma}; \text{D}m\text{Q}n\})|}{u^+_{\text{MKM-99}}(y^+)}\,, \tag{5.1}$$

and the RMS value of the primary fluctuation

$$u'u'^+_{\text{RMS,norm}}(y^+) = \frac{|u'u'^+_{\text{MKM-99}}(y^+) - u'u'^+_{\text{RMS}}(y^+, \{\text{Ma}; \text{D}m\text{Q}n\})|}{u'u'^+_{\text{MKM-99}}(y^+)}\,. \tag{5.2}$$

Disregarding the specific Mach number, the difference between the LBM and the Navier-

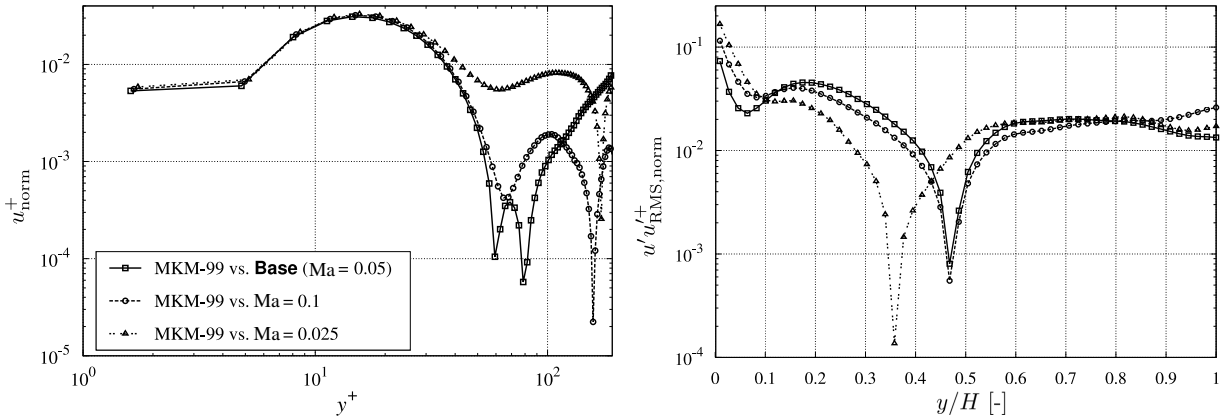

Figure 5.11: Predicted differences displayed by the BGK model for the mean velocity U^+ (left) and the RMS value of $u'u'^+_{\text{RMS}}$ (right) for the larger (Ma = 1/10) and the smaller (Ma = 1/40) Mach number when compared with the baseline results at Ma = 1/20 and the MKM-99 reference data on grid No. 2.

Stokes reference solution is in the per mil, i.e., $\mathcal{O}(10^{-3})$, regime or below, with the most considerable deviations in the buffer layer and the viscous sublayer. Moreover, Fig. 5.12 representatively compares the norm

$$E^x_{uu,\text{norm}}(y^+) = \frac{|E^x_{uu,\textbf{Base}}(y^+) - E^x_{uu}(y^+, \text{Ma})|}{E^x_{uu,\textbf{Base}}(y^+)} \tag{5.3}$$

of the streamwise 1D energy spectra E^x_{uu} extracted at $y^+ = 40$ and $y^+ = 178$. The differences are in the percent, i.e., $\mathcal{O}(10^{-2})$, regime and increase with the wave number. In addition, the norm for reducing the Mach number is generally larger than the difference experienced from a Mach number increase, which might reveal minor room for improvement. In conjunction with the BGK model, the discretization influence has been briefly studied on grid No. 2. The benefits of a D3Q27 discretization over the baseline D3Q19 approach are small. As indicated by the mean velocity illustrated in Fig. 5.13, the results of the BGK model have shifted a small step toward the C-AO results through an increased von Kármán parameter $\kappa = 0.394$ and a slightly augmented log law parameter $C^+ = 5.4$. The differences originate from a reduction of near-wall RMS and shear stress values which return a slightly better-related agreement with the MKM-99 reference data, cf. Fig. 5.14. The agreement between the two stencils for a simple unidirectional shear flow is perhaps expected, and results should be handled cautiously for more complex flows.

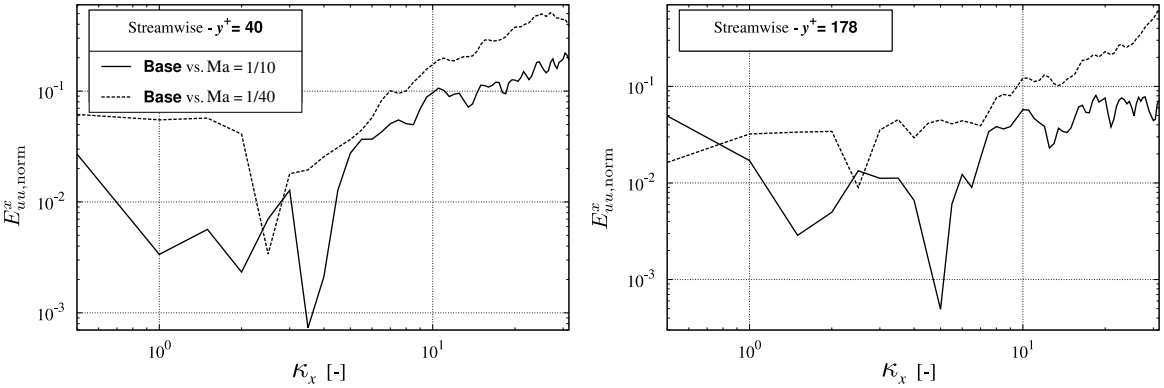

Figure 5.12: Predicted differences displayed by the BGK model for the streamwise 1D energy spectrum E^x_{uu} at $y^+ = 40$ (left) and $y^+ = 178$ (right) for the larger (Ma = 1/10) and the smaller (Ma = 1/40) Mach number when compared with the baseline results at Ma = 1/20 on grid No. 2.

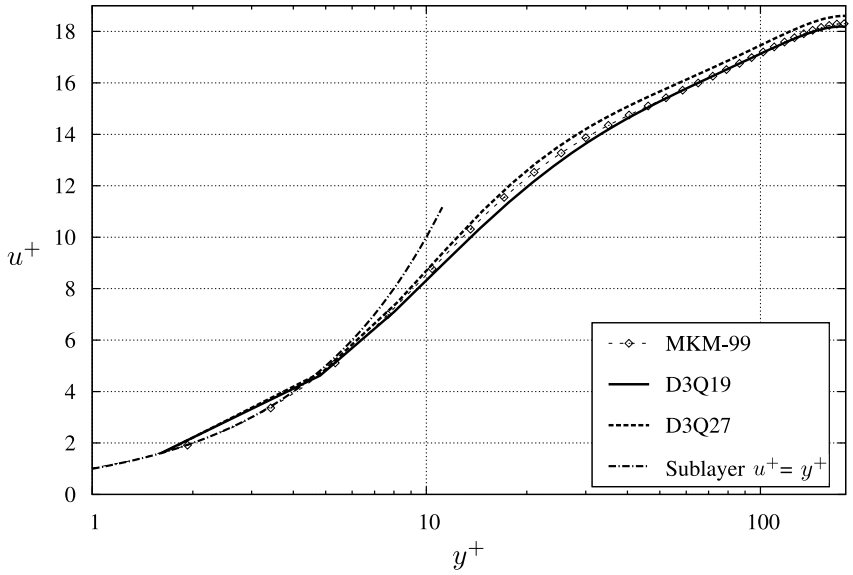

Figure 5.13: Predicted nondimensional mean velocity obtained for the BGK model on grid No. 2 ($\Delta x^+ = 3.3$) for the baseline (D3Q19) and the D3Q27 discretization.

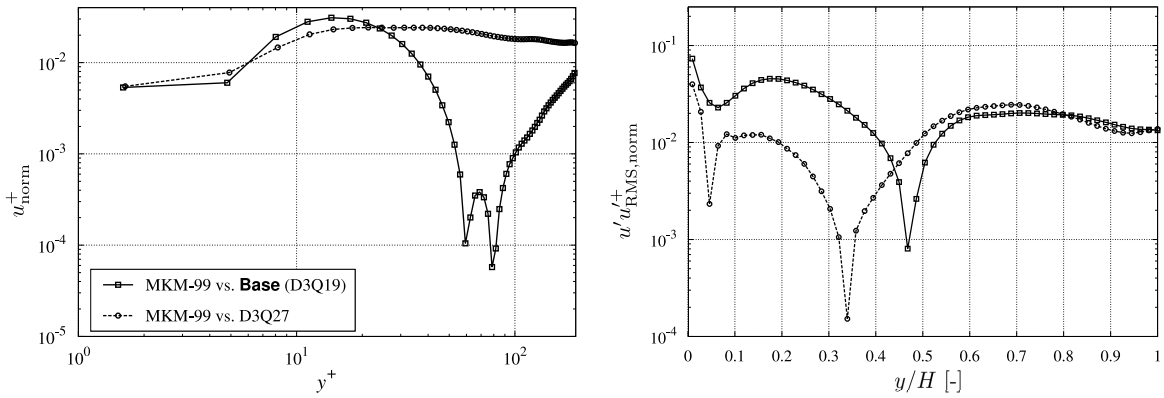

Figure 5.14: Predicted mean velocity and RMS differences obtained for the BGK model on $\Delta x^+ = 3.3$ (grid No. 2) for the baseline D3Q19 and the D3Q27 discretization.

Coarser Grid Results

Figure 5.15 illustrates exemplary snapshots of the last simulation time step of the instantaneous streamwise (u) velocity component in the x-y symmetry plane for the three finest grids. In addition, Tab. 5.4 outlines the predicted mean flow results computed on grid No. 3 featuring $\Delta x^+ = 6$, where Fig. 5.16 illustrates the related mean streamwise velocity profile. The BGK results seem to deteriorate least pronounced when the grid

Table 5.4: Computed mean values of the bulk (u_B), centerline (u_C) and friction (u_τ) velocity besides parameters of the log law $u^+ = \ln(y^+)/\kappa + C^+$ for grid No. 3 ($\Delta x^+ = 6$) alongside with the MKM-99 reference data.

Model	BGK	MRT	C-AO	MKM-99
u_B/u_τ	16.83	20.92	20.59	15.73
u_C/u_τ	19.75	23.98	23.74	18.30
u_C/u_B	1.17	1.15	1.15	1.16
κ	0.385	0.550	0.426	0.380
C^+	6.70	14.98	11.87	5.03

is coarsened. The C-AO approach delivers a proper inclination of the log law, and the MRT approach displays significant deficiencies. It is noted that the MRT and the BGK simulations both fail when the lattice spacing is further increased, i.e., $\Delta x^+ \geq 7$ (BGK) and $\Delta x^+ \geq 8$ (MRT). With attention directed to the near-wall behavior of the normalized turbulence intensities merged in Fig. 5.17, it is observed that the BGK model converges much faster to the final result than the other two collision models for the three finest grids. The intensities decrease for the MRT and the C-AO model when the grid is coarsened. Erroneously, the BGK model displays a slightly enhanced near-wall intensity when changing from the second finest grid (No. 2) to the next coarser grid (No. 3), which reveals the first signs of an unphysical behavior. Inspecting the MRT results discloses indications of instabilities for grid No. 4b ($\Delta x^+ = 8$), which are distinctly visible from the superelevated wall-normal and the lateral intensities (left) in the outer regime and the respective spectra (right) shown in Fig. 5.18. The MRT deficiencies in an attenuated form also exist for the 4a ($\Delta x^+ = 8$) grid, see also Fig. 5.15 (center). The evaluation exposes that the instabilities displayed by the MRT model occur first in the outer part of the log law.

In contrast to the MRT model, the BGK model displays first instabilities in the vicinity of the outer buffer layer, as indicated by the quantities evaluated in Fig. 5.19. Furthermore, Fig. 5.20 shows a comparison of the streamwise 1D energy spectra E^x_{uu} for all three collision models on grid 4a (BGK; $\Delta x^+ = 7$) resp. on grid 4b (MRT and C-AO; $\Delta x^+ = 8$) for a near-wall (left) and a core flow position (right). Here, solely the C-AO model remains stable, even for a coarse resolution of $\Delta x^+ = 8$.

The previous findings are confirmed by Fig. 5.21, which represents the evolution of the anisotropy coefficient, defined via $-\overline{u'v'}/(u'_{\mathrm{RMS}}\, v'_{\mathrm{RMS}})$, with increased lattice spacing. The shear stress is not significantly affected by initial instabilities, and its ratio to the square of the friction velocity might seem acceptable, but the anisotropy is reduced. The figure also affirms that the BGK model starts to fail in the inner part of the boundary layer, whereas

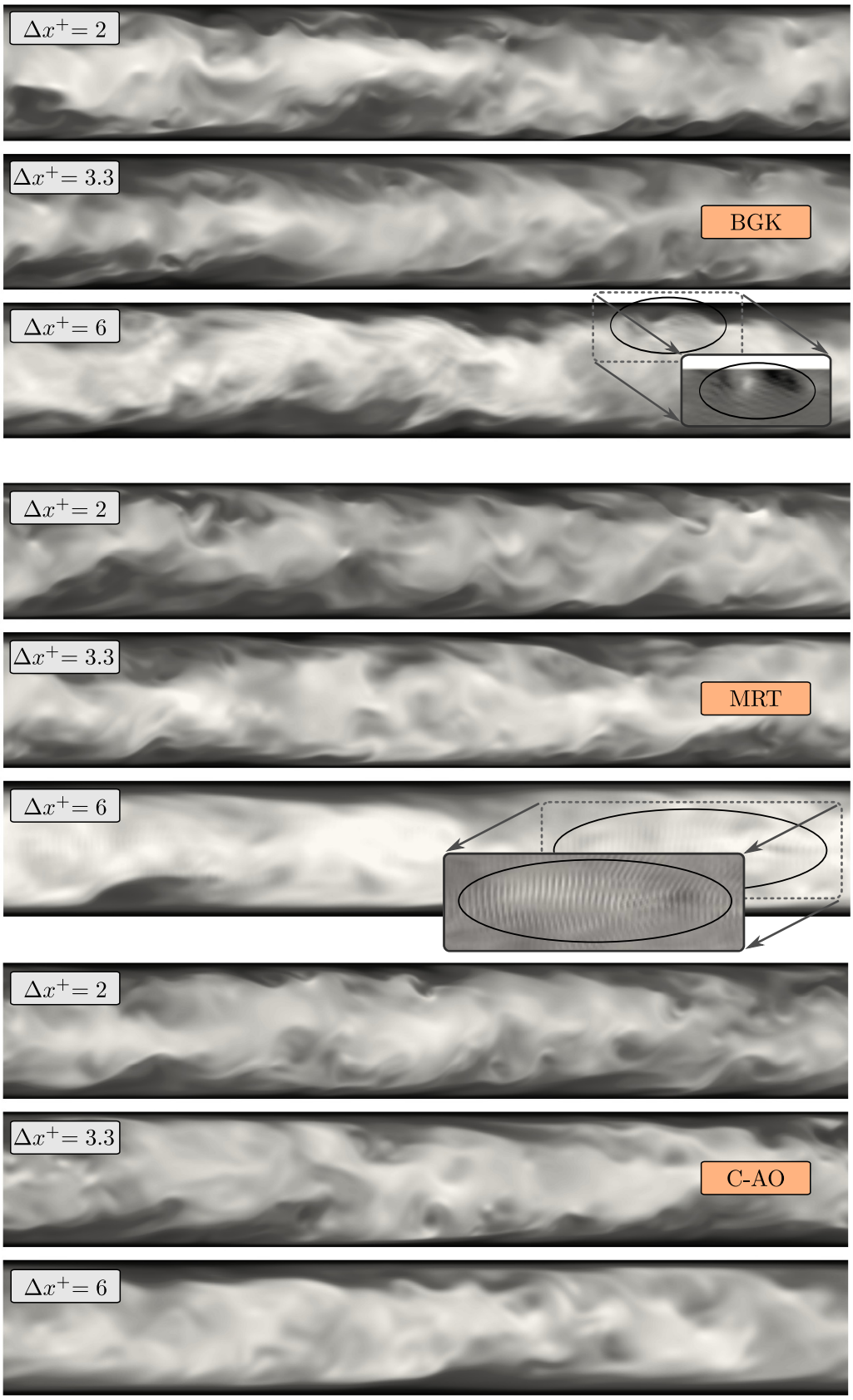

Figure 5.15: Instantaneous streamwise velocity (u) component snapshots in the x-y center plane predicted by the BGK (top group), MRT (center group) and C-AO (bottom group) model each for $\Delta x^+ = \{2; 3.3; 6\}$ (top; center; bottom subfigures). The BGK and MRT image details of $\Delta x^+ = 6$ refer to pressure contours that display instabilities more clearly.

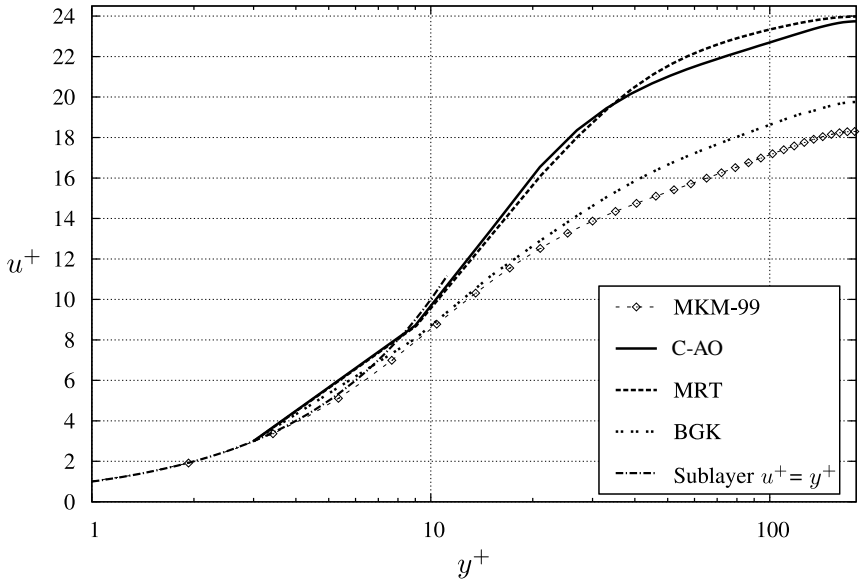

Figure 5.16: Predicted nondimensional mean velocity for grid No. 3 ($\Delta^+ = 6$).

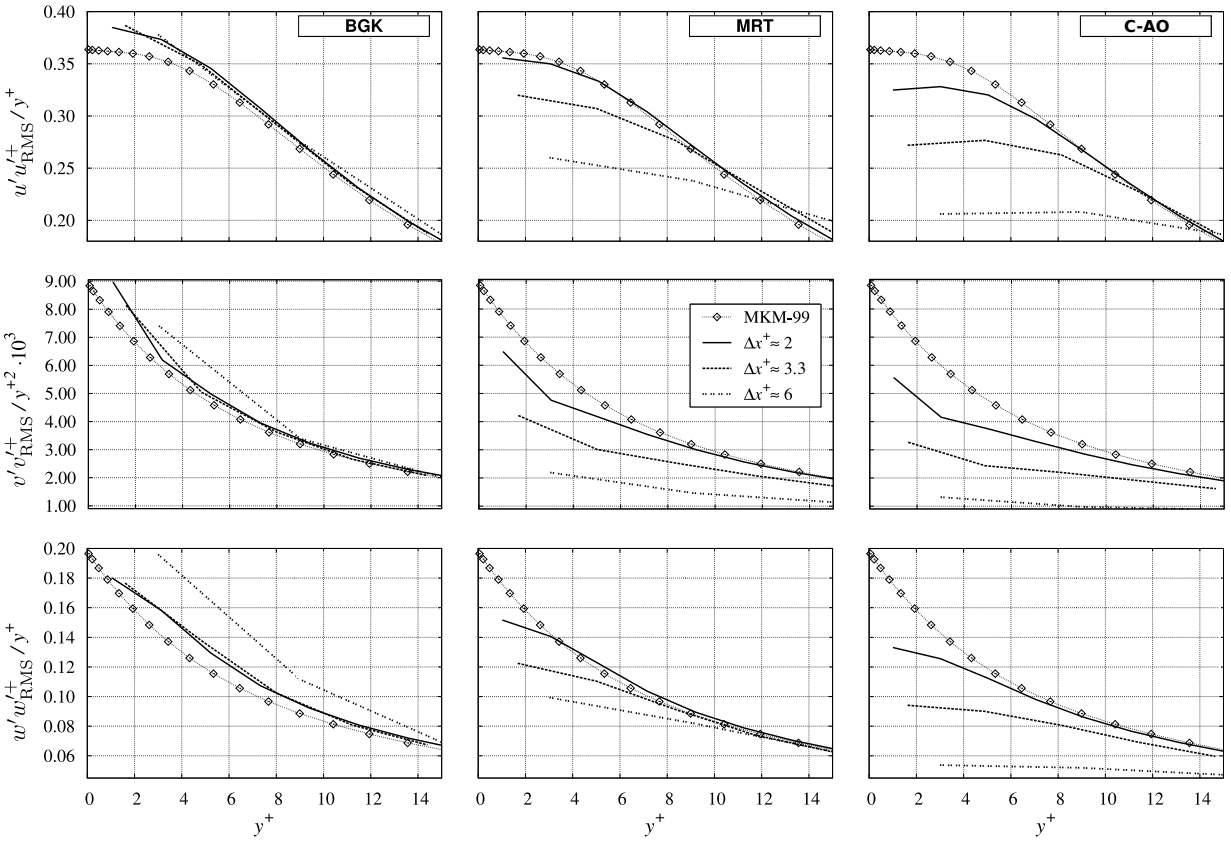

Figure 5.17: Resolution sensitivity of the near-wall normalized turbulence intensities for the BGK (left), MRT (center) and the C-AO (right) model computed on the three finest grids $\Delta x^+ = \{2; 3.3; 6\}$.

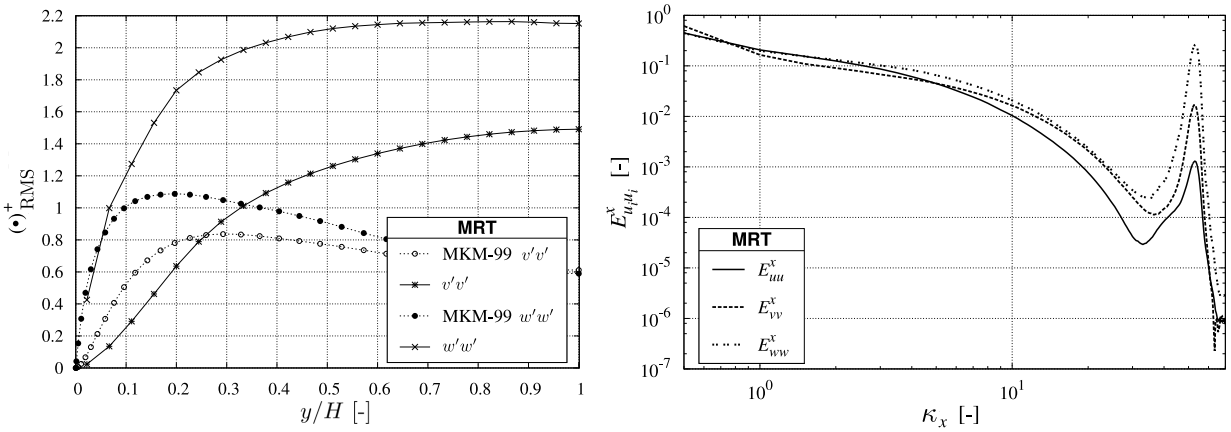

Figure 5.18: RMS ($v'v'^+_{\mathrm{RMS}}$; $w'w'^+_{\mathrm{RMS}}$) values (left) predicted by the MRT model on grid No. 4b ($\Delta x^+ = 8$) supplemented by the streamwise 1D energy spectra E^x (right) at an outer location, i.e., $y^+ = 178$.

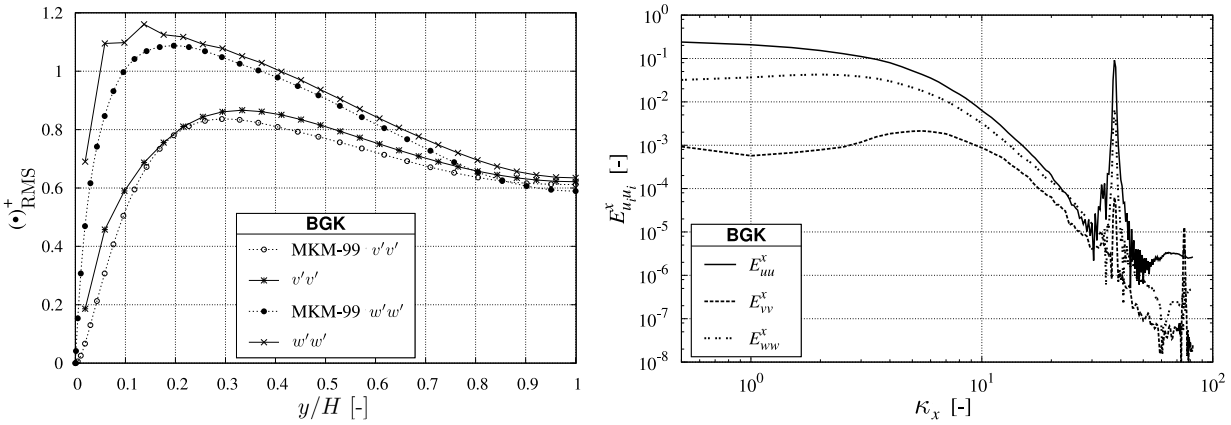

Figure 5.19: RMS ($v'v'^+_{\mathrm{RMS}}$; $w'w'^+_{\mathrm{RMS}}$) values (left) predicted by the BGK model on grid No. 4a ($\Delta x^+ = 7$) supplemented by the streamwise 1D energy spectra E^x (right) at an inner location, i.e., $y^+ = 5$.

the MRT model suffers from a similar phenomenon originating from the core flow region. On the contrary, the C-AO model delivers a relatively stable coincidence of anisotropy for all grids.

With attention given to the two-point correlations' evolution for the initial coarsening from $\Delta x^+ = 2 \rightarrow 6$, the BGK model shows only minor changes in the structure-indicating minima for the near-wall spanwise (top) two-point correlations R^z_{uu} and R^z_{vv}, while the C-AO model exhibit a clear shift of the minima, cf. Fig. 5.22. The MRT $R^z_{\{uu;vv\}}$ results are similar to those of the C-AO, so their display is left out for clarity.

The expected increase of the near-wall streamwise correlations $R^x_{\{uu;vv\}}$ is observed with an increase of the grid spacing for the C-AO (and likewise for the MRT) model. However, the results of the BGK model display a decrease in these correlations as shown in Fig. 5.22 (bottom). Moreover, the BGK result erroneously shows a negative R^x_{vv} passage between $x^+ \approx \{100, \ldots, 400\}$, which similarly marks the onset of instabilities. The C-AO model's spanwise R^z_{vv} (top right) two-point correlations always displays clear indications of streamwise vortices, even for an inadequate coarse resolution. The size of the vortices increases

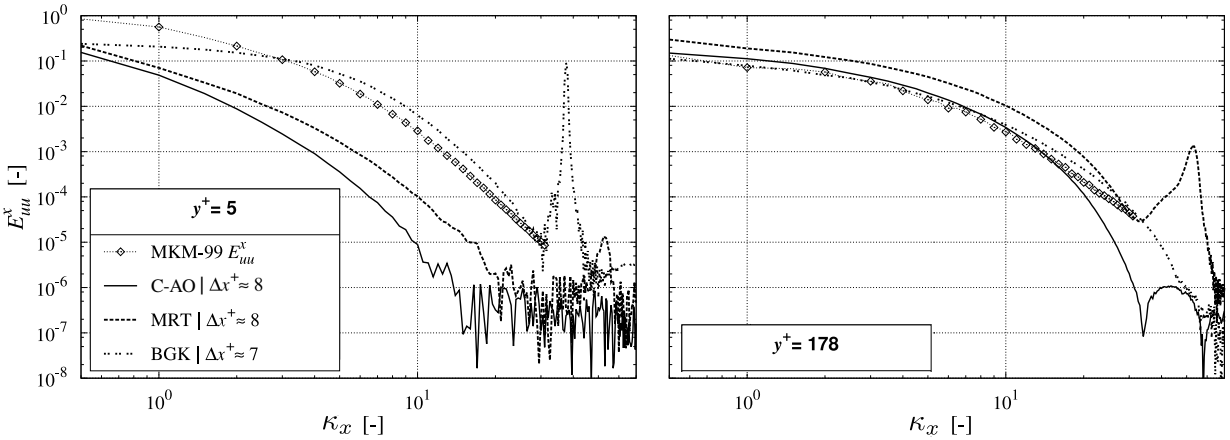

Figure 5.20: Predicted streamwise energy spectra E^x_{uu} at an inner ($y^+ = 5$) and an outer ($y^+ = 178$) location (left; right).

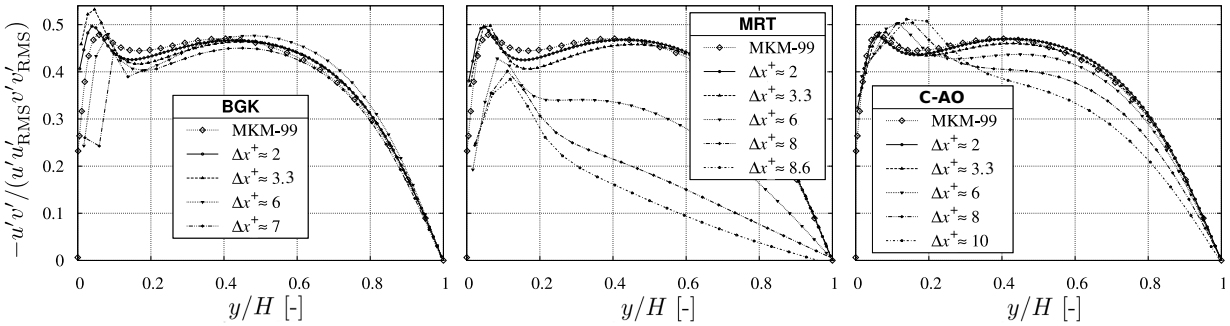

Figure 5.21: Grid sensitivity of the predicted anisotropy coefficient for the BGK (left), MRT (center) and C-AO (right) model in comparison with MKM-99 data.

moderately with the resolution, and the shift of R^z_{vv} indicates an increase of the associated length scale. The streamwise two-point correlations, particularly those of the primary velocity R^x_{uu}, returned by the C-AO model are significantly enhanced when the grid spacing is increased. In fact, the values found at the end of the domain decline to continuously increasing finite values, e.g., $R^x_{uu} \to 0.15\,[0.65]$ close to the wall (left) or $R^x_{uu} \to 0.08\,[0.23]$ in the core flow (right) for $\Delta x^+ = 6\,[12]$, cf. Fig. 5.23. The phenomenon is not observed in the results of the other two collision models.

Figure 5.24 displays isosurface plots of the streamwise vorticity component $\omega_x = \partial w/\partial y - \partial v/\partial z$ for the various collision models and three resolutions each. Unlike the other two collision models, the vortices displayed by the C-AO significantly stretch in the longitudinal direction when the grid is coarsened, specifically visible for the transition from $\Delta x^+ = 6 \to 8$. The latter significantly supports the stability of the simulations and explains why the model is deemed to have some implicit SGS modeling features. A typical demonstration is given in Fig. 5.25, which reveals that the energy density is progressively redistributed into larger scales in line with an increased, slightly hyper-viscous decline of small-scale energy when the grid is coarsened.

In conclusion, the C-AO model reflects the resolution-dependent damping of small-scale structures similar to an SGS model. Subgrid scale effects are traditionally modeled using a gradient-based isotropic eddy viscosity in the LES context. The most prominent exam-

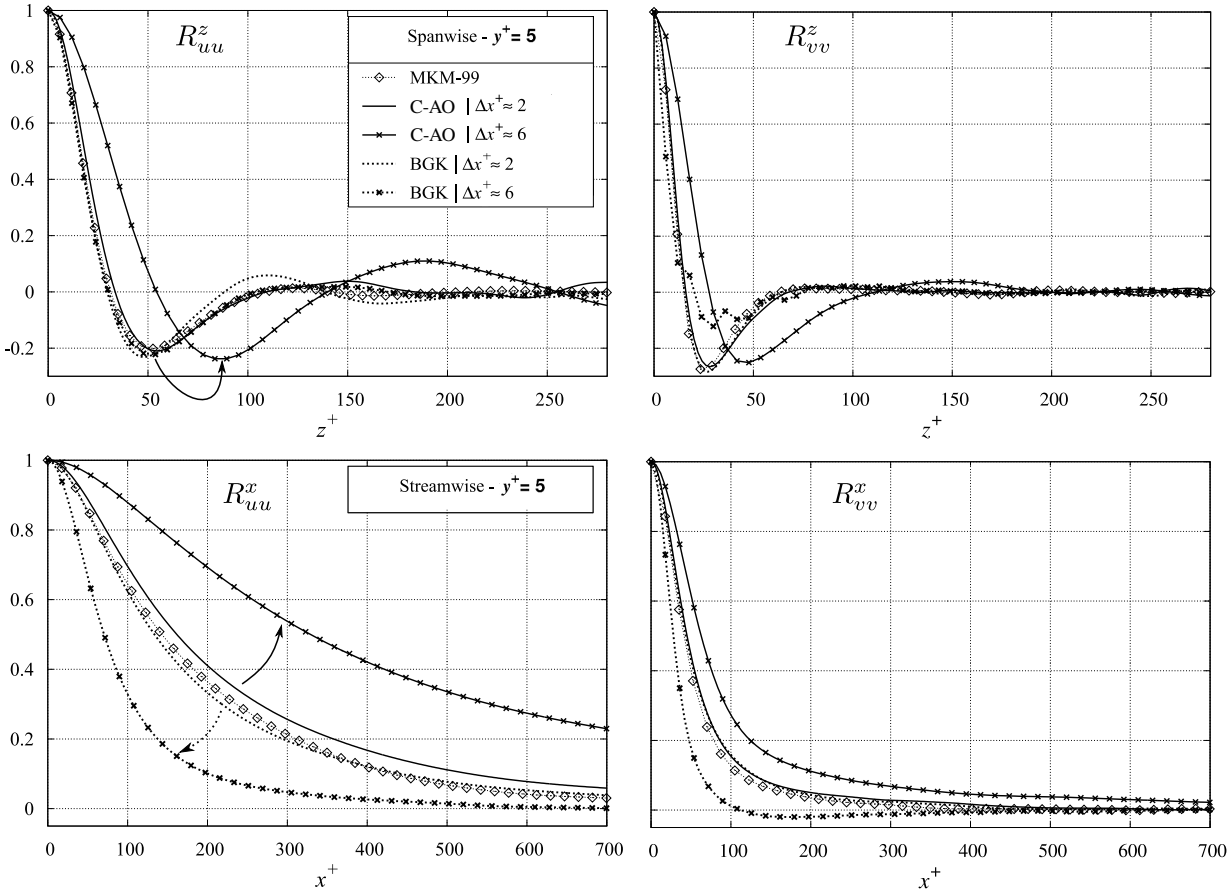

Figure 5.22: Spanwise (top) and streamwise (bottom) TPCs $R^{z/x}_{uu}$ (left) and $R^{z/x}_{vv}$ (right) at $y^+ = 5$ employing $\Delta x^+ = \{2; 6\}$ for the BGK [dashed] and the C-AO [solid] model in comparison with MKM-99 data.

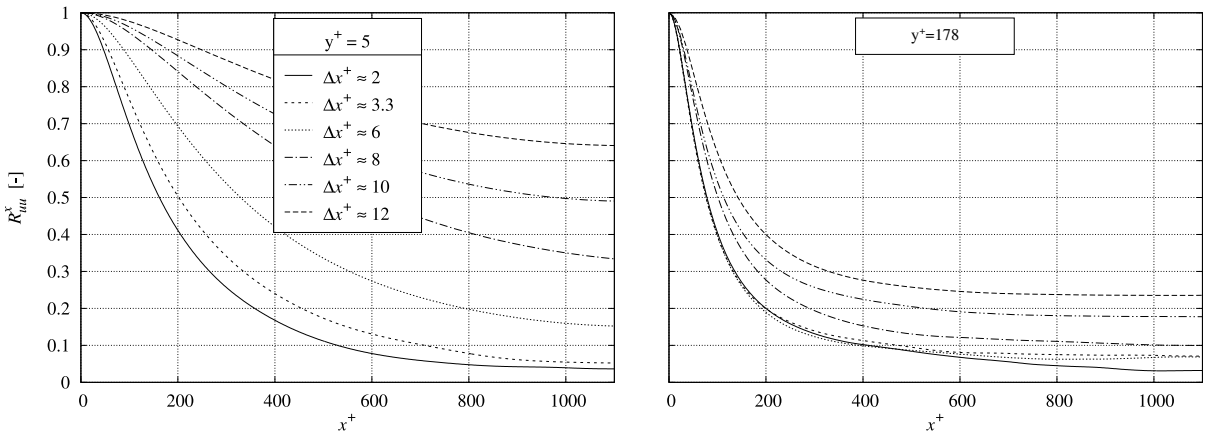

Figure 5.23: Streamwise TPC R^x_{uu} at $y^+ = 5$ (left) and $y^+ = 178$ (right) employing $\Delta x^+ = \{2, \ldots, 12\}$ for the C-AO model.

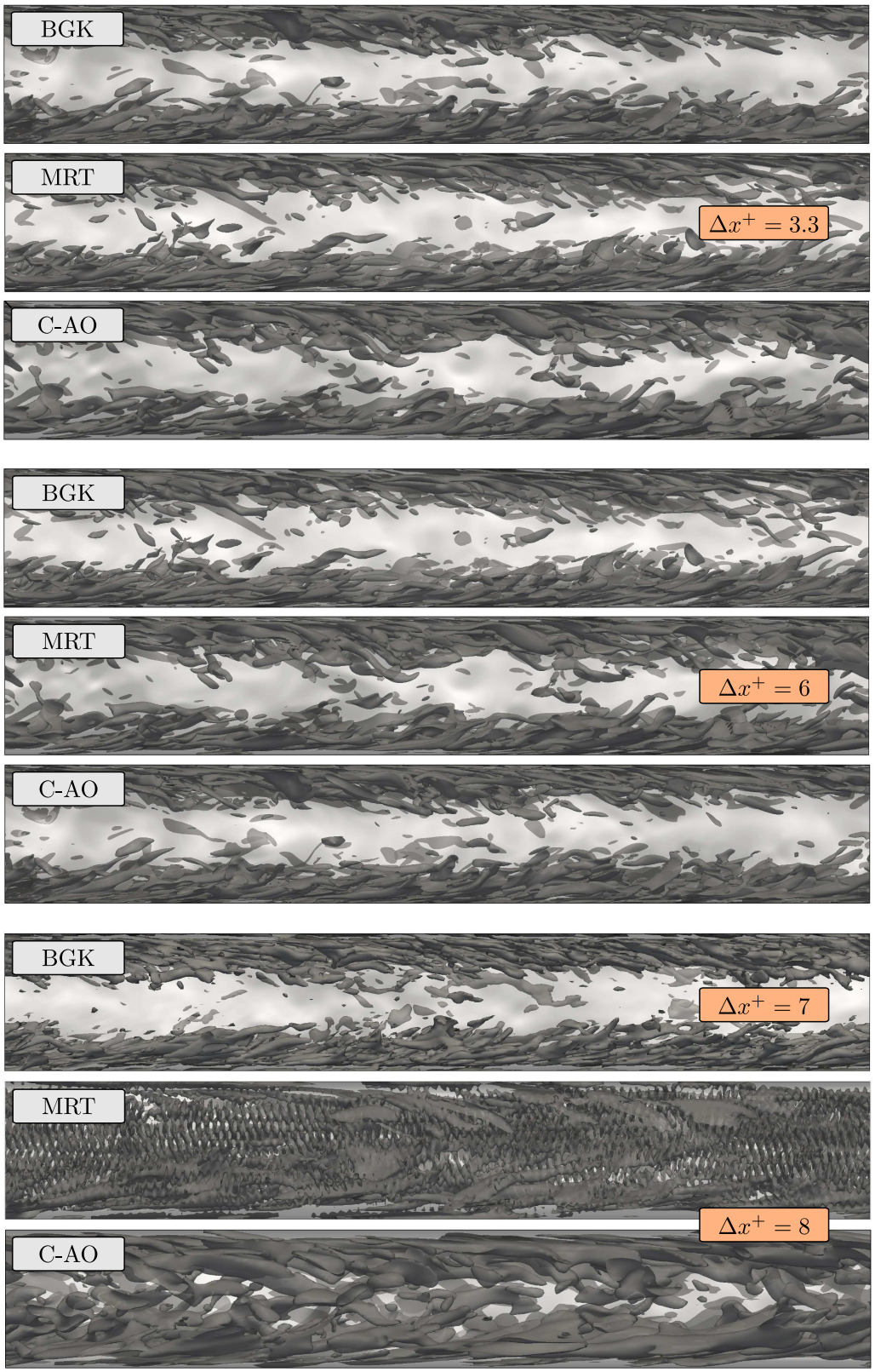

Figure 5.24: Progression of streamwise vortices under successively grid coarsening illustrated by the lateral view on isosurfaces of $\omega_x = \partial w/\partial y - \partial v/\partial z$ predicted by the BGK (top subfigures), MRT (center subfigures) and C-AO (bottom subfigures) model for $\Delta x^+ = 3.3$ (top group), $\Delta x^+ = 6$ (center group) and $\Delta x^+ = 7$[8] (bottom group).

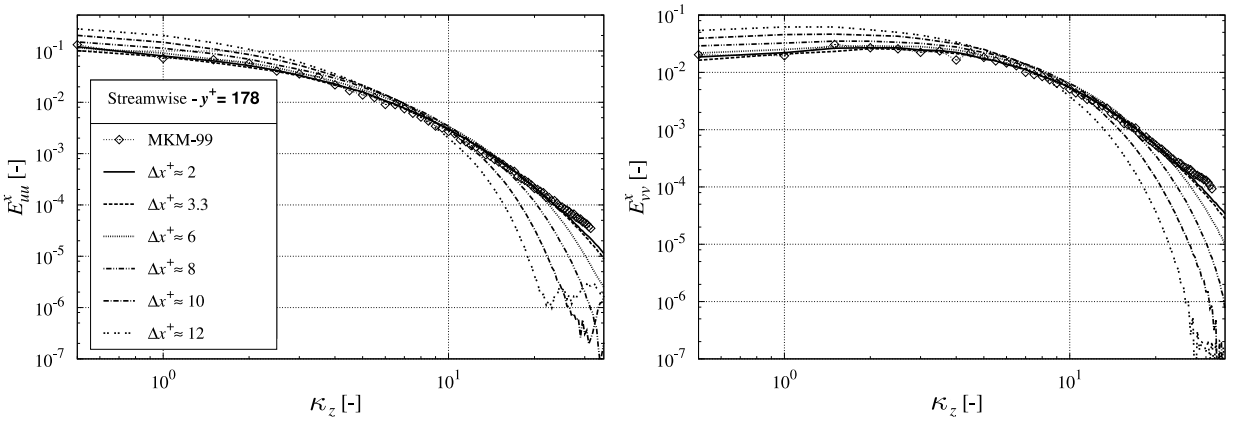

Figure 5.25: Resolution sensitivity of the streamwise energy spectra E^x_{uu} (left) and E^x_{vv} (right) at $y^+ = 178$ returned by the C-AO model.

ple is the Smagorinsky-Lilly closure, as outlined in Sec. 3.1.4. When attention is directed to LBM, the expression of turbulent stresses is linked to the approach's baseline rationale. Chen et al. [2004] derived turbulent stresses from a second-order Chapman-Enskog expansion, resulting in a nonlinear (essentially non-isotropic) eddy viscosity framework supplemented by memory effects. Different from traditional turbulence modeling practices, this nonlinear closure is not controlled by additional coefficients related to empirical or heuristic approaches but is subjected to the specific choice of the relaxation time and, thus, the level of turbulent fluctuations. Further LES contributions from empirical closures can, of course, be added to mimic the influence of unresolved physics.

As regards the C-AO model, an inherent SGS treatment is assumed, featuring substantial anisotropic contributions because of the rather strong anisotropy in response to grid coarsening displayed by the TPC evaluations. Moreover, it is interesting to note that the directionality displayed by the C-AO model seems to correlate with the velocity and not the velocity gradient since the streamwise velocity is the only relevant mean velocity component but mean streamwise gradients are zero. This suggests a directional mixing length embedded in the subgrid response of the C-AO model, which might be part of a memory term that works on higher wave numbers and explains the apparent directionality of length scales when the grid is coarsened. The assumption is confirmed by comparing the DNS C-AO results with results returned by an LES-stabilized MRT approach on grid No. 4b featuring $\Delta x^+ = 8$ in Fig. 5.26, where the occurring vortex structures are qualitatively similar in size. The employed LES stabilization refers to a standard constant Smagorinsky SGS model using $C_S = 0.1$. Figure 5.26 compares a side view of the streamwise vortices for these two simulation approaches. An additional not explicitly depicted comparison of the spanwise TPC reveals that the streamwise vortices of the LES approach are somewhat larger. Their streamwise length, however, seems fairly similar, slightly shorter [longer] in the near-wall [core flow] region for the MRT-LES.

Conclusions

An accurate prediction of incompressible turbulence physics with LBM requires Mach numbers $\mathrm{Ma} \leq 0.1$ and a spatial resolution in the range of the Kolmogorov scale. As indicated by previous researchers, an adequate domain size is also essential to capture the details.

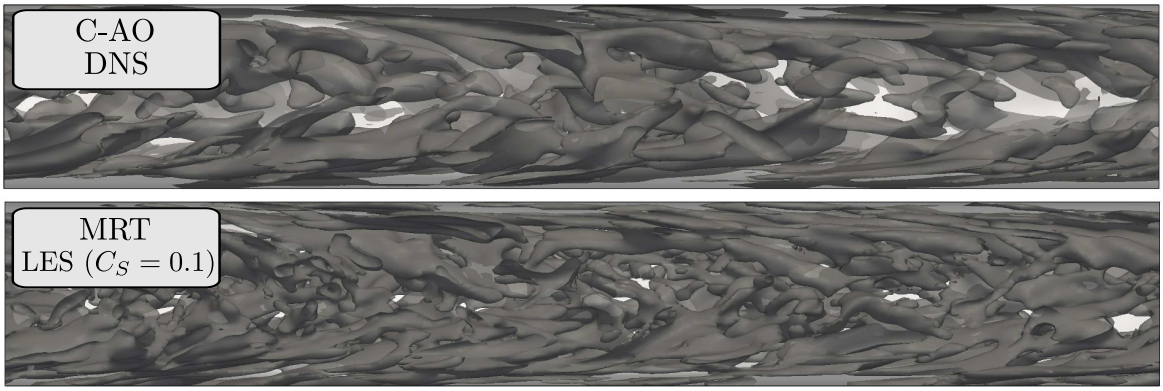

Figure 5.26: Comparison of lateral view snapshots on isosurfaces of the streamwise vorticity component $\omega_x = \partial w/\partial y - \partial v/\partial z$ for the C-AO DNS (top) and MRT LES (bottom) approach for $\Delta x^+ = 8$.

Under such circumstances, the D3Q19 BGK model offers satisfactory predictive accuracy, which seems slightly superior to the more advanced MRT and C-AO approach. However, all investigated collision models capture the relevant physical details under ideal, i.e., DNS conditions. The C-AO approach uniquely returns streamwise correlation lengths rigidly aligned to the lattice spacing. While this delays the convergence to formerly reported DNS Navier-Stokes data in the limit of fine grids, it also provides stable, meaningful results when the resolution is insufficient without considering a SGS model, revealing inherent mechanisms to mimic unresolved aspects.

Different from the C-AO model, the BGK and MRT models require stabilization when the lattice distance exceeds twice the Kolmogorov scale. The BGK model's instabilities originate in the outer buffer layer, whereas the MRT model starts to become unstable in the core flow.

5.2 (Severly) Under-Resolved Simulations

As a further step, the prediction accuracy is investigated in severe under-resolved conditions. Based on the precedent TCF studies, the considered collision operators are the BGK model and the two cumulant variants, i.e., the C-AO and C-P set of relaxation rates. The MRT model is omitted in further studies. On the one hand, the MRT's computational effort is almost similar to the cumulant model's. On the other hand, the MRT is inferior in both stability and accuracy which justifies to restrict the explored model space. To this end, opposing the most simple BGK and promisingly complex cumulant model is considered reasonable. The simple BGK collision operator is included to ascertain the influence of the underlying velocity space, i.e., D3Q19 vs. D3Q27 for the present scope. Additionally, the C-AO and, specifically, the C-P model, motivated by promising results in the literature, e.g., Geier et al. [2017a,b] or Pasquali [2016], are benchmarked for TGV and TCF simulations for resolutions up to $\Delta x^+ = 18$, matching a buffer layer location of the first fluid node.

The subsequent studies are based on two test cases, i.e., the Taylor-Green vortex followed by the turbulent channel flow.

Taylor-Green Vortex

The test case specifics of the performed TGV simulations are outlined in Tab. 5.5, where a fixed low Reynolds number of Re = 1600 and a constant Mach number of Ma = 1/20 are employed, and the level of under-resolution is uniquely adjusted through the spatial grid discretization. Since the TGV features free-shear decaying turbulence entailing the absence of u_τ, likewise Δx^+ is undefined. Hence, the resolution is denoted by the cube's number of lattice nodes per edge length, i.e., four different homogeneous isotropic grids with $N = N_\mathrm{i} = \{64; 96; 128; 256\}$ resulting totals of $N_\mathrm{tot} = \{262\,144; 884\,736; 2\,097\,152; 16\,777\,216\}$ grid nodes. All TGV simulations do not use an explicit turbulence model.

Table 5.5: Test case specifications for the TGV resolution benchmark.

	Specification
Test case	TGV at Re = 1600
Reference data	Brachet et al. [1983]
	Marié and Gloerfelt [2017]
Collision Models	BGK (D3Q19/D3Q27)
	C-AO, C-P (non-regularized)
Turbulence Modeling	none/implicit
Wall Modeling	none
Physical quantities	$\nu_P = 10^{-6}\,\mathrm{m^2 s^{-1}}$, $L = 0.1\,\mathrm{m}$
Domain size	$-\pi L \leq \{x; y; z\} \leq \pi L$
Δx^+	inapplicable
Ma	1/20

Initially, the study aims to outline the benefits of a D3Q27 stencil over the more economic D3Q19. To this end, the resolved TKE dissipation's resolution dependence of the BGK model is compared for both velocity spaces in Fig. 5.27. In line with the D3Q19 BGK ($N = 256$) results of Marié and Gloerfelt [2017], a fair predictive agreement with the reference data from Brachet et al. [1983] is seen for all resolutions of the D3Q19 discretization in the laminar phase for $t_c \leq 5$. Subsequently, the two coarser grids, i.e., $N = \{64; 96\}$ [red; orange], display severe robustness issues for the D3Q19 (left) approach, where the coarsest grid fails to predict transition to turbulence due to an inadequate computational model, while the second [orange] grid reasonably manages to pass transition but exhibits serious difficulties to enter the fully turbulent state commencing at the global ε maximum.

The inadequacy of the computational model is twofold and disclosed in conjunction with coarse grids. Firstly, the anisotropic D3Q19 stencil is suboptimal for the turbulent regime as the flow exhibits features of non-unidirectional shear. Secondly, the collision model gets more influential for complex under-resolved flows. On the contrary, results obtained from the $N = \{128; 256\}$ resolutions are in excellent agreement with the reference data in the first two phases until $t_c \leq 10$, and deviations within the subsequent decay phase are sufficiently small. The results get more accurate by including 27 instead of 19 collocation points, and the method's robustness significantly improves as depicted by Fig. 5.27 (right). Nonetheless, the BGK D3Q27 simulation fails to predict the fully turbulent regime employing the coarsest discretization. It is noted that other choices of the numerical parameters,

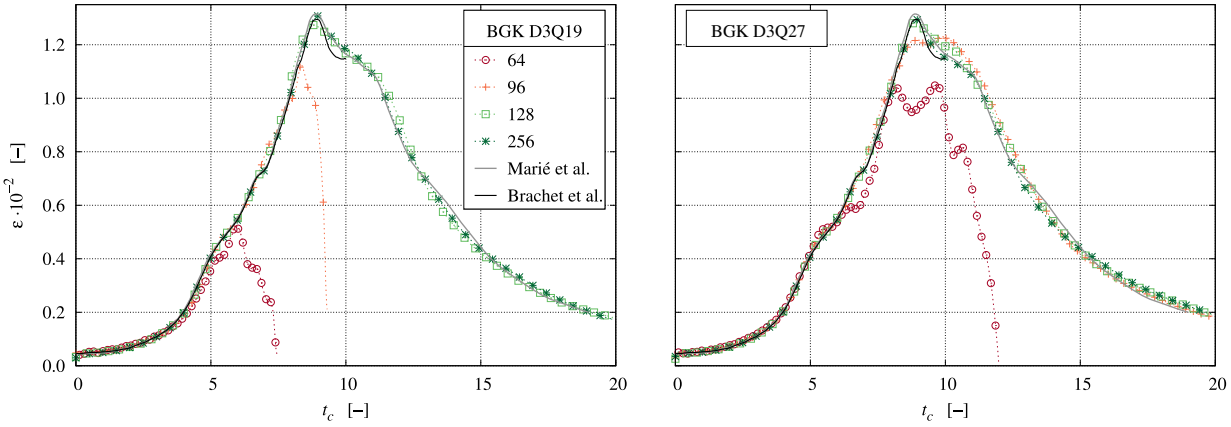

Figure 5.27: Temporal evolution of the (resolved) TKE dissipation predicted by the BGK model based on the D3Q19 (left) and D3Q27 (right) velocity space.

e.g., the employed Mach number or the precision of the employed variables (SP vs. DP), do not alter the outcome.

When attention is given to the cumulant model, which is only defined on the D3Q27 velocity space, the benefits of an advanced collision model appear. As indicated by Fig. 5.28, the accuracy of the included variants is significantly increased compared to the BGK model. Though the C-AO model (left) reflects difficulties in simulating the transition to the fully

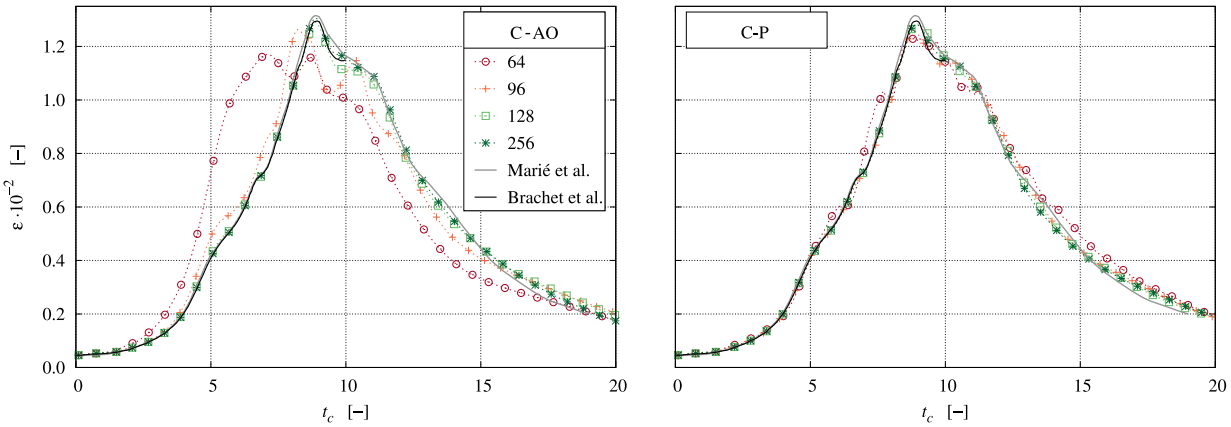

Figure 5.28: Temporal evolution of the (resolved) TKE dissipation predicted by the cumulant model based on the C-AO (left) and C-P (right) set of relaxation rates.

turbulent state in the second phase ($5 \leq t_c \leq 10$) for the coarse grids, specifically for $N = 64$ [red] and marginally for $N = 96$ [orange], the results of the C-P model (right) are fairly insensitive to the employed grid resolution. The expenditures in terms of computational time of the cumulant model exceed the BGK efforts by about 10% when using the identical velocity space (D3Q27) for the TGV case.

Turbulent Channel Flow

Motivated by the results of the TGV study and the initital C-AO TCF study, cf. Sec. 5.1, a subsequent TCF investigation is employed to assess the C-P capabilities on increasingly

under-resolved grids up to $\Delta x^+ = 18$, cf. Tab. 5.6. To this end, the regularization, cf. (3.111) to (3.114), is disabled, respectively not required, and the full parameterization of $\omega_{\{3;4;5\}}$ is used, where no instabilities emerge for the utilized resolutions. Compared

Table 5.6: Test case specifications for benchmarking the non-regularized C-P model.

	Specification
Test case	TCF at $\mathrm{Re}_\tau = 180$ $\rightarrow \mathrm{Re}_B \approx 2750$, $\mathrm{Re}_C \approx 3200$
Reference data	Moser et al. [1999] (MKM-99)
Collision Model	C-P (non-regularized)
Turbulence Modeling	none/implicit
Wall Modeling	none
Wall BC	SBB with $q \equiv 0.5$
Physical quantities	$\nu_P = 1.5 \cdot 10^{-5}\,\mathrm{m^2 s^{-1}}$, $H = 0.05\,\mathrm{m}$
Domain size	$4\pi H(x) \times 2\pi H(z) \times 2H(y)$
Δx^+	$\{2, \ldots, 18\}$
Ma	1/20

to the C-AO study, cf. Tab. 5.2, 4 additional coarser grids are employed, cf. Tab. 5.7. The $\Delta x^+ = \{12; 14\}$ discretizations are classified as VLES grids, whereas the two coarsest resolutions comply with typical RANS grids.

Table 5.7: Grid number, spatial resolution, total amount of grid points and grid classification. The gray entries match with those grids in Tab. 5.2.

No.	Δx^+	$N_x \times N_y \times N_z$	N_{tot}	Classification
1	2	1120 × 184 × 562	115 816 960	DNS
2	6	382 × 62 × 192	4 547 328	LES
3	10	232 × 38 × 118	1 040 288	LES
4	12	192 × 31 × 98	583 296	LES/VLES
5	14	168 × 28 × 86	404 544	VLES
6	16	148 × 24 × 75	266 400	VLES/RANS
7	18	134 × 22 × 68	200 464	RANS

Mean Flow

Figure 5.29 (left) depicts the mean velocity profiles obtained from the C-P model. Results are deemed to be quite accurate and display a small sensitivity to the resolution. To illustrate the improvements associated with the C-P, Fig. 5.29 (right) displays the predicted mean flow data obtained by the BKG model (D3Q19), the employed MRT model (D3Q19), the C-AO and the C-P model (both D3Q27) for a moderate resolution of $\Delta x^+ \approx 6$.

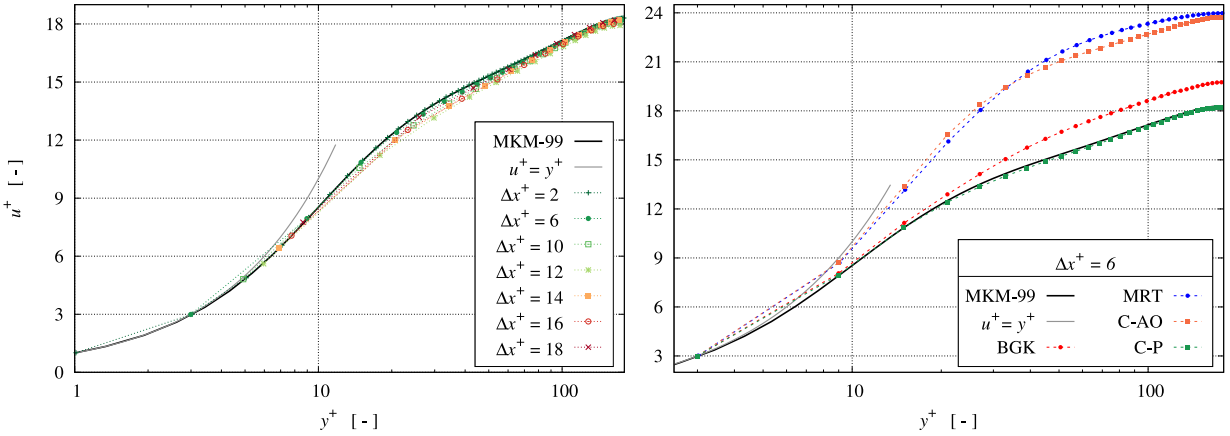

Figure 5.29: Mean primary velocity predicted by the C-P model for $\Delta x^+ = \{2, \ldots, 18\}$ (left). Mean velocity predicted by the BGK and MRT (both D3Q19), the C-AO and the C-P model (D3Q27) for $\Delta x^+ \approx 6$ (right).

The figure reveals the crucial benefits of the C-P model over the other alternatives and underlines that a seamlessly fair predictive accuracy for a larger range of resolutions is far to be guaranteed.

Reynolds Stresses, Two-Point Correlations and Energy Spectra

A closer inspection of the results obtained from the C-P model follows from an analysis of the Reynolds stresses depicted by Fig. 5.30 and Fig. 5.31. These illustrate comparisons of the present LBM results with benchmark Navier-Stokes data from Moser et al. [1999] for the employed range of seven grids. The C-P results for the DNS-type grid are in excellent agreement with the reference data. Furthermore, accurate predictions are seen for all grids that maintain $\Delta x^+ \leq 10$. The most remarkable results are obtained for the coarsest (RANS-type) resolution featuring $\Delta x^+ = 18$ with only 10 grid points across the half-channel height. Except for the unresolved peaks and a subtle tendency toward isotropy, the predictive agreement with DNS Navier-Stokes data is persuasive, particularly as regards the crucial shear stress.

Figure 5.32 shows TPCs obtained at two different near-wall locations, i.e., $y^+ = 19$ and $y^+ = 40$ by the C-P model. The corresponding energy spectra are depicted in Fig. 5.33. The R^z_{uu}-minima clearly reveal the extent of the turbulent streaks in line with Navier-Stokes results and the R^z_{vv}-minima indicate the existence of streamwise vortices. Small deficiencies appear in the near-wall region when the flow is grossly under-resolved. However, displayed data confirms an excellent overall agreement of the C-P results with reference data.

Conclusions

Compared to the BGK, MRT and also to the C-AO model, the employed C-P is clearly superior in simulating the TCF in under-resolved conditions since it adequately resolves the turbulent motion without needing any ad hoc filtering or modeling over a wide range of resolutions. This motivates to increase the challenge toward non-unidirectional separated shear flows and higher Reynolds numbers.

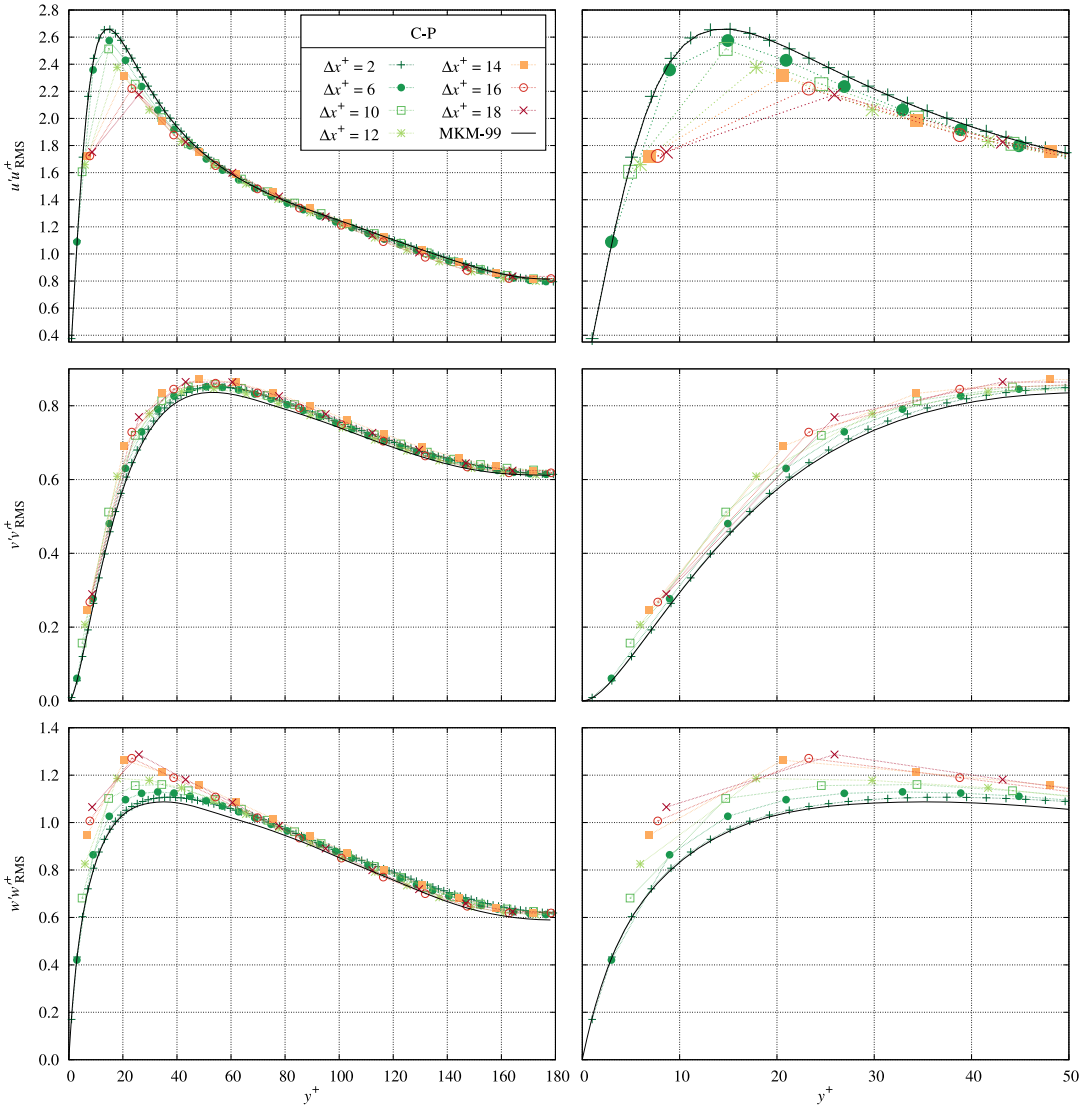

Figure 5.30: Comparison of the C-P streamwise (top), spanwise (center) and wall-normal (bottom) RMS predictions (left) and additional detail of $y^+ \in [0, 50]$ (right).

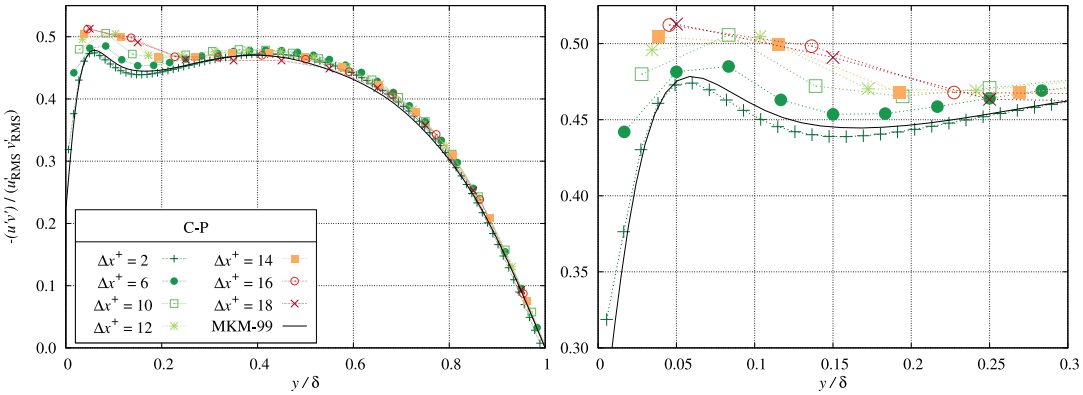

Figure 5.31: Comparison of the C-P predicted Reynolds stress anisotropies $-(\overline{u'v'})/(u'u'^{+}_{\mathrm{RMS}}\, v'v'^{+}_{\mathrm{RMS}})$ with reference data (left) and detailed view for $y/\delta \in [0, 0.3]$ (right).

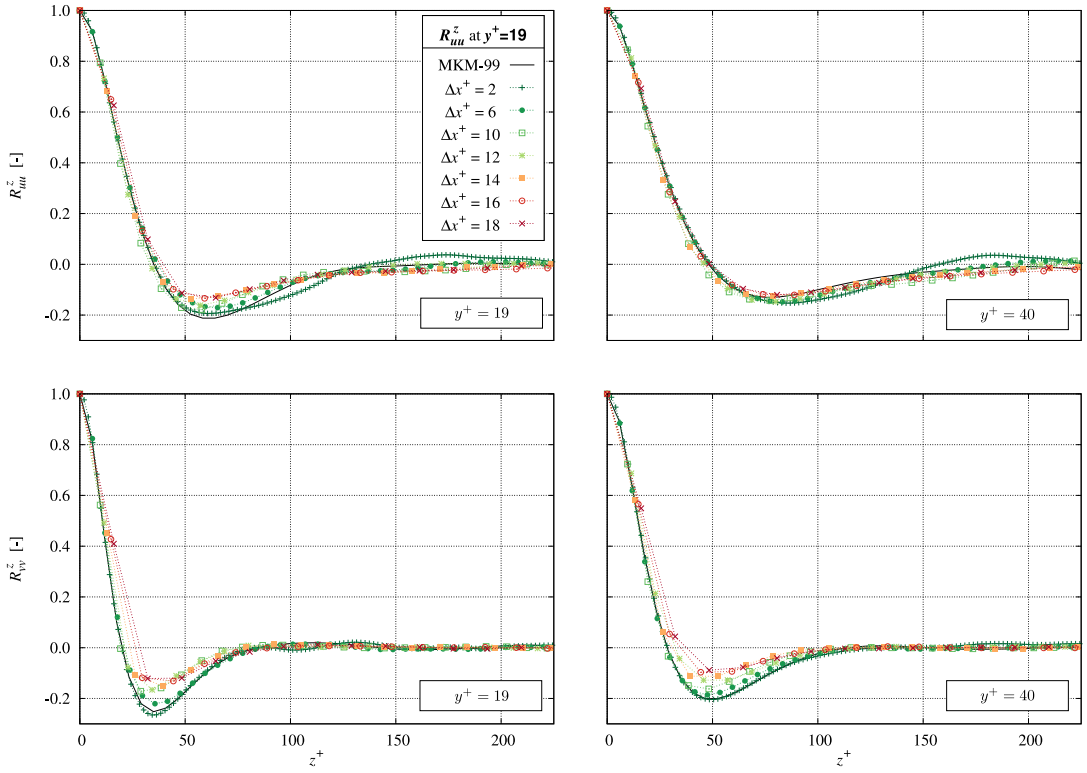

Figure 5.32: Comparison of the spanwise TPCs R^z_{uu} (top) and R^z_{vv} (bottom) at two different wall distances $y^+ = 19$ (left) and $y^+ = 40$ (right).

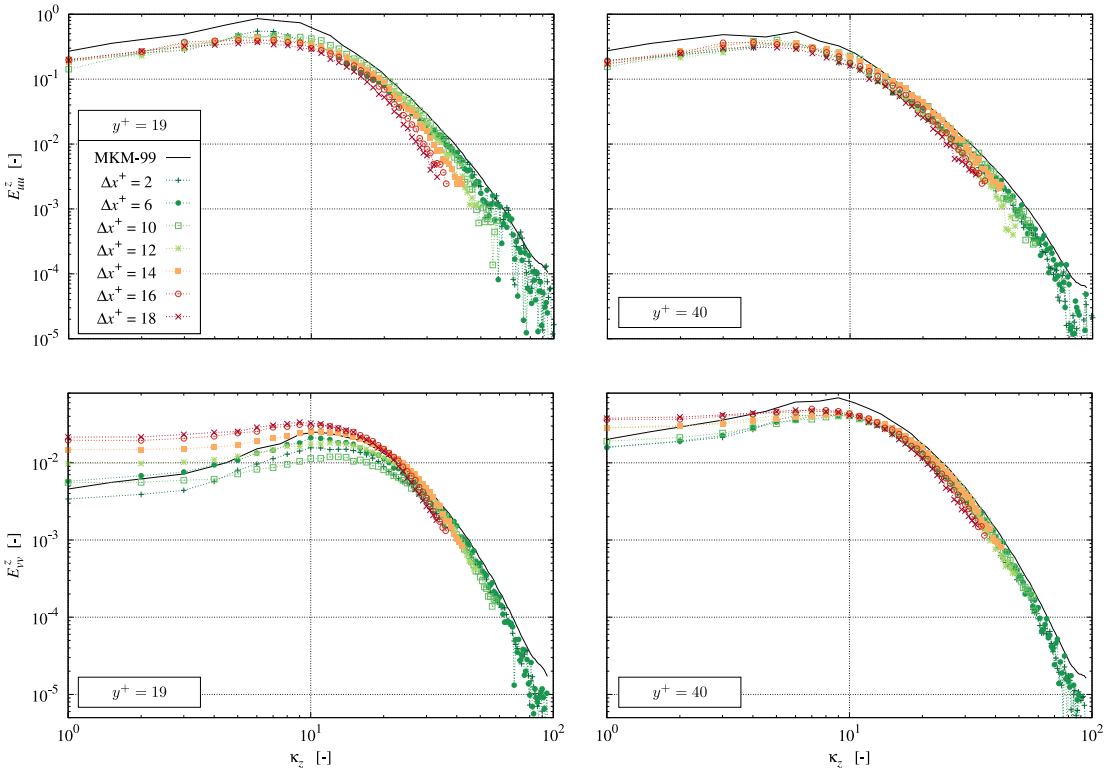

Figure 5.33: Comparison of the spanwise 1D energy spectra E^z_{uu} (top) and E^z_{vv} (bottom) at two different wall distances $y^+ = 19$ (left) and $y^+ = 40$ (right).

6 Cumulant Model Advancement

This chapter involves the principal contributions of the present thesis addressing the advancement of the parameterized cumulant (C-P) collision model. The latter has proven to be well-suited for the simulation of turbulent flows based on the preliminary benchmark studies outlined in the previous chapter. The identified implicit turbulence modeling capability, distinguished by accurate flow field predictions and high numerical stability, serves as a starting point for further analyses since it offers a substantial potential for under-resolved engineering applications.

6.1 Regularization

The first section includes a profound analysis of the C-P regularization influences. Following on from the previously outlined TCF and TGV investigations at low Reynolds numbers using fully-resolved to moderately under-resolved discretizations and motivated by the identified favorable applicability of the original Geier et al. [2017a] C-P model for the simulation of free and wall-bounded shear flows, the more complex PHF test case, additionally involving flow separation and reattachment in non-unidirectional shear, is employed to thoroughly assess the value of the regularization parameter λ (3.115).

6.1.1 Benchmark Specifics

The attention of the present PHF study is given to four different (bulk) Reynolds numbers, i.e., $\mathrm{Re}_B = \{700; 2800; 10600; 37000\}$ illustrated in Fig. 6.1, where results are compared with solutions of Navier-Stokes-based DNS and LES for all investigated Reynolds numbers. Moreover, experimental reference data is available for $\mathrm{Re} = \{10600; 37000\}$. Subsequently,

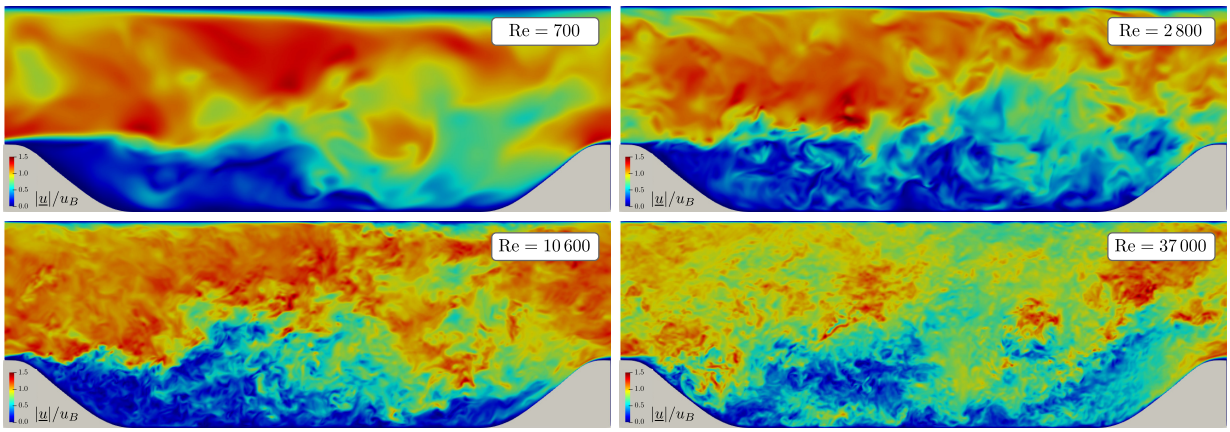

Figure 6.1: Instantaneous normalized velocity magnitude in the x-y center plane for the four investigated Reynolds numbers $\mathrm{Re} = \{700; 2800; 10600; 37000\}$.

the Reynolds number subscript B is omitted, and an index is only displayed for relations deviating from the bulk. Emphasis is given to assess the influence of the C-P model's stability-enhancing regularization parameter λ (3.115) and its relation to the required resolution.

Table 6.1 summarizes the essential test case specifics. It is noted that all simulations are subject to the waiver of wall modeling, and an explicit turbulence closure is only applied for supplementary testing. The discussion involves mean flow data as well as Reynolds stresses and is supplemented by one-dimensional power spectra. Results reveal an interplay between the λ-value and the (near-wall) resolution of the grid.

Table 6.1: Test case specifications for the regularization analysis.

	Specification
Test case	PHF at $\mathrm{Re} = \mathrm{Re}_B = \{700; 2800; 10600; 37000\}$
Reference data	ERCOFTAC database, Rapp et al. [2009] • *LESOCC* DNS by Breuer and Rodi [1996] • *MGLET* DNS & LES by Manhart et al. [2001] • Experiments by Rapp and Manhart [2011]
Collision Model	C-P (standard regularization)
Turbulence Modeling	implicit; standard constant Smagorinsky
Wall Modeling	none
Wall BC	IBB with $q \in [0, 1)$ on the curved hill geometry and $q \equiv 0.5$ on planar walls
Physical quantities	$\nu_P = 1.01 \cdot 10^{-6}\,\mathrm{m^2 s^{-1}}$, $H = 0.05\,\mathrm{m}$
Domain size	$9H(x) \times 4.5H(z) \times 3.035H(y)$
Δx^+	$\{2, \ldots, 100\}$
Ma	$\{1/90; 1/30; 1/10\}$

All employed discretizations refer to homogeneous isotropic Cartesian grids, where the baseline (medium) grid resolves the height of the hill with $N_H = 28$ lattice nodes. With this choice, the distance between the bottom and top wall H_{BT} also corresponds to even multiples of the spatial scaling factor $\Lambda_{x,28} = 1.786 \cdot 10^{-3}\,\mathrm{m}$, i.e., $N_{BT} = 85$. In this setup, the subgrid distance matches $q_{H\,|\,T\,|\,B} = 0.5$ at the crest of the hill ($x = 0$), the top wall, and the plane lower part of the bottom wall ($1.93 \leq x/H \leq 7.07$). The grid arrangement aims to suppress influences from $q \neq 0.5$, which, thus only occur along the curved hill boundary sections. Doubling the number of lattice nodes to $N_H = 56$ results in a refined grid that also satisfies the $q = 0.5$ condition.

Coarsening the baseline grid, no integer multiples between both H and H_{BT} exist. Applying a consistent refinement level of 2 leads to $N_H = 14$, whereby the H_{BT} discretization corresponds to $N_{BT} = 42.5$, yielding $q_T = 0$ for $q_{H\,|\,B} = 0.5$. Therefore, the top wall is slightly shifted by $\Lambda_{x,14}/2$ to constrain $q_T = 0.5$, increasing the domain height by 1.15% and $N_{BT} = 43$. This ensures minimal interference from the top wall boundary condition. Details of the investigated grids, including the number of lattice nodes and FP times $t_{\mathrm{FP}} = N_x/u_B \approx 15.6 N_H/\mathrm{Ma}$, valid for the baseline Mach number of $\mathrm{Ma} = 1/30 = \sqrt{3}\,u_B$ related to the bulk velocity, are given in Tab. 6.2.

Table 6.2: Investigated grids and related flow-pass times for Ma = 1/30.

N_H	$N_x \times N_y \times N_z$	N_{tot}	t_{FP}
14	$126 \times 45 \times 63$	357 210	6550
28	$252 \times 87 \times 126$	2 762 424	13100
56	$504 \times 172 \times 252$	21 845 376	26200

Again $N_y = N_{BT} + 2$ applies due to the consideration of the additional solid boundary nodes, whereas N_x and N_z match $9H$, resp. $4.5H$, owing to periodicity. In addition to diffusive (N_H) scaling analyses, acoustic scaling influences are assessed through a Mach number variation. Scaling the baseline value by a factor of three results in a finer (Ma = 1/90) and a respectively coarser (Ma = 1/10) temporal resolution. While linear relations, i.e., $\nu \sim \Delta N_H$ and $\bar{\mathrm{f}}_x \sim \Delta N_H$, apply for diffusive scaling, the acoustic scaling deviates by featuring a quadratic dependence on $\bar{\mathrm{f}}_x \sim \Delta \mathrm{Ma}^2$, whereas $\nu \sim \Delta \mathrm{Ma}$ holds. Table 6.3 summarizes the main parameters for the investigation of the chosen baseline Reynolds number, i.e., Re = 2800, in conjunction with diffusive (column-wise) and acoustic (row-wise) scaling using $\lambda_{\text{def}} = 10^{-2}$. Mind that the experienced deviations from the targeted bulk Reynolds numbers are fairly small.

Table 6.3: Simulation parameters for a target bulk Reynolds number of Re = 2800 using the default limiter value $\lambda_{\text{def}} = 10^{-2}$ under acoustic (Ma) and diffusive (N_H) scaling.

Ma		$N_H = 14$	$N_H = 28$	$N_H = 56$
1/10	ν	$2.89 \cdot 10^{-4}$	$5.77 \cdot 10^{-4}$	$1.15 \cdot 10^{-3}$
	$\bar{\mathrm{f}}_x$	$3.10 \cdot 10^{-6}$	$1.49 \cdot 10^{-6}$	$7.07 \cdot 10^{-7}$
	Re	2799.4 (−0.02%)	2802.2 (+0.08%)	2798.0 (−0.07%)
1/30	ν	$9.62 \cdot 10^{-5}$	$1.92 \cdot 10^{-4}$	$3.85 \cdot 10^{-4}$
	$\bar{\mathrm{f}}_x$	$3.56 \cdot 10^{-7}$	$1.63 \cdot 10^{-7}$	$7.85 \cdot 10^{-8}$
	Re	2801.5 (+0.05%)	2799.5 (−0.02%)	2796.4 (−0.13%)
1/90	ν	$3.21 \cdot 10^{-5}$	$6.41 \cdot 10^{-5}$	$1.28 \cdot 10^{-4}$
	$\bar{\mathrm{f}}_x$	$3.94 \cdot 10^{-8}$	$1.89 \cdot 10^{-8}$	$9.00 \cdot 10^{-9}$
	Re	2801.1 (+0.04%)	2806.8 (+0.24%)	2802.4 (+0.09%)

Unless explicitly stated otherwise in the following, the regularization parameter and the Mach number refer to the default/baseline values, i.e., $\lambda = \lambda_{\text{def}} = 10^{-2}$ and Ma = 1/30.

6.1.2 Results and Discussion

Initially, the results for the present baseline Reynolds number of Re = 2800 combined with the fine grid ($N_H = 56$) are reported. Following this, resolution studies for both acoustic and diffusive scaling are performed using $\lambda_{\text{def}} = 10^{-2}$, before the influence of the regularization parameter is assessed more in-depth. Build upon the baseline Reynolds number findings, results for the three other Reynolds numbers are presented.

Baseline Study for Re = 2800

Figure 6.2 displays the nondimensional wall distance $y^+_{T\,|\,B}$ of the wall-adjacent fluid nodes along the top T [dashed lines] and bottom B [solid lines] boundaries of the domain. The vertical gray line at $x/H = 5.43$ indicates the reattachment point (RP) position taken from Breuer et al. [2006], which serves as the first indicator for the resolution quality. It is evident that the coarse [red] grid RP prediction significantly deviates from the prediction of the other two grids, which both agree much better with the reference data.

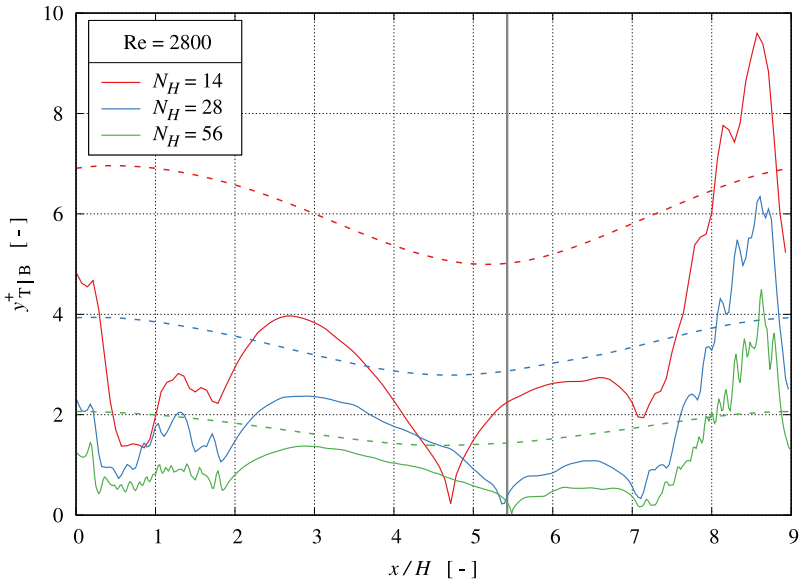

Figure 6.2: Nondimensional wall distance $y^+_{T\,|\,B}$ under diffusive scaling at the bottom [solid] and top [dashed] wall for Re = 2800. The vertical gray line indicates the reported DNS reattachment point.

The maximum $y^+_{T,\max}$ values at the top wall occur above the crest, where the flow is accelerated, and refer to 7 ($N_H = 14$), 4 (N_H=28) and 2 (N_H=56) wall units for the three grids. Due to the smaller velocities in the recirculation and reattachment region, the nondimensional resolution of the bottom wall is mostly better. However, it deteriorates when the flow accelerates ($x/H > 7.1$), and the wall distances deviate from $q = 0.5$. The respective maxima approximately refer to 10 (N_H=14), 6 (N_H=28), and 4 (N_H=56) wall units and occur nearly upstream of the crest. In conclusion, all three resolutions correspond to LES grids, and the fine grid is deemed close to a DNS resolution since the field lattice spacing is around $\Delta x^+ \approx 3$.

Mean Flow

Figure 6.3 displays averaged profiles of the longitudinal velocity component (top) and the Reynolds shear stress (bottom) for Re = 2800. They are in fair predictive agreement with the DNS reference data sets, i.e., *LESOCC* [red] and *MGLET* [blue]. The depicted Reynolds shear stress components reveal minor deviations around the extreme values of the profiles located at $2 \leq x/H \leq 6$. Overall, the C-P model provides a remarkable predictive agreement with DNS data when using the fine grid.

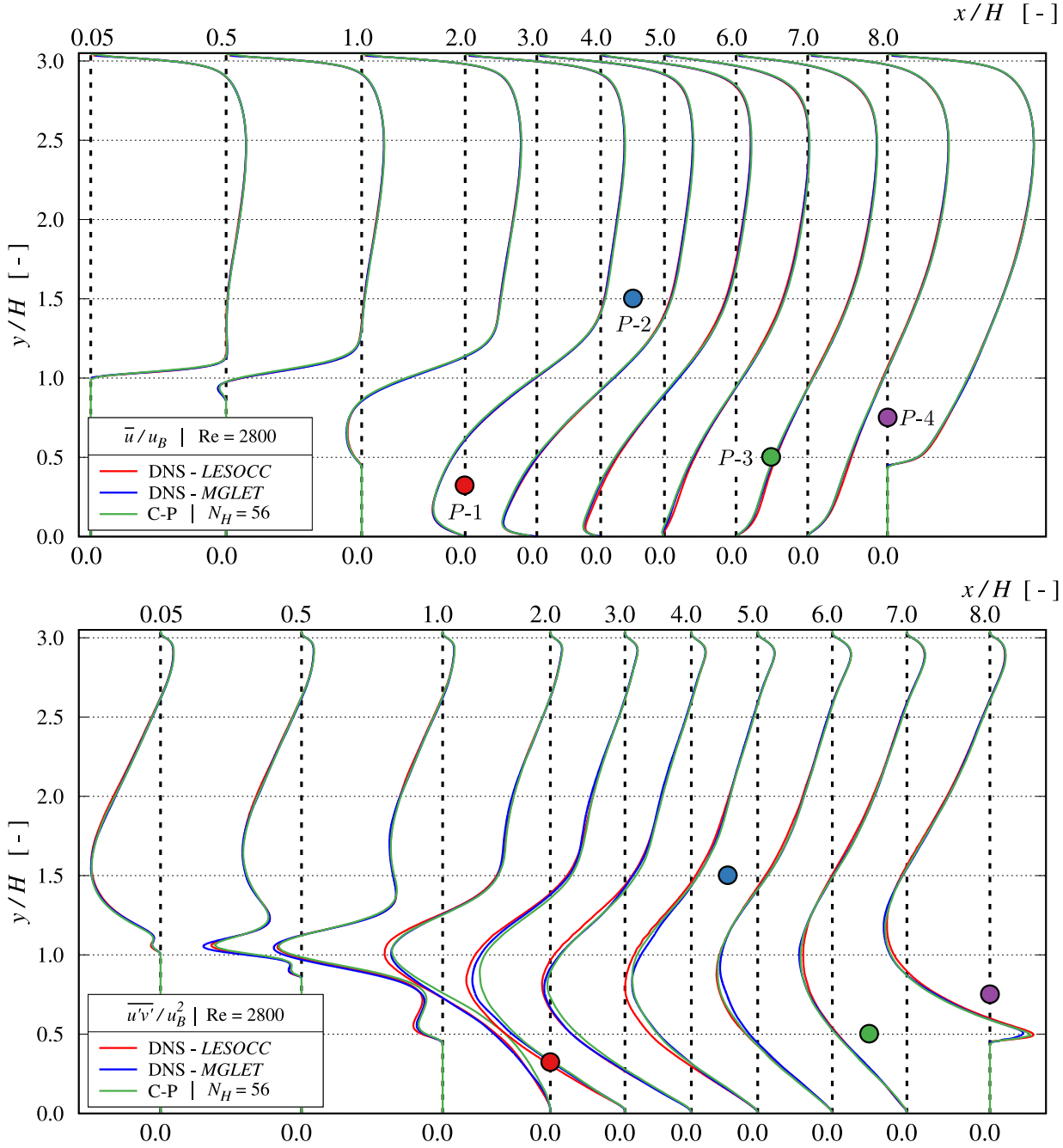

Figure 6.3: Comparison of averaged longitudinal velocities (top) and Reynolds shear stresses (bottom) predicted by the C-P model on the fine grid with DNS reference data for Re = 2800.

Turbulence Statistics

Figure 6.4 shows the turbulent energy spectra *PSD* of the longitudinal (u), vertical (v), and lateral (w) direction. Each figure includes four spectra corresponding to the four reference points of the flow field, cf. Tab. 4.2. In large parts, the spectra for the acceleration (P-4) and the reattachment (P-3) location overlap. As expected from the relatively low Reynolds number, the inertial range, featuring the classical $PSD(f) \propto f^{-5/3}$ proportionality, is

restricted to a narrow frequency regime of $\Delta f_{\text{inertial}} \approx \mathcal{O}(10^1)$. The confinement is most pronounced in the recirculation regime [red], where the spectra energy-containing and energy-dissipating parts tend to overlap and are less severe for the core flow position [blue]. The sloping toward the dissipation range is almost identical for the three velocity components. Some deviations of the energy levels are observed in the production range, where the lateral component displays the most distinct location-dependent variations, and the levels are generally augmented for the reattachment location (P-3), cf. Fig. 6.4 (right).

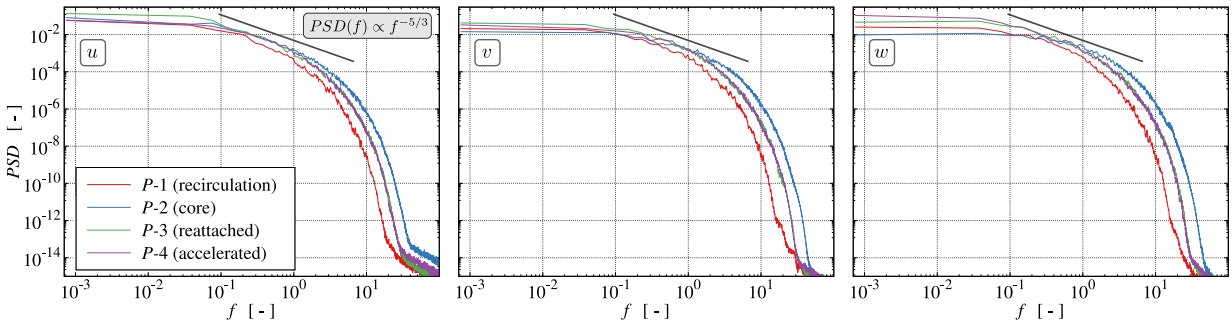

Figure 6.4: Computed turbulent energy spectra PSD of the three Cartesian velocity components u (left), v (center) and w (right) evaluated at the four points outlined in Fig. 4.6 for $\mathrm{Re} = 2800$ on the fine grid.

Figure 6.5 depicts anisotropy invariant maps (AIM) for four profiles located at $x/H = \{0.05; 0.5; 3; 6\}$. The representation of the discrete points distributed in y-direction employs a diverging color bar ranging from blue (bottom wall) to red (top wall). A commonality of all displayed maps includes the alignment of both near-wall regions with the two-component turbulence abscissa. As wall influences decrease, a trend toward isotropic $3c$ turbulence is formed and reaches a global y_B maximum in the upper region of the domain at approximately $y/H = 2/3$ [orange].

For clarity, the detailed discussion of the AIM begins at $x/H = 6$ and is supported by characteristic markers added to Fig. 6.5 [bottom right]. Close to the top wall, the trajectory [1] falls almost centered on the x-axis at $x_B = 0.45$. In this regime, the vertical fluctuation vanishes, and the longitudinal contribution exceeds the lateral one. Away from the wall, the boundary layer gradient $\mathrm{d}\overline{u}/\mathrm{d}y$ contributes to an increase of $\overline{u'^2}$ which shifts the trajectory in the $1c$ direction and yields the global x_B maximum [2]. Subsequently, the wall damping attenuates, and the vertical component $\overline{v'^2}$ develops [3]. The $3c$ trend ends at $y_B \approx 0.55$, where the AIM turns toward the right axisymmetric expansion edge of the triangle [4]. The latter is attributed to the longitudinal acceleration of the flow, whereby the lateral (w) dynamics gradually decrease concurrent with the decreasing influence of the top wall. At the same time, the $\overline{u'^2}$ and $\overline{v'^2}$ are of a similar order of magnitude. In the center of the channel [green], the longitudinal component represents the major contribution [5]. As the lower wall is progressively approached, the longitudinal and lateral normal stresses reduce, and the trajectory shifts toward the left edge associated with axisymmetric contraction [6]. The vertical normal stress component is negligible for $0.4 > y/H > 0.1$. The other two components are approximately equal and decrease at a similar rate as the bottom wall is approached. In the vicinity of the lower wall [7], a large gradient $\mathrm{d}\overline{u}/\mathrm{d}y$ feeds an augmented level of longitudinal normal stress.

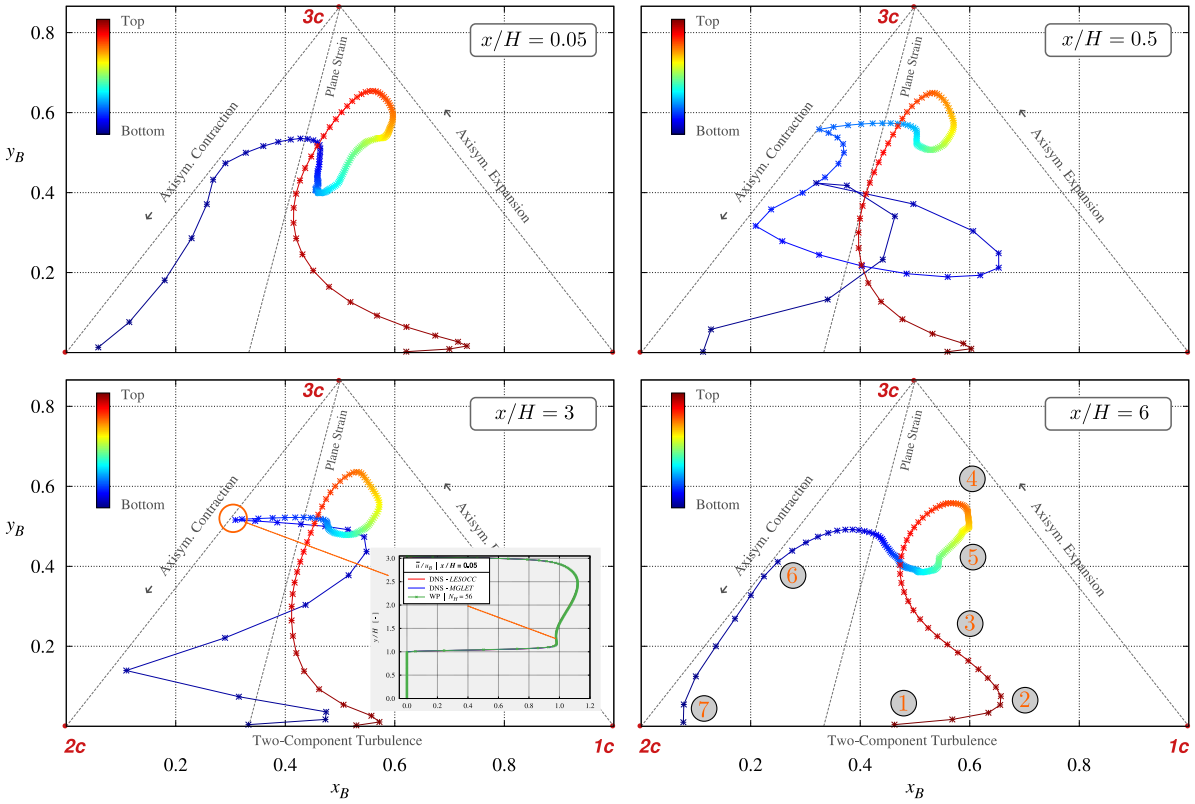

Figure 6.5: AIM at four distinctive $x/H = \{0.05; 0.5; 3; 6\}$ positions for Re = 2800 obtained from the fine grid.

The AIM trajectory of the recirculation zone profile located at $x/H = 3$ displays two deviations from the map at $x/H = 6$. These include a more pronounced and sharper $1c$ trend at the top wall [red] region in response to the stronger flow confinement and a greater distance from the axisymmetric contraction limit within the bottom, i.e., recirculating flow, region [blue] after touching this edge where the gradient $\mathrm{d}\overline{u}/\mathrm{d}y$ vanishes in line with the $\overline{u}$ minimum, cf. Fig. 6.3 (top). Moving further upstream to $x/H = 0.5$, the part of the trajectory located inside or near the recirculation zone [blue to cyan] is characterized by significant and sudden changes of the Reynolds stress anisotropy, which agrees with either local extrema or inflection points. The AIM closest to the crest [top left] displays features that are supported by the corresponding $\overline{u}$ velocity profile in Fig. 6.3. Due to strong acceleration above the crest, the bottom wall branch is shifted toward the $1c$ state. The upper wall behavior follows the behavior seen at $x/H = 0.5$, and the footprint of the two vanishing primal velocity gradient positions close to the bottom wall is observed again.

Acoustic Scaling (Re = 2800)

To assess the sensitivity of the C-P operator to the temporal resolution, three Mach numbers are investigated for the finest grid with $N_H = 56$, cf. Tab. 6.3. Investigations employ $\lambda_{\mathrm{def}} = 10^{-2}$ and refer to the baseline value of Ma = 1/30, as well as one larger (Ma = 1/10) and one smaller (Ma = 1/90) Mach number, respectively.

Mean Flow

Figure 6.6 displays representative exemplary longitudinal velocity and Reynolds shear stress profiles at two positions of the flow field. While the left column shows a profile close to the separation point at the crest ($x/H = 0.5$), the right column refers to a location slightly downstream of the reattachment point ($x/H = 6$). The *MGLET* DNS result [black line] serves as a reference. Predictive differences induced by the variation of the Mach number are small, and the C-P results agree reasonably well with the DNS results. A minor but noticeable deviation arises for the Reynolds shear stress, most distinct for the finest time step at $y/H = 0.85$ in the downstream location.

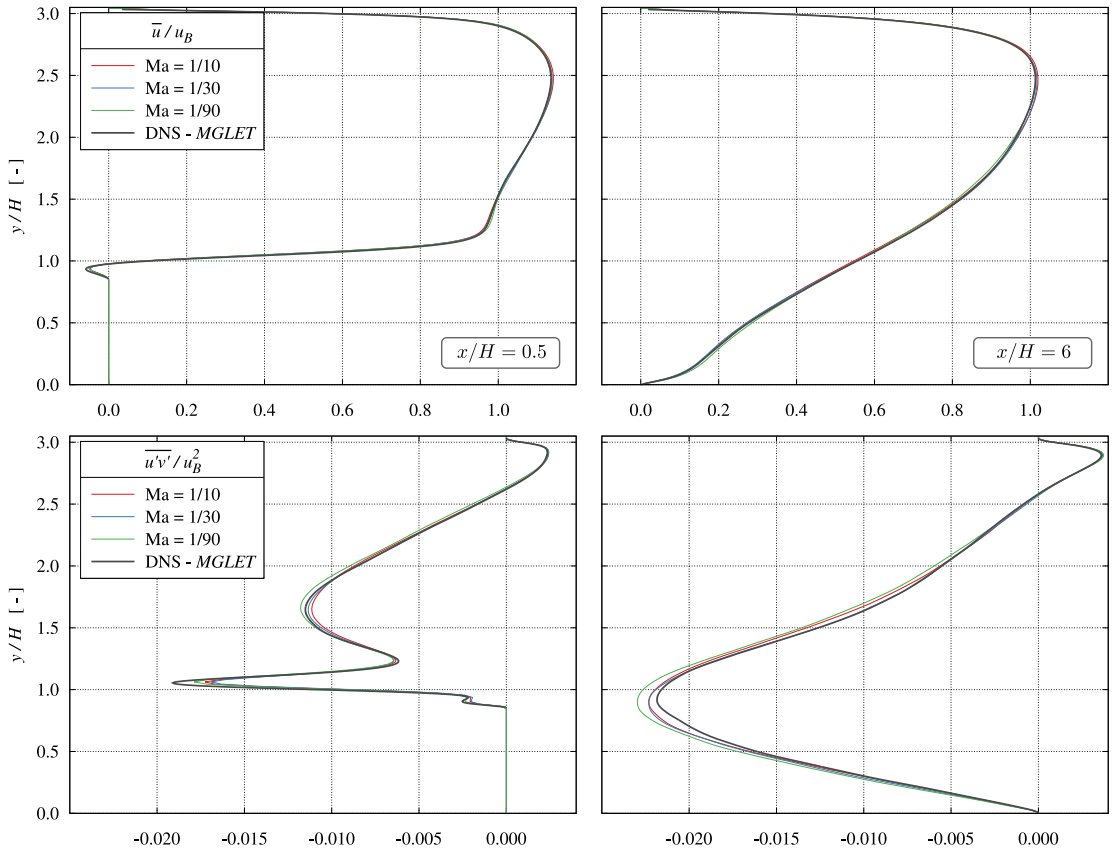

Figure 6.6: C-P vs. *MGLET* DNS reference: averaged longitudinal velocity component $\overline{u}/u_B$ (top) and Reynolds shear stress $\overline{u'v'}/u_B^2$ (bottom) profiles under acoustic scaling exemplarily depicted at two positions for Re = 2800 on the fine grid.

A more comprehensive analysis assesses the relative L_2 error norm against reference *MGLET* DNS results. To this end, Tab. 6.4 summarizes the (unweighted) integral error norms of the ten selected profiles for the longitudinal and vertical velocity components. Its almost constant value confirms the minor influence of the underlying temporal resolution. It is noted that spatial resolution changes do not alter this finding, and similar results were obtained for the coarser grids but are not displayed to save space. Moreover, and again not displayed to safe space, the AIMs shown in Fig. 6.5 do not depict any significant differences in response to a Mach number variation.

Table 6.4: Relative integral $L_2(\vartheta)$ error norm (C-P vs. *MGLET* DNS) under acoustic scaling of selected flow quantities for Re = 2800.

ϑ	Ma = 1/90	Ma = 1/30	Ma = 1/10
$\overline{u}/u_B$	$7.71 \cdot 10^{-3}$	$6.83 \cdot 10^{-3}$	$7.61 \cdot 10^{-3}$
$\overline{v}/u_B$	$5.15 \cdot 10^{-2}$	$4.96 \cdot 10^{-2}$	$4.20 \cdot 10^{-2}$

Turbulent Spectra

In addition to the mean flow data, Fig. 6.7 shows *PSD* spectral data. Particularly, the *PSD* of the longitudinal (u) component is exemplary depicted at two locations, i.e., in the core (P-2) and the reattaching (P-3) flow regime, cf. Fig. 4.6.

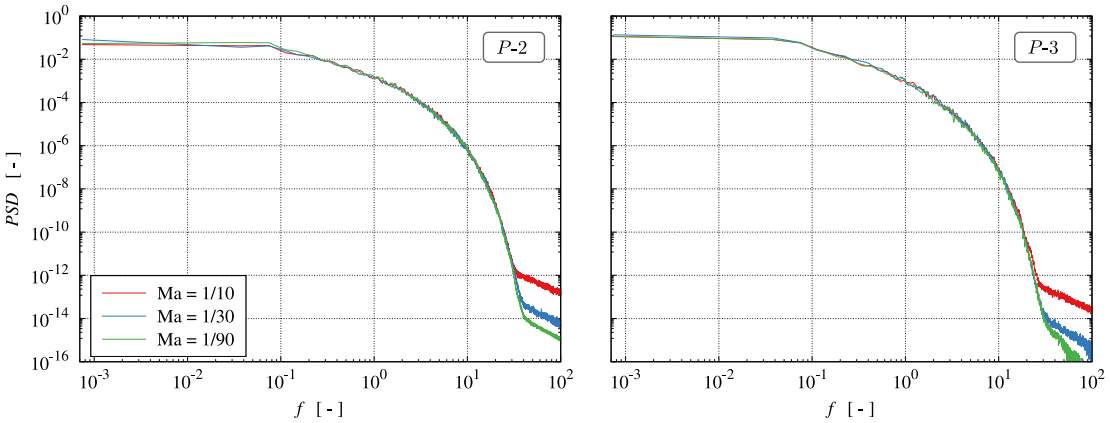

Figure 6.7: Longitudinal (u) turbulent energy spectra *PSD* under acoustic scaling exemplarily depicted at two points for Re = 2800 on the fine grid.

No substantial differences are observed between the three Mach numbers. The length and the slope of the inertial range are identical for all displayed spectra. Minor deviations in the high-frequency cut-off range are attributed to the data processing scheme and have no physical meaning.

Diffusive Scaling (Re = 2800)

This section reports the sensitivity of the results to diffusive scaling, where three consecutive resolutions are investigated, i.e. $N_H = \{14; 28; 56\}$, and compared with *MGLET* DNS reference data.

Mean Flow

Figure 6.8 outlines the averaged flow results at four x/H locations. Compared with the DNS reference solution [black], the coarse grid results [red] significantly overpredict the longitudinal velocity component above the crest at $x/H = 0.05$ and $y/H \approx 1.2$. This defect is due to under-resolving the thin boundary layer in the acceleration regime upstream of the crest and mitigates with increasing wall distance, i.e., for $y/H > 1.75$. The associated larger shear stress gradient magnitude delays flow separation, and no substantial

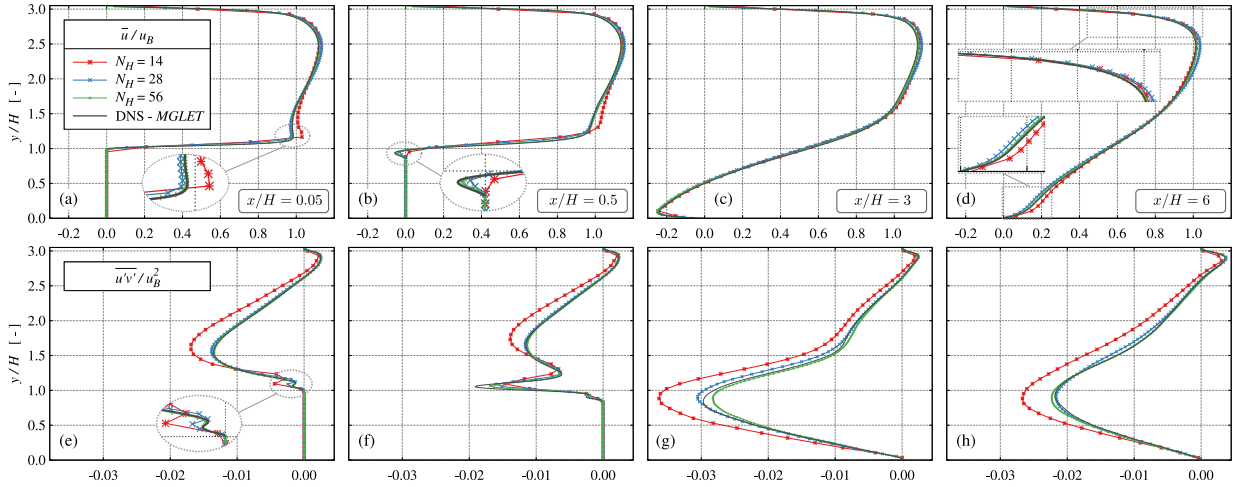

Figure 6.8: C-P vs. *MGLET* DNS reference: averaged longitudinal velocity component $\overline{u}/u_B$ (top) and Reynolds shear stress $\overline{u'v'}/u_B^2$ (bottom) at four distinctive $x/H = \{0.05; 0.5; 3; 6\}$ (from left to right) positions under diffusive scaling for $\mathrm{Re} = 2800$.

recirculation regime is formed at $x/H = 0.5$ **(b)**. All mean velocity data agree at $x/H = 3$ **(c)**. At the same time, Reynolds shear stress magnitudes predicted on the coarse grid reveal larger gradients and peak values around the dividing streamline again. This, in turn, enhances the recovery of the reattaching shear flow for the coarse grid at $x/H = 6$ **(d)**. The predictive agreement of the fine grid $\overline{u}$ results with the reference solution is marginally better than the medium grid results in the recovery regime. Moreover, these improvements yield small changes in the upper boundary layer for continuity reasons.

With attention given to the resolution influences on the integral L_2 error norm displayed in Fig. 6.9, the more subtle vertical velocity component $\overline{v}$ depicts an almost linear dependency of the error norm across the total resolution spectrum. While the dashed blue lines

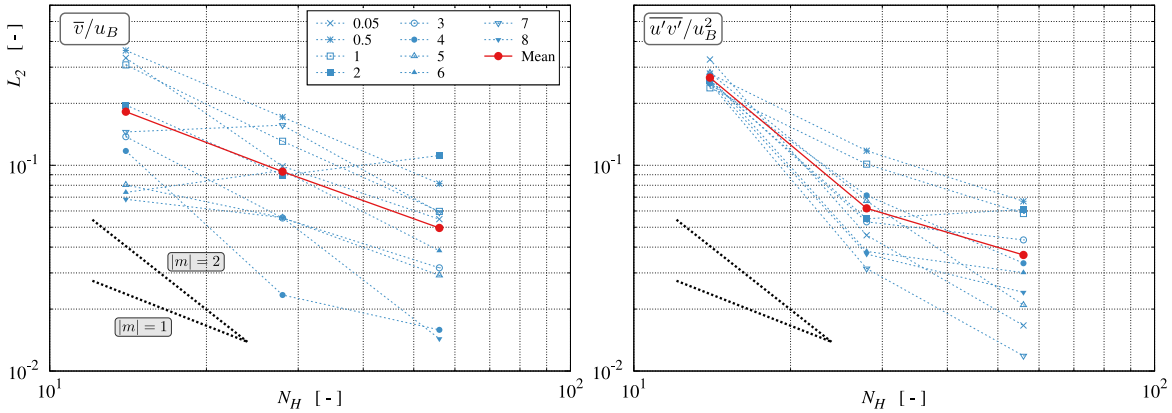

Figure 6.9: Relative L_2 norm (C-P vs. *MGLET* DNS) of the vertical velocity $\overline{v}/u_B$ (left) and Reynolds shear stress $\overline{u'v'}/u_B^2$ (right) under diffusive scaling for $\mathrm{Re} = 2800$.

indicate the relative error norms for the ten selected profiles, the solid red line represents their (unweighted) mean value. As could be expected by the Reynolds stresses displayed in the Fig. 6.8, they reveal a stronger sensitivity to the resolution, which is of order two in

the coarse grid regime and lower in the fine grid regime. This trend is representative and relates to the limiter's influence, as will be outlined further.

Turbulent Structures

The observations found for the mean flow data are confirmed by the AIM trajectories depicted in Fig. 6.10 for a near-crest location at $x/H = 0.05$ (left) and a recovery location at $x/H = 6$ (right). Resolution-related differences are more pronounced at $x/H = 0.05$, where the reduction in resolution confines the AIM pathway toward the vicinity of the plane strain line, and at least one of the eigenvalues equals zero. The axisymmetric states above the bottom wall are insufficiently resolved. Moreover, the augmentation of the primary normal stress component close to the top wall and the related shift toward the one-component regime is suppressed, particularly at $x/H = 6$. Much smaller deviations

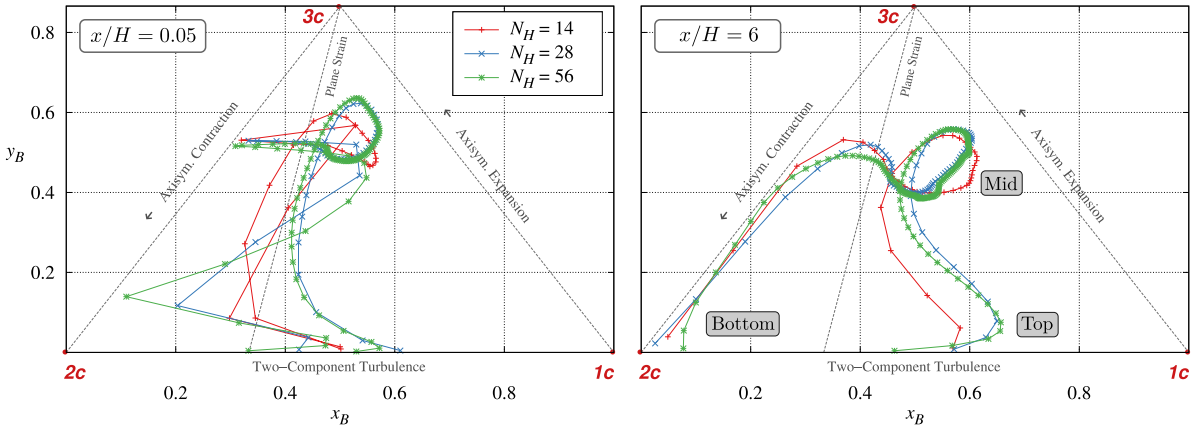

Figure 6.10: Influence of diffusive scaling on the Reynolds stress anisotropies depicted at two positions for Re = 2800.

between the medium and the fine grid are seen for all the above-discussed aspects. In general, the ability to resolve flow anisotropies is enhanced with the resolution. This observance might hint at an earlier onset of dissipative structures in frequency space and a corresponding reduction of the inertial range when coarsening the grid.

Figure 6.11 shows the predicted turbulent spectra obtained for all three velocity components at a core flow location P-2, cf. Fig. 4.6. The graphs reveal a shift of the inertial range's upper end by almost one order of magnitude when quadrupling the resolution from $N_H = 14$ to $N_H = 56$. Between the medium and the fine grid, a more gradual onset of dissipative influences is observed in combination with a small increase in the upper inertial range frequency for the fine grid. The resolution-induced differences are similar for other locations, albeit slightly more pronounced for the recirculation regime (P-1).

Illustrative snapshots of the velocity magnitude $|\underline{u}|/u_B$ and the averaged (resolved) turbulent kinetic energy k/u_B^2 in the x-y center plane are shown in Fig. 6.12 for all three resolutions. Evidently, the coarse mesh [top row] features relatively large structures and misses several details. As outlined by the black boxes [top left], the $N_H = 14$ simulation fails to resolve the shear layer while approaching the crest of the hill at the downstream end of the domain. For the coarse grid, the large structures are associated with a stable, almost horizontal – perhaps even upward-directed – separated shear layer downstream of the crest as well as an increased mean turbulence intensity above the dividing streamline,

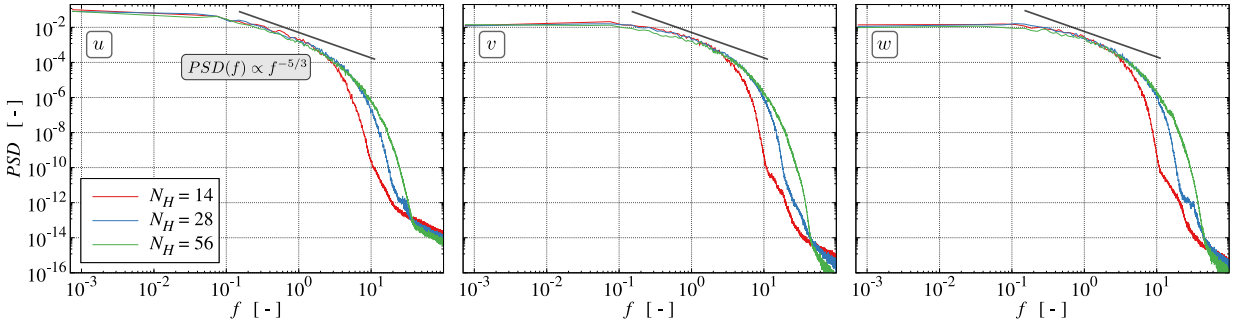

Figure 6.11: Turbulent energy spectra PSD of the longitudinal u (left), vertical v (center) and lateral w (right) velocity component under diffusive scaling exemplarily depicted at P-2 (core flow) for $\mathrm{Re} = 2800$.

which is consistent with the findings from Fig. 6.8. The observed deficits are induced by the inability to accurately resolve the thin shear flow in the accelerated regime.

An increase in resolution reduces the thickness of the predicted shear layer at the crest and changes the direction of the streamlines, as additionally outlined in Fig. 6.13. When approaching the crest, the coarse grid streamlines do not follow the curved hill shape like the fine grid streamlines. In addition an upward motion is seen for $N_H = 56$ which reduces the turbulence producing mean flow gradients and can not be observed for the coarse grid $N_H = 14$. Moreover, coarse grid streamlines indicate a stronger thickening of the top boundary layer until $x/H \approx 7$, which is compensated during the acceleration region. The flow is more inclined toward the top for the coarse grid. Albeit the fine grid [bottom left] snapshot in Fig. 6.12 reveals more details of the turbulent structures than the medium grid results [center left], the mean turbulence intensities agree rather well. Mind that the evaluation point used for the spectra in Fig. 6.11 is located in the core flow (P-2) regime, where no substantial resolution-based differences occur for the large structures.

Regularization Parameter Analysis (Re = 2800)

This section addresses the impact of the value assigned to the regularization parameter λ under diffusive scaling. Reported results are confined to $\mathrm{Re} = 2800$ and the baseline Mach number of $\mathrm{Ma} = 1/30$.

Owing to $\lambda_{\mathrm{def}} = 10^{-2}$, one would intuitively expect the cumulant magnitude expressions in (3.111)−(3.114) to reach up to values around 10^{-2} or higher. However, the present results reveal peak values around 10^{-3} for coarser resolutions, which indicates that subtle changes of $\omega_{\{3;4;5\}}$ in the order of 1% in the direction of C-AO are of distinct significance. The latter is understood by the generally low values of the higher-order relaxation rates, which are around $\omega_{\{3;4;5\}} \approx \mathcal{O}(10^{-3})$ – $\mathcal{O}(10^{-2})$. A strong link between the grid resolution and the cumulant magnitude expressions is observed. Likewise, a minor link between these expressions and changes in the Reynolds number is seen. Furthermore, a weak proportionality is perceived when attention is directed to the nonlinear interaction between the cumulant magnitude expressions under a λ-variation.

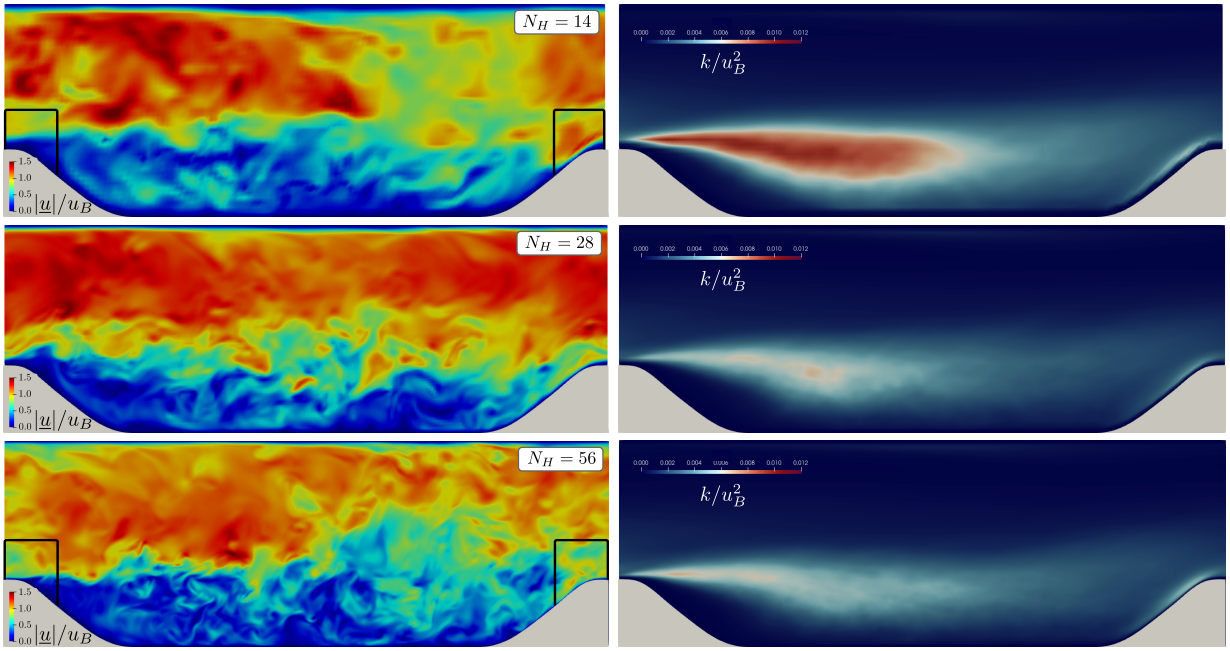

Figure 6.12: Normalized instantaneous velocity magnitude (left) and resolved TKE (right) in the x-y center plane under diffusive scaling (top; center; bottom) for Re = 2800.

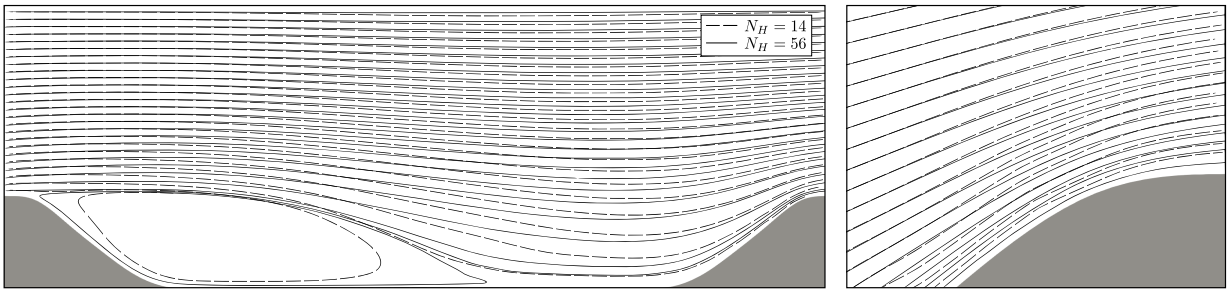

Figure 6.13: Comparison of averaged flow field streamlines obtained with the coarse [dashed] and the fine grid [solid] in the x-y center plane for Re = 2800.

Mean Flow

Figure 6.14 depicts the nondimensional wall distance y_T^+ along the top wall of the domain. The plot involves information for three λ-values and three spatial resolutions, i.e., $N_H = \{14; 28; 56\}$ [red; blue; green]. For the underlying Reynolds number, the first fluid node does not exceed the buffer layer for all simulations, i.e., $y_T^+ < 7.5$. This is also true for the bottom wall where $y_B^+ < 12$ holds, not shown to save space. Next to the default value of $\lambda_{\text{def}} = 10^{-2}$ [dashed], two supplementary values which differ by four orders of magnitude from the default value are used, viz. $\lambda = 10^{-6}$ [solid] and $\lambda = 10^{2}$ [dotted]. These values refer to the C-AO model ($\lambda = 10^{-6}$), as well as modifications in the order of 100% (λ_{def}) and 1% ($\lambda = 10^2$) of the non-regularized $\omega_{\{3;4;5\}}$ values, respectively. As indicated by Fig. 6.14, the regularization's influence increases distinctly in under-resolved conditions. Decreasing the limiter value introduces numerical diffusion and reduces the flow dynamics and wall shear stress. Along the top wall, the y_T^+ variation amounts to

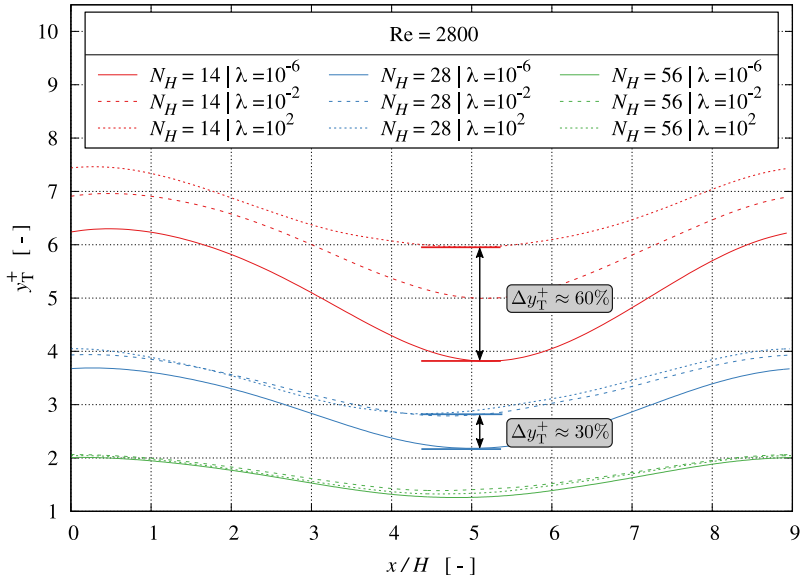

Figure 6.14: Influence of limiter the value $\lambda = \{10^{-6}; 10^{-2}; 10^{2}\}$ on the nondimensional wall distance y_T^+ at the top wall for Re = 2800 under diffusive scaling.

approximately 60[30]% for the coarse[medium] in response to the limiter's variation. On the contrary, the variations returned by the fine grid computation remain fairly moderate and fall below 10% over the entire domain. Figure 6.15 shows the relative L_2 error norm of the longitudinal (left) and vertical (right) mean velocity components as a function of the spatial resolution. For brevity, the plots are limited to the integral values of the ten specific

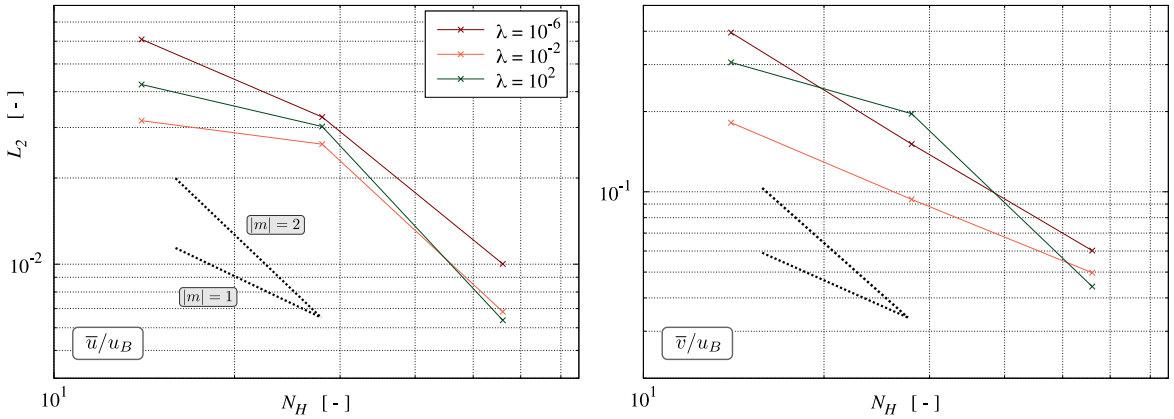

Figure 6.15: Influence of the limiter value $\lambda = \{10^{-6}; 10^{-2}; 10^{2}\}$ [red; orange; green] on the integral L_2 norm (C-P vs. *MGLET* DNS) of the longitudinal (left) and vertical (right) velocity component for Re = 2800 under diffusive scaling.

profiles. Overall, the default value $\lambda_{\text{def}} = 10^{-2}$ [orange] yields the smallest errors for the observed quantities over the investigated range of spatial resolutions. Using $\lambda = 10^{-6}$ [dark red] provides an almost constant slope of $|m| \approx 1.4$ for both quantities. In contrast, increasing the limiter value reveals a different behavior. For $\lambda = 10^{2}$ [green], all error norms have a pronounced slope change. In the fine grid regime, the convergence primarily improves toward $|m| \approx 2$, while a lower inclination ($|m| \leq 1$) is seen for the coarse grid regime, i.e., $N_H = 24 \rightarrow 12$. The resolution reduction influences the convergence behavior

for the coarser grids, suggesting the underlying λ-values to be inappropriate. To this end, Fig. 6.16 illustrates results obtained from a narrower range, i.e. $\lambda = \{10^{-2}; 10^{-1}; 10^{0}\}$. The figure reveals that $\lambda = 10^{-1}$ seems a reasonable choice, which is also confirmed by the below-discussed assessment of spectra for different λ-values.

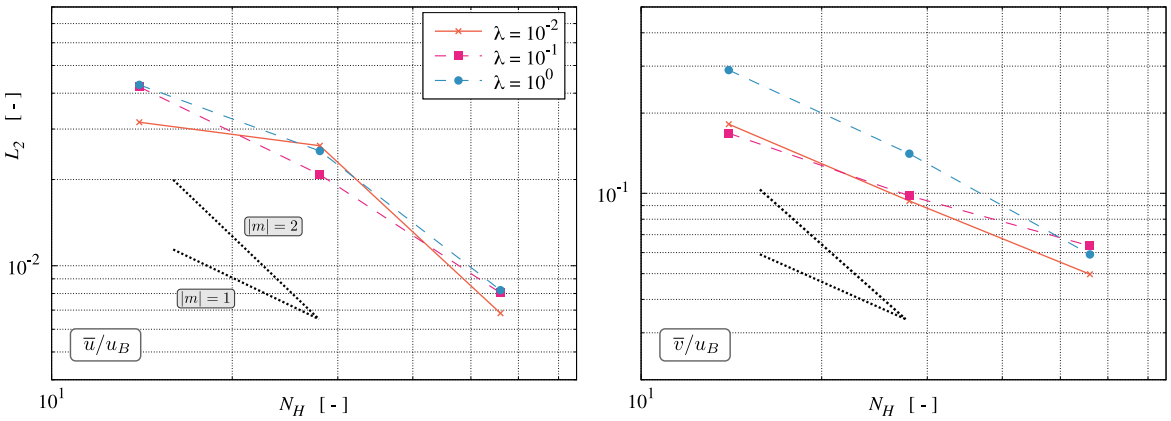

Figure 6.16: Influence of the limiter value $\lambda = \{10^{-2}; 10^{-1}; 10^{0}\}$ on the integral L_2 error norm (C-P vs. *MGLET* DNS) of the longitudinal (left) and vertical (right) velocity component for Re = 2800 under diffusive scaling.

Turbulent Structures

The influence of the limiter on the characteristics of the resolved Reynolds stress tensor is outlined by Fig. 6.17 (top). The figure depicts the AIM for the three investigated spatial resolutions using the broader limiter spectrum also assessed in Fig. 6.15. The reported results refer to a profile extracted at $x/H = 6$, located close to the reattachment point along the bottom wall. It is emphasized that similar results were observed for the other profile locations. Again, the most pronounced response to the λ choice appears for the coarse resolution (left), whereas the trajectories for the different limiter values almost converge for the fine grid (right). The figure reveals that λ distinctly alters the turbulence characteristics of the top wall boundary layer. Here, significant deviations occur along the $\overline{2c-1c}$ abscissa and propagate into the core flow when the resolution is reduced. For the coarser grids, results obtained for $\lambda = 10^{-1}$ [light green] provide the best overall agreement with the fine grid data.

Figure 6.17 (bottom) depicts representative energy spectra of the vertical (v) velocity component in the core flow regime (P-2). Each subfigure refers to a fixed resolution N_H and displays data obtained for $\lambda = \{10^{-6}; 10^{-2}; 10^{-1}; 10^{2}\}$. To support the discussion of details, the abscissa is limited to $10^{-1} \leq f \leq 10^{2}$. While an increase in the resolution generally yields a more gradual sloping toward the dissipative scales, many details are identical for all three resolutions. The low frequency ($f \leq 10^{0}$) production regime is deemed independent of both the resolution and the limiter value, and all curves approximately originate from $PSD(f = 10^{-1}) \approx 10^{-2}$.

When the normalized frequencies approach unity, the graphs enter the inertial range, where the obtained slope is close to the expected value of $-5/3$, irrespective of the resolution and limiter value. As alluded to earlier, a grid refinement results in an extension of the inertial range. However, the extent of the inertial range is also linked to the limiter value,

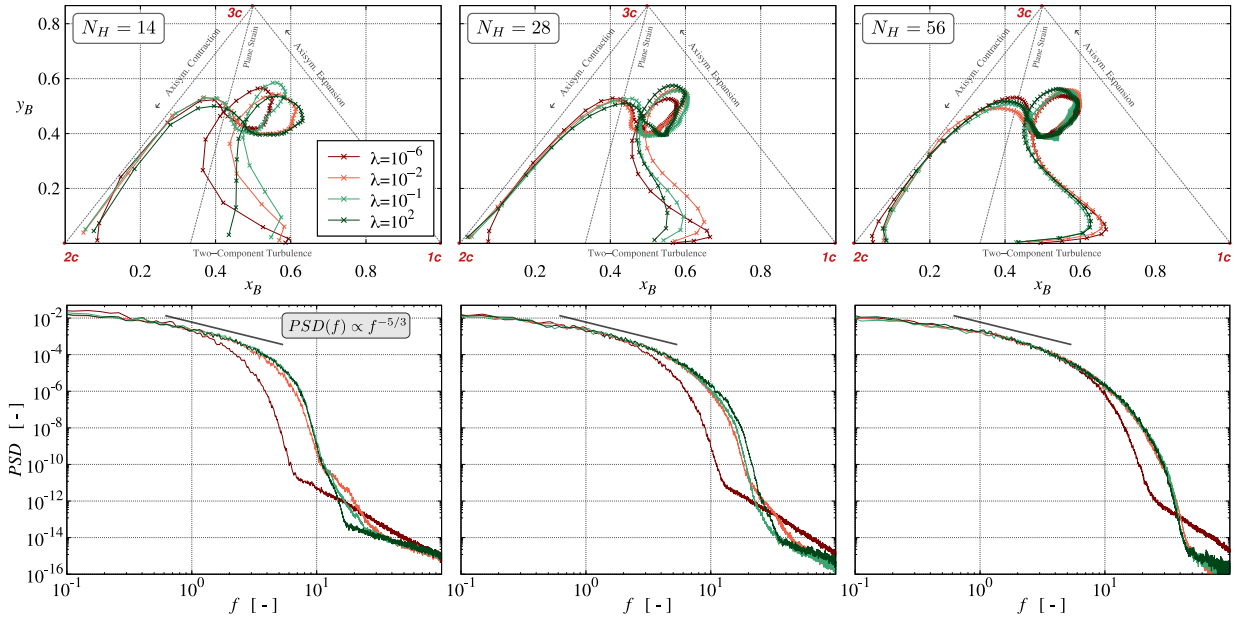

Figure 6.17: Influence of the limiter value $\lambda = \{10^{-6}; 10^{-2}; 10^{-1}; 10^{2}\}$ on the Reynolds stress anisotropies at $x/H = 6$ (top) and on the turbulent energy spectra PSD of the vertical (v) component at the P-2 core flow location (bottom) for $\mathrm{Re} = 2800$ and $N_H = \{14; 28; 56\}$ (left; center; right).

which distinctly occurs for the coarse grid (left). In particular, low (10^{-6}; C-AO) λ-values attenuate the dynamics and significantly reduce the width of the inertial range. On the other hand, increasing λ above the default value can extend the inertial range. Considering the fine grid results (right), the spectras' deviation as a function of λ diminishes, and only the C-AO model [dark red] deviates from the other three curves.

Reynolds Number Study

Subsequently, the influence of Reynolds number variation and analyses of the prospects of adjusting λ are addressed.

Re = 700

For the lowest considered Reynolds number of $\mathrm{Re} = 700$, the resolution of the near-wall flow is displayed in Fig. 6.18. The maximum $y^+_{B,\max}$ values of the three grids are 5 [red], 3 [blue] and 2 [green] wall units. The figure suggests that the fine grid fully resolves the Kolmogorov scale except for a small interval within the accelerated flow region, i.e., $8.25 \leq x/H \leq 8.75$. The $y^+_{T\,|\,B}$ characteristics confirm the results of the prior baseline study, cf. Fig. 6.2, and approximately scale with the Reynolds number ratio. Minor deviations are attributed to λ influences in under-resolutions. Grid convergence toward the referenced reattachment point, cf. Breuer et al. [2009], at $x/H = 5.34$ [gray vertical] is noted from Fig. 6.18.

The averaged profiles of the longitudinal velocity and Reynolds shear stress are depicted in Fig. 6.19. They display a good agreement between the medium [blue] and fine [green] grid results and also reproduce the DNS reference data obtained from *LESOCC* [black]. Only the coarse grid [red] yields deviations in all four plots. Most apparent defects occur

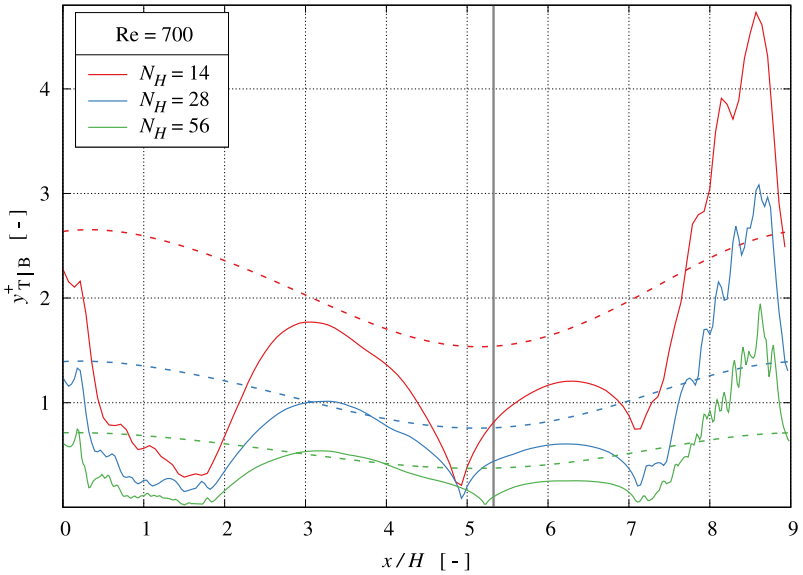

Figure 6.18: Nondimensional wall distance $y^+_{T\,|\,B}$ under diffusive scaling at the bottom [solid] and top [dashed] wall for Re = 700.

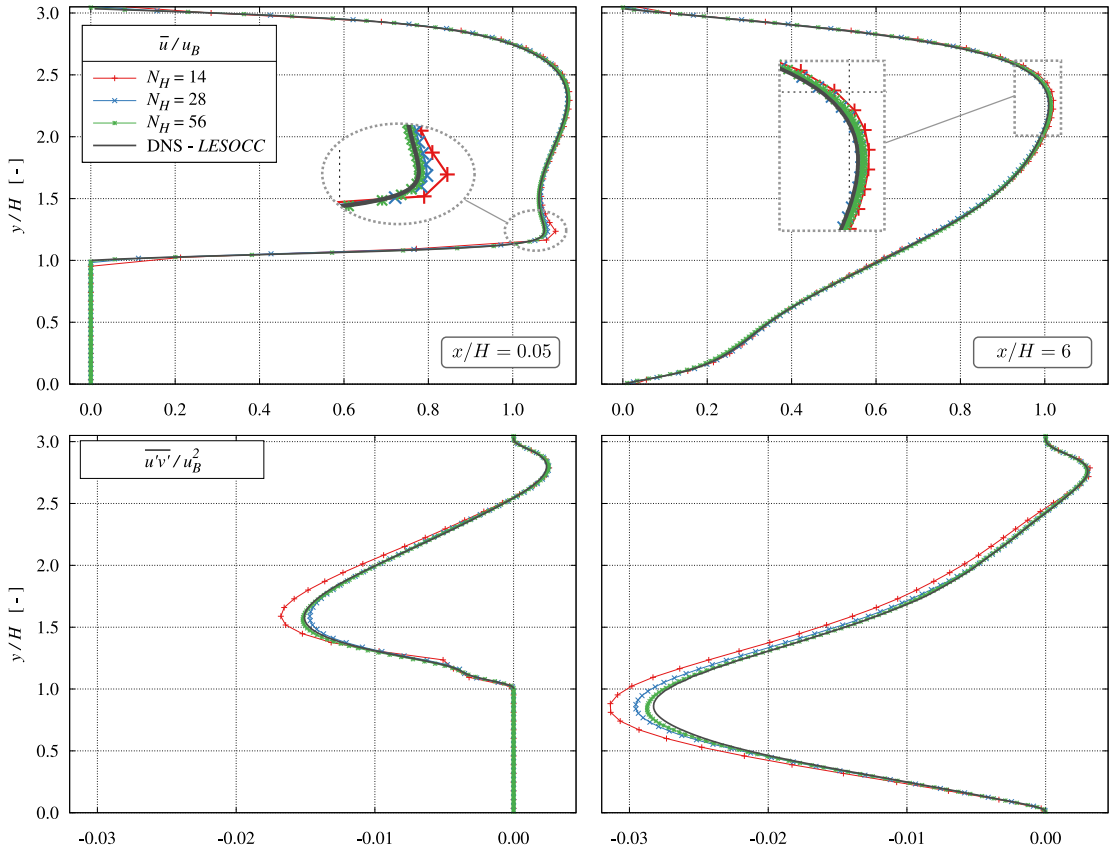

Figure 6.19: C-P vs. *LESOCC* DNS reference: averaged longitudinal velocity component $\overline{u}/u_B$ (top) and Reynolds shear stress $\overline{u'v'}/u_B^2$ (bottom) at two distinctive positions $x/H = \{0.05; 6\}$ (left; right) under diffusive scaling for Re = 700.

in the vicinity of the crest due to a misrepresentation of the accelerated shear upstream of the crest. As the flow recovers from separation, the results of all three resolutions almost coincide at $x/H = 6$ (top right). Based on this evaluation, $N_H = 28$ [blue] provides an adequate spatial resolution for $\mathrm{Re} = 700$ as the finer grid does not alter the solution.

This conclusion is supported by the energy spectra extracted at the core flow position (P-2) composited in Fig. 6.20. While the spectra returned by the medium [blue] and the fine [green] grid are almost identical, the coarse grid spectrum [red] shows a smaller equilibrium range.

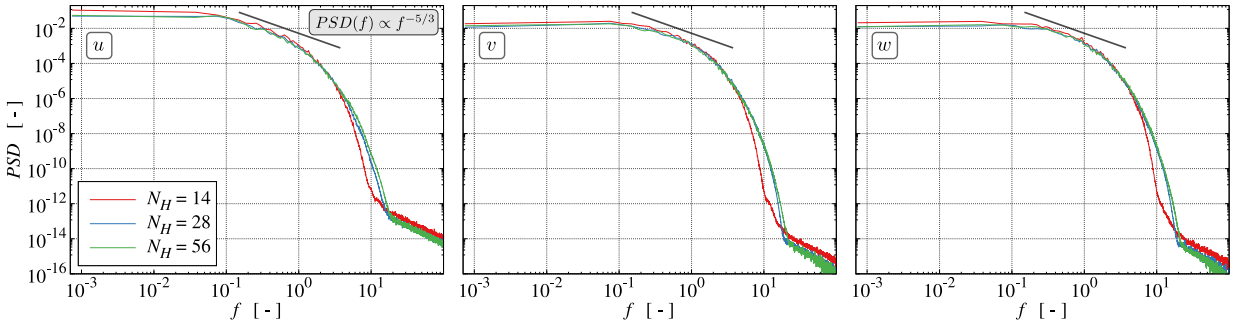

Figure 6.20: Turbulent energy spectra PSD of the longitudinal u (left), vertical v (center) and lateral w (right) velocity component under diffusive scaling exemplarily depicted at P-2 (core flow) for $\mathrm{Re} = 700$.

Figure 6.21 displays the v spectra response at P-2 to a variation of λ for the three grids. For fixed N_H, the spectra are virtually converged for $\lambda = 10^{-1}$, $\lambda = 10^{-3}$ and $\lambda = 10^{-4}$ on the coarse, medium and fine grid, respectively, where 10^{-3} and 10^{-4} are merely reported and not visualized. Thus, the λ limit value gradually decreases as the grid is refined. Nonetheless, $\lambda = 10^{-1}$ is an adequate and almost resolution-independent choice for this rather low Reynolds number.

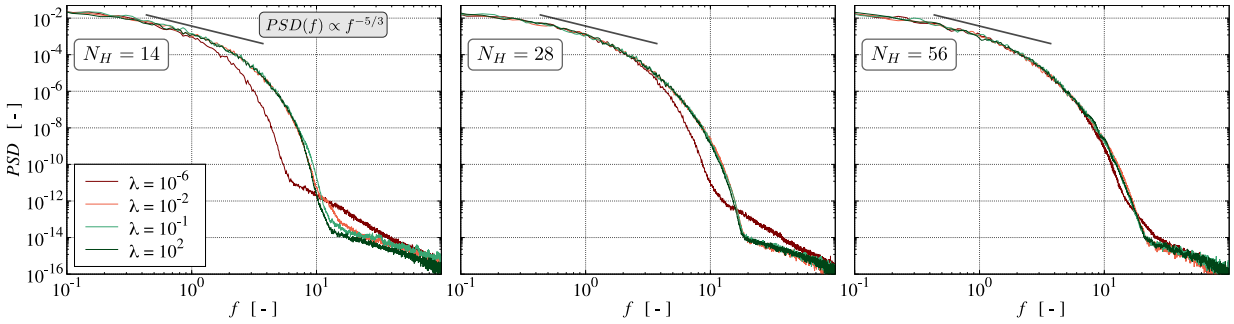

Figure 6.21: Influence of the limiter value $\lambda = \{10^{-6}; 10^{-2}; 10^{-1}; 10^{2}\}$ on the turbulent energy spectra of the vertical (v) component at P-2 (core flow) for $\mathrm{Re} = 700$ and $N_H = \{14; 28; 56\}$ (left; center; right).

Re = 10600

Studies of $\mathrm{Re} = 10600$ are of interest due to the availability of both experimental, cf. Rapp and Manhart [2011], and numerical, cf. Breuer and Rodi [1996] and Manhart et al. [2001], LES data sourced from the ERCOFTAC database, cf. Rapp et al. [2009]. The

predicted nondimensional wall distances along the bottom and top wall are not displayed to safe space. For $\lambda_{\text{def}} = 10^{-2}$, they resemble the results for Re = 2800 displayed in Fig. 6.2, though the y^+ levels are higher here. The global maxima of $y^+_{B,\max}$ for the three grids occur slightly upstream of the crest along the lower wall and refer to 18 ($N_H = 14$), 14 ($N_H = 28$) and 10 ($N_H = 56$) wall units. Peak values along the top wall are subject to minor variations and quantify $y^+_{T,\text{av}} \approx \{15, 8, 5\}$ on average. Employing a log law correlation, e.g., $u^+(y^+) = 8.3\,(y^+)^{1/7}$ from Werner and Wengle [1993], reveals an underprediction of y^+ of approximately 15% for the coarse grid compared to the linear relation $u^+ \sim y^+$. In contrast, the medium and fine grid predictions seem proper. The grid resolution is classified as LES for $N_H = 56$ and VLES for $N_H = \{14; 28\}$.

Figure 6.22 depicts selected averaged flow quantities, i.e. $\overline{u}$, $\overline{v}$ and $\overline{u'v'}$ at two upstream, i.e., $x/H = \{0.05; 1\}$, and two downstream positions, i.e., $x/H = \{7; 8\}$, of the crest. The

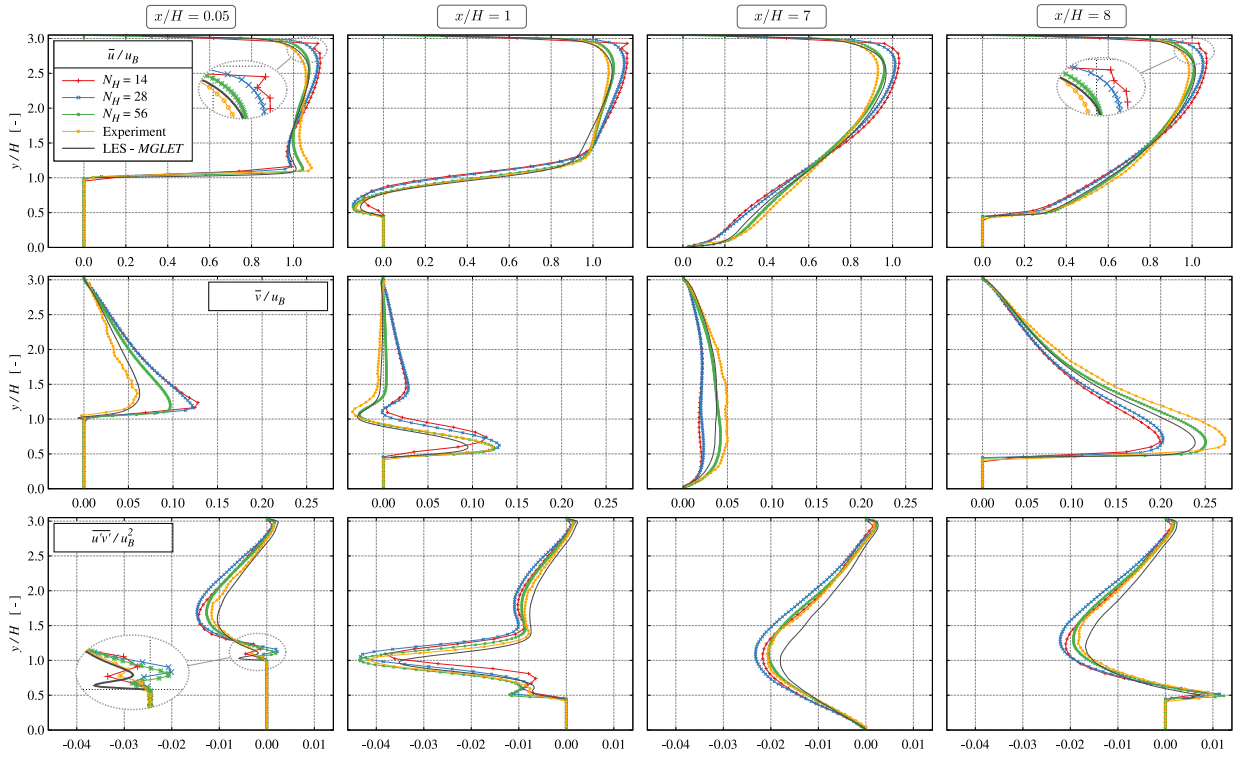

Figure 6.22: C-P vs. *MGLET* LES and experimental references: averaged longitudinal $\overline{u}/u_B$ (top) and vertical $\overline{v}/u_B$ (center) velocity component and Reynolds shear stress $\overline{u'v'}/u_B^2$ (bottom) at four distinctive $x/H = \{0.05; 1; 7; 8\}$ (from left to right) positions under diffusive scaling for Re = 10600.

fine grid appears adequate and provides a fair resolution of the separating flow, the initial separation, the recovery, and the accelerating flow. Mean flow predictions are slightly closer to the experimental data than the LES reference data, for which displayed Reynolds stresses only include resolved contributions. The most evident differences between the LBM results and the experimental data occur on the top of the hill. They are attributed to misrepresenting the accelerated upstream flow, which would benefit from finer grids. The predictive accuracy for the Reynolds stress is also fair, particularly in the downstream region.

A peculiar feature is the sign difference of $\overline{u'v'}$ predicted around $y/H = 1.2$ for the

separating flow at $x/H = 0.05$ [bottom left]. This is attributed to curvature effects and an erroneous upward-directed mean flow near the bottom wall shortly behind the inlet, cf. Fig. 6.23.

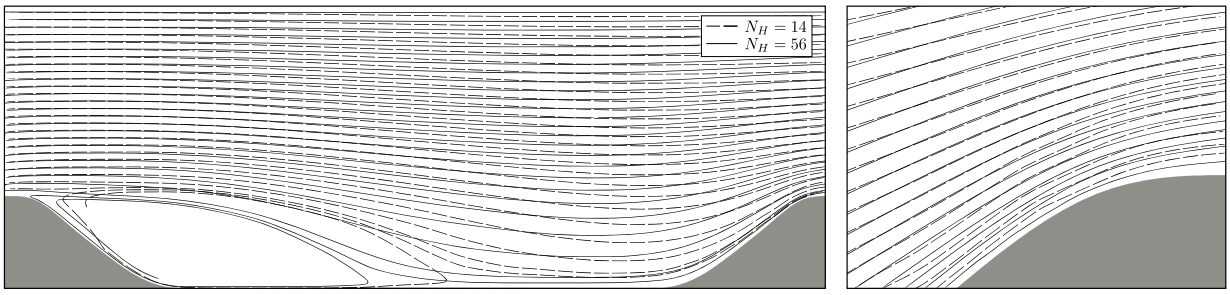

Figure 6.23: Comparison of averaged flow field streamlines obtained with the coarse [dashed] and the fine grid [solid] in the x-y center plane for Re = 10600.

When attention is directed to the medium grid [blue], detrimental effects of the resolution occur between the hills. The strong acceleration of the flow at $x/H = 8$ and the related thin shear layer is not as well captured as for $N_H = 56$. The global flow is noticeably displaced toward the top wall, and the recovery at $x/H = 7$ is likewise weaker. As a result, the bottom boundary layer thickens, the intensity of the wall-normal velocity weakens, and mean velocity gradients are reduced. These trends continue for the coarse [red] grid results. Due to the inadequate resolution, the displacement of the global flow field toward the top wall becomes more pronounced, and gradients of the bottom longitudinal velocity are further reduced. Neglecting a turbulence model and wall modeling strategies, the prediction of the longitudinal velocity along the top wall is insufficient. It clearly exceeds the resolution limits, as indicated by the kinks in Fig. 6.22 [top row]. The upper wall inaccuracies of the $\overline{u}$ profiles are also seen for lower λ-values on the coarse grid.

For additional testing, a standard Smagorinsky SGS model is employed for Re = 10600. Whether the parameterization inolves the unaltered $\omega_{\{3;4;5\}}(\omega)$ or altered $\omega_{\{3;4;5\}}(\omega_e)$ viscosity-related relaxation rate has virtually no impact on the results for the present range of resolutions. Thus, the results do not substantially improve the accuracy of the accelerated flow but support the predictions along the top wall. Here, the resolution is too coarse without the SGS for the coarse grid along the entire wall, and using an SGS yields approximately 20% smaller y^+ values, but much fewer changes along the bottom wall. Increasing the resolution attenuates the SGS influences, which mainly refer to the upper boundary layer, as outlined by Fig. 6.24. Moreover, the present SGS results match the findings of a PHF study of Chang et al. [2014], who employed an immersed boundary Navier-Stokes procedure connected with a dynamic Smagorinsky model on an anisotropic Cartesian grid with a resolution close to the $N_H = 28$ resolution in this case. The authors conclude that predictions without wall modeling yield better results and report similar predictive trends to the present study.

In line with the results obtained for the lower Reynolds numbers, the spectra in Fig. 6.25 indicate a substantial widening of the inertial range with increasing resolution. All spectra show a kink within the dissipation range, which indicates the activity of the regularization and is shifted toward higher frequencies as the resolution increases. For sufficiently large values of λ, the regularization is confined to the dissipative scales at the upper bounds of the spectra. When decreasing the value of λ, the regularization influences overlap with

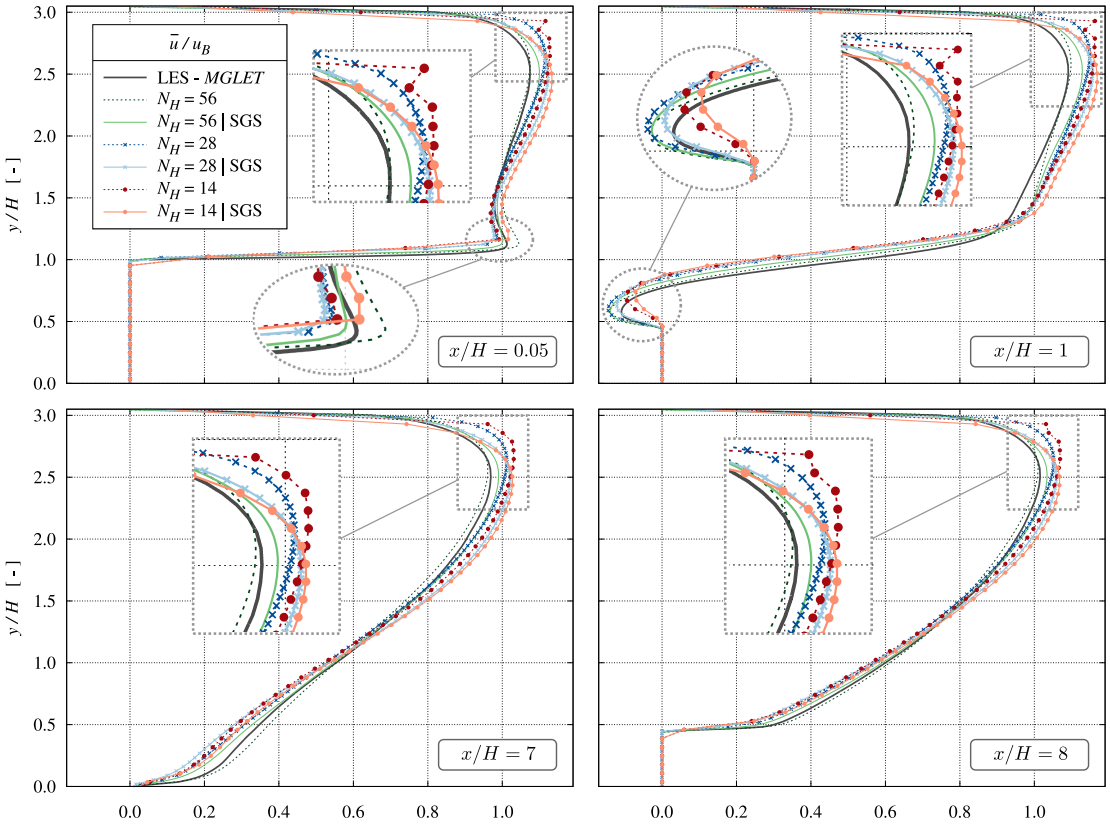

Figure 6.24: C-P vs. *MGLET* LES reference: averaged longitudinal $\overline{u}/u_B$ velocity component at four distinctive $x/H = \{0.05; 1; 7; 8\}$ positions under diffusive scaling with additional consideration of an SGS model for Re = 10600.

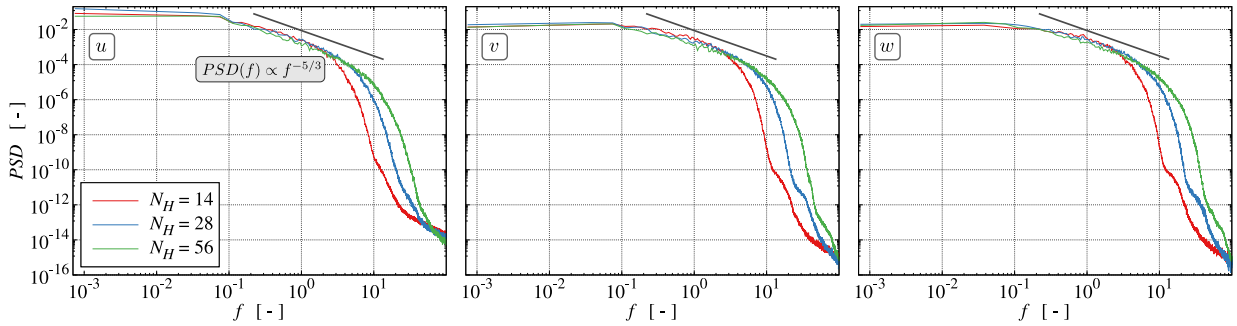

Figure 6.25: Turbulent energy spectra *PSD* of the longitudinal u (left), vertical v (center) and lateral w (right) velocity component under diffusive scaling exemplarily depicted at *P*-2 (core flow) for Re = 10600.

the inertial range, also cf. Fig. 6.17 (bottom). This effect will be discussed in more detail for the $N_H = 28$ grid, making the related differences more apparent. To this end, Fig. 6.26 outlines the sensitivity of $\overline{u}$ profiles to changes of λ-value at $x/H = \{0.05; 1; 7; 8\}$ on the medium grid. Herein dashed lines represent the default limiter result, where the

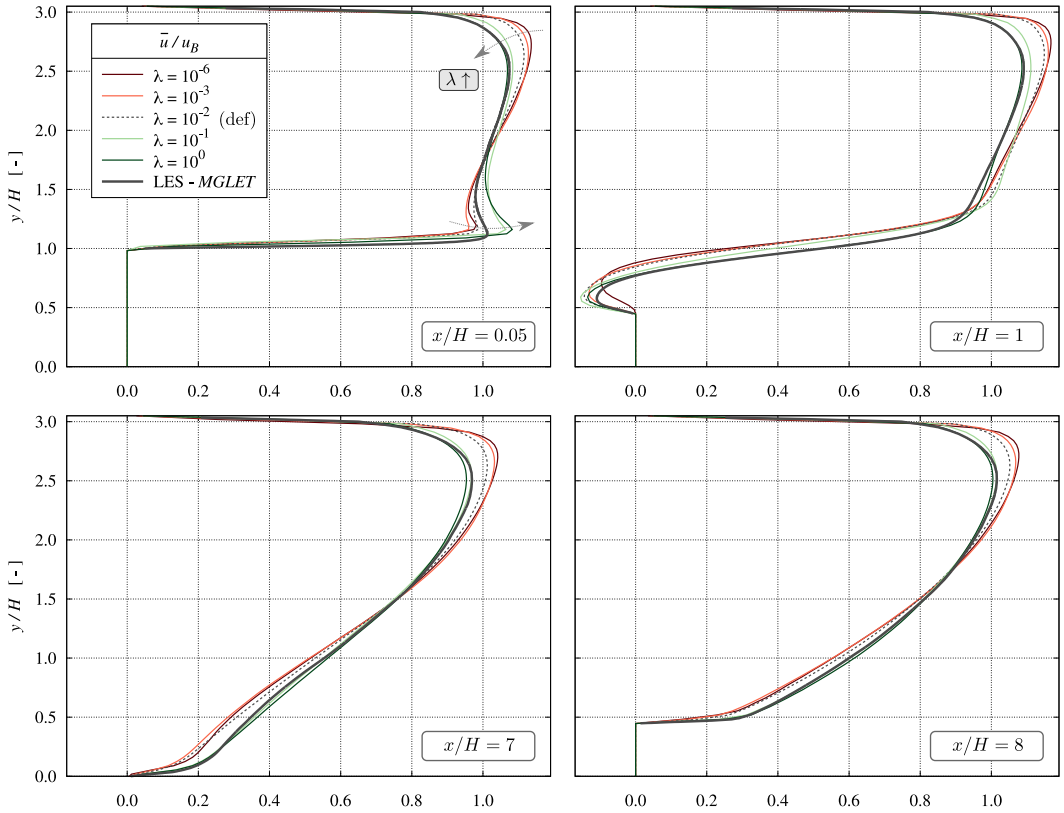

Figure 6.26: C-P vs. *MGLET* LES reference: averaged longitudinal $\overline{u}/u_B$ velocity component predicted with 5 values of the regularization parameter λ depicted at four $x/H = \{0.05; 1; 7; 8\}$ locations for $\mathrm{Re} = 10600$ on the medium grid.

flow field starts to be globally displaced, and the recovery is delayed. The regularization-suppressed flow dynamics are less when increasing the limiter value. The dynamics release significantly improves the agreement with the numerical reference and the $N_H = 56$ results. On the contrary, a decrease of λ restrains the resolved dynamics, thus promoting global displacement toward the top wall. The stability limit for this grid is $\lambda^{10600}_{\mathrm{max},28} = 10^0$.

In order to pursue the previous findings quantitatively, Fig. 6.27 contains plots of the respective L_2 norms for the entire predicted flow field. The left figure reveals a gradually improved agreement of the predicted longitudinal $(\overline{u}/u_B)$ velocity profiles for $\lambda > 10^{-2}$, whereby the unweighted mean integral error [red] is reduced by a factor of four between $\lambda = 10^{-2}$ and $\lambda = 10^0$. The sensitivity decreases for $\lambda > 1.5 \cdot 10^{-1}$ and $L_2 \approx 2.1 \cdot 10^{-2}$ appears as the converged value before exceeding the stability limit. The illustrations feature two colored horizontal lines representing the integral L_2 norms of the coarse [orange] and the fine [green] grid obtained by the default limiter value. A similar trend is observed for the vertical $(\overline{v}/u_B)$ velocity component (right). Hence, the predictive accuracy is substantially governed by the interplay between the λ-value and the spatial resolution, provided that the resolution is not too coarse. Present results indicate a required lattice spacing based (local/cell) Reynolds number of $\mathrm{Re}_{\Delta x} = \mathrm{Re}_B/N_H \leq 750$ or near-wall resolutions of $y^+ \approx 15$.

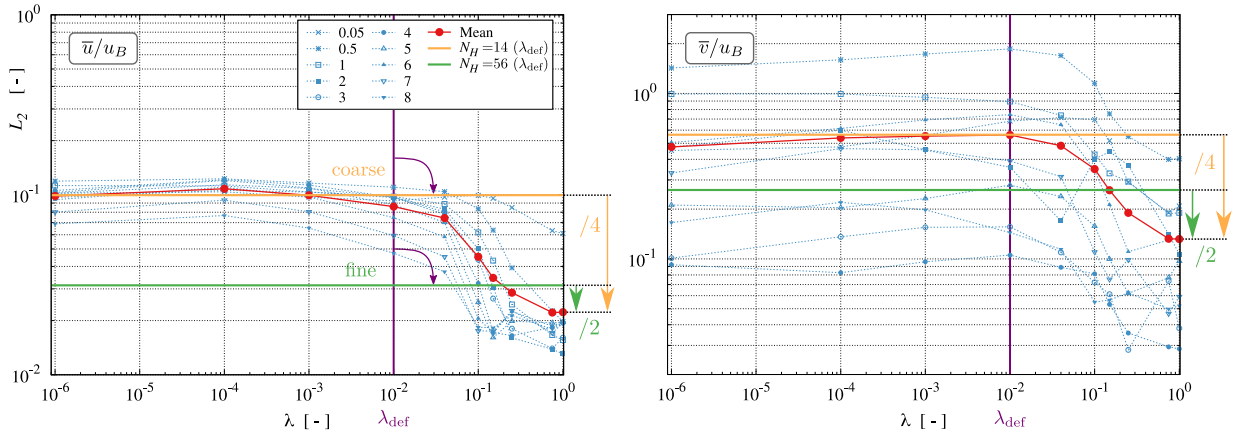

Figure 6.27: Influence of the regularization parameter on the $L_2\{\overline{u}/u_B; \overline{v}/u_B\}$ norm (C-P vs. *MGLET*) using $\lambda = \{10^{-6}, ..., 10^{0}\}$ for Re = 10600 on the medium grid. Horizontal lines indicate the integral L_2 norms employing the default limiter on the coarse [orange] resp. fine [green] grid.

The resolution-regularization interplay is somewhat critical, as outlined by Fig. 6.28 (left), which displays the *PSD* of the lateral velocity (w) component within the accelerated flow (P-4) for a variation of λ on the coarse grid. The unphysical increase of energy in the

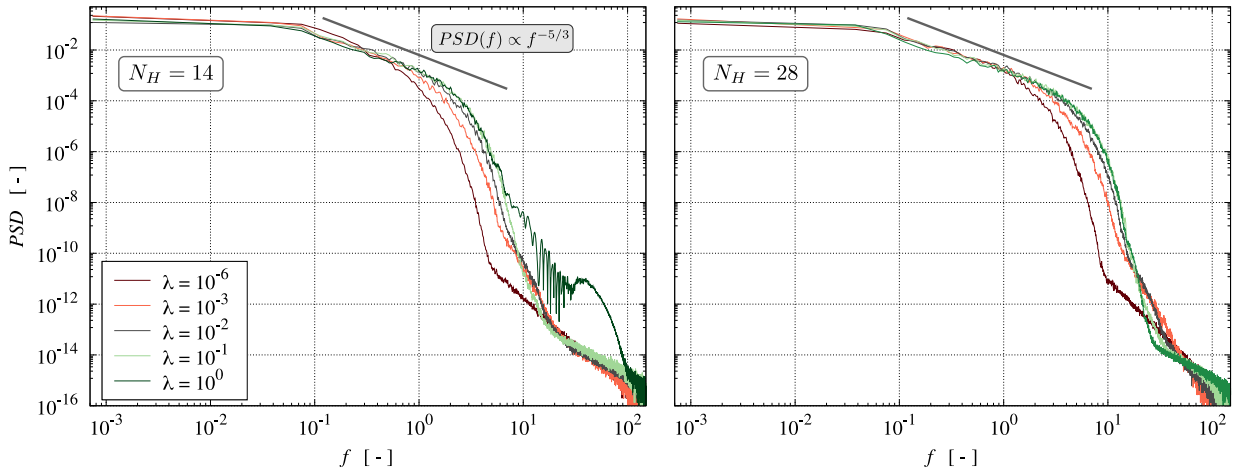

Figure 6.28: Influence of the limiter value λ on the turbulent energy spectra of the lateral (w) component at P-4 (accelerated flow) for Re = 10600 on the coarse (left) and medium (right) grid.

high-frequency regime for $\lambda = 10^0$ [dark green], which refers to the identified optimal value for the medium grid, clearly indicates the limits of an adjustment. Similar to the findings for Re = 2800, the optimal λ-value increases with the resolution and reads $\lambda^{10600}_{opt,56} = 10^{-1}$ and $\lambda^{10600}_{opt,14} = 5 \cdot 10^{-1}$ for the fine and the coarse grid.

Figure 6.29 depicts two longitudinal (u) energy spectra in response to the variation of the regularization parameter $\lambda = \{10^{-6}; 10^{0}\}$ and the resolution $N_H = \{28; 56\}$ at a core (P-2; left) and accelerated (P-4; right) flow location. While the slopes of the inertial and dissipation range depend only marginally on λ and N_H, both parameters clearly influence the width of the inertial range. For a fixed resolution, the λ-dependent widening is more

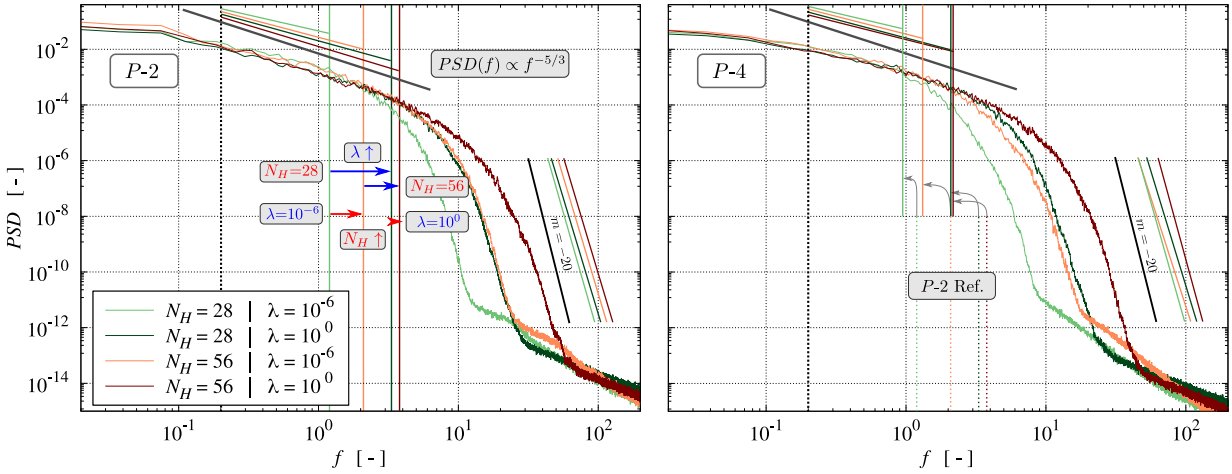

Figure 6.29: Influence of the limiter value $\lambda = \{10^{-6}; 10^{0}\}$ and spatial resolution $N_H = \{28; 56\}$ on *PSD* of the longitudinal (u) component at a core (left) and accelerated (right) flow location for Re = 10600.

pronounced for the coarser grid as indicated by the blue arrows ($\lambda \uparrow$) connecting the $N_H = 28$ [green] and $N_H = 56$ [red] colored verticals. In conjunction with fixed λ-values, the impact of grid refinement ($N_H \uparrow$) is larger [red arrows] for $\lambda = 10^{-6}$ which verifies the strict dependence on N_H identified in the scope of the baseline analysis for the lowest employed limiter value, cf. L_2 norm plots of Fig. 6.15 [dark red]. For $\lambda = 10^{0}$, the extent of the inertial range changes only marginally when increasing the resolution from $N_H = 28$ [dark green] to $N_H = 56$ [dark red]. Nevertheless, the spatial resolution strongly affects the dissipation regime and the width of the equilibrium range. This dependence is also characterized by the enrichment with higher-frequency contributions and shifting the f-kink position within the dissipation range.

Figure 6.30 compares the velocity magnitude ($|\underline{u}|/u_B$) and the (resolved) Reynolds-averaged TKE (k/u_B^2) in the x-y center plane for the optimal and the lowest λ-value on the $N_H = 28$ grid. Subtle but influential differences are evident for the optimal λ-

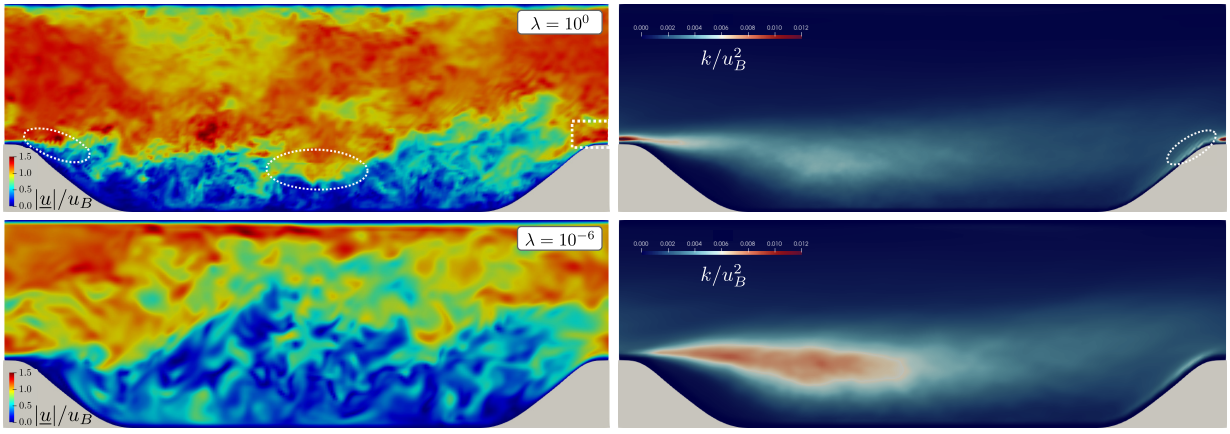

Figure 6.30: Influence of the limiter value $\lambda = \{10^{0}; 10^{-6}\}$ (top; bottom) on the instantaneous velocity magnitude (left) and turbulent kinetic energy (right) in the x-y center plane for Re = 10600 on the medium grid.

value associated with the smallest possible regularized $\omega_{\{3;4;5\}}$ values, cf. white markings in the top row figures. The structures displayed by λ_{opt} are essentially smaller than for $\lambda = 10^{-6}$, and the mixing of low and high momentum fluid close to the reattachment point at $x/H = 4.7$ is enhanced. Also, the separating shear layer is less upward-directed in the inlet region and remains much thinner in the acceleration regime. The strong shearing causes a more pronounced turbulence intensity in the inlet region with an enhanced early mixing in the upstream zone of the separation. However, far less turbulence intensity arises near the (mean) dividing streamline.

Exchanging the default ($\lambda = 10^{-2}$) by the optimal value, i.e., also corresponding to the maximum in this case ($\lambda_{\text{opt}} = \lambda_{\text{max}} = 10^{0}$), significantly improves the predictive performance for $N_H = 28$, as outlined in Fig. 6.31. Results of the turbulence model-free C-P simulation applying λ_{opt} appropriately match the reference LES and experimental data. A substantial change is noticed for the increased λ-value at the $x/H = 0.05$ location,

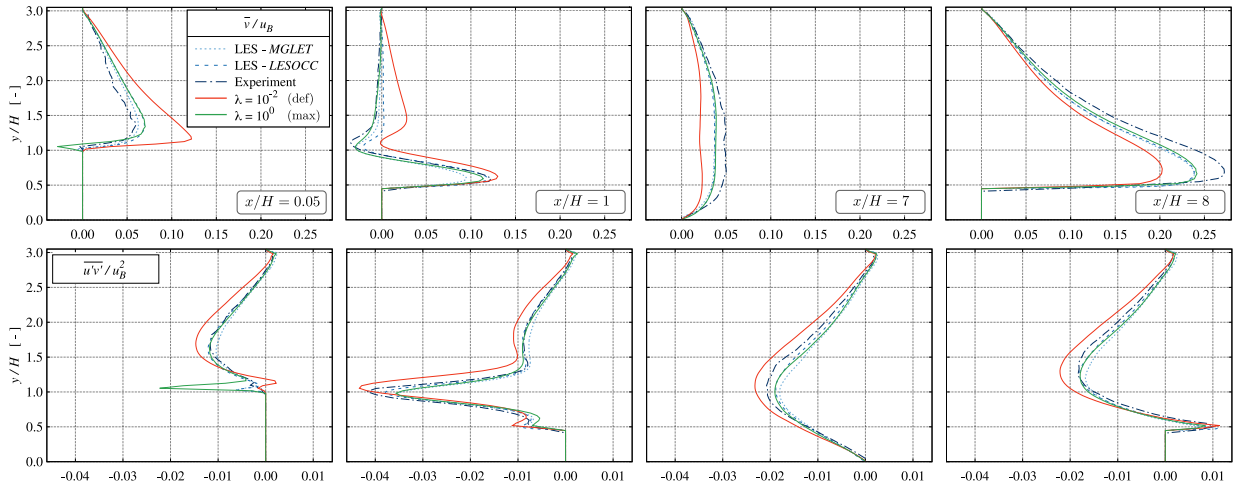

Figure 6.31: C-P vs. *MGLET* & *LESOCC* (both LES) and experimental references: averaged vertical $\overline{v}/u_B$ (top) velocity component and Reynolds shear stress $\overline{u'v'}/u_B^2$ (bottom) predicted with two λ-values (default and maximum) at $x/H = \{0.05; 1; 7; 8\}$ (from left to right) for Re = 10600 on the medium grid ($N_H = 28$).

where the flow is directed downwards and not upwards, in line with LES reference data, and the Reynolds shear stress is no longer changing sign near the bottom wall. A crucial advantage of the C-P model is the direct control through λ without generating further artificial interference, provided that the spatial resolution is adequate, i.e., $y^+ \approx 10 - 15$ matching the lower half of the buffer layer region.

Re = 37000

Figure 6.32 (left) shows the $y^+_{T\,|\,B}$ pathways for the three grids when the Reynolds number is increased to Re = 37000. Only the fine grid is sufficient, and results for the medium and the coarse grid indicate the same resolution-induced failures that were already intensively discussed for Re = 10600 ($N_H = 14$), cf. Fig. 6.32 (right). Brief verifications of the predicted shear stresses by replacing the linear relation through a more realistic wall function, i.e., $u^+(y^+) = 8.4\,(y^+)^{1/7}$, indicate a substantial underprediction of the shear

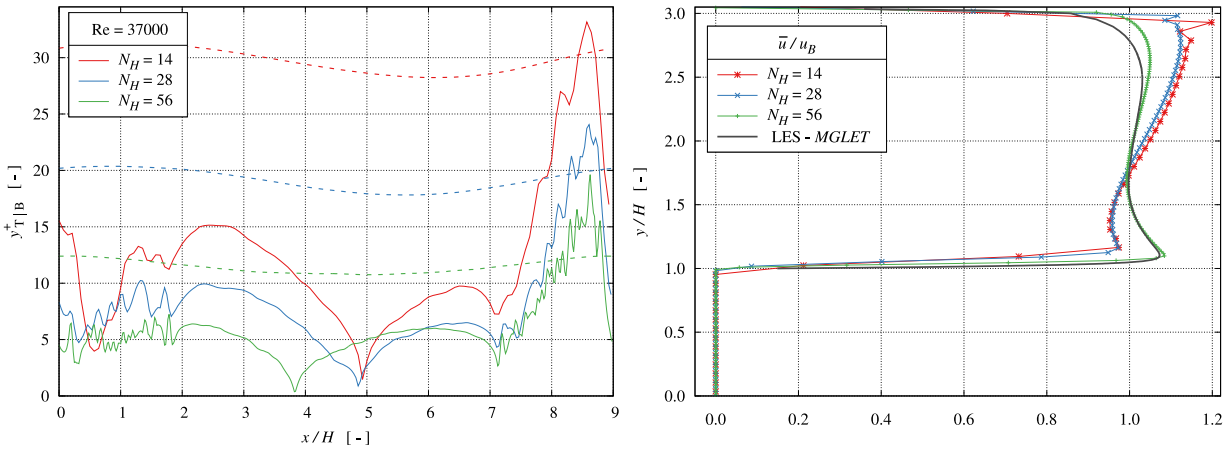

Figure 6.32: Selected diffusive scaling results for Re = 37000: computed nondimensional wall distance $y^+_{T\,|\,B}$ at the bottom [solid] and top [dashed] wall (left) and averaged longitudinal velocity component $\overline{u}/u_B$ extracted at $x/H = 0.05$ (right).

stress by approximately 100[40]% for the coarse[medium] grid. Hence, both meshes are ascertained inadequate for simulating Re = 37000. Due to the coarser resolution for this Reynolds number and the associated lower stability limit, the deviation of the optimal value $\lambda^{37000}_{\text{opt},56} = 5 \cdot 10^{-1}$ from the default is small. Analog to the changes observed for Re = 10600, an increase of λ from the default value to the optimum value results in substantial improvements. Again, predictions of the recovery, acceleration, and near crest regions improve qualitatively and quantitatively. Figure 6.33 compares exemplary longitudinal velocity profiles returned by $\lambda_{\text{def}} = 10^{-2}$ as well as the optimal $\lambda^{37000}_{\text{opt},56}$ with reference LES and experimental data. Overall, the present C-P slightly outperforms the reference LES in combination with the optimal λ-value. Mind that the isotropic LBM grid is about five times larger than the NS grid.

Figure 6.34 motivates the choice of the optimal value from the progression of the integral $L_2(\lambda)$ norms. The latter are approximately reduced by a factor of 2 for the longitudinal velocity and 1.5 for the vertical velocity related to λ_{def}. The green dashed lines indicate the error level obtained for Re = 10600 using the optimal medium grid λ-value, cf. Fig. 6.27, which are close to the fine grid accuracy for Re = 37000 applying the optimal limiter $\lambda^{37000}_{\text{opt},56}$. Mind that the analysis of the spectral convergence might reveal slightly different optimal values.

6.1.3 Synopsis

Finally, a comparative analysis of the four investigated Reynolds numbers is conducted under diffusive and acoustic scaling to condense the results. To this end, Fig. 6.35 depicts the integral L_2 norms of the longitudinal velocity as a function of the Reynolds (left) and Mach number (right). For the acoustic scaling (right), the results refer to the default value $\lambda_{\text{def}} = 10^{-2}$, and medium grid results are omitted to improve the clarity. The acoustic scaling is not intertwined with either Re or N_H influences. The variation of the error level with Ma is very moderate, with the most significant slopes in the range of $m \approx 0.2$.

As regards the diffusive scaling aspects (left), solid lines depict results obtained with the default λ-value, whereas dashed lines refer to results obtained with an optimal choice of λ

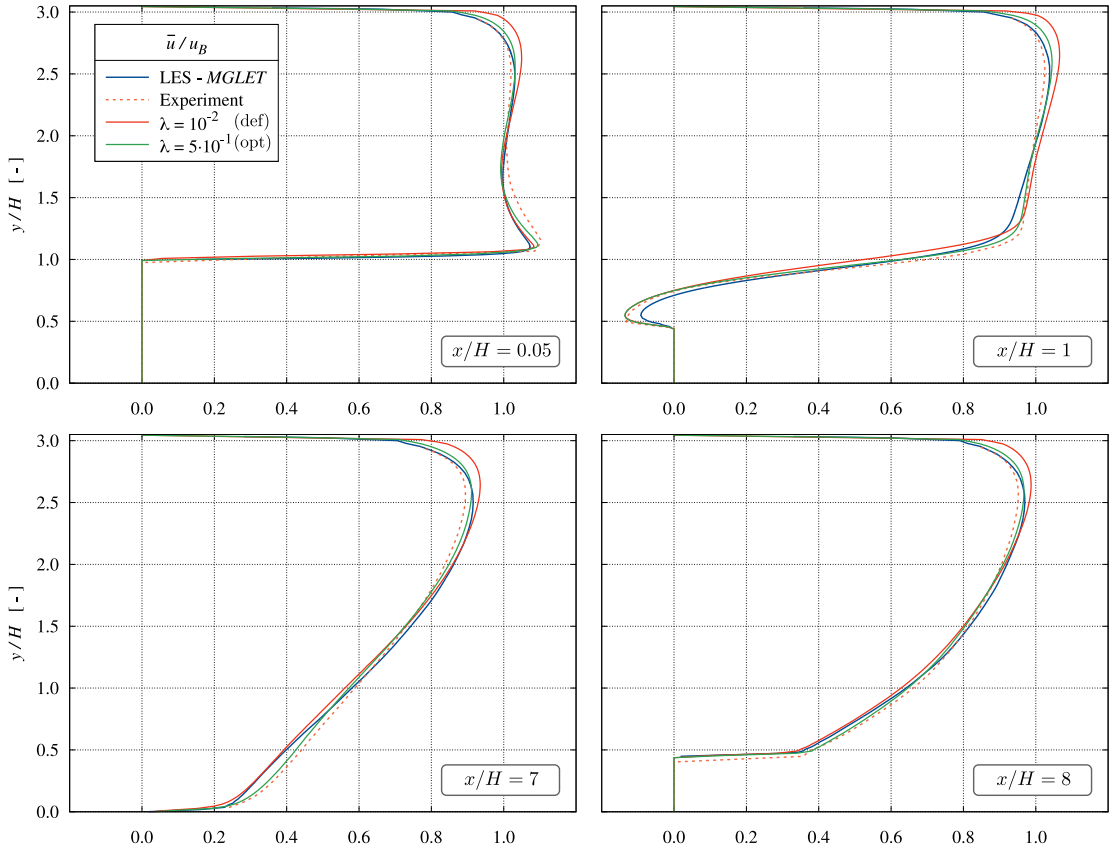

Figure 6.33: C-P vs. *MGLET* LES and experimental references: averaged longitudinal $\overline{u}/u_B$ velocity component predicted with two λ-values (default and optimum) at $x/H = \{0.05; 1; 7; 8\}$ for Re = 37000 on the fine grid ($N_H = 56$).

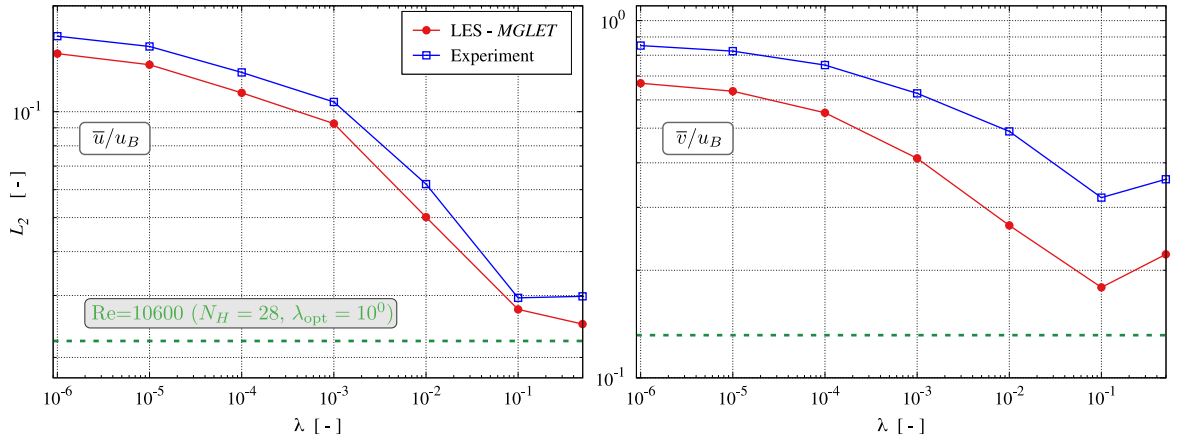

Figure 6.34: Influence of the limiter value $\lambda = \{10^{-6}, \ldots, 5{\cdot}10^{-1}\}$ on the integral $L_2\{\overline{u}/u_B; \overline{v}/u_B\}$ (left; right) norms (C-P vs. *MGLET* LES [red] & Experiment [blue]) for Re = 37000 on the fine grid ($N_H = 56$).

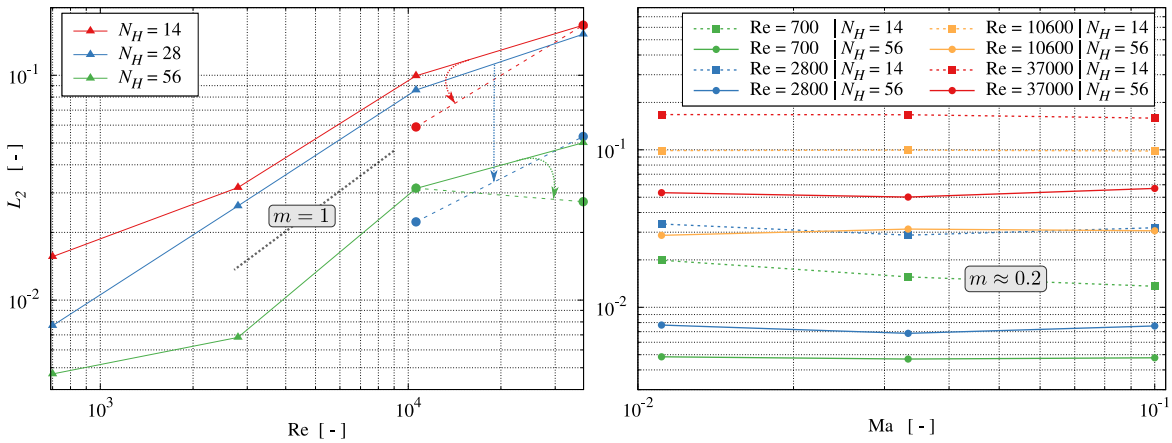

Figure 6.35: Integral $L_2(\overline{u}/u_B)$ error norms (C-P vs. *LESOCC* & *MGLET*) of the longitudinal velocity component $\overline{u}/u_B$ for varying Reynolds numbers: diffusive scaling for the default [solid] and optimal [dashed for Re = $\{10600; 37000\}$, cf. Tab. 6.6] limiter value (left), acoustic scaling on the coarse [dashed] and fine [solid] grid employing $\lambda_{\text{def}} = 10^{-2}$ (right).

for the two higher Reynolds numbers. A pronounced sensitivity to the Reynolds number and, thereby, to the resolution is observed between Re = 2800 and Re = 10600. Both decreasing (Re = 700) and increasing (Re = 37000) the Reynolds number reduces the L_2 slope. The resolution reaches grid convergence for the low Reynolds number regime, and the details of the approach, particularly the influence of the regularization, become less vital. For this reason, results for an optimal choice of λ are only given for the larger Reynolds numbers. For the high Reynolds number, the opportunities of adjusting the regularization diminish in line with the lower stability preserving upper limits of λ, and improvements are only detected for the more stable fine grid.

Figure 6.36 complements the diffusive scaling results of Fig. 6.35 (left) by observing the change of the predictive agreement plotted over the (local) cell Reynolds number $\text{Re}_{\Delta x} = u_B\,\Delta x/\nu$ for the mean axial velocity and turbulent shear stress component. Here, improvements of a change of the regularization parameter become more obvious. Due to the discontinuous overlap of $\text{Re}_{\Delta x}(\text{Re}, N_H)$ of the underlying simulations, cf. Tab. 6.6, the lines are additionally colored by the underlying Reynolds numbers. Table 6.5 offers a summary of the stability limits with respect to the maximum possible value of $\lambda^{\text{Re}}_{\text{max},N_H}$ for the respective Reynolds number and resolution N_H at Ma = 1/30. For Re = 700, all reso-

Table 6.5: Stability limits $\lambda^{\text{Re}}_{\text{max},N_H}$ for Ma = 1/30.

Re	$N_H = 14$	$N_H = 28$	$N_H = 56$
700	10^{6}	10^{6}	10^{6}
2800	10^{3}	10^{6}	10^{6}
10600	10^{0}	10^{0}	10^{1}
37000	10^{-1}	$5 \cdot 10^{-1}$	$5 \cdot 10^{-1}$

lutions feature inherent stability over the entire range of investigated $\lambda \in [10^{-6}, \ldots, 10^{6}]$. Maximum possible values reduce when the Reynolds number increases and the resolution

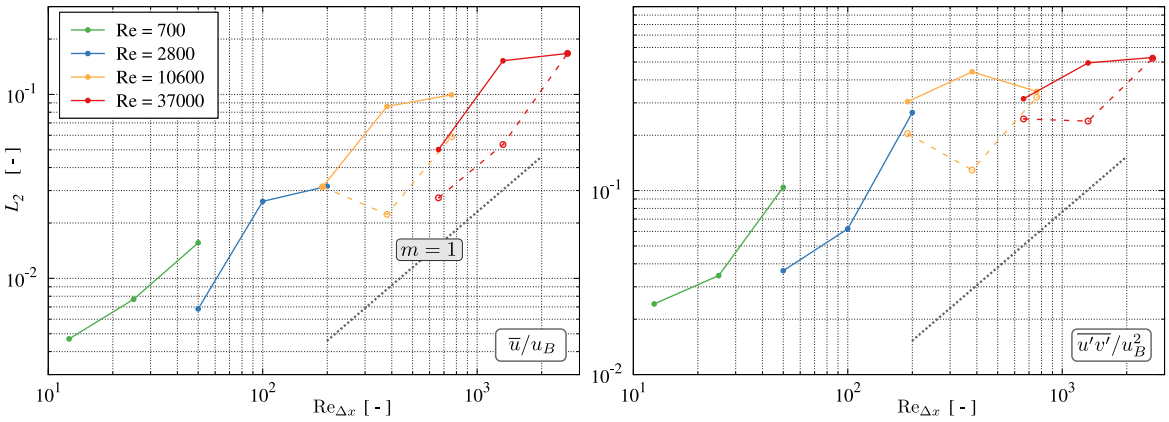

Figure 6.36: Influence of the cell Reynolds number $\mathrm{Re}_{\Delta x} = \mathrm{Re}/N_H = \{12.5, ..., 2640\}$ on the integral $L_2\{\overline{u}/u_B, \overline{u'v'}/u_B^2\}$ (left; right) error norm for the default [solid] and optimal [dashed] limiter values for two selected flow quantities.

decreases. It is emphasized that maximum values do not necessarily coincide with the optima, cf. conclusions below. Additionally, turbulent energy spectra of the v component are illustrated in Fig. 6.37. Each subfigure displays the results of the four different Reynolds numbers for a fixed resolution N_H. Here, the entire frequency range plots correspond to $\lambda_{\mathrm{def}} = 10^{-2}$. In contrast, companion cutouts describe the changes in the dissipation range when increasing the limiter value to the case-specific optimum. For Re = 700, the spectra

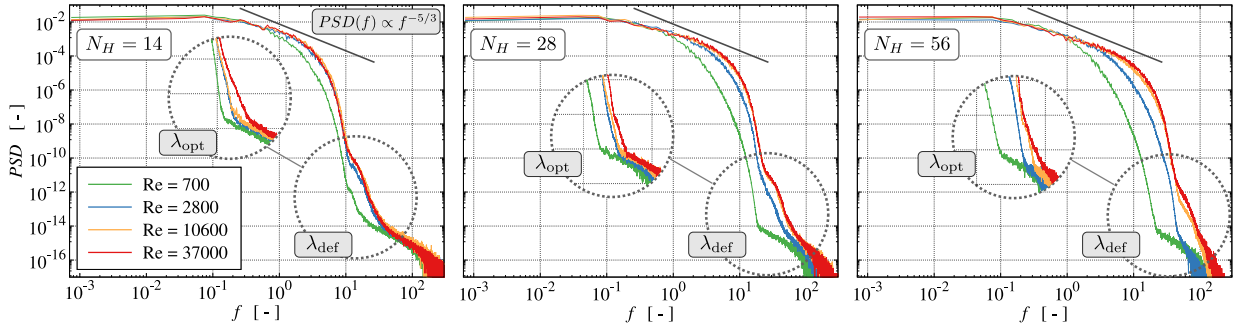

Figure 6.37: Turbulent energy spectra PSD in vertical (v) direction for Re = $\{700; 2800; 10600; 37000\}$ on each grid $N_H = \{14; 28; 56\}$ (left; center; right) at P-2 (core flow) using the default limiter value $\lambda_{\mathrm{def}} = 10^{-2}$. The circled areas display the change of the dissipation range when applying the optimal limiter value λ_{opt}.

are deemed grid- and limiter-converged since a variation of λ does not significantly alter the spectra. In all cases, applying λ_{opt} eliminates the kink associated with the onset of the regularization, which is distinctly seen for Re $\geq$ 2800 using λ_{def}. An indication of the resolution requirements for Re = 37000 is outlined by the almost congruent spectra for Re = 10600 [orange] and Re = 37000 [red] for all grids. Just for the fine grid (right), small extensions of the inertial range are observed when increasing Re.

Conclusions

Based on the reported periodic hill test case results, the C-P model is considered a robust and efficient opportunity to simulate separated turbulent flows without employing a

classical turbulence model. In line with former studies on simple turbulent channel flows, cf. Sec. 5.1 and 5.2, the C-P outperforms previous non-parameterized and C-AO collision operators. Moreover, the regularization ensures a sufficient level of numerical stability. The finding applies for wall-resolved DNS and LES grids up to a spatial resolution of $\Delta x^+ \approx 30$ ($y^+ \approx 15$). The acoustic scaling studies' results reflected a negligible sensitivity to the Mach number in the range of $1/10 \leq \mathrm{Ma} \leq 1/90$ for all tested resolutions and Reynolds numbers.

The seamless blend from DNS to (V)LES is a distinct advantage of the regularized C-P collision model, and the resolution requirements are relatively moderate, as already pointed out by Geier et al. [2017b]. Deducing, the stability preserving regularization can be interpreted as a dynamic turbulence model mainly confined to the upper dissipative frequencies by addressing the higher relaxation rates. The related regularization parameter λ is usually assigned to a constant (heuristic) value with $\lambda_{\mathrm{def}} = 10^{-2}$, and modifications were barely addressed in the literature before. This default value seems conservative, whereas lower λ-values rapidly drive the simulation toward the C-AO approach and hamper the resolution of the flow dynamics. In contrast, results might benefit from increasing the λ-value as the resolution transits from $\Delta x^+ \approx 10$ to coarser $\Delta x^+ \approx 30$ (VLES) resolutions to avoid the damping of intensive turbulence generation in the buffer layer. The risks to impede the stability and robustness of the simulation are moderate for lower Reynolds numbers but increase for higher Reynolds numbers where the stability limits approach $\lambda_{\mathrm{max}} = 10^{-1}$ in the present studies. Given the attainable predictive accuracy, this value seems more appropriate than the default value $\lambda_{\mathrm{def}} = 10^{-2}$. In severely under-resolved conditions, e.g., $\Delta x^+ \geq 30$, the additional use of a conventional (constant Smagorinsky) SGS model may help in parts but was no panacea for the investigated flow.

Complementing the resolution of the near-wall flow regime, the upper thresholds of the regularization parameter λ can be rated by the cell Reynolds number. For the investigated PHF, the bulk velocity relation $\mathrm{Re}_{\Delta x} = u_B \, \Delta x / \nu = \mathrm{Re}/N_H \lesssim 750$ exposed as a viable criterion to run simulations with an increased $\lambda = 10^{-1}$, cf. Tab. 6.6. As outlined in this table, the specific λ maxima decrease from the finest ($\mathrm{Re} = 700$, $N_H = 56$) to the coarsest ($\mathrm{Re} = 37000$, $N_H = 14$) resolution. Unlike λ_{max}, the identified optima are confined to a narrow range $\lambda_{\mathrm{opt}} \in [10^{-1}; 10^{0}]$, where the lower value is an universal good choice. The sixth and seventh columns display the nondimensional wall distances $y^+_{T,\mathrm{av}}(\lambda_\delta)$ along the top wall. Respective deviations from the different choices of λ remain rather small. However, as the resolution deteriorates, the imposed wall boundary condition and the related assumption on the wall shear become the primary source of error beyond $y^+ \geq 15$, as indicated by the square bracketed values obtained from an alternative profile, i.e., $u^+(y^+) = 8.4\,(y^+)^{1/7}$ here. In such cases, the investigated grids (†) featuring $40\,[50] \leq \Delta x^+ \leq 60\,[120]$ are classified as too coarse since any limiter choice does not remedy prevailing upper wall defects. Supplementary, Fig. 6.38 offers a visualization of the tabulated data.

Analyzing the modifications of the relaxation rates $\omega_{\{3;4;5\}}$ due to the influence of the regularization parameter λ, it appears that an alternative regularization approach that automatically restrains a low level of dynamics might refer to relative changes of the parameterized relaxation rates $\omega_{\{3;4;5\}}$ and provides the motivation and starting point for the research outlined in the subsequent Sec. 6.2.1.

Table 6.6: Optimal limiter choice λ_{opt} and classification of the grid types based on the particular y^+ maxima for the investigated parameter space (Re, N_H).

Re	N_H	$\text{Re}_{\Delta x}$	$\lambda_{\max}$	λ_{opt}	$y^+_{T,\text{av}}(\lambda_\delta)$		Grid type
					λ_{def}	λ_{opt}	
700	56	12.5	10^6	no influence	0.5	$\equiv$	DNS
	28	25	10^6	no influence	1.0	$\equiv$	LES
	14	50	10^6	10^{-1}	2.0	$\equiv$	LES
2800	56	50	10^6	10^{-1}	1.6	$\equiv$	LES
	28	100	10^6	10^{-1}	3.2	$\equiv$	LES
	14	200	10^3	10^{-1}	6.3	$\equiv$	LES
10600	56	190	10^1	10^{-1}	4.8	5.0	LES
	28	380	10^0	10^0	8.9	9.7	VLES
	14	760	10^0	$5 \cdot 10^{-1}$	14.5 [16.7]	15.9 [18.3]	VLES limit
37000	56	660	$5 \cdot 10^{-1}$	$5 \cdot 10^{-1}$	11.1	12.4	VLES
	28	1320	$5 \cdot 10^{-1}$	✘	19.0 [26.6]	✘	RANS (†)
	14	2640	10^{-1}	✘	30.5 [61.0]	✘	RANS (†)

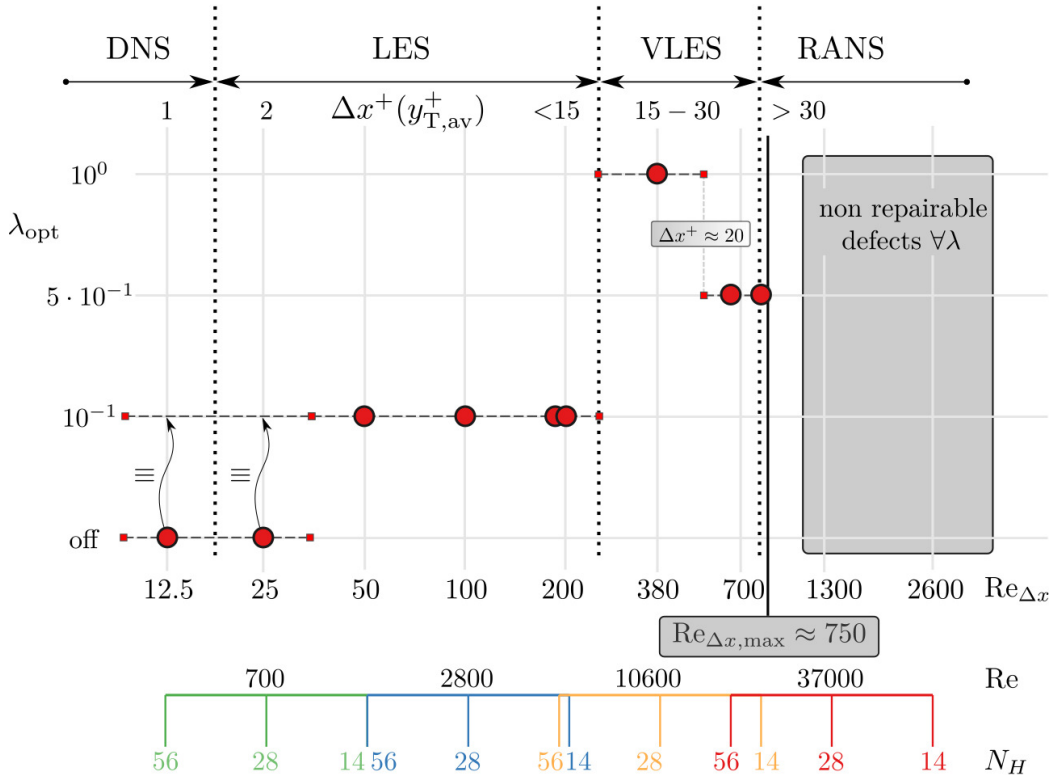

Figure 6.38: Optimal limiter dependency λ_{opt} for varying grid types ranging from DNS to RANS.

6.2 Turbulence Modeling

The outcome of the preceding PHF study motivated research on a generalization of the regularization ansatz. To this end, a resolution-sensitive formulation of the limiter is presented in Sec. 6.2.1, which exclusively addresses the dissipative high-wave number/frequency scales and neither affects the production nor the inertial range. For enabling simulations on distinctly under-resolved grids, the second development refers to an explicit local, dynamic, cumulant-based SGS model outlined in Sec. 6.2.2, additionally acting on the (lower) inertial regime of the spectrum.

6.2.1 Limiter Adjustment

As indicated by (3.66), the ω value approaches 2 in the low-viscosity (high Reynolds) number limit and thereby yields vanishing third-order rates $\omega_{\{3;4;5\}} \to 0$ resulting from (3.103) to (3.105). Negligibly small relaxation rate values virtually imply retaining the pre-collision cumulant states during the collision, which in turn hampers the numerical stability. To regularize the third-order relaxation rates in the limit $\omega_{\{3;4;5\}} \to 0$, Geier et al. [2017a] suggested a regularization, also labeled limiter, of the parameterization via (3.111) to (3.114) through

$$\tilde{\omega}_{\{3;4;5\},\epsilon} = \omega_{\{3;4;5\}} + \frac{\mathbf{C}_\epsilon(1-\omega_{\{3;4;5\}})}{\mathbf{C}_\epsilon + (\rho\lambda)} = \frac{\mathbf{C}_\epsilon + (\rho\lambda)\omega_{\{3;4;5\}}}{\mathbf{C}_\epsilon + (\rho\lambda)}\,. \tag{6.1}$$

Here, $\mathbf{C}_\epsilon$ refers to a positive third-order cumulant related expression, e.g., $|C_{120}-C_{102}|$, and ρ is a normalized density close to unity. The suffix ϵ points toward different transformation parts that employ the regularized rates using different cumulant expressions $\mathbf{C}_\epsilon$ as outlined below.

The regularization (6.1) is controlled by a positive parameter λ. The respective limit states yield $\lim_{\lambda\to\infty}\tilde{\omega}_{\{3;4;5\},\epsilon} = \omega_{\{3;4;5\}}$ and $\lim_{\lambda\to 0}\tilde{\omega}_{\{3;4;5\},\epsilon} = 1$. The regularization parameter is usually assigned to a heuristic, empirical constant value ($\lambda = 10^{-2}$) which follows from typical values of $\mathbf{C}_\epsilon$ and $\omega_{\{3;4;5\}}$. The regularization (6.1) greatly supports the robustness of the WP model. For example, Geier et al. [2017b] computed a sphere at a very high Reynolds number without a turbulence model, and the present PHF simulations are inherently stable without employing an explicit turbulence model even for coarse discretizations up to $\Delta x^+ \approx 100$, cf. Sec. 6.1. However, the study in Sec. 6.1 also revealed that the predictive accuracy could significantly improve from an increase of λ when the resolution is in a typical LES-regime within $10 \leq \Delta x^+ \leq 50$.

Analyzing the regularization (6.1) for attached and separated engineering shear flows at different resolutions reveals generally small values of $\mathbf{C}_\epsilon \approx 10^{-3} << \rho\lambda$ and motivates to estimate $\tilde{\omega}_{\{3;4;5\},\epsilon} \approx \omega_{\{3;4;5\}} + \mathbf{C}_\epsilon/(\rho\lambda)$. Moreover, typical relaxation rate values read $\omega_{\{3;4;5\}} \approx \mathcal{O}(10^{-3}) - \mathcal{O}(10^{-2})$. This indicates that subtle additions of $\omega_{\{3;4;5\}}$ in the order of $\mathbf{C}_\epsilon/(\rho\lambda) \approx 0.1$ can have a distinct influence, and motivates suggesting an increase of λ to reduce $\mathbf{C}_\epsilon/(\rho\lambda)$ and attenuate the shift of $\tilde{\omega}_{\{3;4;5\},\epsilon}$ toward equilibrium restoring unit values. A more rigorous analysis starts by recalling that the viscosity-related relaxation rate approaches a value of $\omega = 2$ in the high-Reynolds number limit of (3.66). With a focus on turbulent flows, therefore $\omega \approx 2 - \epsilon$ is assumed, where ϵ is a small positive number. Introducing this approximation into the parameterization (3.103) to (3.105) and

a linearization of the resulting expressions for small ϵ values, gives

$$\lim_{\epsilon\to 0}\,\omega_3 = \frac{40\epsilon}{14\epsilon+8} \approx 5(2-\omega)\,, \tag{6.2}$$

$$\lim_{\epsilon\to 0}\,\omega_4 = \frac{-8\epsilon}{14\epsilon-8} \approx (2-\omega)\,, \tag{6.3}$$

$$\lim_{\epsilon\to 0}\,\omega_5 = \frac{96\epsilon}{20\epsilon+64} \approx 1.5\,(2-\omega)\,. \tag{6.4}$$

A resolution-aware description of the high-Reynolds number limit of ω could employ the approximations (6.2) to (6.4) to derive a resolution-sensitive regularization of $\omega_{\{3;4;5\}}$. The latter is obtained from a simple analysis of the expression (3.66) by introducing the cell Reynolds number as a measure for the resolution, cf. (3.58), which gives $\nu = u_B/\mathrm{Re}_{\Delta x}$, and with $u_B = \mathrm{Ma}/\sqrt{3}$ follows

$$\begin{aligned}
\omega &= \left(\frac{2}{6\frac{u_B}{\mathrm{Re}_{\Delta x}}+1}\right) = \frac{2\mathrm{Re}_{\Delta x}}{2\sqrt{3}\mathrm{Ma}+\mathrm{Re}_{\Delta x}} \\
&= \frac{2\mathrm{Re}_{\Delta x}+4\sqrt{3}\mathrm{Ma}-4\sqrt{3}\mathrm{Ma}}{2\sqrt{3}\mathrm{Ma}+\mathrm{Re}_{\Delta x}} = \frac{2\left(2\sqrt{3}\mathrm{Ma}+\mathrm{Re}_{\Delta x}\right)-4\sqrt{3}\mathrm{Ma}}{2\sqrt{3}\mathrm{Ma}+\mathrm{Re}_{\Delta x}} \\
&= 2-\frac{4\sqrt{3}\mathrm{Ma}}{2\sqrt{3}\mathrm{Ma}+\mathrm{Re}_{\Delta x}} \approx 2-\beta\frac{\mathrm{Ma}}{\mathrm{Re}_{\Delta x}}\,.
\end{aligned} \tag{6.5}$$

Mind that β is of the order $\mathcal{O}(10^0)$ but can vary slightly, depending on the velocities that are employed to define the Mach and the Reynolds number, as the Mach number is usually compiled from an augmented, i.e., expected maximum, velocity value. Combining (6.2) to (6.4) with (6.5) the proportionalities

$$2-\omega_1 \sim \lim_{\varepsilon\to 0}\omega_{\{3;4;5\}} \sim \frac{\mathrm{Ma}}{\mathrm{Re}_{\Delta x}} \tag{6.6}$$

are obtained. This motivates to formulate a regularization

$$\tilde{\omega}_{\{3;4;5\}} \sim \omega_{\{3;4;5\}}\left[1+\ldots\left(\frac{\mathrm{Re}_{\Delta x}}{\mathrm{Ma}}\right)\right] \tag{6.7}$$

of the parameterized rates (3.103) to (3.105), that does not vanish in the high-Reynolds number limit. The suggested regularization employs the same cumulant expressions $\mathbf{C}_\epsilon$ as Geier et al. [2017a] to address the individual characteristics of the regularized expression, e.g., $\mathbf{C}_{3,1} = |C_{120}+C_{102}|$ et cetera, yielding

$$\tilde{\omega}_{3,1} = \omega_3\left(1+\mathcal{C}_\omega|C_{120}+C_{102}|\right)\,, \tag{6.8}$$

$$\tilde{\omega}_{4,1} = \omega_4\left(1+\mathcal{C}_\omega|C_{120}-C_{102}|\right)\,, \tag{6.9}$$

$$\tilde{\omega}_{3,2} = \omega_3\left(1+\mathcal{C}_\omega|C_{210}+C_{012}|\right)\,, \tag{6.10}$$

$$\tilde{\omega}_{4,2} = \omega_4\left(1+\mathcal{C}_\omega|C_{210}-C_{012}|\right)\,, \tag{6.11}$$

$$\tilde{\omega}_{3,3} = \omega_3\left(1+\mathcal{C}_\omega|C_{201}+C_{021}|\right)\,, \tag{6.12}$$

$$\tilde{\omega}_{4,3} = \omega_4\left(1+\mathcal{C}_\omega|C_{201}-C_{021}|\right)\,, \tag{6.13}$$

$$\tilde{\omega}_5 = \omega_5\left(1+\mathcal{C}_\omega|C_{111}|\right)\,. \tag{6.14}$$

Mind that the cumulant expressions $\mathbf{C}_\epsilon$ vanish in the low-Reynolds number, i.e., fully-resolved, limit. The resolution-sensitive regularization parameter is assigned to

$$\mathcal{C}_\omega = \mathrm{Re}_{\Delta x}/(10\,\mathrm{Ma}), \tag{6.15}$$

which matches the order of magnitude of $\mathrm{Re}_{\Delta x}/(4\sqrt{3}\,\mathrm{Ma})$ occurring in (6.5).

To further judge the regularization, a few aspects of the cumulant expressions $\mathbf{C}_\epsilon$ are essential:

(1) the different expressions are of similar characteristics and order of magnitude,

(2) they are sensitive to the strain rate and increase with the strain rate value,

(3) they scale approximately linearly with the Mach number and vanish when the grid is refined.

Figure 6.39 outlines the Mach number dependency for an exemplary cumulant expression, here $C_\epsilon = |C_{210}+C_{012}|$. The figure refers to turbulent channel flow simulations at $\mathrm{Re}_\tau = 180$

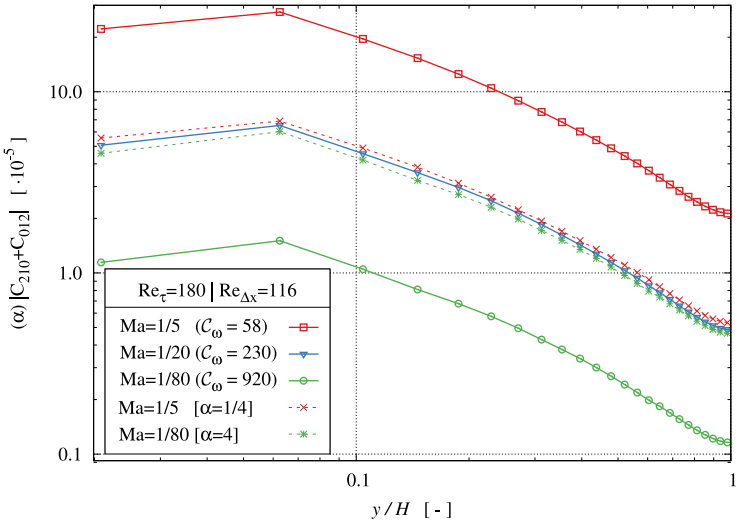

Figure 6.39: Mach number dependency of the exemplary cumulant expression $|C_{210} + C_{012}|$ assessed by a TCF simulation at $\mathrm{Re}_\tau = 180$. Displayed abscissa values range from the wall ($y/H = 0$) to the centerline ($y/H = 1$). All simulations were performed without explicit turbulence modeling and refer to a fixed spatial resolution ($\Delta x^+ = 7.5$, $\mathrm{Re}_{\Delta x} = 116$) in combination with three different Mach numbers $\mathrm{Ma} = \{1/5\,[\mathrm{red}]; 1/20\,[\mathrm{blue}]; 1/80\,[\mathrm{green}]\}$. Dashed lines represent expressions for $\mathrm{Ma} = \{1/5; 1/80\}$ scaled with $\alpha = 1/(20\mathrm{Ma})$.

and reveals a virtually linear increase of $|C_{210} + C_{012}|$ with the employed Mach number, which secures $\mathcal{C}_\omega\,\mathbf{C}_\epsilon \sim \mathrm{Re}_{\Delta x}$. Mind that displayed results refer to a fairly well-resolved case with $\Delta x^+ = 7.5$, where no additional eddy viscosity is required.

6.2.2 Dynamic Cumulant-Based Subgrid Scale Model

When attention is directed to coarse grid simulations, e.g., resolutions beyond $\Delta x^+ \geq 50$, the predictive capabilities of the regularized C-P model reach their limits in simulating

engineering shear flows. The regularization acts upon higher-order, i.e., third-order, cumulant expressions. As demonstrated in the previous Sec. 6.1, it addresses a fairly confined frequency range in the dissipation regime and does not affect the energy-containing and lower inertial ranges. Hence, an additional model is required to mimic the unresolved turbulent scales not addressed by the regularization.

To this end, the definition of a dynamic Smagorinsky parameter $\mathcal{C}_{\mathrm{S}}$ based on cumulant expressions is targeted. The calligraphic notation serves as a distinction from the standard constant Smagorinsky coefficient C_S, cf. (2.53). Typical values approximately fall within the range $C_S \in [0.1, 0.2]$, where constant values are frequently assigned to the lower bound, i.e., $C_S = 0.1$ or slightly higher in the context of LBM, e.g., cf. Haussmann et al. [2019, 2020], Gaedtke et al. [2020] or Han et al. [2021a]. Employing an analogue ansatz as described in Sec. 6.2.1, viz.

$$\mathcal{C}_{\mathrm{S}} = \mathcal{C}_{\mathrm{LES}} |C_{210} + C_{012}| \,, \tag{6.16}$$

is assumed. Mind that the characteristics of the various cumulant expressions $\mathbf{C}_\epsilon$ employed in equations (6.8) to (6.14) are fairly similar. Hence, the selection of $|C_{210}+C_{012}|$ is deemed uncritical, and other choices would only require readjusting $\mathcal{C}_{\mathrm{LES}}$ along the route outlined in the remainder. The task is to model $\mathcal{C}_{\mathrm{LES}}$, where a resolution-dependent formulation is sought, i.e., $\mathcal{C}_{\mathrm{LES}} = f(\mathrm{Ma}, \mathrm{Re}_{\Delta x})$.

For this purpose, initially the interplay between $\mathcal{C}_{\mathrm{LES}}$, $|C_{210}+C_{012}|$ and the Mach number is assessed. Motivated by results of the regularization study displayed in Fig. 6.39, again $\mathcal{C}_{\mathrm{LES}} \sim 1/\mathrm{Ma}$ is imposed to avoid undesired temporal resolution influences on $\mathcal{C}_{\mathrm{S}}$. A first heuristic closure that does not consider the spatial resolution reads

$$\mathcal{C}_{\mathrm{LES}} = 20/\mathrm{Ma} \,. \tag{6.17}$$

The latter was obtained from a large amount of TCF and PHF studies to provide an orientation for an upper value of $\mathcal{C}_{\mathrm{LES}}$, and yields parameter values in the desired range $\mathcal{C}_{\mathrm{S}} \in [0.05, 0.2]$ as exemplified in Fig. 6.40 (right), which shows time-averaged contour plots for the flow over a periodic hill for two different (bulk) Reynolds numbers. Instantaneous data for $\mathcal{C}_{\mathrm{S}}$ are supplemented on the left side of this figure to demonstrate the dynamic structure depicting capabilities of the chosen ansatz (6.16).

Computations reveal resolution-dependent time-averaged maximal values in the range of $0.09\,(\Delta x^+ \approx 3, \mathrm{Re}_{\Delta x} = 50) \leq \mathcal{C}_{\mathrm{S}} \leq 0.2\,(\Delta x^+ \approx 30, \mathrm{Re}_{\Delta x} = 750)$. It is interesting to note that, unlike many dynamic SGS approaches for Navier-Stokes simulations, e.g., cf. Germano et al. [1991] or Ghosal et al. [1995], no spatial or temporal averaging of computed $\mathcal{C}_{\mathrm{S}}$-value is required to stabilize the simulations for the present cumulant-based dynamic SGS approach, which is deemed highly beneficial for practical applications.

Figure 6.41 illustrates results obtained for a TCF at $\mathrm{Re}_\tau = 550$, which serves as a reference case for the resolution-dependent formulation of $\mathcal{C}_{\mathrm{LES}}$ explained below. Displayed results refer to $H/\Lambda_x = 24\,[= N_H]$ grid points across the half channel height H which yields $\Delta x^+ = 23$ and $\mathrm{Re}_{\Delta x} = 415$. The depicted comparison involves three different Mach numbers, i.e., $\mathrm{Ma} = \{1/5; 1/20; 1/80\}$, and employs the regularization defined through (6.15). Specifically, Fig. 6.41 (left) focuses upon the variation of $|C_{210} + C_{012}|$ with Ma for a fixed value of $\mathcal{C}_{\mathrm{LES}} = 400$ which reveals $|C_{210} + C_{012}| \sim \mathrm{Ma}$. The illustrated study of Fig. 6.41 (right) employed $\mathcal{C}_{\mathrm{LES}} = 20/\mathrm{Ma} = \{100; 400; 1600\}$ to assess the variation of the eddy viscosity with Ma and $|C_{210} + C_{012}|$. It is emphasized that the eddy viscosity only

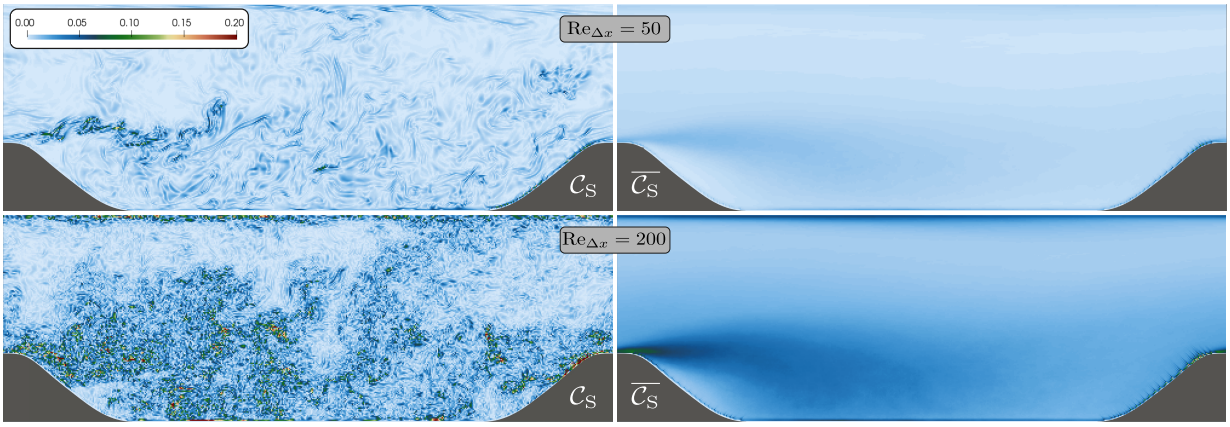

Figure 6.40: Instantaneous (left) and time-averaged (right) contours of the dynamic Smagorinsky parameter $\mathcal{C}_\mathrm{S} = 20|C_{210} + C_{012}|/\mathrm{Ma}$ obtained for a periodic hill flow at $\mathrm{Re}_{\Delta x} = 50$ [$\mathrm{Re}_B = 2800$, top] and $\mathrm{Re}_{\Delta x} = 200$ [$\mathrm{Re}_B = 10600$, bottom] using $\mathrm{Ma} = 1/10$ with $\mathcal{C}_\omega = \{50; 200\}$ from (6.15).

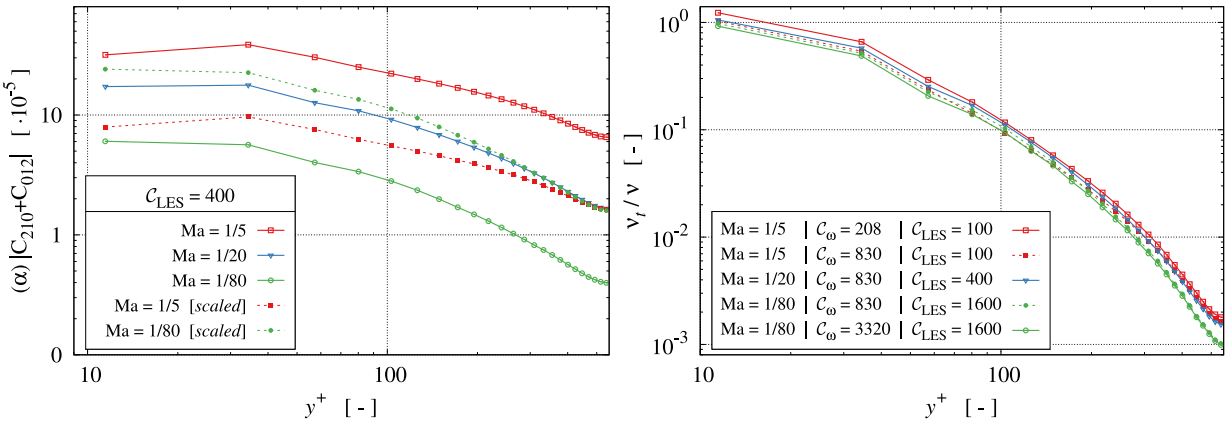

Figure 6.41: Turbulent channel flow simulations at $\mathrm{Re}_\tau = 550$ resolved with $\Delta x^+ = 23$ ($\mathrm{Re}_{\Delta x} = 415$): Mach number influence on the cumulant expression $|C_{210} + C_{012}|$ using $\mathcal{C}_\mathrm{LES} = 400$ (left; dashed line data scaled by Ma) and computed eddy viscosities (right) obtained with a $\mathcal{C}_\mathrm{LES} = 20/\mathrm{Ma}$.

reaches a peak value of $\nu_t/\nu \approx 1$ at the wall nearest location of $y^+ \approx 12$ on the displayed high Reynolds number grid, but vanishes on low Reynolds number grids for $y^+ \to 0$ due to the vanishing cumulant expression $|C_{210} + C_{012}|$, see also Fig. 6.52.

Figure 6.41 (right) indicates $|C_{210} + C_{012}| \sim \mathrm{Ma}$ due to $\nu_t/\nu \sim \mathcal{C}_\mathrm{LES}\,|C_{210} + C_{012}| \approx$ constant for $\mathcal{C}_\mathrm{LES} \sim 1/\mathrm{Ma}$ and, thus, that the time-averaged cumulant expression $|C_{210} + C_{012}|$ approximately scales with $\mathcal{C}_\mathrm{LES}^{-1}$. Moreover, the influence of the regularization parameter $\mathcal{C}_\omega$ on the cumulant expression diminishes when the eddy viscosity is active, even for the low eddy viscosity levels experienced in this case. This observation is confirmed by supplementary data using a fixed regularization value of $\mathcal{C}_\omega = 830$ added to the right graph of Fig. 6.41, and might support the scale-separation arguments between regularizing the high-frequency dissipation regime and turbulence modeling in the inertial regime.

Similar to the formulation of the regularization parameter $\mathcal{C}_\omega$ via (6.15), an influence of $\mathrm{Re}_{\Delta x}$ is also sought for the dynamic Smagorinsky parameter $\mathcal{C}_\mathrm{S}$, which should ideally vanish

for $\mathrm{Re}_{\Delta x} \to 0$. To this end, the spatial resolution dependent behavior of $|C_{210} + C_{012}|$ is analyzed in consideration of $\mathcal{C}_{\mathrm{LES}}$ reciprocally scaling with $|C_{210} + C_{012}|$. On this, Fig. 6.42 displays time-averaged results obtained for the turbulent channel flow at $\mathrm{Re}_\tau = 550$ and $\mathrm{Ma} = 1/10$. The displayed data is compiled for a wide range of resolutions, which reach

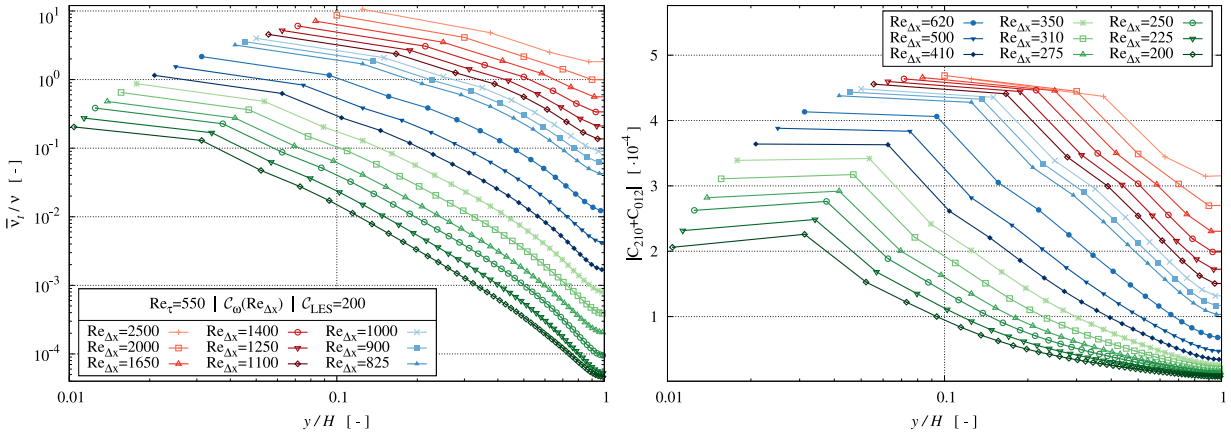

Figure 6.42: Turbulent channel flow simulations at $\mathrm{Re}_\tau = 550$ and $\mathrm{Ma} = 1/10$: Grid resolution sensitivity of the time-averaged eddy viscosity (left) and the cumulant expression $|C_{210} + C_{012}|$ (right) using a range of resolutions from $H/\Lambda_x = 4$ to $H/\Lambda_x = 48$. Computations refer to $\mathcal{C}_{\mathrm{S}} = 20\,|C_{210} + C_{012}|/\mathrm{Ma}$ and $\mathcal{C}_\omega = \mathrm{Re}_{\Delta x}/(10\,\mathrm{Ma})$.

from $H/\Delta x = 4$ lattice nodes ($\mathrm{Re}_{\Delta x} \approx 2500$, $\Delta x^+ \approx 140$) to $H/\Delta x = 48$ nodes ($\mathrm{Re}_{\Delta x} \approx 200$, $\Delta x^+ \approx 11$). A total of 18 resolutions were investigated, including nine coarse grids with 4 to 12 nodes, three medium grids with 16 to 24 nodes, and six finer grids with 28 to 48 nodes along with the half-channel height, respectively. Coarse grids are incremented by one node, whereas medium and fine grids are incremented by four nodes. Results were obtained from the regularization (6.15) and the heuristic initial guess $\mathcal{C}_{\mathrm{LES}} = 20/\mathrm{Ma} = 200$.

As depicted by the right graph of Fig. 6.42, the cumulant expression substantially decreases when the resolution improves, particularly in the low-shear regime near the centerline, which serves as a reference location. Furthermore, a saturation of the $|C_{210} + C_{012}|$ increase is depicted for gradually coarsened grids, and the difference between near-wall and centerline values of $|C_{210} + C_{012}|$ slightly decreases. The normalized eddy viscosity behaves similarly. However, the value range between the near-wall and the centerline locations spans several orders of magnitude for the fine grids.

Aiming to estimate of the scaling of $|C_{210} + C_{012}|$ with the local cell Reynolds number $\mathrm{Re}_{\Delta x}$, again the results of the 18 resolutions for $\mathrm{Re}_\tau = 550$ are consulted. Figure 6.43 (right) depicts the results of a regression analysis which reveals $|C_{210} + C_{012}| \sim \mathrm{Re}_{\Delta x}^{-0.65}$.

The respective left graph shows scaled data already displayed in Fig. 6.42 (right), and demonstrates a fairly reasonable agreement of the scaled (near) centerline cumulant expressions. Due to the reciprocal behavior of $\mathcal{C}_{\mathrm{LES}}$ and $|C_{210} + C_{012}|$ the assumption $\mathcal{C}_{\mathrm{LES}} \sim \sqrt{\mathrm{Re}_{\Delta x}}/\mathrm{Ma}$ is deduced that employs a slightly downscaled exponent of 0.5 instead of 0.65 to counteract unfavorable lower deviations from the underlying value of 20/Ma on the finer grids. In summary, the LES parameterization reads

$$\mathcal{C}_{\mathrm{LES}} = 0.35\,\frac{\sqrt{\mathrm{Re}_{\Delta x}}}{\mathrm{Ma}}\,, \tag{6.18}$$

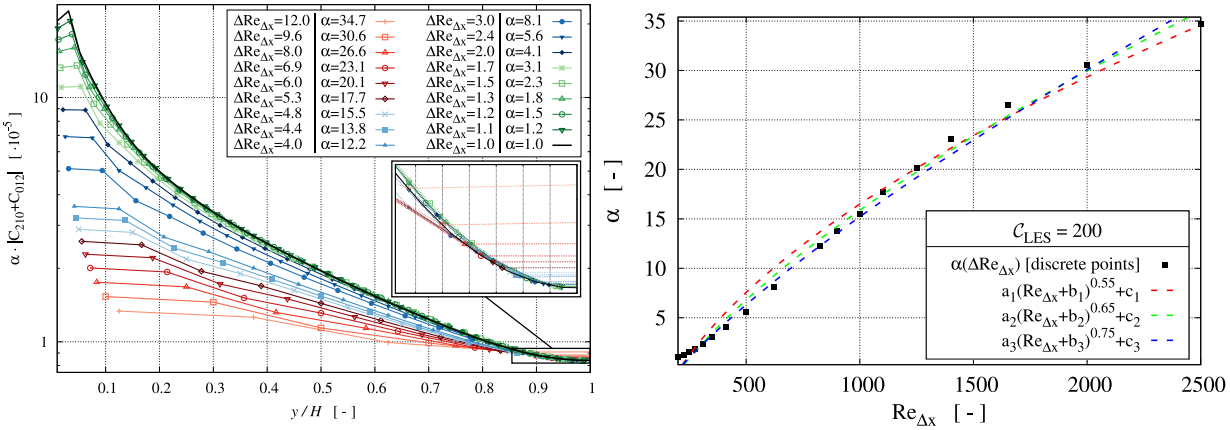

Figure 6.43: Turbulent channel flow simulations at $\mathrm{Re}_\tau = 550$, $\mathrm{Ma} = 1/10$ with $\mathcal{C}_{\mathrm{LES}} = 20/\mathrm{Ma}$ and $\mathcal{C}_\omega = \mathrm{Re}_{\Delta x}/(10\mathrm{Ma})$: Resolution-dependent scaling of the time-averaged cumulant expression $\alpha|C_{210}+C_{012}|$ (left) using a range of resolutions from $H/\Lambda_x = 4$ to $H/\Lambda_x = 48$. The right graph depicts the evolution of the scaling factor α with the cell Reynolds number $\mathrm{Re}_{\Delta x}$, where $a_{\{1;2;3\}} = \{0.61; 0.28; 0.12\}$, $b_{\{1;2;3\}} = -\{50; 40; 30\}$ and $c_{\{1;2;3\}} = -\{10; 8; 6\}$.

where the empirical parameter 0.35 follows from matching the initial guess (6.17) for very coarse resolutions, i.e., $\Delta x^+ \approx 170$ or $\mathrm{Re}_{\Delta x} \approx 3500$ from which follows $20 \approx 0.35\sqrt{\mathrm{Re}_{\Delta x}}$. The dependency (6.18) was verified with studies for $\mathrm{Re}_\tau = 550$ for a moderate ($N_H = 22$, $\mathrm{Re}_{\Delta x} = 500$) and a very coarse ($N_H = 4$, $\mathrm{Re}_{\Delta x} = 2500$) resolution. Investigations of the present study are limited to $\mathrm{Re}_{\Delta x} \leq 10800$, yielding a maximum of $\mathcal{C}_{\mathrm{LES}} = 36.4/\mathrm{Ma}$. One might thus also limit the numerator of (6.18), e.g., in line with the first approach $\mathcal{C}_{\mathrm{LES}} = 20/\mathrm{Ma}$ employing

$$\mathcal{C}_{\mathrm{LES}} = \min(20, 0.35\sqrt{\mathrm{Re}_{\Delta x}})/\mathrm{Ma}\,. \tag{6.19}$$

Suggested Turbulence Model

The suggested cumulant collision model development employs the C-P parameterization of the third-order relaxation rates (3.103) to (3.105) as per Geier et al. [2017a]. The parameterization is regularized using (6.8) to (6.14) together with the proposed resolution-sensitive regularization parameter $\mathcal{C}_\omega = \mathrm{Re}_{\Delta x}/(10\,\mathrm{Ma})$ from (6.15). Beyond, the C-P is augmented by a dynamic SGS model based on (3.44) by replacing the viscosity-related (first) relaxation rate $\omega\,[=\omega_1]$ by an effective relaxation rate ω_e, viz.

$$\begin{aligned}\omega_e &= \frac{2}{\tau}\left(1+\sqrt{1+\frac{18\,\mathcal{C}_{\mathrm{S}}^2\,\overline{Q}}{\tau^2}}\right)^{-1} \\ &= \frac{2}{\tau}\left(1+\sqrt{1+\frac{18\left(\frac{\min(20,0.35\sqrt{\mathrm{Re}_{\Delta x}})}{\mathrm{Ma}}\,|C_{210}+C_{012}|\right)^2\overline{Q}}{\tau^2}}\right)^{-1},\end{aligned} \tag{6.20}$$

where τ is the unaltered relaxation time (3.16) depending on the kinematic viscosity of the underlying fluid.

A note of caution is necessary as regards the influence of the SGS on the parameterized cumulant model. According to the parameterization (3.103) to (3.105), the relaxation rates $\omega_{\{3;4;5\}}$ depend on ω. Hence, two options exist to compute $\omega_{\{3;4;5\}}$ in combination with the dynamic eddy viscosity, one using the SGS-modified ω_e and one using the unmodified ω. The present studies employed the unmodified ω in conjunction with the parameterization. Related differences between the options were examined and deemed negligible for fine grids. For the coarser grids ($\Delta x^+ \geq 30$), minor deviations, which are more pronounced for the Reynolds stresses than for the mean velocity, are observed for the 2 to 3 wall-nearest grid points.

6.2.3 Verification Specifics

Table 6.7 provides an overview of the TCF simulation specifications employed for proving the developed limiter adjustment and dynamic cumulant-based SGS model. The highest included Reynolds number of $\mathrm{Re}_\tau = u_\tau H/\nu = 5200$, complying with a bulk-related value of $\mathrm{Re}_B \approx 129200$, exceeds the previously simulated TCF, cf. Chap. 5, by a factor of 30, and is 3.5 times larger than the PHF maximum bulk Reynolds number, cf. Sec. 6.1.

Table 6.7: Test case specifications for the turbulence modeling verification.

	Specification
Test case	TCF at $\mathrm{Re}_\tau = \{180; 550; 2000; 5200\}$ $\rightarrow \mathrm{Re}_B \approx \{2750; 9900; 43900; 129200\}$
Reference data	• Moser et al. [1999] and Kim et al. [1987] for $\mathrm{Re}_\tau = 180$ • Bernardini et al. [2014] for $\mathrm{Re}_\tau = \{550; 2000\}$ • Lee and Moser [2015] for $\mathrm{Re}_\tau = \{2000\}$
Collision Model	C-P with **proposed regularization**, cf. Sec. 6.2.1
Turbulence Modeling	**proposed dynamic cumulant-based** SGS, cf. Sec. 6.2.2
Wall Modeling	IMEM of Asmuth et al. [2021] with C^1 reference polyonmials, cf. Appendix B
Wall BC	IBB with $q \equiv 0.5$
Physical quantities	$\nu_P = 1.5 \cdot 10^{-5}\,\mathrm{m^2 s^{-1}}$, $H = 0.05\,\mathrm{m}$
Domain size	$6\pi H(x) \times 2\pi H(z) \times 2H(y)$
Δx^+	$\{4, \ldots, 430\}$
Ma	$\{1/80; 1/20; 1/5\}$

Figure 6.44 exemplarily illustrates the spatial domain, supplemented by isosurface plots of the Q-criterion, cf. Dubief and Delcayre [2000], compiled for $\mathrm{Re}_\tau = 2000$. Included results address three resolutions for each considered Re_τ, featuring $N_H = \{12; 24; 48\}$ lattice nodes along the half-channel height H, cf. Tab. 6.8 for details of the employed grids. The flow-pass time (3.53) amounts to $t_{\mathrm{FP}} \approx 37.9 N_H/\mathrm{Ma}$.

The domain size is $6\pi H$ in streamwise (x), $2\pi H$ in spanwise (z) and $2H$ in wall-normal direction (y) and agrees with the studies of Bernardini et al. [2014]. It aims to accommodate the largest expected turbulent structures, hence the streamwise extent is enlarged by $2\pi H$ compared to the initial benchmark to account for the increased Reynolds number. All

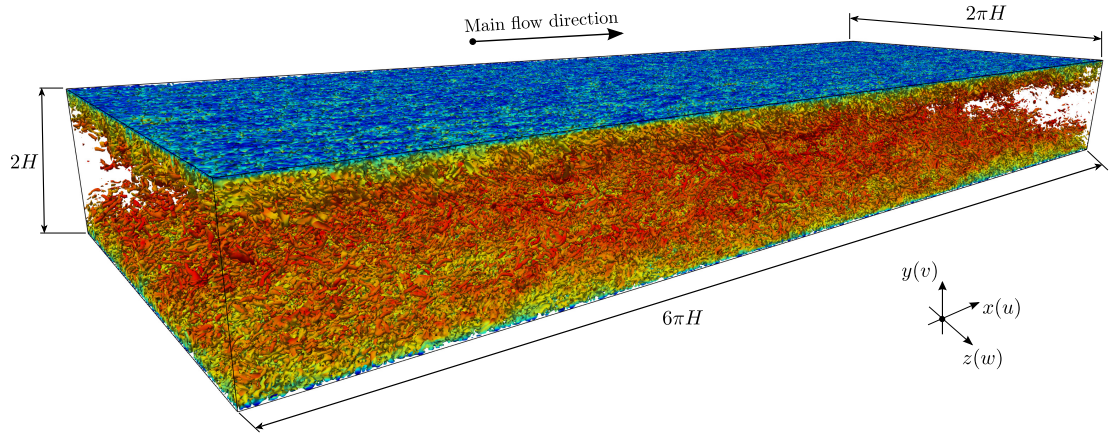

Figure 6.44: Illustration of the employed channel flow domain supplemented by Q-criterion isosurfaces colored by the streamwise velocity (u) obtained from a fine grid ($N_H = 48$) simulation of $\mathrm{Re}_\tau = 2000$.

twelve computations employ an isotropic, homogeneous spatial discretizations. In wall-normal direction $N_y = 2(N_H + 1)$ applies, attributed to two solid boundary nodes along with $y^+ = \Delta x^+/2$ of the wall adjacent fluid nodes. Although the grid layout involves $q \equiv 0.5$ at the top and bottom wall of the channel, the previously applied SBB solid boundary treatment is replaced by the IBB scheme that distinctly improved the numerical stability and accuracy in the case of large gradients. Three Mach numbers are utilized to

Table 6.8: Investigated grids and related flow-pass times for $\mathrm{Ma} = 1/20$.

N_H	$N_x \times N_y \times N_z$	N_{tot}	t_{FP}
12	$227 \times 26 \times 76$	448 552	9100
24	$453 \times 50 \times 152$	3 442 800	18200
48	$906 \times 98 \times 303$	26 902 764	36400

assess the acoustic scaling, where the medium Mach number of $\mathrm{Ma} = 1/20$ presents the baseline.

Statistical convergence of the evaluated flow quantities, i.e., the mean velocity, the Reynolds stresses, and the two-point correlations, is ensured by the following procedure. The latter commences with an initial transient phase of 50FP, followed by another 50FP to compute time-averaged velocity values $\overline{u}_{\mathrm{i}}$. The Reynolds stress tensor $\overline{R}_{\mathrm{ij}}(\overline{u}_{\mathrm{i}}, u_{\mathrm{i}})$ and the two-point correlations $R_{\vartheta}^{\{x;z\}}(\overline{u}_{\mathrm{i}}, u_{\mathrm{i}})$ are obtained during the subsequent 100FP. Thus, the duration of each simulation refers to 200FP, which is close to the amount stated in Sec. 5.1 for the medium grid featuring $\Delta x^+ = 6$.

Table 6.9 provides an overview of the computed test matrix referring to diffusive scaling for each considered Re_τ. Hereby, the LB viscosity ν spans two orders of magnitude, while the nondimensional grid resolution is bounded by $4 \leq \Delta x^+ \leq 430$ and $60 \leq \mathrm{Re}_{\Delta x} \leq 10800$. The last column of denotes the deviation of the achieved (a) and targeted (t) bulk Reynolds number, i.e., $(\mathrm{Re}_{B,\mathrm{a}}/\mathrm{Re}_{B,\mathrm{t}} - 1) \cdot 100$ [%]. The former follows from a spatial average of the streamwise velocity component in the y-z inlet slice of the domain, where the employed

Table 6.9: Considered twelve setups, including their respective spatial resolution parameters N_H, Δx^+, $\mathrm{Re}_{\Delta x}$, kinematic LB viscosity, target (t) bulk Reynolds number and its current percentage deviation for $\mathrm{Ma} = 1/20$.

Re_τ	N_H	Δx^+	$\mathrm{Re}_{\Delta x}$	ν	$\mathrm{Re}_{B,\mathrm{t}}$	Re_B dev. [%]
	48	3.8	58	$4.32 \cdot 10^{-4}$		+2.6
180	24	7.5	115	$2.16 \cdot 10^{-4}$	2750	−0.5
	12	15.0	230	$1.08 \cdot 10^{-4}$		+3.2
	48	11.5	208	$1.20 \cdot 10^{-4}$		+3.7
550	24	22.9	415	$6.02 \cdot 10^{-5}$	9900	+2.1
	12	45.8	830	$3.01 \cdot 10^{-5}$		+0.8
	48	42.1	915	$2.72 \cdot 10^{-5}$		−2.6
2000	24	84.3	1830	$1.36 \cdot 10^{-5}$	43900	+0.1
	12	168.5	3660	$6.80 \cdot 10^{-6}$		−3.3
	48	108.3	2690	$9.25 \cdot 10^{-6}$		−2.4
5200	24	216.7	5380	$4.62 \cdot 10^{-6}$	129200	−2.6
	12	433.3	10760	$2.31 \cdot 10^{-6}$		−2.3

value is additionally averaged in time over all FP. The latter $\mathrm{Re}_{B,\mathrm{t}}$ follows from Dean's correlation (2.32) for the prescribed Re_τ. The observed maximal deviations of approximately $\pm 4\%$ are deemed sufficiently small. Minor deviations of subsequently displayed normalized properties, e.g., $u_\mathrm{i}^+ = \overline{u}_\mathrm{i}/u_\tau$ or $R_\mathrm{ij}^+ = \overline{R}_\mathrm{ij}/u_\tau^2$, are attributed to small inaccuracies of the assumed correlation and, thus, might be reduced by alternative assessments of u_τ.

Data Recording and Processing

This section includes a synopsis of data processing aspects. Statistical averages of $\overline{u}_\mathrm{i}$ and $\overline{R}_\mathrm{ij}$ are extracted from time-averaged data in the centered y-z plane located at $x/H = 3\pi$. A major share of the data displayed in Sec. 6.2.4 refers to profiles along the vertical direction (y). To this end, the time-averaged data is spatially averaged in the spanwise direction (z), though the mean's ergodic nature virtually reveals any differences between the different time-averaged profiles and the space-time-averaged profiles. Nevertheless, the spatial averaging distinctly accelerates convergence. Temporal-averaged TPCs rest upon entire, wall-parallel (x-z) data planes located at four wall distances, i.e., $\Theta = y/H = \{0.1; 0.25; 0.5; 1\}$, where y represents the physical wall distance. These planes are subsequently condensed to the displayed one-dimensional data in streamwise (x) or spanwise (z) directions. The distances refer to the following discrete lattice nodes N_y for the three grids

$$N_y(\Theta, N_H) = \begin{cases} \{1;\ 3;\ 6; 12\} & N_H = 12 \\ \{2;\ 6; 12; 24\} & N_H = 24 \\ \{4; 12; 24; 48\} & N_H = 48 \end{cases}, \tag{6.21}$$

where the index starts from 0, i.e., the solid boundary node. No interpolation is applied for the near-wall location $y/H = 0.1$, which strictly corresponds to $\{1.2, 2.4, 4.8\}\,\Delta x$ on the three grids. Therefore, the specific assignments refer to the lower neighbors, which impairs

an inter-grid comparison at the near-wall location $\Theta = 0.1$ as indicated by the different buffer layer locations outlined in Tab. 6.10.

Table 6.10: Resulting $y^+_\Theta = y^+(N_H, \mathrm{Re}_\tau)$ values at the considered wall distances $\Theta = y/H$ for computing two-point correlations and resulting energy spectra.

N_H	Re_τ	$y^+_{\Theta=0.1}$	$y^+_{\Theta=0.25}$	$y^+_{\Theta=0.5}$	$y^+_{\Theta=1}$
12	180	7	37	82	172
	550	23	115	252	527
	2000	84	421	927	1938
24	180	11	41	86	176
	550	34	126	264	539
	2000	126	463	969	1980
48	180	13	43	88	178
	550	40	132	269	544
	2000	147	484	990	2001

Since the $\Theta = 0.1$ plane is extracted at the first [second] fluid node of the coarse [medium] grid, one expects the location to be affected by the wall modeling. Wall function concepts usually refer to averaged flow properties, and a wall function generally suppresses turbulent dynamics. Therefore, results of the $\Theta = 0.1$ plane are assumed to show more substantial deviations from DNS data for all simulations that do not resolve the viscous sublayer at $\mathrm{Re}_\tau = 550$ and $\mathrm{Re}_\tau = 2000$.

Results obtained on the different grids are assigned to a particular color, where green indicates fine grid results ($N_H = 48$), blue denotes to medium grid results ($N_H = 24$), and red refers to coarse grid solutions ($N_H = 12$). Black lines refer to the respective reference data reported, cf. Tab. 6.7. Note that the simulations of Lee and Moser [2015] and Bernardini et al. [2014], to some extent, cover virtually the same Reynolds numbers and the respective data for these matches. Hence, the remainder simply distinguishes between $\mathrm{Re}_\tau = \{180; 550; 2000\}$ and $\mathrm{Re}_\tau = 5200$ is only referred to in the end for a supporting comparison versus the conventional constant Smagorinsky SGS model, cf. Fig. 6.63−6.64 and Appendix C. TPCs and spectra computed for $\mathrm{Re}_\tau = 550$ are compared to DNS reference data of Moser et al. [1999] for $\mathrm{Re}_\tau = 590$. The Re_τ deviation of 7% is considered negligible.

6.2.4 Results and Discussion

The suitability of the present domain size and periodic BC is demonstrated in Fig. 6.45 and Fig. 6.46 through exemplary TPCs and energy spectra of the normal stresses in both stream- and spanwise directions for the most challenging Reynolds number,i.e., $\mathrm{Re}_\tau = 2000$. Displayed correlations refer to fine grid results at the mid-height position, where all path-lines decline to sufficiently small values. Furthermore, the minimum spanwise correlation for the streamwise component displays the frequently observed half-streak spacing at this wall distance. The corresponding spectra shown in Fig. 6.46 drop with an increasing slope by approximately 5[3] orders of magnitude between the low and the high wave numbers

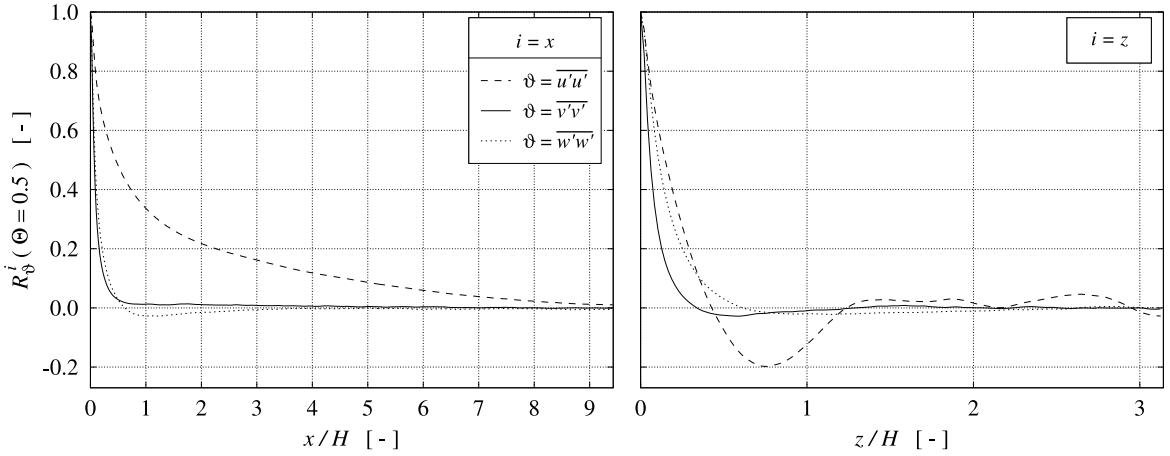

Figure 6.45: Stream- (left) and spanwise (right) two-point correlations obtained from the fine grid ($N_H = 48$) for $\mathrm{Re}_\tau = 2000$ at $\Theta = 0.5$.

in the streamwise[spanwise] direction. Additionally, the $E^+ \sim (\kappa^+)^{-5/3}$ proportionality of the inertial range is displayed and the $\overline{u'u'}$ component in spanwise direction [dashed, right] is smoothed by an unweighted, centered three-point moving average filter applied for $k_z^+ > 0.7$.

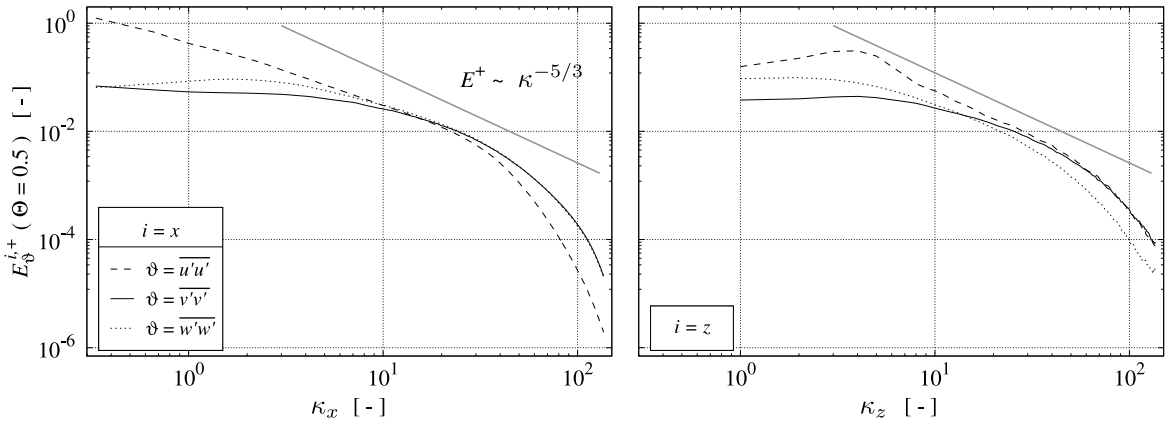

Figure 6.46: Stream- (left) and spanwise (right) normalized turbulent energy spectra obtained from the fine grid ($N_H = 48$) for $\mathrm{Re}_\tau = 2000$ at $\Theta = 0.5$.

Mean Flow

Figure 6.47 depicts profiles of the nondimensional mean primal velocity $u^+(y^+)$ obtained for the three considered Reynolds numbers on each of the three grids. Overall, the results are reasonably accurate and display a surprisingly small sensitivity to the resolution. In conjunction with the lowest Reynolds number $\mathrm{Re}_\tau = 180$ (top left), the wall-adjacent fluid node is still located inside the viscous sublayer (fine, medium grid) or lies inside the buffer layer (coarse grid). Hence, only a weak deviation from the no-slip velocity is observed in Tab. 6.11, which outlines the x component u_W of the wall velocity vector, see also Sec. 3.1.5 (vii) and the corresponding Fig. 3.5. The table also indicates that the respective variance increases when the resolution deteriorates but always remains small.

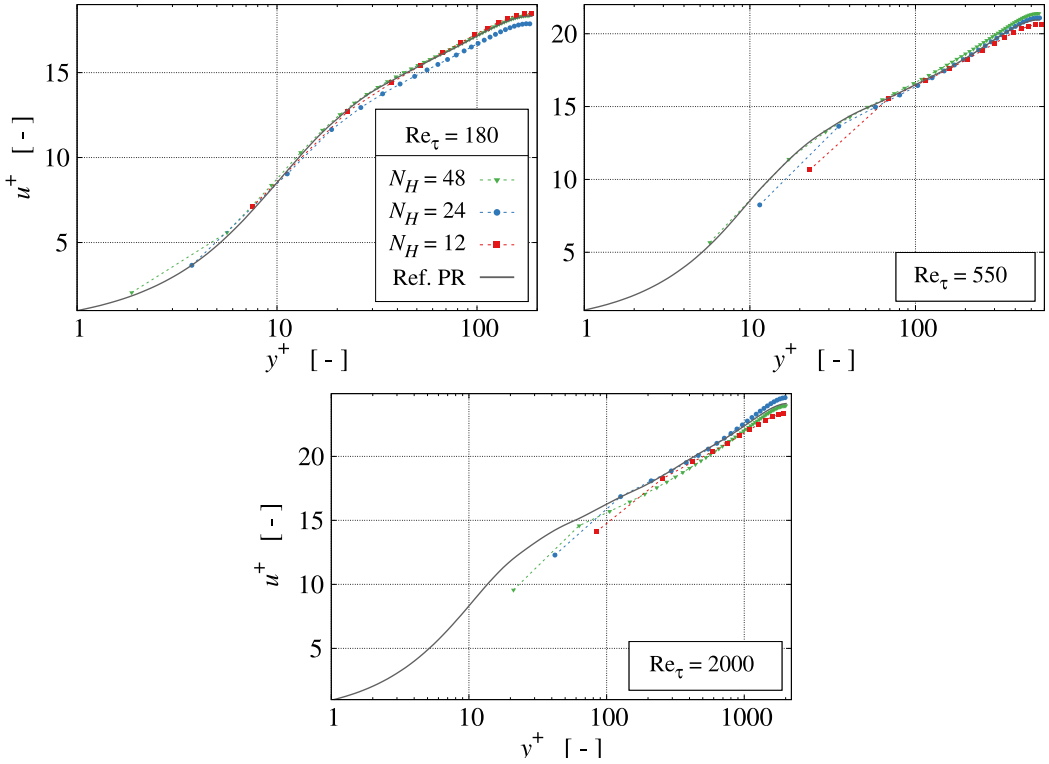

Figure 6.47: Nondimensional mean velocity profiles for the three considered Re_τ in comparison with the polynomial reconstruction (Ref. PR) of the reference data.

Table 6.11: Temporal mean value ($\overline{u}_W^+$) and variance ($\sigma^2_{\overline{u}_W^+}$) of the nondimensional streamwise wall velocity component.

Re_τ	N_H	$\overline{u}_W^+$	$\sigma^2_{\overline{u}_W^+}$ $[\cdot 10^{-3}]$
180	48	0.108	0.034
	24	0.056	0.785
	12	0.665	1.365
550	48	0.246	0.205
	24	0.707	0.497
	12	2.076	2.386
2000	48	1.279	0.526
	24	3.362	0.913
	12	5.151	2.457

With attention directed to the two higher Reynolds numbers, wall function influences increase along with an increase in the wall velocity u_W. In such situations, deficiencies are observed in the vicinity of the first and second interior grid nodes in Fig. 6.47 (top right; bottom). They are attributed to an *overshoot* phenomenon, cf. Brasseur and Wei [2010] or Asmuth et al. [2021], induced by small eddy viscosity levels predicted at the very near-wall fluid node(s). The latter is attributed to the wall function being afflicted with reduced turbulent dynamics. The missing dynamics adversely affect the present SGS model that

operates with third-order cumulant expressions dampened by wall function influences.

However, except for the overpredicted velocity gradients at the wall-nearest nodes which will be addressed in Sec. 6.3, the mean velocity profiles match the log law, even for the high Reynolds number, where the resolution is coarsened to $\Delta x^+ = 170$. The biggest discrepancy of the computed wall shear stress is observed for $\mathrm{Re}_\tau = 2000$ on the fine grid, where the prescribed wall shear is underpredicted by approximately 3%. Mind that normalizations employ a prescribed reference u_τ in line with Re_τ. Moreover, minor deviations occur in the wake regime. Here, the bulk velocity deviation (Re_B dev.) might be explained by a minor mismatch of the employed correlations, cf. Tab. 6.9.

Shear Stress Decomposition

The abovementioned overshoot phenomenon is better understood by analyzing the particular shear stress contributions and the total shear stress. Concerning the latter, Fig. 6.48 indicates a reasonable agreement of the $|\tau_W|$-normalized total shear stress with the theoretical (nondimensional) linear function $\tau_{\mathrm{lin}} = 1 - y/H$, see also (2.25) and derivation thereof, disregarding the Reynolds number or the employed resolution. The present deviations,

$$\mathrm{L}_1(\tau_{\mathrm{tot}}) = \frac{\tau_{\mathrm{tot}} - \tau_{\mathrm{lin}}}{\tau_{\mathrm{lin}}}\,, \tag{6.22}$$

increase with the Reynolds number but remain approximately constant along the abscissa, indicating a slope mismatch by mostly 5%. Mind that the linear distribution vanishes at

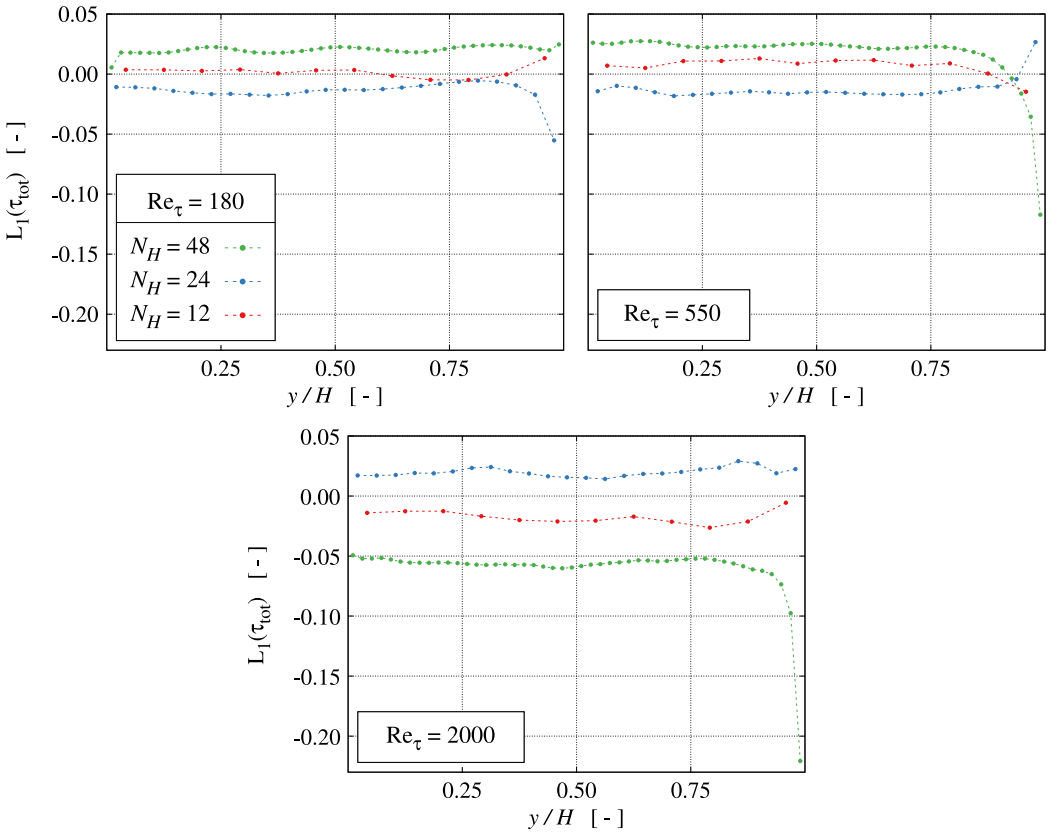

Figure 6.48: Relative deviation of the present total shear stress from a linear stress relation.

$y/H = 1$, which impairs the evaluation of relative differences close to the centerline, i.e., the L_1 validity loses significance for $y/H > 0.9$.

Profiles of the individual normalized shear stress components, i.e., the modeled SGS, viscous, and resolved parts, are displayed in Fig. 6.49. It is observed that the viscous contributions obtained with different grids for specific Reynolds numbers [solid lines] eminently agree with each other for $\mathrm{Re}_\tau = 180$, i.e., they all snap on the green fine grid curve, which is not necessarily the case for the higher Reynolds numbers. Moreover, Fig. 6.49 (top left) reveals the dominance of the resolved stresses τ_{res} [dotted lines] from the third (fine and medium) or second (coarse) lattice node and beyond toward the domain's interior. The latter is also the case when increasing the Reynolds number (top right; bottom) or

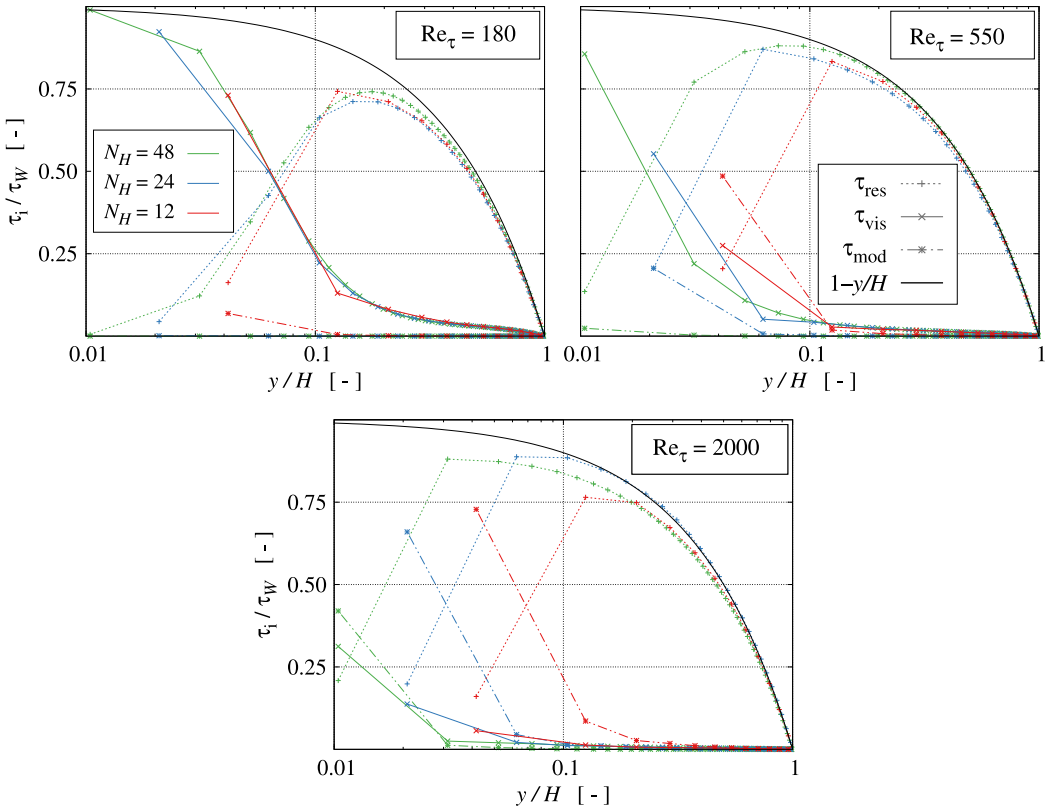

Figure 6.49: Comparison of nondimensional resolved [dotted], viscous [solid] and modeled [dashed] shear stress profiles with the linear total stress relation [solid black].

the lattice spacing, thereby amplifying wall function influences. The respective (large) predicted resolved shear stresses suddenly drop when entering the buffer layer in the direction of the wall. For the coarse grids, the decrease occurs almost abruptly. In conjunction with $\mathrm{Re}_\tau = 180$, the near-wall results of the coarse grid remain close to the finer grids because the mean velocity gradient is well captured. However, increasing the Reynolds numbers reveals more significant disparities between resolved shear stress levels predicted by the coarse, medium, and fine grids near the wall. The latter is accompanied by a mismatch of the mean velocity gradient, which also induces an overprediction of the (nondimensional) turbulence energy production

$$P_k^+ = -\overline{u'v'}\,\frac{\mathrm{d}\overline{u}}{\mathrm{d}y}\left(\frac{\nu}{u_\tau^4}\right) \quad [-]\,, \tag{6.23}$$

cf. evaluation illustrated in Fig. 6.50.

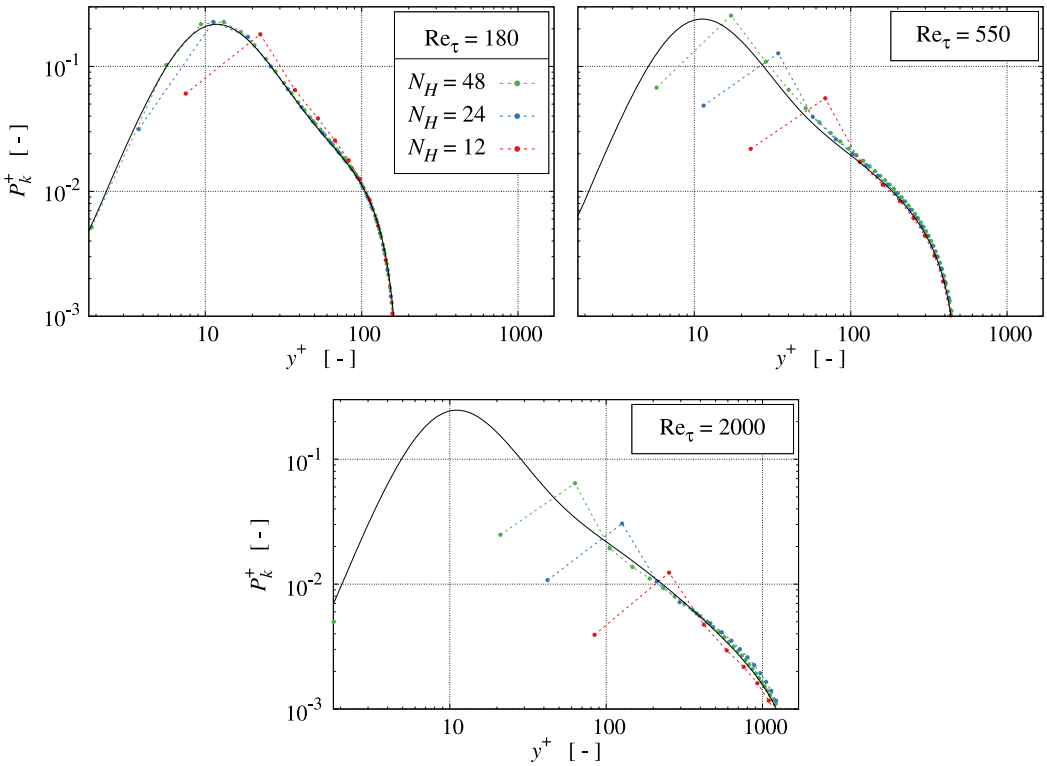

Figure 6.50: Comparison of the turbulence energy production rate (6.23) with DNS reference data of Lee and Moser [2015].

The SGS contribution should balance the reduction of resolved turbulent shear when approaching the wall. However, if the wall-adjacent eddy viscosity and thereby the modeled shear stress is underpredicted, this is compensated by an overpredicted (mean) velocity gradient. In this regard, a poor resolution of the turbulence generating buffer layer poses a challenge to the present cumulant-based SGS/wall function combination, cf. the medium ($y_2^+ \approx 25$) and the coarse ($y_2^+ \approx 70$) grid results for $\mathrm{Re}_\tau = 550$, and all results for $\mathrm{Re}_\tau = 2000$ featuring $y_2^+ \approx \{60, ..., 250\}$. Since the wall function substantially attenuates the turbulent dynamics and does not recover abruptly on coarser meshes, this impedes the cumulant-based SGS model in a few wall-adjacent coarse grid nodes. Figure 6.51 displays the overestimation of the mean velocity gradient near the wall in conjunction with the coarse grid simulation at $\mathrm{Re}_\tau = 550$ [red] and all simulations at $\mathrm{Re}_\tau = 2000$. The evaluation refers to the second-order FD ratio, i.e.,

$$\phi = \frac{(\mathrm{d}\overline{u}/\mathrm{d}y)_{\mathrm{pre}}}{(\mathrm{d}\overline{u}/\mathrm{d}y)_{\mathrm{rec}}} \ [-] \,, \tag{6.24}$$

of the present (pre) LBM and reconstructed (rec) reference, cf. Appendix B, mean velocity profiles.

Likewise, Fig. 6.52 depicts the averaged normalized eddy viscosity $\overline{\nu}_t/\nu$ (left) and an estimate of the discrepancy between the predicted and the required eddy viscosity (right)

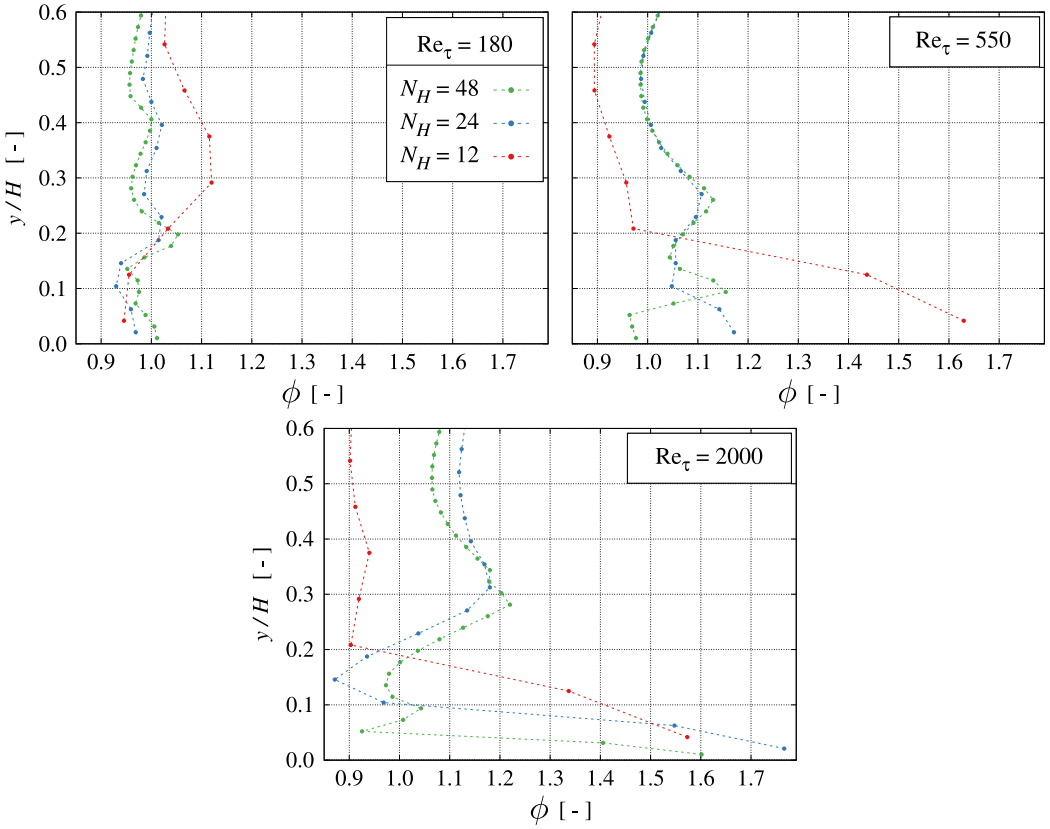

Figure 6.51: Ratio of the predicted to the reconstructed velocity gradient.

through

$$\Psi = \frac{(\nu + \overline{\nu}_t)\left(\frac{\mathrm{d}\overline{u}}{\mathrm{d}y}\right)_{\mathrm{rec}} + |\overline{u'v'}|}{u_\tau^2} - \tau_{\mathrm{lin}} \;\; [-]\,, \tag{6.25}$$

which again outlines the near-wall defect for the higher Reynolds numbers.

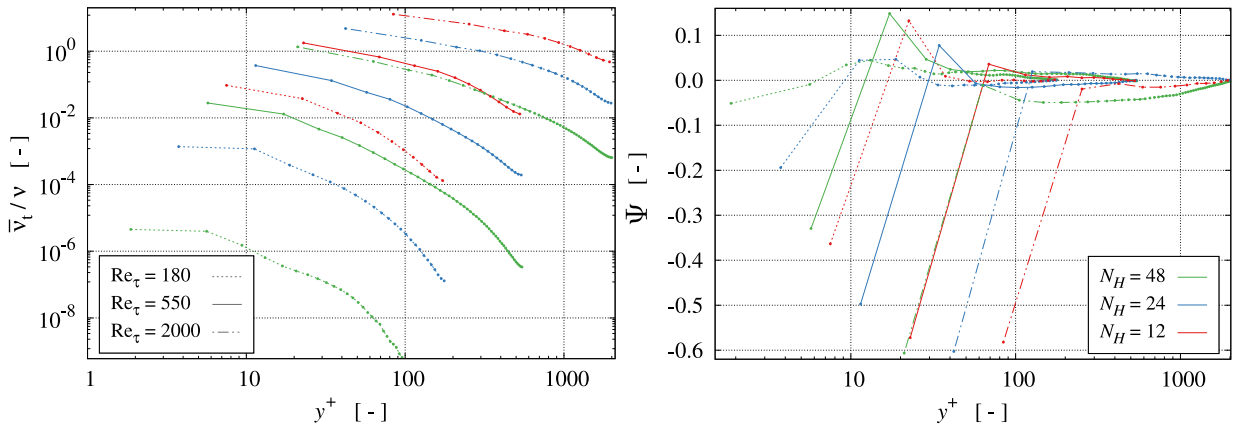

Figure 6.52: Averaged normalized eddy viscosity $\overline{\nu}_t/\nu$ (left), estimated discrepancy (Ψ) between the predicted and the required eddy viscosity (right).

While the eddy viscosity is generally negligible for $\mathrm{Re}_\tau = 180$ [dotted] and remains minor for $\mathrm{Re}_\tau = 550$ [solid], significant eddy viscosity levels are observed at $\mathrm{Re}_\tau = 2000$

[dashed], particularly for the coarse grid, where $\overline{\nu_t}/\nu = \{1, \ldots, 10\}$ over large sections of the domain. From Fig. 6.53 it is noted that the overshooting characteristics follows the soft transition displayed by empirical universal wall functions, e.g., according to Spalding [1961], and reduces when augmenting the eddy viscosity at the wall-adjacent interior fluid nodes.

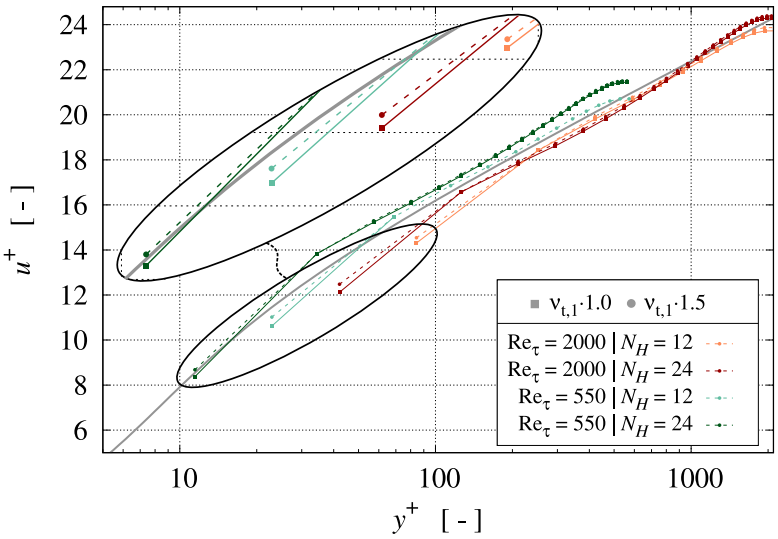

Figure 6.53: Comparison of mean the velocities in the buffer layer predicted with the present [squares] approach ($\nu_{t,1} \cdot 1.0$) and a 50% augmentation [circles] of the near-wall (first fluid node) eddy viscosity ($\nu_{t,1} \cdot 1.5$) against a second-order Spalding [1961] law [solid gray].

Resolved Turbulence Field

Figure 6.54 shows the predicted resolved Reynolds stress anisotropies, whereas Fig. 6.55 displays profiles of the resolved Reynolds normal stress components. The latter results of the present modified C-P model are compared to DNS data [black lines] obtained from Moser et al. [1999] and Bernardini et al. [2014]. For the low Reynolds number $\mathrm{Re}_\tau = 180$ in Fig. 6.55 (top left), the SGS contributions are negligible, cf. also Fig. 6.52, and the resolved Reynolds stresses reveal a fair coincidence with the reference data. The anisotropy prediction deteriorates as the resolution coarsens and the modeling influences increase. The respective right graphs of Fig. 6.54 and Fig. 6.55 distinctly reveal an erroneous shift toward an isotropic ($2c$) partitioning tendency of the wall-parallel normal stresses, i.e., $\overline{u'u'}$ and $\overline{w'w'}$, near the wall when the grid is coarsened.

Since the barycentric coordinate y_B vanishes at the solid boundary, the wall-normal velocity fluctuation (v') is attenuated due to wall damping and wall function influences. As the Reynolds number increases, the resolution of the employed grids deteriorates, and the attenuation of the wall-normal fluctuation extends further toward the centerline. Simultaneously, the shift from $1c$ toward $2c$ turbulence in the near-wall region proceeds.

Increasing the wall function influence by increasing the Reynolds number or reducing the resolution induces a substantial reduction of the streamwise correlation length $\lambda^+(R^{x,+}_{u'u'})$, as outlined below. Moreover, the TPCs indicate that the under-resolved near-wall flow shares some features with the core flow.

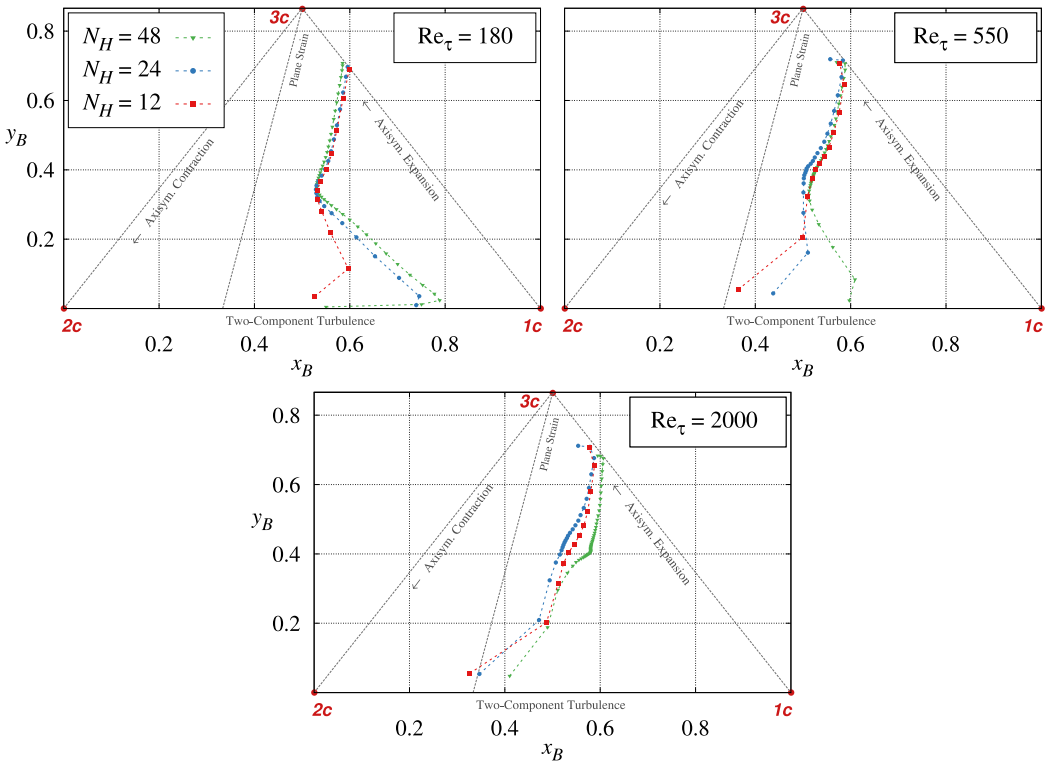

Figure 6.54: Barycentric representation of the (resolved) Reynolds stress anisotropies. The abscissa ($y_B = 0$) refers to the wall location.

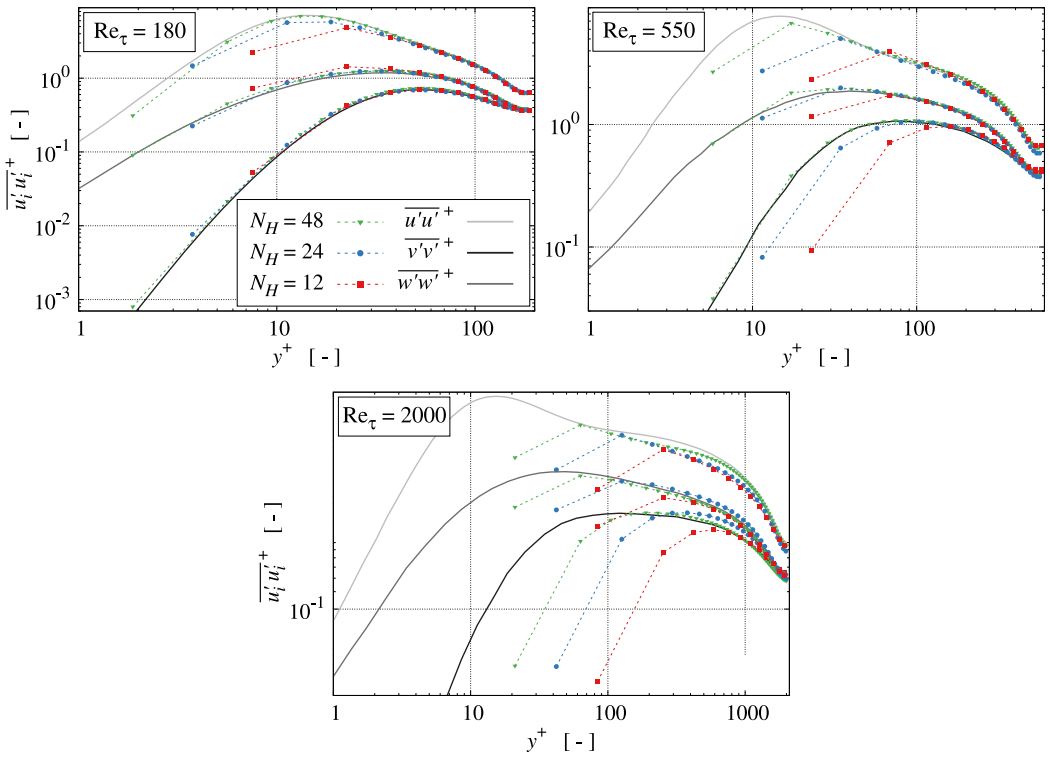

Figure 6.55: Nondimensional (resolved) Reynolds normal stresses supplemented by reference data.

Two-point Correlations and Correlation Lengths

The occurrence and location of minima displayed by the spanwise (z) TPCs (R^z_ϑ) allow the identification of structures and represent an estimate of their size. Figure 6.56 (top 2×3 tile) depicts these correlations obtained for $\mathrm{Re}_\tau = 180$ in the $\Theta = 0.1$ (top subfigures) and $\Theta = 0.25$ (bottom subfigures) planes. The data is plotted in outer (z/H) scaling and compared to DNS reference data of Moser et al. [1999] [black lines]. The predictive

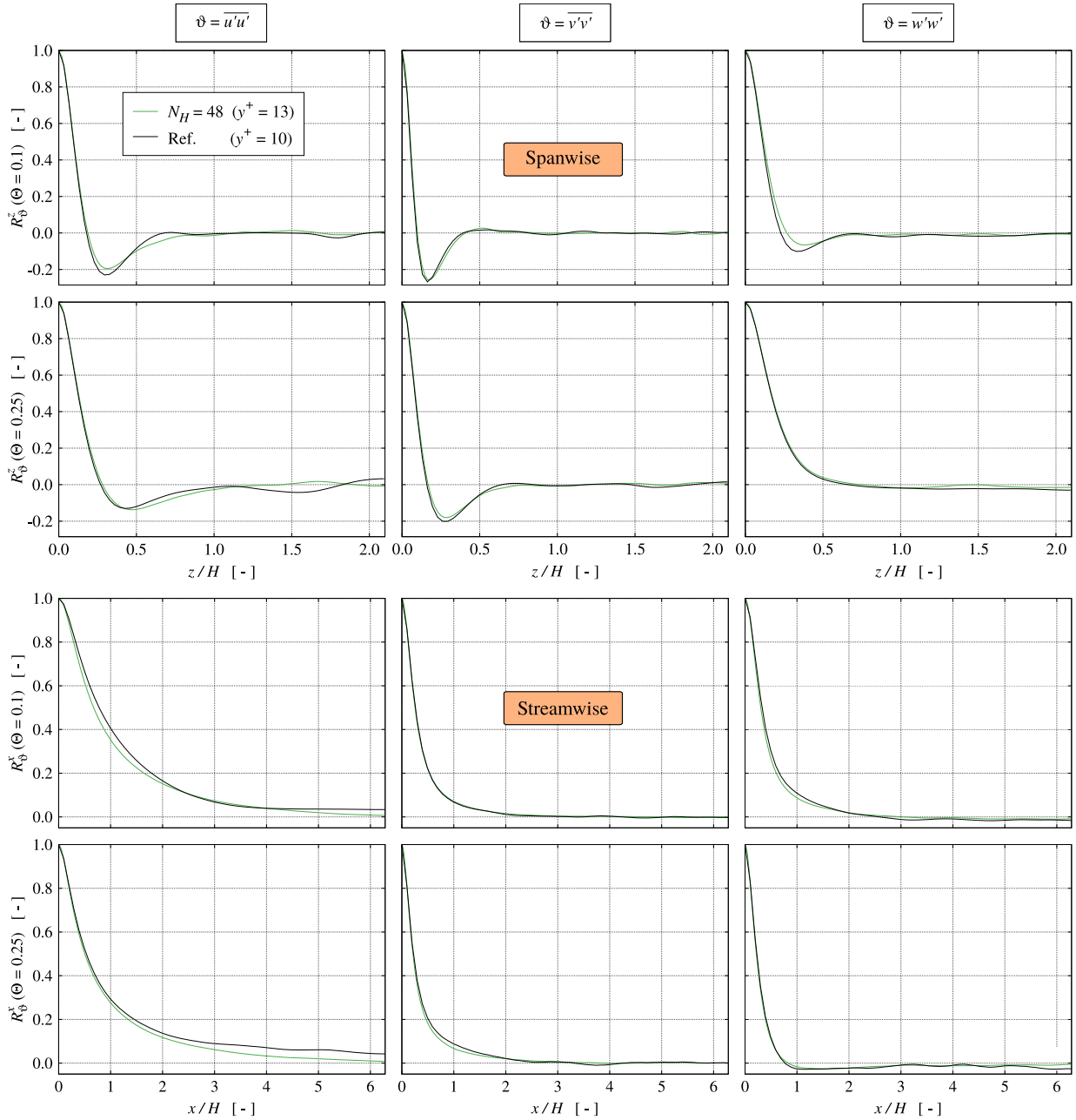

Figure 6.56: Spanwise (top 2×3 tile) and streamwise (bottom 2×3 tile) TPCs obtained from the fine grid for $\mathrm{Re}_\tau = 180$ at $\Theta = 0.1$ (top subfigures) and $\Theta = 0.25$ (bottom subfigures) for $\vartheta = \{\overline{u'u'}; \overline{v'v'}; \overline{w'w'}\}$ (left; center; right).

agreement between the fine-grid LBM results and the reference DNS data is generally fair. Streamwise vortices are indicated by the minima of $R^z_{\overline{v'v'}}$ (top row center) located between

$z/H \approx 0.17$ ($z^+ \approx 30$) at $\Theta = 0.1$ and $z/H \approx 0.28$ ($z^+ \approx 50$) at $\Theta = 0.25$, and provide an impression about their diameter. Consistent with formerly reported results, the $R^z_{\overline{v'v'}}$ minimum is located closer to the wall than the minimum of $R^z_{\overline{u'u'}}$. The latter separates the high-speed fluid from the low-speed fluid at approximately half the mean streak spacing. The evolution of the companion streamwise correlations is more straightforward and shows a fair predictive agreement, as indicated by the results in Fig. 6.56 (bottom 2×3 tile).

As identifying particular predictive differences between the various TPCs is intricate, integral values are frequently used to support an assessment. For instance, an early analysis by Tritton [1967] revealed that the normalized streamwise correlation length of the streamwise velocity maximizes at the end of the buffer layer, e.g., around $y^+ \approx \{20, ..., 30\}$, where the respective peak values significantly exceed the y^+ value and subsequently drop in the log layer. Relating to this, Fig. 6.57 describes the evolution of the predicted streamwise correlation lengths (4.16) for all three normal stress components as a function of the Reynolds number and the grid resolution. The figures' abscissae are each limited individually, and a row-wise constant scaling by decimal powers applies, i.e., 10^3 ($\overline{u'u'}$), resp. 10^2 ($\overline{v'v'}$, $\overline{w'w'}$). The present C-P results are compared with reference data extracted from

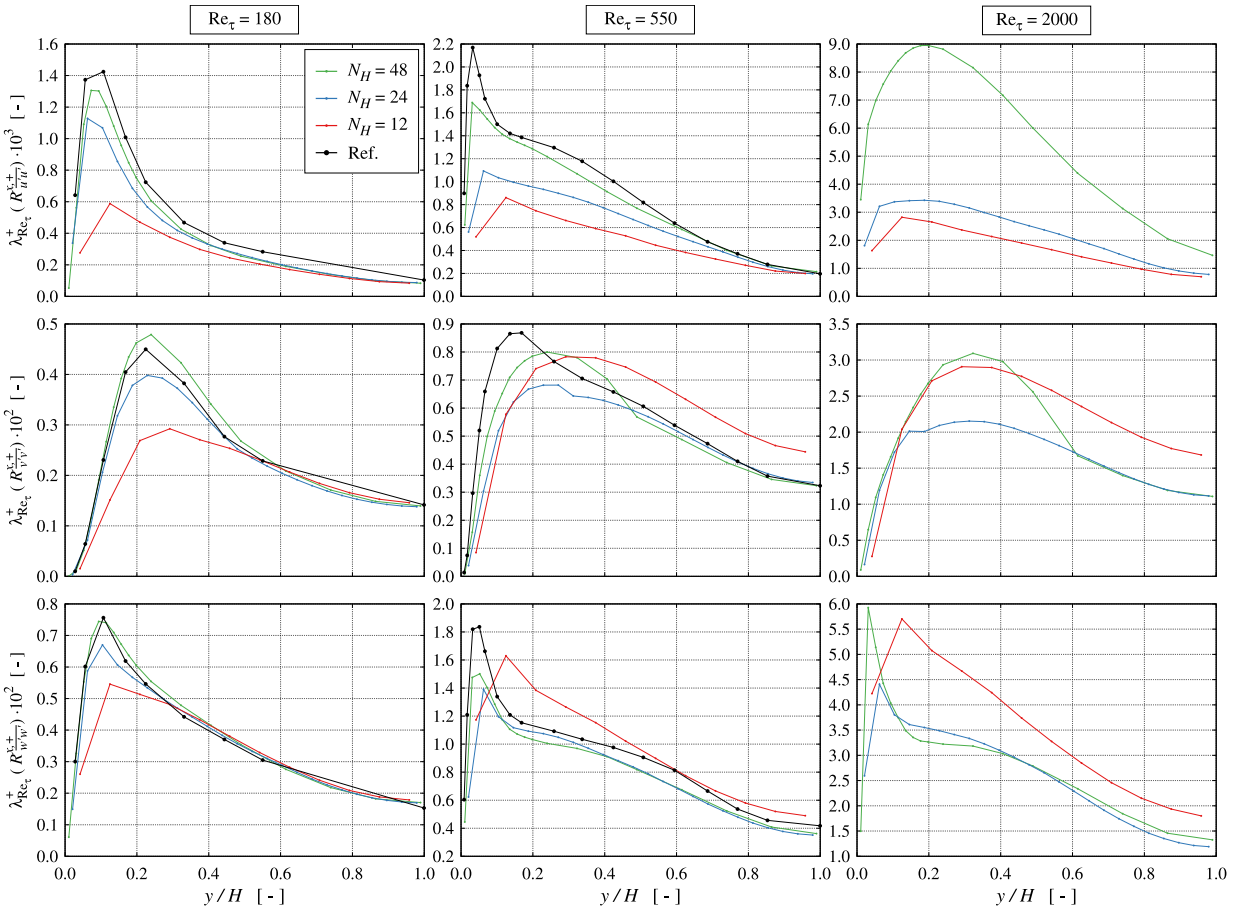

Figure 6.57: Streamwise correlation lengths for $\overline{u'u'}$ (top), $\overline{v'v'}$ (center), $\overline{w'w'}$ (bottom) column-wise displayed for $\mathrm{Re}_\tau = \{180; 550; 2000\}$ (left; center; right) each for $N_H = \{12; 24; 48\}$ [red; blue; green] plotted in outer scaling.

DNS simulations of Moser et al. [1999] for $\mathrm{Re}_\tau = \{180; 590\}$, while no data is available for the highest Reynolds number. As already mentioned above, the figures prove a sig-

nificant length-scale reduction in streamwise direction for the coarser grids. The latter yields similarities between the near-wall and the centerline region of the respective TPCs, as displayed in Fig. 6.58 for $\mathrm{Re}_\tau = 550$.

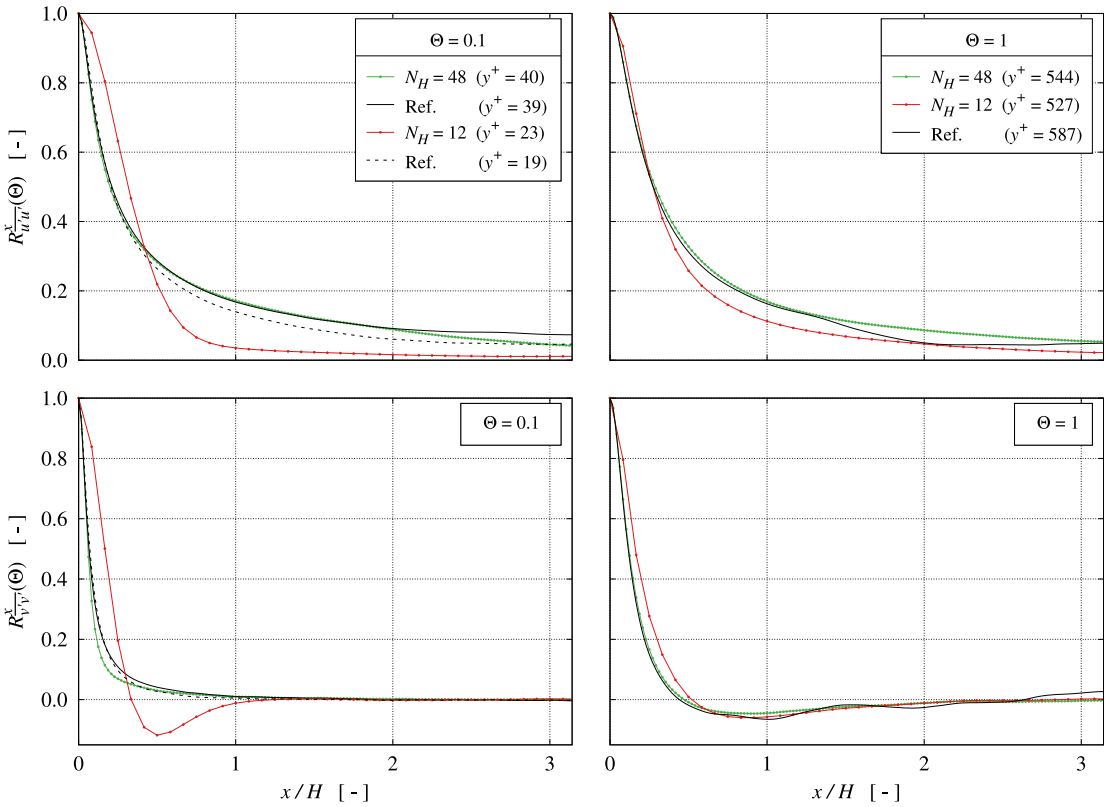

Figure 6.58: Streamwise R^x_ϑ TPCs, $\vartheta = \overline{u'u'}$ (top) and $\vartheta = \overline{v'v'}$ (bottom), obtained from the fine [green] and coarse [red] for $\mathrm{Re}_\tau = 550$ at a near-wall $\Theta = 0.1$ (left) and the centerline position $\Theta = 1$ (right) supplemented by reference data.

On the contrary, the spanwise length scales shown in Fig. 6.59 are substantially shorter, cf. abscissae value ranges, besides reflecting smaller gradients in the vertical direction. Hence, grid resolution influences are far less pronounced than in the streamwise direction.

Energy Spectra

Figure 6.60 compares the computed streamwise (x) and spanwise (z) turbulent energy spectra for $\mathrm{Re}_\tau = \{180; 550; 2000\}$ with reference data obtained from DNS simulations, where the displayed reference data [solid lines] refers to Moser et al. [1999] for $\mathrm{Re}_\tau = \{180; 590\}$ and Lee and Moser [2015] for $\mathrm{Re}_\tau = 2000$. The results are labeled by the $y^+ = y^+(\Theta, N_H = 48, \mathrm{Re}_\tau)$ values, cf. Tab. 6.10, and complemented by the closest values of the reference data set as indicated in square brackets. Constant y-intercepts apply row-wise (ϑ), while x-ranges coincide column-wise (Re_τ). Displayed results refer to four different wall distances, i.e., $y/H = \Theta = \{0.1; 0.25; 0.5; 1\}$, and are restricted to fine grid LBM computations with $N_H = 48$ points across the channel-half height, since the present resolution deteriorates by an increase in the Reynolds number.

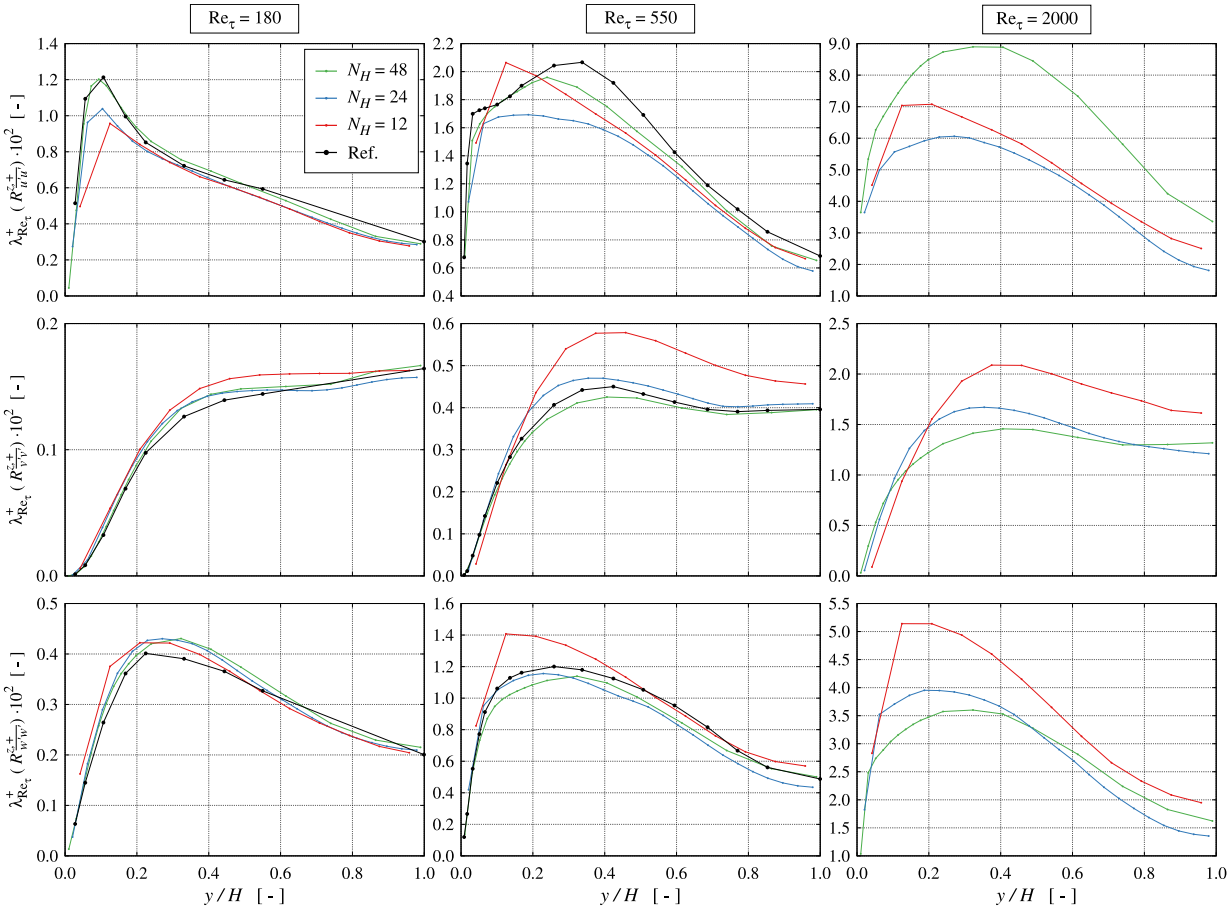

Figure 6.59: Spanwise correlation lengths for $\overline{u'u'}$ (top), $\overline{v'v'}$ (center), $\overline{w'w'}$ (bottom) column-wise displayed for $\mathrm{Re}_\tau = \{180; 550; 2000\}$ (left; center; right) each for $N_H = \{12; 24; 48\}$ [red; blue; green] plotted in outer scaling.

Concerning $\mathrm{Re}_\tau = 180$ (left column), the modified C-P model results show a convincing agreement with the reference DNS data, with minor reservations for the wall nearest location where the opposed y^+ values differ by 30% ($y^+ = 13$ vs. $y^+ = 10$), impairing the comparability. However, this case is certainly less challenging, as the resolution is close to DNS. With attention directed to the medium Reynolds numer (center column), the resolution refers to $\Delta x^+ = 11.5$, and the influence of the resolution-triggered regularization is clearly observed in the evolution of the streamwise spectra. As already discussed for the more complex PHF, cf. Sec. 6.1, the steep decline of the higher wave number parts of the spectra ($k_x^+ > 60$) is induced by the regularization, affecting the suppression of potential instabilities.

Except for the dissipative high-wave number regime and a slight tendency to pull some of the unresolved high-wave number content into the upper-wave numbers of the inertial range for $\Theta = 0.1$ [red] and $\Theta = 0.25$ [orange], the predictive agreement with the employed reference DNS data is deemed fair. Results displayed for $\mathrm{Re}_\tau = 2000$ were compiled for $\Delta x^+ = 42$, revealing both regularization and SGS influences. Results for the dominating $E^{x,+}_{u'u'}$ spectra are in fair agreement with the reference data in the energy-containing range. The width of the inertial range is substantially reduced, and the present C-P spectra start declining with an increasing slope at $\kappa_x > 40[60]$ for the lower[upper] locations, cf. right

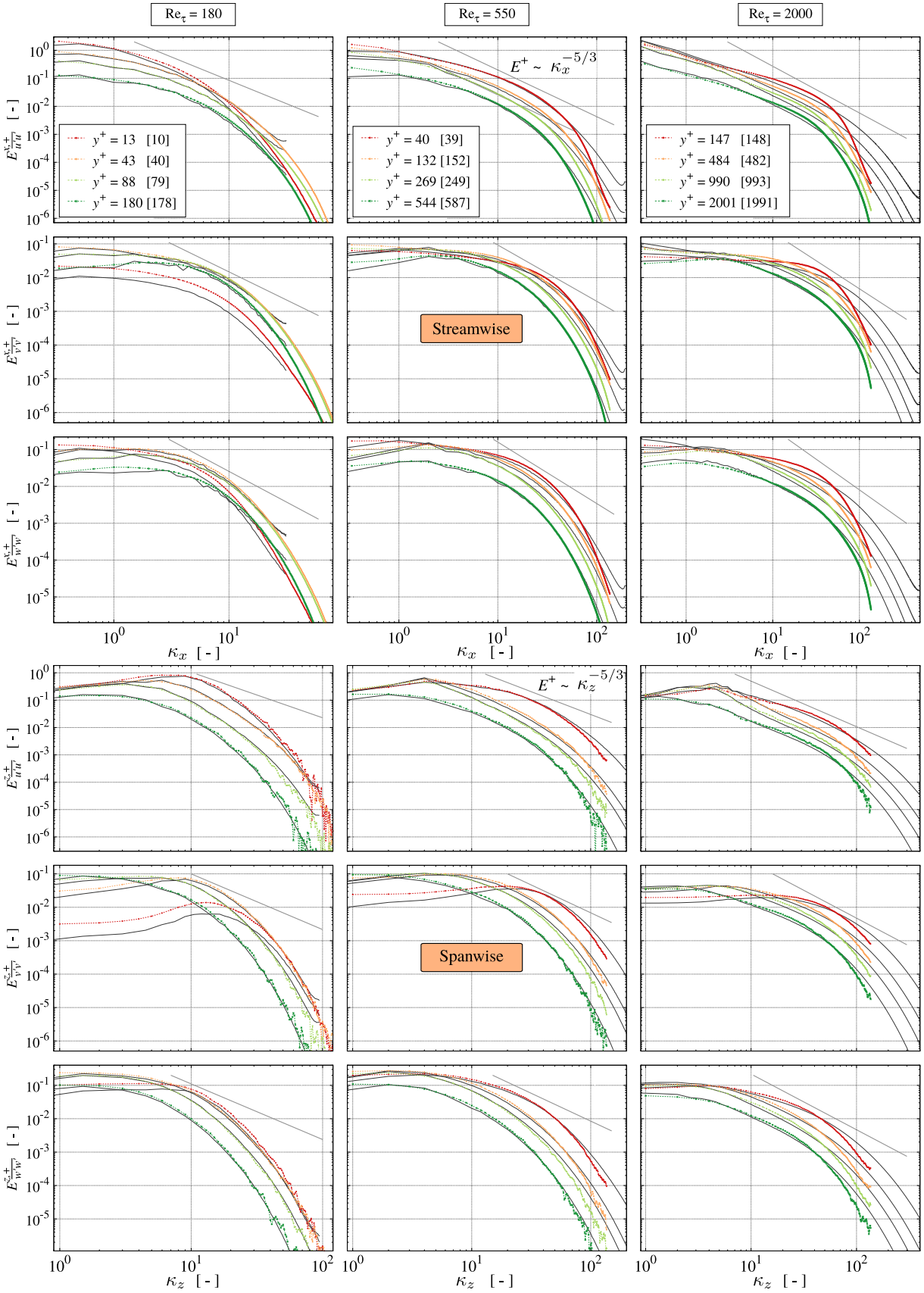

Figure 6.60: Streamwise [top 3 × 3 tile] and spanwise [bottom 3 × 3 tile] spectra for $\vartheta = \{\overline{u'u'}; \overline{v'v'}; \overline{w'w'}\}$ (top; center; bottom) obtained from fine grid simulations for $\mathrm{Re}_\tau = \{180; 550; 2000\}$ (left; center; right) at wall-normal positions $\Theta = \{0.1; 0.25; 0.5; 1\}$ [dark red; orange; light green; dark green].

column of the top tile. The increase of the inertial range content is more pronounced for the lower locations [red; orange] than for the upper ones, affecting the spectra at $\Theta = 0.5$ [light green]. It is found that the spanwise spectra, depicted in Fig. 6.60 (bottom tile), generally agree better with the reference data for the higher Reynolds numbers, as could also be expected from the TPCs and the correlation lengths results discussed above.

Figure 6.61 compares the stream- (left) and spanwise (right) energy spectra for $\mathrm{Re}_\tau = 2000$ obtained on the coarse [red] and the fine [green] grid for the $\overline{u'u'}$ (top) and $\overline{w'w'}$ (bottom) components, where solid lines display reference data of Lee and Moser [2015]. The correlating N_H-dependent y^+ values at $\Theta = 0.5$ are given in the upper left key, deviating by a maximum of 7% on the coarse grid from the reference value. The figures

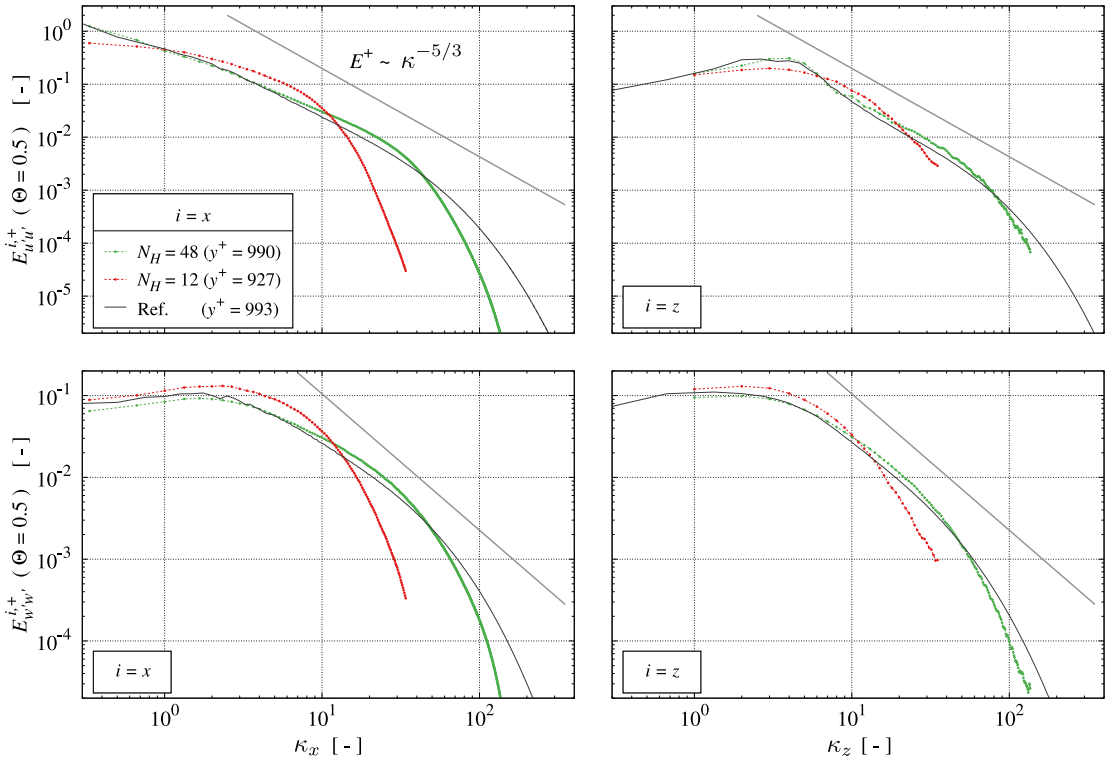

Figure 6.61: Stream- (left) and spanwise (right) turbulent energy spectra for $\vartheta = \{\overline{u'u'}; \overline{w'w'}\}$ (top; bottom) obtained from fine [green] and coarse [red] resolution for $\mathrm{Re}_\tau = 2000$ at $\Theta = 0.5$.

confirm the finding of the previous discussion, i.e., grid coarsening reduces the resolved part of the inertial range to $\kappa_x \lesssim 20$ and introduces an earlier onset of TKE dissipation. Nonetheless, the low-frequency dynamics is still captured as also outlined by Fig. 6.62.

Application to $\mathrm{Re}_\tau = 5200$

To convey the capabilities of the present suggestion, complementary results for a Reynolds number of $\mathrm{Re}_\tau = 5200$ are involved. To this end, Fig. 6.63 displays the predictions of the mean flow (left) and shear stress contributions (right), supplemented by the Reynolds normal stresses depicted in Fig. 6.64. The employed wall function refers to $u^+(y^+) = \ln(y^+)/0.39 + 4.7$ which is in line with the reference of Lee and Moser [2015]. Due to the enhanced y^+-related wall distance of the first fluid node, the buffer zone and transition

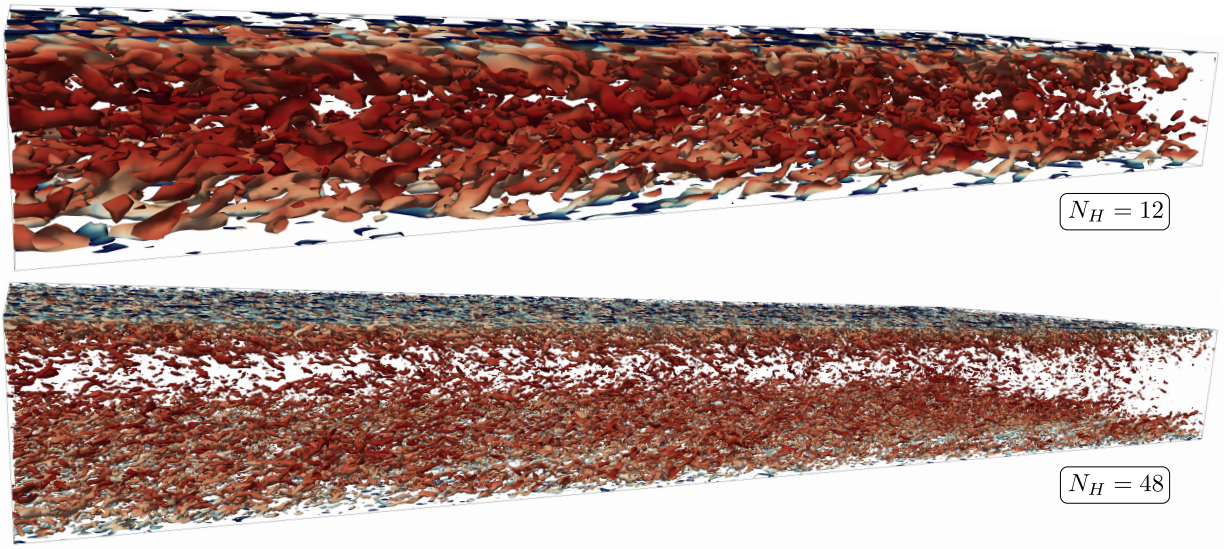

Figure 6.62: Illustration of turbulent structures based on the nondimensional streamwise vorticity component $\omega_x^+ = (\partial w/\partial y - \partial v/\partial z)\ N_H/u_\tau$ for $\mathrm{Re}_\tau = 2000$ obtained from the coarse (top) and fine (bottom) grid. Displayed isosurfaces refer to $0.2\omega_{x,\mathrm{max}}^+$ and are colored by the velocity magnitude.

influences diminish, and the predictive agreement with DNS data slightly improves in direct comparison to $\mathrm{Re}_\tau = 2000$.

Additionally, Appendix C outlines a comparison of mean velocities and resolved Reynolds stresses against a conventional constant Smagorinsky LES approach using $\mathcal{C}_\mathrm{S} = 0.15$, which is often used in industrial applications. The comparison refers to $\mathrm{Re}_\tau = \{180; 550; 2000\}$ and reveals the benefits of the present approach, in particular an improved level of resolved stresses. The overshoot phenomenon is also observed for $\mathrm{Re}_\tau = 2000$ with the conventional approach, but related near-wall predictions clearly deteriorate for lower Reynolds numbers and improved resolutions.

Conclusions

The previous PHF investigations, cf. Sec. 6.1, already displayed a remarkable turbulence prediction capability of the initial C-P model by Geier et al. [2017a], where, except for the general regularization of the parameterized $\omega_{\{3;4;5\}}$ rates, no dedicated turbulence model is needed in well-resolved flows featuring $\Delta x^+ \lesssim 10$. However, this threshold still distinctly constrains the C-P application for coarse resolutions, which quickly occur at higher Reynolds numbers, i.e., flows of technical interest. To this end, the two building block modifications introduced in the present section aim to advance these limits. Firstly, an alternative regularization of the parameterized third-order relaxation rates is suggested, which is deemed sufficient to dissipate the TKE of the high-wave number turbulent scales and accurately computes flows with fine to moderate resolutions characterized by $\Delta x^+ \lesssim 20$. Secondly, a third-order cumulant expression is employed to formulate a local dynamic Smagorinsky-type SGS model that acts on lower wave numbers, gradually retreats toward the DNS limit, and provides the necessary subgrid scale contributions for (very) coarse resolutions. Both enhancements are sensitized to the resolution through

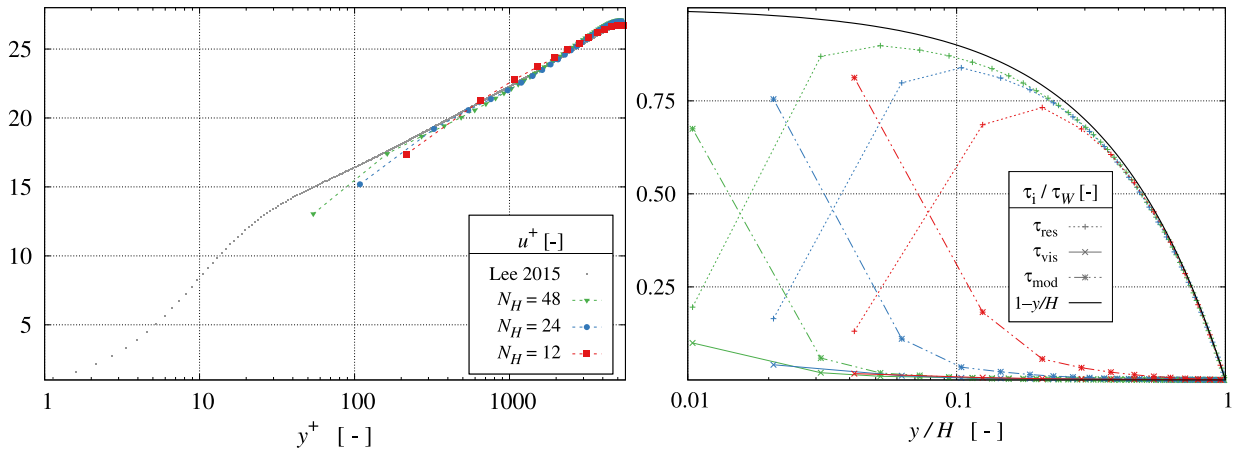

Figure 6.63: Nondimensional mean velocity profiles (left) and shear stress contributions (right) for $\mathrm{Re}_\tau = 5200$.

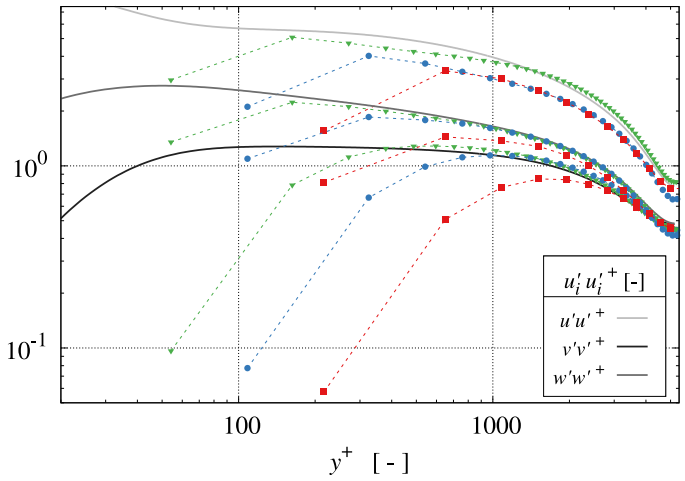

Figure 6.64: Resolved Reynolds normal stresses for $\mathrm{Re}_\tau = 5200$.

the cell Reynolds number (spatial) and the Mach number (temporal). The modifications' influences seamlessly vanish for highly-resolved grids and interact favorably with the investigated cases. Furthermore, the coupling to a wall function involves minimal additional efforts and supports the consistent transition to the fine-grid limit.

The benchmark of the advanced C-P model is comprehensively assessed by TCF simulations originating from low Reynolds numbers ($\mathrm{Re}_\tau = 180$), involving close to DNS resolutions with $\Delta x^+ < 4$, and extent to computationally more demanding Reynolds numbers ($\mathrm{Re}_\tau = 5200$) featuring coarsest resolutions of $\Delta x^+ > 400$, using isotropic homogeneous Cartesian grids. The verification studies indicate the modified C-P model's remarkable robustness and predictive performance. A remaining deficit refers to the interaction between the SGS model and the wall function, where the dynamic character of the SGS model suffers from the missing dynamics of the wall function in coarse resolutions, viz. $\Delta x^+ \gtrsim 30$. Since the very near-wall eddy viscosity is predicted to be too small, an overshoot of the predicted velocity gradient between the two wall-nearest nodes is induced to balance the resolved shear in the interior. However, this does not significantly harm the remainder of the flow, and the prediction of the turbulent dynamics rapidly recovers toward the interior

flow, which is also supported by the high Reynolds number studies.

6.3 Turbulent Wall Model

Figure 6.65 displays exemplary mean flow results (left), supplemented by the averaged resolved, viscous, and modeled turbulent shear stress contributions (right) obtained from the modified, i.e, employing the limiter adjustment and dynamic SGS model of Sec. 6.2, C-P approach for the TCF at $\mathrm{Re}_\tau = \{180; 2000\}$. Both of these simulations were performed on a homogeneous, isotropic, Cartesian grid using $N_H = 24$ nodes per half-channel height. The figure reveals a remaining issue of the modified C-P model near the wall for $\mathrm{Re}_\tau = 2000$ [red], where a velocity overshoot phenomenon, e.g., cf. Brasseur and Wei [2010] or Asmuth et al. [2021], is observed. For the higher Reynolds number, the resolved stresses suffer from the missing dynamics of the wall function, and the predicted wall-adjacent modeled stresses are too small. As a consequence, the gradient of the mean flow is overpredicted near the wall to compensate for the underestimated turbulent stresses.

Similar results are present for other Reynolds numbers in Fig. 6.47, where the problem is particularly prominent for $\Delta x^+ > 20$. Related misinterpretations of the averaged flow field might yield substantially wrong predictions of the wall shear stress and heat transfer rate at higher Reynolds number flows of engineering interest. Depending on the local flow situation, the modeled shear stress contributions are up to 30% wrong in response to the overshoot phenomenon.

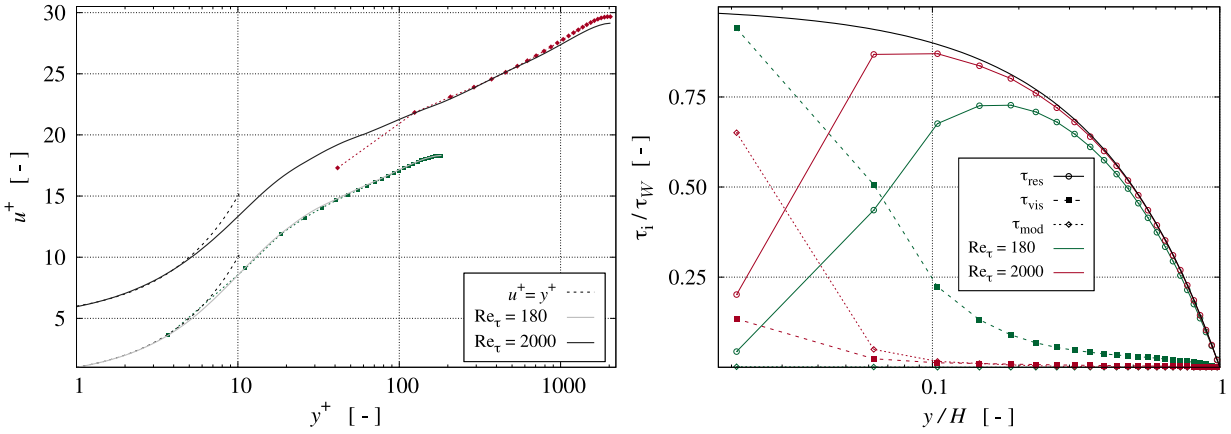

Figure 6.65: Comparison of predicted nondimensional mean velocity profiles $u^+(y^+)$ obtained by the modified C-P for $N_H = 24$ along the half-channel height [linked symbols] and DNS [solid lines] references (left). To improve the presentation, the mean velocity profile for $\mathrm{Re}_\tau = 2000$ is shifted by $\Delta u^+ = 5$ velocity units in vertical direction. Evolution of the (averaged) resolved [solid/circles], viscous [dashed/squares], modeled [dotted/diamonds] and total [black line] normalized shear stress contributions (right).

The approach introduced below tries to convey the merits of a simple (virtual) wall positioning method that adjusts the location of the wall between the solid node and the first fluid node to the resolution, thereby neutralizing the overshoot phenomenon. Supplementary, the further enriched C-P model is assessed for very high Reynolds numbers and coarse resolutions that reach up to 45 grid points between the top and bottom walls

of a channel flow at $\mathrm{Re}_B \approx 1.7 \cdot 10^6$ besides providing guidelines on meaningful resolution limits. It is to be noted that the upper $\mathcal{C}_{\mathrm{LES}}$ threshold of (6.19) comes into effect for $\mathrm{Re}_{\Delta x} \approx 3250$ or $\Delta x^+ \approx 130$ for the present Mach number of $\mathrm{Ma} = 0.1$. The resolution sensitivity of the proposed combination of regularization (cf. Sec. 6.2.1), subgrid scale model (cf. Sec. 6.2.2) and universal wall function (present) allows activating these three features irrespective of the resolution quality without additional user input, i.e., for DNS, LES, and VLES simulations close to classical URANS.

6.3.1 Verification Specifics

The investigated TCF dimensions agree with those from the previous study, i.e., $6\pi H$ in stream- (x), $2\pi H$ in spanwise (z) and $2H$ in wall-normal direction (y). Two additional higher Reynolds numbers are employed for analyzing the modified C-P capabilities, cf. Tab. 6.12 besides all further verification specifics.

Table 6.12: Test case specifications for the turbulent wall model verification.

	Specification
Test case	TCF at $\mathrm{Re}_\tau = \{180; 550; 2000; 5200; 20000; 50000\}$
	$\rightarrow \mathrm{Re}_B \approx \{2750; 9900; 43900; 129200; 602500; 1717000\}$
Reference data	• Moser et al. [1999] and Kim et al. [1987] for $\mathrm{Re}_\tau = 180$
	• Bernardini et al. [2014] for $\mathrm{Re}_\tau = \{550; 2000\}$
	• Lee and Moser [2015] for $\mathrm{Re}_\tau = \{2000\}$
Collision Model	C-P with **proposed regularization**, cf. Sec. 6.2.1
Turbulence Modeling	**proposed dynamic cumulant-based** SGS, cf. Sec. 6.2.2
Wall Modeling	IMEM of Asmuth et al. [2021] with
	• C^1 reference polyonmials, cf. Appendix B
	• log law specification (for $\mathrm{Re}_\tau \geq 5200$)
	employing the **proposed virtual wall shift**
Wall BC	IBB with $q \equiv 0.5$
Physical quantities	$\nu_P = 1.5 \cdot 10^{-5}\,\mathrm{m^2 s^{-1}}$, $H = 0.05\,\mathrm{m}$
Domain size	$6\pi H(x) \times 2\pi H(z) \times 2H(y)$
Δx^+	$\{4, \ldots, 2200\}$
Ma	1/10

The investigations are performed on various grids characterized by the resolution of the half-channel height (N_H) and support investigating an extensive range of nondimensional resolutions, i.e., $4 \lesssim \Delta x^+ \lesssim 2200$. As indicated by Tab. 6.13, each Reynolds number is investigated on four grids that coarsen from dark green to red. The selected resolutions aim at an approximately equal change in Δx^+ while considering resolutions of particular interest. The Mach number is assigned to $\mathrm{Ma} = 0.1$ in response to previously reported investigations, and the simulation sequence, i.e., the number of flow passes (FP), is equivalent to that from Sec. 6.2.3.

Table 6.13: Summary of the investigated grids, nondimensional lattice spacings $\Delta x^+(\mathrm{Re}_\tau, N_H)$ and color codes of Fig. 6.70.

Re_τ	180		550		2 000		5 200		20 000		50 000	
Re_B	2 800		9 900		43 400		129 200		602 500		1 717 000	
	N_H	Δx^+	N_H	Δx^+	N_H	Δx^+	N_H	Δx^+	N_H	Δx^+	N_H	Δx^+
■	48	3.8	29	19	36	56	24	220	36	555	48	1 040
▲	24	7.5	24	23	24	83	18	290	29	690	36	1 390
●	18	10	16	34	17	118	14	370	24	825	29	1 740
◆	12	15	12	46	12	167	12	430	21	960	23	2 170

6.3.2 Results and Discussion

As indicated by selected results shown in Fig. 6.65, fair average velocities, Reynolds stresses, spectra and correlation lengths were reported for $\mathrm{Re}_B \approx \{2800, \ldots, 130000\}$ using the modified C-P model formulation described in Sec. 6.2.4. An exception refers to significant overestimated near-wall gradients for the higher Reynolds numbers. This deficit is related to the wall model's interference with the cumulant-based SGS model, wherefore a straightforward enhancement is sought that alleviates these deficits.

To understand the rationale of the suggested correction, it is essential to note that the second fluid node serves as a reference location for constructing the wall function. The latter iteratively computes a consistent shear stress τ_W in line with the velocity prediction. Thus, the related (instantaneous) shear stress velocity $u_\tau = \sqrt{|\tau_W|/\rho)}$ provides a valid $< y_2 u_\tau/\nu, u_2/u_\tau >$ combination at the second fluid node for a given wall distance y_2 and a simulated (instantaneous) velocity u_2 at this node. The alteration consists of virtually manipulating the first fluid node's nondimensional wall distance y_1^+ from its standard value of $y_1^+ = \Delta x^+/2$, i.e., without changing the actual grid, cf. sketch in Fig. 6.66 (left). Since no deficits occur for an adequate resolution of the near-wall regime at all, no wall distance modification is required for $\Delta x^+ \leq 15$. A comprehensive parameter study is performed for a wide range of Reynolds numbers $\mathrm{Re}_\tau = \{550, \ldots, 50000\}$ to compile the appropriate wall location shift. As indicated by the circles in both representations of Fig. 6.66, a fair correlation for an adequate near-wall distance of the first fluid node reads

$$y_1^+(\Delta x^+) = \Delta x^+ \begin{cases} 0.5\,, & \Delta x^+ \leq 15 \\ 0.15\,(1 + 35/\Delta x^+)\,, & \Delta x^+ > 15 \end{cases}. \tag{6.26}$$

On the one hand, this virtual shift of the y^+ origin reduces the wall distance. On the other hand, the relative reduction decreases with increasing distance, and the manipulation substantially shifts the wall distance of the first fluid node. At the same time, the reduced distance increases the third-order cumulant expression at the first fluid node inside the Smagorinsky parameter $\mathcal{C}_\mathrm{S}$ (6.16) roughly linearly for high Reynolds number flows, cf. Fig. 6.67 (right) and the derivation of the regularization term in Sec. 6.2.1. This yields an increase in the eddy viscosity $\nu_t = (\mathcal{C}_\mathrm{S}^2\Delta)^2\,\overline{S}$ that approximately scales with $\mathcal{C}_\mathrm{S}^2$, cf. Fig. 6.67 (left) and Fig. 6.68 (left).

As indicated by Fig. 6.69 (left), the velocity gradient between the solid node and the reference second fluid node, i.e., the centered velocity gradient at the first fluid node,

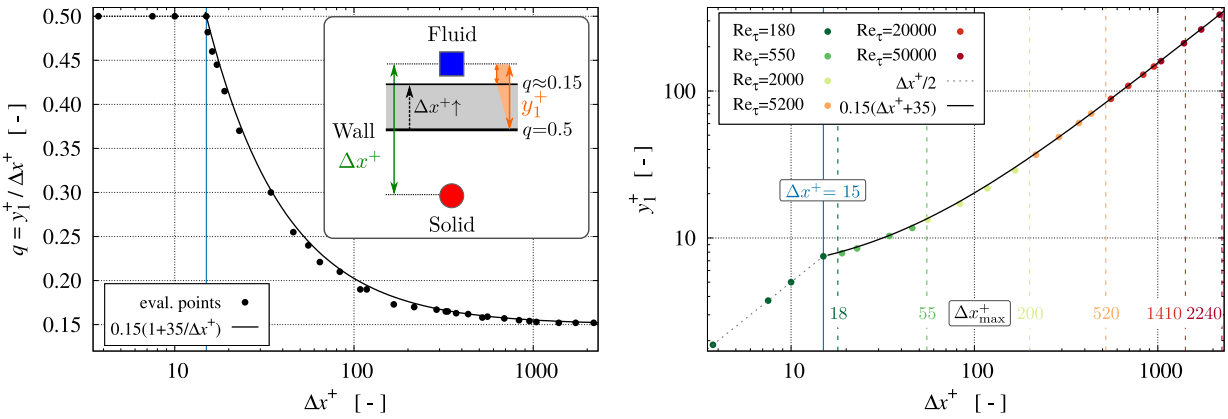

Figure 6.66: Evolution of the suggested nondimensional wall distance of the wall-adjacent fluid node y_1^+ in normalized (left) and non-normalized (right) format, depending on the grid resolution Δx^+ as described in (6.26). Colored dots display evaluated discrete y_1^+ optima of each Reynolds number and grid. Furthermore, the reasonable maximum (6.27) for each of the underlying Reynolds numbers is illustrated by colored dashed vertical lines.

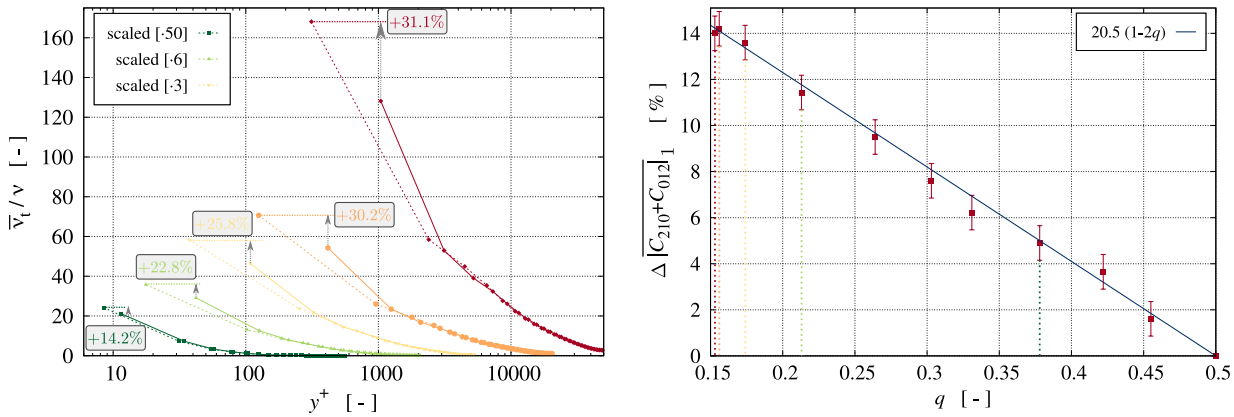

Figure 6.67: Comparison of the normalized predicted (averaged) eddy viscosity obtained from a centered ($q = 0.5$) wall location [solid] and an adjusted wall location [dotted] for $\mathrm{Re}_\tau = \{550; 2000; 5200; 20000; 50000\}$ on the $N_H = 24$ grid (left). Increase in the (averaged) cumulant expression $\overline{|C_{210} + C_{012}|}_1$ at the first fluid node as a function of the wall location parameter $q = y_1^+/\Delta x^+$ (right). Error bars refer to $\Delta\overline{|C_{210} + C_{012}|}_1 \pm 0.75\%$. Colored verticals correspond to the modified q values of (**a**), whereas further data points refer to $\mathrm{Re}_\tau = 550$ simulations employing $N_H = \{12; 16; 19; 29; 32\}$ from left to right.

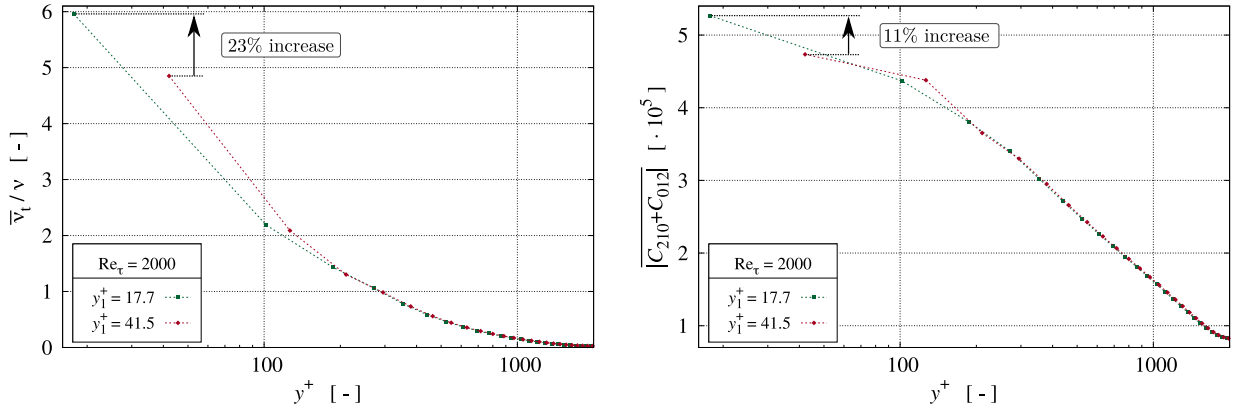

Figure 6.68: Increase in the normalized (averaged) eddy viscosity (left) the related change in the (averaged) cumulant expression (right) at the first fluid node in response to a shift in the wall position as per (6.26) for $\mathrm{Re}_\tau = 2000$ with a full lattice spacing of $\Delta x^+ = 83$.

does virtually not change. The latter is supported by the example given in Fig. 6.68 and Fig. 6.69, where $|\tau_{\mathrm{mod}}| = \nu_t \, \overline{S} = \mathcal{C}_{\mathrm{S}}^2 \, \Delta^2 \, \overline{S}^2$ increases by 24% in response to a 23% increase in the eddy viscosity and an 11% augmentation of $\mathcal{C}_{\mathrm{S}}$. The unaltered strain rate at the first fluid node is crucial to control the modeled stress by the mere change in the third-order cumulant expression $|C_{210} + C_{012}|_1$ at the first fluid node in response to the shift in the wall location while leaving the grid and the numerical approach unchanged. It is also noted that

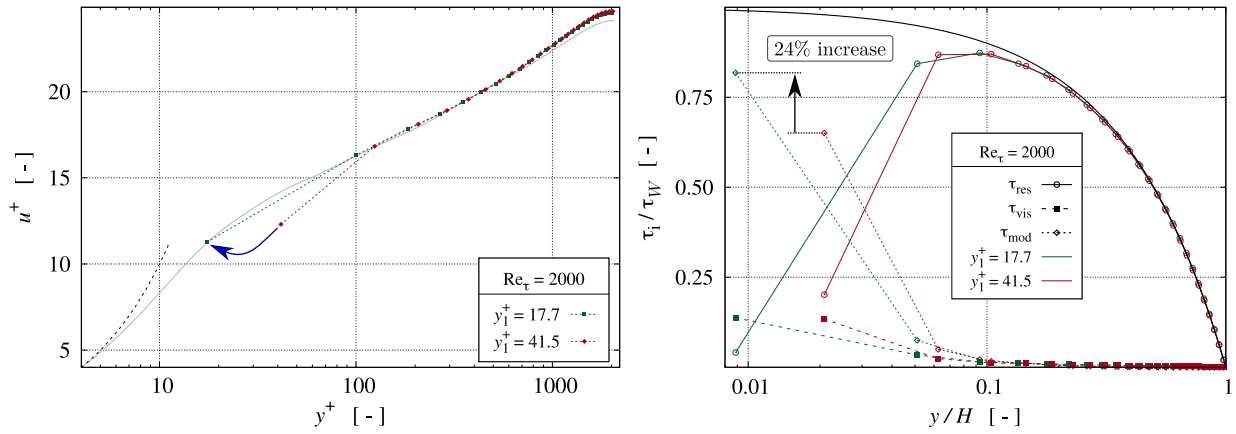

Figure 6.69: Nondimensional mean velocity profiles for $\mathrm{Re}_\tau = 2000$ on a grid featuring $\Delta x^+ = 83$ (left). The red velocity graph coincides with the red graph in Fig. 6.65 (left) and refers to the standard grid layout with $y_1^+(\Delta x^+) = 0.5\,\Delta x^+ \neq y_1^+(\Delta x^+, \mathrm{Re}_\tau)$. The green curve depicts results from the suggested $y_1^+(\Delta x^+, \mathrm{Re}_\tau) = 0.15 \Delta x^+ \, (1 + 35/\Delta x^+)$ manipulation, cf. (6.26). The overshoot vanishes when the modeled shear stress increases due to an increase in the eddy viscosity, as displayed by the normalized τ_i partition pathlines (right).

the influence of the suggested wall positioning modification is almost exclusively restricted to the computed eddy viscosity (and the cumulants) at the first fluid node, cf. Fig. 6.67 (left), which, therefore, can be interpreted as a local adjustment of the SGS model to the

wall function.

Figure 6.70 displays the predicted nondimensional mean velocity profiles of the three lower (top) and higher (bottom) Reynolds numbers, respectively. In the top figure, solid

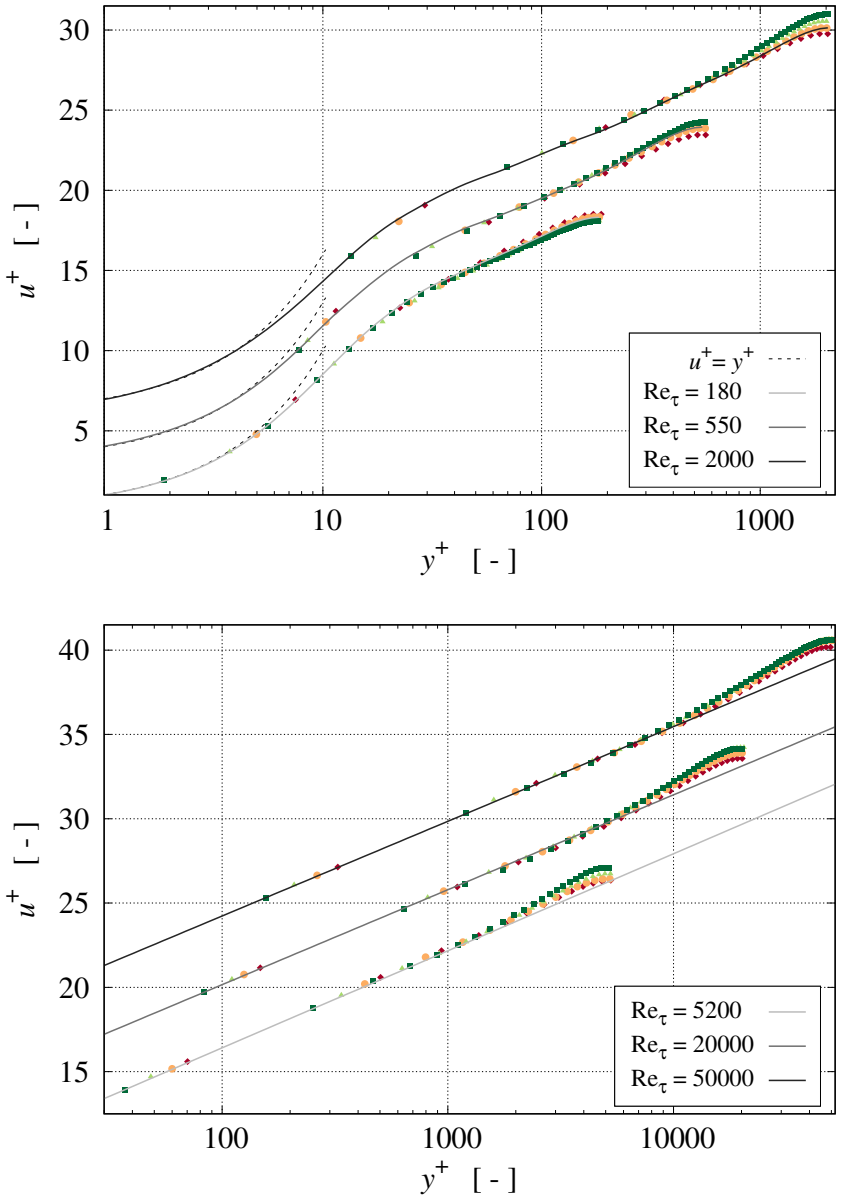

Figure 6.70: Nondimensional mean velocity profiles for three lower (top) and higher (bottom) Reynolds numbers.

grayscaled lines refer to reconstructions of discrete reference data sets, cf. Appendix B. To improve the comparison, the profiles for $\mathrm{Re}_\tau = 550\,[2000]$ are vertically shifted by $\Delta u^+ = 3\,[6]$. In the bottom figure, with ascending Re_τ the characteristic parameters of the log law, $u^+(y^+) = \ln(y^+)/\kappa + C^+$, are $\kappa(\mathrm{Re}_\tau) = \{0.40; 0.41; 0.41\}$ and $C^+(\mathrm{Re}_\tau) = \{4.9; 4.9; 5.0\}$. Likewise, the profiles for $\mathrm{Re}_\tau = 20000$ [50000] are vertically shifted by $\Delta u^+ = 4\,[8]$. All results are obtained by adjusting the wall location according to (6.26).

Since all wall-adjacent nodes are located above the buffer layer for the higher Reynolds

numbers displayed in Fig. 6.70 (bottom), the lower bound of the abscissa is set to $y^+ = 30$ in order to emphasize the logarithmic layer and the wake flow. The characteristic of the logarithmic layer is in fair predictive agreement with the parameters reported by Nikitin et al. [2000] for turbulent channel flow LES up to $\mathrm{Re}_\tau = 80000$ indicated with $\kappa = 0.41$ and $C^+ = 5.2$. Further analysis of the mean flow profiles reveals the sensitivity of the present extended C-P model to predict wake flows, cf. Coles [1956], depending on the resolution. In line with previous LES or DES simulations, e.g., those of Cabot et al. [1999] or Keating and Piomelli [2006], the present modified C-P model also portrays an attenuation of the wake flow when the resolution is coarsened. The latter is caused by a weaker reduction in the resolved stresses in the outer regime of the boundary layer, as illustrated in Fig. 6.71. Mind

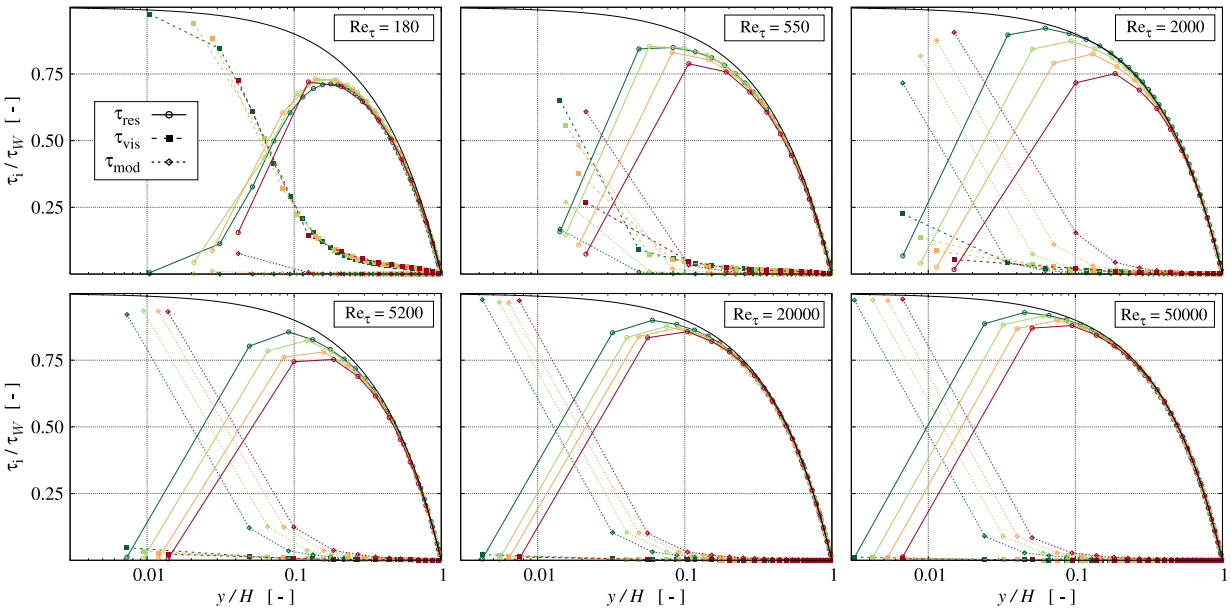

Figure 6.71: Comparison of the (averaged) nondimensional resolved [solid/circles], viscous [dashed/squares], and modeled [dotted/diamonds] shear stress contributions extended by the linear total stress relation $\tau_{\mathrm{tot}}/\tau_W = 1 - y/H$ [solid black].

that wake flow occurs beyond a critical Reynolds number, e.g., $\mathrm{Re}_\tau \geq 1000$, cf. Schultz and Flack [2013], and, hence, no substantial grid sensitivity is observed for the two lower Reynolds numbers in Fig. 6.70 (top). Furthermore, no significant change in the reduction in resolved stress toward the exterior boundary layer region is displayed in Fig. 6.71 (top left; top center) when the grid is coarsened. The analysis of the wake prediction yields a heuristic criterion for the maximum grid coarseness, i.e., $\Delta x^+_{\mathrm{max}} = \Delta x^+_{\mathrm{max}}(\mathrm{Re}_\tau)$, through

$$\Delta x^+_{\mathrm{max}} = \begin{cases} \mathrm{Re}_\tau/10\,, & \mathrm{Re}_\tau \lesssim 10^4 \quad [\,\text{capture wake}\,] \\ 10\sqrt{\mathrm{Re}_\tau}\,, & \mathrm{Re}_\tau > 10^4 \quad [\,\text{capture wake \& maintain validity of (6.26)}\,] \end{cases} . \tag{6.27}$$

For the investigated Reynolds numbers $\mathrm{Re}_\tau = \{180; 550; 2000; 5200; 20000; 50000\}$, the coarsest resolutions derived from (6.27) read $\Delta x^+_{\mathrm{max}}(\mathrm{Re}_\tau) = \{18; 55; 200; 520; 1410; 2240\}$, which are close to the coarsest (◆) investigated discretizations, cf. Tab. 6.13.

Conclusions

The proposed universal wall function resolves the priorly remaining overshoot deficit. To this end, the virtual adjustment of the wall-adjacent fluid node's wall distance comes at negligible computational expenses and favorably influences the near-wall cumulant expressions, employed to attain a resolution-sensitive formulation of the SGS model. The manipulation yields the required interplay between the wall function and the SGS model nearby the wall.

To render the predictive benefits, attention is devoted to a comprehensive range of bulk Reynolds numbers of $\mathrm{Re}_B \approx \{3 \cdot 10^3, \ldots, 1.7 \cdot 10^6\}$ on grids between $4.5 \cdot 10^5$ and $2.7 \cdot 10^7$ nodes that feature resolutions of $\Delta x^+ \approx \{4, \ldots, 2200\}$. The results indicate that the unified model is able to capture all investigated turbulent channel flows without further adjustments or user input.

7 Summary and Outlook

This thesis scrutinized different lattice Boltzmann method (LBM) collision models for the simulation of turbulent shear flows and, in particular, aimed at defining meaningful resolution limits to capture all relevant flow physics adequately. As a result of the initially conducted studies, the entire focus is on a recently published model, i.e., the parameterized cumulant (C-P), which provides the most accurate and robust framework in its native implementation. The enhanced approach stands out due to its universality in efficiently simulating wall-modeled large eddy simulations (LES) of high Reynolds number flows based on a self-adaptive, seamless blend between resolving and modeling the turbulent motion without requiring additional user input.

The scrutinization commenced with wall-bounded turbulent channel flow (TCF) simulations at a low Reynolds number ensuring fully developed turbulence, i.e., $\mathrm{Re}_\tau = 180$ resp. $\mathrm{Re}_B = 2750$. The direct numerical simulations (DNS), employing about 115 million grid nodes, of three common collision models, i.e., the Bhatnagar, Gross and Krook (BGK), a multiple-relaxation-time (MRT), and the seminal – all-one – cumulant (C-AO), depict no fundamental deviations, where the major evaluated quantities are turbulent spectra, two-point correlations, and mean profile data enriched by instantaneous field data to judge structure sizes and possible instabilities visually. Results of the assessment change under grid coarsening, where, different from the cumulant model, the BGK and MRT models become unstable when the spatial discretization exceeds twice the Kolmogorov scale. The BGK model's instability originates in the outer buffer layer, whereas the MRT model starts to become unstable in the core flow. Without applying an LES closure, the reasonable limits read $\Delta x^+ = \{3.5; 4; 6\}$ for BGK, MRT, and C-AO. It was shown that the latter model also provides stable results distinctly beyond $\Delta x^+ > 6$. However, the structure sizes are far too large, and the mean velocity profile displays a deficient acceleration of the core flow in these cases. Hence, the wall-adjacent fluid node at $y^+ = \Delta x^+/2$ has to be located within the viscous sublayer, which implies an exceedingly fine (uniform) Cartesian grid resolution and poses severe feasibility restrictions in an engineering context. When comparing the TCF and the decaying free-shear Taylor-Green vortex prediction accuracy of the two published cumulant models, i.e., the C-AO and C-P, the latter is clearly superior in slightly under-resolved conditions up to $\Delta x^+ = 18$. The identified potential was ascribed to the implicit LES capabilities of the eponymous parameterization and motivated more in-depth research of the C-P. Further investigations of the other collision models have been omitted thereafter as they were considered definitely inferior in achieving the strived goal of the work.

The subsequent studies addressed the C-P's properties in wall-resolved simulations of a periodic hill flow test case. The presence of flow separation and reattachment pose higher demands on the model than the simpler wall-bounded TCF requires. Grid studies revealed a strong potential for optimization regarding the regularization (or limiter) value acting on the model's parameterization. The constant default is usually assigned to a conservative

value of 10^{-2}, which provides abundant stability by introducing numerical damping for a wide range of resolutions. In its infinitesimal limit, the parameterization is turned off, and the C-P converges to the C-AO, hampering the resolution of the flow dynamics. To this end, increasing the default by maximal two orders of magnitude favorably affected the predictive accuracy in under-resolved conditions, i.e., $\Delta x^+ < 30$. It has been shown that the regularization acts like a stability ensuring (turbulence) model, which is confined to the dissipative upper-frequency or large wave number part of the energy spectrum. Since the formulation strongly differs from a traditional explicit LES model, the resolution-dependent interplay of the parameterization and regularization is ascribed to the C-P collision model's inherent, implicit LES capability. A multitude of simulations sampling various spatial and temporal resolutions for $700 \leq \mathrm{Re}_B \leq 37000$ employing different limiter values lead to an alternative semi-empirical formulation of the native implementation. The proposed approach is resolution-sensitive by incorporating the spatial discretization through the cell Reynolds number, i.e., $\mathrm{Re}_{\Delta x} = u\Delta x/\nu$ and the temporal increment by the Mach number. In addition to these constant simulation input parameters, which usually always have to be specified, dynamic runtime cumulant expressions are involved in completing the self-adaptive optimization ansatz.

An explicit LES model was introduced to extend the resolution limit. To this end, the renowned algebraic Smagorinksky-Lilly closure was employed in a modified form. The latter refers to replacing the constant Smagorinsky parameter with a dynamic one, closely oriented to the aforementioned resolution-sensitive limiter approach. Moreover, a wall function had to be added since, due to the underlying uniform Cartesian grid layout, wall-resolved simulations are unrealizable for the targeted high Reynolds number flows employing efficiently coarse grids. The interplay of the developed components, i.e., the resolution-sensitive approaches for the limiter and subgrid scale (SGS) model combined with the selected wall modeling scheme, was tested for TCF simulations for Reynolds numbers up to $\mathrm{Re}_\tau = 5200$, where the coarsest resolution was $\Delta x^+ = 430$. Although results mainly indicated a remarkable predictive performance, a deficit related to the interaction between the proposed dynamic SGS model and the wall function, which lacked flow dynamics, inevitably caused erroneous predictions of the near-wall gradients, while the remainder of the flow was not significantly harmed.

Adjusting the employed wall function was the last component ultimately allowing for overall consistent wall-modeled LES, where a virtual shift of the wall position induces the missing near-wall dynamics. Finally, the approach considering all developed modifications and enhancements was tested for TCF simulations up to $\mathrm{Re}_\tau = 50000$ ($\mathrm{Re}_B = 1.7 \cdot 10^6$) featuring a maximum isotropic grid spacing of $\Delta x^+ \approx 2200$. It is noted that the evolved approach is constrained to plane walls since the wall function requires a costly generalization next.

To make the developed LBM framework factually suitable for real industrial flows involving complex geometries, **future research** efforts inevitably have to address the severe open issue regarding the geometric generalization of the wall function. The current framework involving the dynamic SGS model interacting with the enhanced virtual wall function is limited to planar axis-aligned boundaries. Thus, arbitrarily shaped geometries can only partially make use of all developed features, as the periodic hill flow test case demonstrates, which includes wall curvatures and only employs the SGS modeling and omits the wall modeling. Once a general solution is successfully derived and implemented,

the next step can include the application-based simulation of profiles, e.g., NACA airfoils or marine propeller blades at various Reynolds numbers and different angles of attack. Far-reaching future simulations might endeavor aerodynamic analyses, e.g., of the generic *Ahmed body* car-type model, cf. Ahmed et al. [1984], and also hydrodynamic investigations, e.g., considering the generic *DARPA suboff* underwater vehicle, cf. Groves et al. [1989], are conceivable.

A Employed Multiple-Relaxation-Time Model

The D3Q19 transformation matrix of Tölke et al. [2006] from particle distribution space to moment space reads

$$\boldsymbol{M} = \tag{A.1}$$

$$\begin{bmatrix}
1\cdot(& 1 & 1 & 1 & 1 & 1 & 1 & 1 & 1 & 1 & 1 & 1 & 1 & 1 & 1 & 1 & 1 & 1 & 1 & 1)\\
c^2\cdot(& -1 & 0 & 0 & 0 & 0 & 0 & 0 & 1 & 1 & 1 & 1 & 1 & 1 & 1 & 1 & 1 & 1 & 1 & 1)\\
c^4\cdot(& 1 & -2 & -2 & -2 & -2 & -2 & -2 & 1 & 1 & 1 & 1 & 1 & 1 & 1 & 1 & 1 & 1 & 1 & 1)\\
c\cdot(& 0 & 1 & -1 & 0 & 0 & 0 & 0 & 1 & -1 & 1 & -1 & 1 & -1 & 1 & -1 & 0 & 0 & 0 & 0)\\
c^3\cdot(& 0 & -2 & 2 & 0 & 0 & 0 & 0 & 1 & -1 & 1 & -1 & 1 & -1 & 1 & -1 & 0 & 0 & 0 & 0)\\
c\cdot(& 0 & 0 & 0 & 1 & -1 & 0 & 0 & 1 & -1 & -1 & 1 & 0 & 0 & 0 & 0 & 1 & -1 & 1 & -1)\\
c^3\cdot(& 0 & 0 & 0 & -2 & 2 & 0 & 0 & 1 & -1 & -1 & 1 & 0 & 0 & 0 & 0 & 1 & -1 & 1 & -1)\\
c\cdot(& 0 & 0 & 0 & 0 & 0 & 1 & -1 & 0 & 0 & 0 & 0 & 1 & -1 & -1 & 1 & 1 & -1 & -1 & 1)\\
c^3\cdot(& 0 & 0 & 0 & 0 & 0 & -2 & 2 & 0 & 0 & 0 & 0 & 1 & -1 & -1 & 1 & 1 & -1 & -1 & 1)\\
c^2\cdot(& 0 & 2 & 2 & -1 & -1 & -1 & -1 & 1 & 1 & 1 & 1 & 1 & 1 & 1 & 1 & -2 & -2 & -2 & -2)\\
c^4\cdot(& 0 & -2 & -2 & 1 & 1 & 1 & 1 & 1 & 1 & 1 & 1 & 1 & 1 & 1 & 1 & -2 & -2 & -2 & -2)\\
c^2\cdot(& 0 & 0 & 0 & 1 & 1 & -1 & -1 & 1 & 1 & 1 & 1 & -1 & -1 & -1 & -1 & 0 & 0 & 0 & 0)\\
c^4\cdot(& 0 & 0 & 0 & -1 & -1 & 1 & 1 & 1 & 1 & 1 & 1 & -1 & -1 & -1 & -1 & 0 & 0 & 0 & 0)\\
c^2\cdot(& 0 & 0 & 0 & 0 & 0 & 0 & 0 & 1 & 1 & -1 & -1 & 0 & 0 & 0 & 0 & 0 & 0 & 0 & 0)\\
c^2\cdot(& 0 & 0 & 0 & 0 & 0 & 0 & 0 & 0 & 0 & 0 & 0 & 0 & 0 & 0 & 0 & 1 & 1 & -1 & -1)\\
c^2\cdot(& 0 & 0 & 0 & 0 & 0 & 0 & 0 & 0 & 0 & 0 & 0 & 1 & 1 & -1 & -1 & 0 & 0 & 0 & 0)\\
c^3\cdot(& 0 & 0 & 0 & 0 & 0 & 0 & 0 & 1 & -1 & 1 & -1 & -1 & 1 & -1 & 1 & 0 & 0 & 0 & 0)\\
c^3\cdot(& 0 & 0 & 0 & 0 & 0 & 0 & 0 & -1 & 1 & 1 & -1 & 0 & 0 & 0 & 0 & 1 & -1 & 1 & -1)\\
c^3\cdot(& 0 & 0 & 0 & 0 & 0 & 0 & 0 & 0 & 0 & 0 & 0 & 1 & -1 & -1 & 1 & -1 & 1 & 1 & -1)
\end{bmatrix}$$

with the lattice speed defined via $c = \Delta x/\Delta t$, which gives $c = 1$, assuming spatial and temporal unit spacings. The resulting moments are termed

$$\boldsymbol{m} = (\rho, e, \epsilon, j_x, q_x, j_y, q_y, j_z, q_z, 3p_{xx}, 3\pi_{xx}, p_{ww}, \pi_{ww}, p_{xy}, p_{yz}, p_{xz}, m_x, m_y, m_z)^\intercal\ . \tag{A.2}$$

The equilibrium moments depending on macroscopic flow quantities, i.e., a constant reference density (ρ_0), the density variation (ρ), and the velocity vector, viz. $u_\mathrm{i} = (u, v, w)^\intercal$, are defined as

$$\begin{aligned}
&m_1^\mathrm{eq} = \rho, \quad m_2^\mathrm{eq} = e^\mathrm{eq} = \rho_0\left(u^2+v^2+w^2\right), \quad m_4^\mathrm{eq} = \rho_0 u, \quad m_6^\mathrm{eq} = \rho_0 v, \quad m_8^\mathrm{eq} = \rho_0\, w,\\
&m_{10}^\mathrm{eq} = 3p_{xx}^\mathrm{eq} = \rho_0\left(2u^2-v^2-w^2\right), \quad m_{12}^\mathrm{eq} = p_{zz}^\mathrm{eq} = \rho_0\left(v^2-w^2\right),\\
&m_{14}^\mathrm{eq} = p_{xy}^\mathrm{eq} = \rho_0\, uv, \quad m_{15}^\mathrm{eq} = p_{yz}^\mathrm{eq} = \rho_0\, vw, \quad m_{16}^\mathrm{eq} = p_{xz}^\mathrm{eq} = \rho_0\, uw,\\
&m_3^\mathrm{eq} = m_5^\mathrm{eq} = m_7^\mathrm{eq} = m_9^\mathrm{eq} = m_{11}^\mathrm{eq} = m_{13}^\mathrm{eq} = m_{17}^\mathrm{eq} = m_{18}^\mathrm{eq} = m_{19}^\mathrm{eq} = 0\,.
\end{aligned} \tag{A.3}$$

The diagonal matrix containing the collision rates reads

$$\boldsymbol{S} = \mathrm{diag}(0, s_a, s_b, 0, s_c, 0, s_c, 0, s_c, s_\omega, s_d, s_\omega, s_d, s_\omega, s_\omega, s_\omega, s_e, s_e, s_e)\,, \tag{A.4}$$

wherein $s_\omega = -\Delta t/\tau = -\omega$ is linked to shear viscosity and $s_a, s_b, s_c, s_d, s_e \in [-2, 0]$, each to be chosen freely, depending on the specific flow under consideration. In line with Tölke et al. [2006] the present MRT studies use $s_a = s_b = s_c = s_d = s_e = \max(s_\omega, -1)$.

B Wall Function Polynomials

The C^1-polynomials $u^+_{\mathrm{Re}_\tau}(y^+)$, cf. Fig. B.1, deposited in the wall function approach, cf. Sec. 3.1.5, are given by (rounded to two decimal places)

$$u^+_{180}(y^+) = \begin{cases} -1.69 \cdot 10^{-3}(y^+)^3 + 1.95 \cdot 10^{-3}(y^+)^2 + 9.96 \cdot 10^{-1} y^+ + 7.68 \cdot 10^{-4} & y^+ < 7 \\ +5.57 \cdot 10^{-4}(y^+)^3 - 4.38 \cdot 10^{-2}(y^+)^2 + 1.30 \cdot 10^{0} \;\; y^+ - 6.58 \cdot 10^{-1} & 7 \leq y^+ < 20 \\ +1.47 \cdot 10^{-4}(y^+)^3 - 1.72 \cdot 10^{-2}(y^+)^2 + 7.40 \cdot 10^{-1} y^+ + 3.17 \cdot 10^{0} & 20 \leq y^+ < 40 \\ +5.95 \cdot 10^{-6}(y^+)^3 - 1.51 \cdot 10^{-3}(y^+)^2 + 1.60 \cdot 10^{-1} y^+ + 1.03 \cdot 10^{1} & 40 \leq y^+ < 80 \\ -4.89 \cdot 10^{-8}(y^+)^3 - 1.43 \cdot 10^{-4}(y^+)^2 + 5.75 \cdot 10^{-2} y^+ + 1.29 \cdot 10^{1} & 80 \leq y^+ < 180 \end{cases} \tag{B.1}$$

$$u^+_{550}(y^+) = \begin{cases} -7.03 \cdot 10^{-4}(y^+)^3 - 1.40 \cdot 10^{-2}(y^+)^2 + 1.07 \cdot 10^{0} \;\; y^+ - 1.77 \cdot 10^{-2} & y^+ < 12 \\ +2.93 \cdot 10^{-4}(y^+)^3 - 2.73 \cdot 10^{-2}(y^+)^2 + 9.54 \cdot 10^{-1} y^+ + 1.53 \cdot 10^{0} & 12 \leq y^+ < 28 \\ +2.52 \cdot 10^{-5}(y^+)^3 - 4.60 \cdot 10^{-3}(y^+)^2 + 3.14 \cdot 10^{-1} y^+ + 7.52 \cdot 10^{0} & 28 \leq y^+ < 53 \\ +5.75 \cdot 10^{-7}(y^+)^3 - 2.94 \cdot 10^{-4}(y^+)^2 + 6.64 \cdot 10^{-2} y^+ + 1.22 \cdot 10^{1} & 53 \leq y^+ < 143 \\ -3.15 \cdot 10^{-9}(y^+)^3 - 1.81 \cdot 10^{-5}(y^+)^2 + 2.25 \cdot 10^{-2} y^+ + 1.46 \cdot 10^{1} & 143 \leq y^+ < 550 \end{cases} \tag{B.2}$$

$$u^+_{2000}(y^+) = \begin{cases} +5.12 \cdot 10^{-4} \;(y^+)^3 - 4.06 \cdot 10^{-2}(y^+)^2 + 1.21 \cdot 10^{0} \;\; y^+ - 2.15 \cdot 10^{-1} & y^+ < 24 \\ +2.63 \cdot 10^{-5} \;(y^+)^3 - 4.73 \cdot 10^{-3}(y^+)^2 + 3.20 \cdot 10^{-1} y^+ + 7.17 \cdot 10^{0} & 24 \leq y^+ < 60 \\ +5.10 \cdot 10^{-7} \;(y^+)^3 - 2.91 \cdot 10^{-4}(y^+)^2 + 6.73 \cdot 10^{-2} y^+ + 1.19 \cdot 10^{1} & 60 \leq y^+ < 182 \\ +1.03 \cdot 10^{-8} \;(y^+)^3 - 2.25 \cdot 10^{-5}(y^+)^2 + 2.02 \cdot 10^{-2} y^+ + 1.46 \cdot 10^{1} & 182 \leq y^+ < 623 \\ -8.79 \cdot 10^{-11}(y^+)^3 - 1.10 \cdot 10^{-6}(y^+)^2 + 5.66 \cdot 10^{-3} y^+ + 1.79 \cdot 10^{1} & 623 \leq y^+ < 2000 \end{cases} \tag{B.3}$$

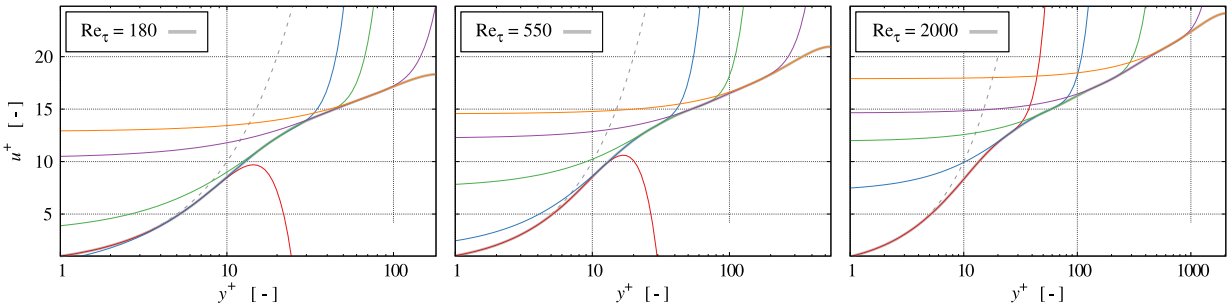

Figure B.1: Polynomial $u^+(y^+)$ reconstruction of the reference data from Kim et al. [1987] and Bernardini et al. [2014] for the three underlying Reynolds numbers $\mathrm{Re}_\tau = \{180; 550; 2000\}$.

C Subgrid Scale Model Comparison

Figures C.1 to C.3 compare the results obtained from the present dynamic cumulant-based (top) and a conventional (bottom) constant ($C_S = 0.15$) Smagorinsky approach for $\mathrm{Re}_\tau = \{180; 550; 2000\}$ (left; center; right) and $\mathrm{Ma} = 0.1$.

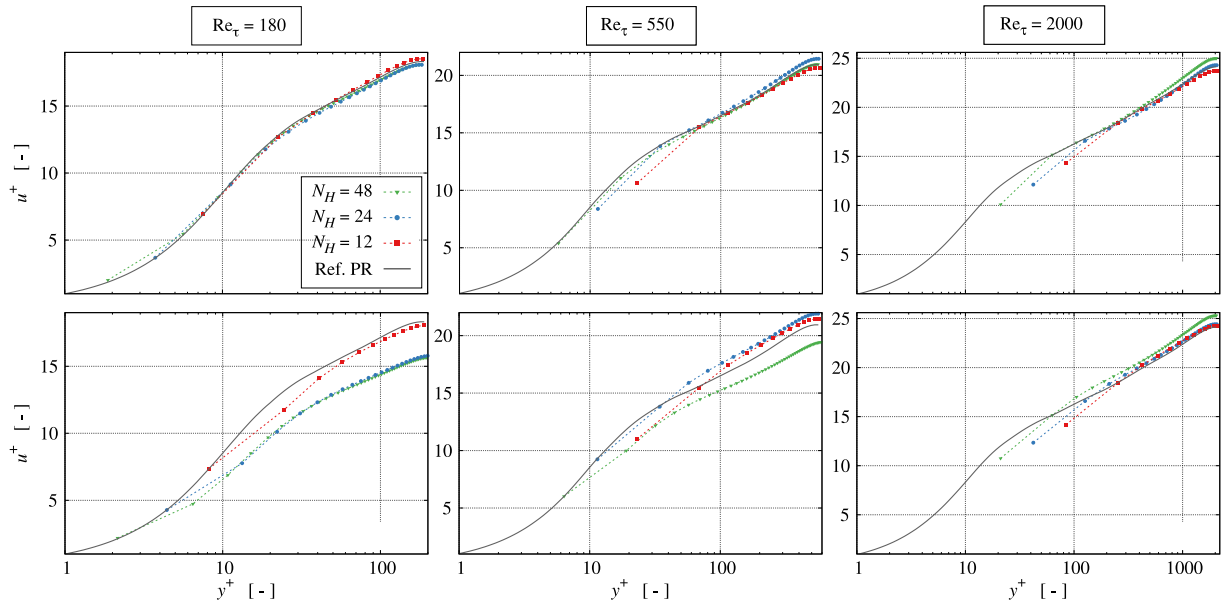

Figure C.1: Predicted mean velocity profiles in comparison with reference polynomial reconstructions (Ref. PR), cf. Appendix B.

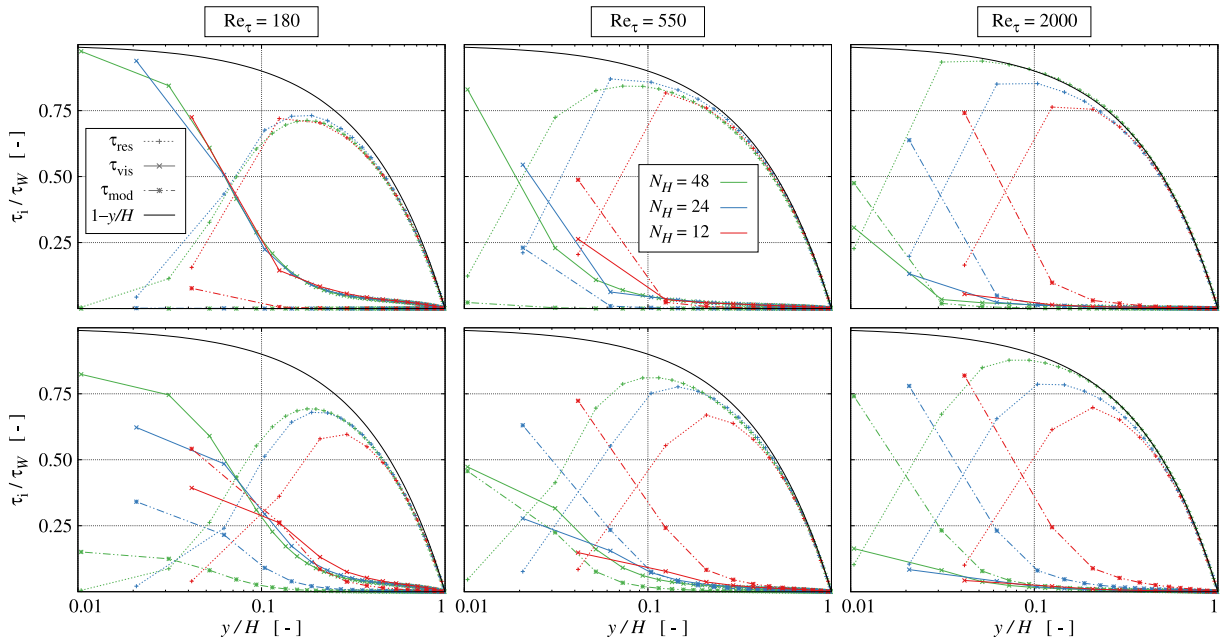

Figure C.2: Comparison of resolved [dotted], viscous [solid] and modeled [dashed] shear stress profiles with a linear total stress relation $\tau_i/\tau_W = 1 - y/H$ [solid black].

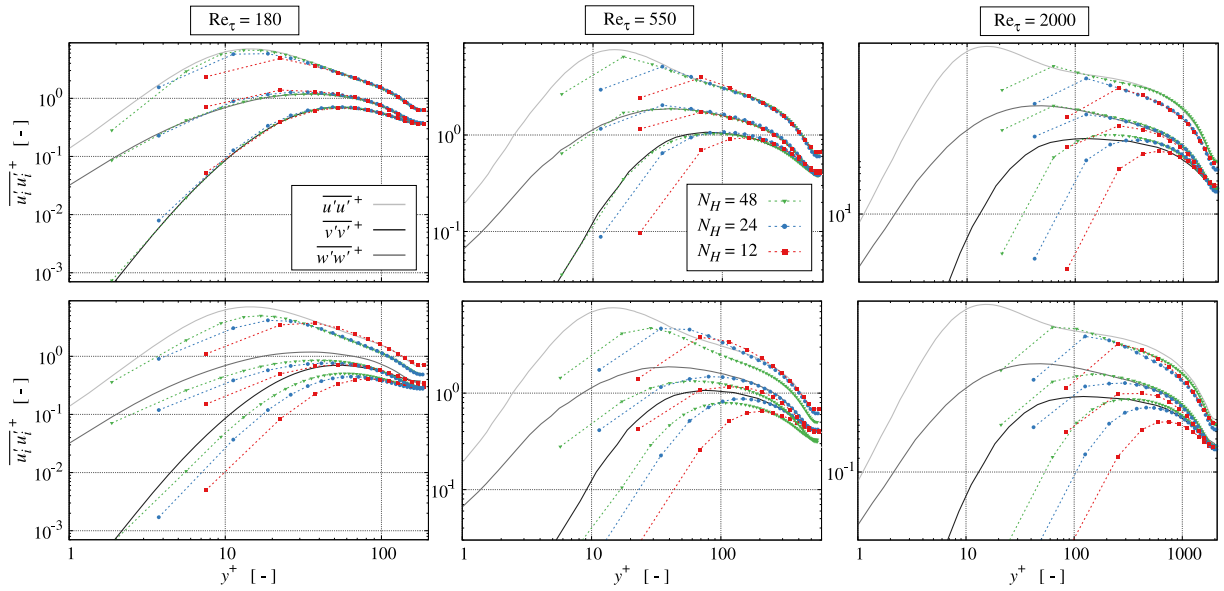

Figure C.3: Resolved Reynolds normal stress predictions supplemented by reference data.

Bibliography

W. Abdel Kareem, S. Izawa, A.-K. Xiong, and Y. Fukunishi. Lattice Boltzmann simulations of homogeneous isotropic turbulence. *Computers & Mathematics with Applications*, 58(5):1055–1061, 2009.

N.A. Adams and S. Hickel. Implicit Large-Eddy Simulation: Theory and Application. In B. Eckhardt, editor, *Advances in Turbulence XII*, volume 132 of *Springer Proceedings in Physics*, pages 743–750. Springer, Berlin Heidelberg, 2009.

S. Ahmed, G. Ramm, and G. Faltin. Some Salient Features of the Time-Averaged Ground Vehicle Wake. Technical Report 840300, SAE International, 1984.

C.K. Aidun and J.R. Clausen. Lattice-Boltzmann method for complex flows. *Annual Review of Fluid Mechanics*, 41(1):439–472, 2010.

J.D. Albertson and M.B. Parlange. Surface length scales and shear stress: Implications for land-atmosphere interaction over complex terrain. *Water Resources Research*, 35(7): 2121–2132, 1999.

G.P. Almeida, D.F.G. Durão, and M.V. Heitor. Wake flows behind two-dimensional model hills. *Experimental Thermal and Fluid Science*, 7(1):87–101, 1993.

G. Amati, S. Succi, and R. Piva. Massively Parallel Lattice-Boltzmann Simulation of Turbulent Channel Flow. *International Journal of Modern Physics C*, 8(4):869–877, 1997.

P. Asinari. Asymptotic analysis of multiple-relaxation-time lattice boltzmann schemes for mixture modeling. *Computers & Mathematics with Applications*, 55(7):1392–1407, 2008.

H. Asmuth. *Efficient Large-eddy Simulation for Wind Energy Applications*. PhD Dissertation, Uppsala University, 2022.

H. Asmuth, H. Olivares-Espinosa, K. Nilsson, and S. Ivanell. The Actuator Line Model in Lattice Boltzmann Frameworks: Numerical Sensitivity and Computational Performance. *Journal of Physics: Conference Series*, 1256(1):012022, 2019.

H. Asmuth, H. Olivares-Espinosa, and S. Ivanell. Actuator line simulations of wind turbine wakes using the lattice Boltzmann method. *Wind Energy Science*, 5(2):623–645, 2020.

H. Asmuth, C.F. Janßen, H. Olivares-Espinosa, and S. Ivanell. Wall-modeled lattice Boltzmann large-eddy simulation of neutral atmospheric boundary layers. *Physics of Fluids*, 33(10):105111, 2021.

G. Aubard, P. Stefanin Volpiani, X. Gloerfelt, and J.-C. Robinet. Comparison of Subgrid-scale Viscosity Models and Selective Filtering Strategy for Large-eddy Simulations. *Flow Turbulence and Combustion*, 91(3):497–518, 2013.

J.S. Baggett, J. Jiménez, and A.G. Kravchenko. Resolution requirements in large-eddy simulations of shear flows. In *Annual Research Briefs*, pages 51–66. Center for Turbulence Research, NASA / Stanford University, 1997.

A. Banari, M. Gehrke, C.F. Janßen, and T. Rung. Numerical simulation of nonlinear interactions in a naturally transitional flat plate boundary layer. *Computers & Fluids*, 203:104502, 2020.

S. Banerjee, R. Krahl, F. Durst, and C. Zenger. Presentation of anisotropy properties of turbulence, invariants versus eigenvalue approaches. *Journal of Turbulence*, 8:N32, 2007.

M. Bernardini, S. Pirozzoli, and P. Orlandi. Velocity statistics in turbulent channel flow up to $\mathrm{Re}_\tau = 4000$. *Journal of Fluid Mechanics*, 742:171–191, 2014.

D. Bespalko, A. Pollard, and M. Uddin. Analysis of the pressure fluctuations from an LBM simulation of turbulent channel flow. *Computers & Fluids*, 54:143–146, 2012.

P.L. Bhatnagar, E.P. Gross, and M. Krook. A Model for Collision Processes in Gases. I. Small Amplitude Processes in Charged and Neutral One-Component Systems. *Physical Review*, 94(3):511–525, 1954.

F. Bösch, S.S. Chikatamarla, and I.V. Karlin. Entropic multirelaxation lattice Boltzmann models for turbulent flows. *Physical Review E*, 92(4):043309, 2015.

J. Boudet, E. Lévôque, and H. Touil. Unsteady Lattice Boltzmann Simulations of Corner Separation in a Compressor Cascade. *Journal of Turbomachinery*, 144(1):011010, 2021.

M. Bouzidi, M. Firdaouss, and P. Lallemand. Momentum transfer of a Boltzmann-lattice fluid with boundaries. *Physics of Fluids*, 13(11):3452–3459, 2001.

M.E. Brachet, D.I. Meiron, S.A. Orszag, B.G. Nickel, R.H. Morf, and U. Frisch. Small-scale structure of the Taylor-Green vortex. *Journal of Fluid Mechanics*, 130:411–452, 1983.

P. Bradshaw. *An Introduction to Turbulence and its Measurement*. Pergamon Press, 1971.

J.G. Brasseur and T. Wei. Designing large-eddy simulation of the turbulent boundary layer to capture law-of-the-wall scaling. *Physics of Fluids*, 22(2):021303, 2010.

M. Breuer and W. Rodi. Large Eddy Simulation for Complex Turbulent Flows of Practical Interest. In E.H. Hirschel, editor, *Flow Simulation with High-Performance Computers II: DFG Priority Research Programme Results 1993–1995*, volume 48 of *Notes on Numerical Fluid Mechanics*, pages 258–274. Vieweg+Teubner Verlag, Wiesbaden, 1996.

M. Breuer, B. Jaffrézic, N. Peller, J. Manhart, M .and Fröhlich, C. Hinterberger, W. Rodi, G. Deng, O. Chikhaoui, S. Sarić, and S. Jakirlić. A Comparative Study of the Turbulent Flow Over a Periodic Arrangement of Smoothly Contoured Hills. In E. Lamballais,

R. Friedrich, B.J. Geurts, and O.J. Métais, editors, *Direct and Large-Eddy Simulation VI*, 6th International ERCOFTAC Workshop on Direct and Large-Eddy Simulation, September 12–14, Poitiers, France, pages 635–642. Springer Netherlands, Dordrecht, 2006.

M. Breuer, N. Peller, C. Rapp, and M. Manhart. Flow over periodic hills – numerical and experimental study in a wide range of Reynolds numbers. *Computers & Fluids*, 38(2): 433–457, 2009.

E. Buckingham. On Physically Similar Systems; Illustrations of the Use of Dimensional Equations. *Physical Review*, 4(4):345–376, 1914.

J. M. Buick and C.A. Greated. Gravity in a lattice Boltzmann model. *Physical Review E*, 61(5):5307–5320, 2000.

W. Cabot and P. Moin. Approximate Wall Boundary Conditions in the Large-Eddy Simulation of High Reynolds Number Flow. *Flow, Turbulence and Combustion*, 63:269–291, 2000.

W. Cabot, J. Jiménez, and J.S. Baggett. On wakes and near-wall behavior in coarse large-eddy simulation of channel flow with wall models and second-order finite-difference methods. In *Annual Research Briefs*, pages 343–354. Center for Turbulence Research, NASA / Stanford University, 1999.

P.-H. Chang, C.-C. Liao, H.-W. Hsu, S.-H. Liu, and C.-A. Lin. Simulations of laminar and turbulent flows over periodic hills with immersed boundary method. *Computers & Fluids*, 92:233–243, 2014.

S. Chapman and T.G. Cowling. *The Mathematical Theory of Non-uniform Gases: An Account of the Kinetic Theory of Viscosity, Thermal Conduction, and Diffusion in Gases.* Cambridge University Press, 1970.

H. Chen, S.A. Orszag, I. Staroselsky, and S. Succi. Expanded analogy between boltzmann kinetic theory of fluids and turbulence. *Journal of Fluid Mechanics*, 519:301–314, 2004.

S. Chen and G.D. Doolen. Lattice Boltzmann method for fluid flows. *Annual Review of Fluid Mechanics*, 30(1):329–364, 1998.

Y. Chen, Q. Cai, Z. Xia, M. Wang, and S. Chen. Momentum-exchange method in lattice Boltzmann simulations of particle-fluid interactions. *Physical Review E*, 88(1):013303, 2013.

S.S. Chikatamarla, C.E. Frouzakis, I.V. Karlin, A.G. Tomboulides, and K.B. Boulouchos. Lattice Boltzmann method for direct numerical simulation of turbulent flows. *Journal of Fluid Mechanics*, 656:298–308, 2010.

H. Choi and P. Moin. Grid-point requirements for large eddy simulation: Chapman's estimates revisited. *Physics of Fluids*, 24(1):011702, 2012.

K.-S. Choi and J.L. Lumley. The return to isotropy of homogeneous turbulence. *Journal of Fluid Mechanics*, 436:59–84, 2001.

D. Chung and D.I. Pullin. Large-eddy simulation and wall modelling of turbulent channel flow. *Journal of Fluid Mechanics*, 631:281–309, 2009.

D.E. Coles. The law of the wake in the turbulent boundary layer. *Journal of Fluid Mechanics*, 1(2):191–226, 1956.

J.W. Cooley and J.W. Tukey. An algorithm for the machine calculation of complex Fourier series. *Mathematics of Computation*, 19:297–301, 1965.

C. Coreixas, G. Wissocq, B. Chopard, and J. Latt. Impact of collision models on the physical properties and the stability of lattice Boltzmann methods. *Philosophical Transactions of the Royal Society A*, 378(2175):20190397, 2020.

R. Dean. Reynolds number dependence of skin friction and other bulk flow variables in two-dimensional rectangular duct flow. *Journal of Fluids Engineering*, 100(2):215–223, 1978.

J.W. Deardorff. A numerical study of three-dimensional turbulent channel flow at large Reynolds numbers. *Journal of Fluid Mechanics*, 41(2):453–480, 1970.

S. Deck. Zonal-Detached-Eddy Simulation of the Flow Around a High-Lift Configuration. *AIAA Journal*, 43(11):2372–2384, 2005.

J. Degrigny, S.-H. Cai, J.-F. Boussuge, and P. Sagaut. Improved wall model treatment for aerodynamic flows in LBM. *Computers & Fluids*, 227:105041, 2021.

P.J. Dellar. Nonhydrodynamic modes and a priori construction of shallow water lattice Boltzmann equations. *Physical Review E*, 65(3):036309, 2002.

D. d'Humières, I. Ginzburg, M. Krafczyk, P. Lallemand, and L.-S. Luo. Multiple-relaxation-time lattice Boltzmann models in three dimensions. *Philosophical Transactions of the Royal Society A*, 360(1792):437–451, 2002.

Y.-H. Dong, P. Sagaut, and S. Marié. Inertial consistent subgrid model for large-eddy simulation based on the lattice Boltzmann method. *Physics of Fluids*, 20(3):035104, 2008.

D. Dorschner, F. Bösch, S.S. Chikatamarla, and I.V. Karlin. Entropic multi-relaxation time lattice Boltzmann model for complex flows. *Journal of Fluid Mechanics*, 801:623–651, 2016.

Y. Dubief and F. Delcayre. On coherent-vortex identification in turbulence. *Journal of Turbulence*, 1:N11, 2000.

E.K. Far, M. Geier, K. Kutscher, and M. Krafczyk. Simulation of micro aggregate breakage in turbulent flows by the cumulant lattice Boltzmann method. *Computers & Fluids*, 140: 222–231, 2016.

D. Fauconnier, C. Bogey, and E. Dick. On the performance of relaxation filtering for large-eddy simulation. *Journal of Turbulence*, 14(1):22–49, 2013.

C. Feichtinger, J. Habich, H. Köstler, G. Hager, U. Rüde, and G. Wellein. A flexible Patch-based lattice Boltzmann parallelization approach for heterogeneous GPU-CPU clusters. *Parallel Computing*, 37(9):536–549, 2011.

Y. Feng, J. Miranda-Fuentes, S. Guo, J. Jacob, and P. Sagaut. ProLB: A lattice Boltzmann Solver of Large-Eddy Simulation for Atmospheric Boundary Layer Flows. *Journal of Advances in Modeling Earth Systems*, 13(3):e2020MS002107, 2021.

R.K. Freitas, A. Henze, M. Meinke, and W. Schröder. Analysis of Lattice-Boltzmann methods for internal flows. *Computers & Fluids*, 47(1):115–121, 2011.

J. Fröhlich. *Large Eddy Simulation turbulenter Strömungen*. B.G. Teubner Verlag, Wiesbaden, 2006.

J. Fröhlich, C.P. Mellen, W. Rodi, L. Temmerman, and M.A. Leschziner. Highly resolved large-eddy simulation of separated flow in a channel with streamwise periodic constrictions. *Journal of Fluid Mechanics*, 526:19–66, 2005.

M. Gaedtke, S. Wachter, M. Rädle, H. Nirschl, and M.J. Krause. Application of a lattice Boltzmann method combined with a Smagorinsky turbulence model to spatially resolved heat flux inside a refrigerated vehicle. *Computers & Mathematics with Applications*, 76 (10):2315–2329, 2020.

W. Gao, W. Zhang, W. Cheng, and R. Samtaney. Wall-modelled large-eddy simulation of turbulent flow past airfoils. *Journal of Fluid Mechanics*, 873:174–210, 2019.

W. Gao, W. Cheng, and R. Samtaney. Large-eddy simulations of turbulent flow in a channel with streamwise periodic constrictions. *Journal of Fluid Mechanics*, 900:A43, 2020.

M. Gehrke and T. Rung. Periodic hill flow simulations with a parameterized cumulant lattice Boltzmann method. *International Journal for Numerical Methods in Fluids*, 94 (8):1111–1154, 2022a.

M. Gehrke and T. Rung. Scale-resolving turbulent channel flow simulations using a dynamic cumulant lattice Boltzmann method. *Physics of Fluids*, 34(7):075129, 2022b.

M. Gehrke and T. Rung. Scrutinizing Dynamic Cumulant Lattice Boltzmann Large Eddy Simulations for Turbulent Channel Flows. *Computation*, 10(10):171, 2022c.

M. Gehrke, C.F. Janßen, and T. Rung. Three-dimensional applications of a GPU-accelerated numerical wind tunnel. In *13th International Conference for Mesoscopic Methods in Engineering and Science, July 18–22, Hamburg, Germany*, (Poster), 2016.

M. Gehrke, C.F. Janßen, and T. Rung. Scrutinizing lattice Boltzmann methods for direct numerical simulations of turbulent channel flows. *Computers & Fluids*, 156:247–263, 2017a.

M. Gehrke, D. Mierke, C.F. Janßen, and T. Rung. GPU-accelerated LBM-VOF two-phase flow simulations with grid refinement. In *7th International Conference on Computational Methods in Marine Engineering, May 15–17, Nantes, France*, (Presentation), 2017b.

M. Gehrke, D. Mierke, T. Rung, and P. Hauer. Validation of a GPU-Accelerated LBM Based Numerical Ice Tank for a Voith Schneider Propulsion System. In *8th International Conference on Computational Methods in Marine Engineering, May 13–15, Gothenburg, Sweden*, (Presentation), 2019.

M. Gehrke, A. Banari, and T. Rung. Performance of Under-Resolved, Model-Free LBM Simulations in Turbulent Shear Flows. In Y. Hoarau, S.-H. Peng, D. Schwamborn, A. Revell, and C. Mockett, editors, *Progress in Hybrid RANS-LES Modelling*, volume 143 of *Notes on Numerical Fluid Mechanics and Multidisciplinary Design*, pages 3–18. Springer International Publishing, Cham, 2020.

M. Geier, A. Greiner, and J.G. Korvink. Cascaded digital lattice Boltzmann automata for high Reynolds number flow. *Physical Review E*, 73(6):066705, 2006.

M. Geier, M. Schönherr, A. Pasquali, and M. Krafczyk. The cumulant lattice Boltzmann equation in three dimensions: Theory and validation. *Computers & Mathematics with Applications*, 70(4):507–547, 2015.

M. Geier, A. Pasquali, and M. Schönherr. Parametrization of the cumulant lattice Boltzmann method for fourth order accurate diffusion part I: Derivation and validation. *Journal of Computational Physics*, 348:862–888, 2017a.

M. Geier, A. Pasquali, and M. Schönherr. Parametrization of the cumulant lattice Boltzmann method for fourth order accurate diffusion part II: Application to flow around a sphere at drag crisis. *Journal of Computational Physics*, 348:889–898, 2017b.

M. Geier, S. Lenz, M. Schönherr, and M. Krafczyk. Under-resolved and large eddy simulations of a decaying taylor-green vortex with the cumulant lattice boltzmann method. *Theoretical and Computational Fluid Dynamics*, 35(2):169–208, 2021.

W.K. George. Is there a universal log law for turbulent wall-bounded flows? *Philosophical Transactions of the Royal Society A*, 365(1852):789–806, 2007.

M. Germano, U. Piomelli, P. Moin, and W.H. Cabot. A dynamic subgrid-scale eddy viscosity model. *Physics of Fluids A: Fluid Dynamics*, 3(7):1760–1765, 1991.

S. Ghosal, T. Lund, P. Moin, and K. Akselvoll. A dynamic localization model for large-eddy simulation of turbulent flows. *Journal of Fluid Mechanics*, 286:229–255, 1995.

I. Ginzburg and P.M. Adler. Boundary flow condition analysis for the three-dimensional lattice Boltzmann model. *Journal de Physique II*, 4(2):191–214, 1994.

I. Ginzburg, F. Verhaeghe, and D. d'Humières. Two-Relaxation-Time Lattice Boltzmann Scheme: About Parametrization, Velocity, Pressure and Mixed Boundary Conditions. *Communications in Computational Physics*, 3(2):427–478, 2008a.

I. Ginzburg, F. Verhaeghe, and D. d'Humières. Study of Simple Hydrodynamic Solutions with the Two-Relaxation-Times Lattice Boltzmann Scheme. *Communications in Computational Physics*, 3(3):519–581, 2008b.

S.S. Girimaji. Boltzmann Kinetic Equation for Filtered Fluid Turbulence. *Physical Review Letters*, 99(3):034501, 2007.

S.S. Girimaji, W. Haase, S.-H. Peng, and D. Schwamborn, editors. *Proceedings of the 5th Symposium on Hybrid RANS-LES Methods, 19–21 March 2014, College Station, Texas*, volume 130 of *Notes on Numerical Fluid Mechanics and Multidisciplinary Design*, 2015. Springer Cham.

X. Gloerfelt and P. Cinnella. Large Eddy Simulation Requirements for the Flow over Periodic Hills. *Flow Turbulence and Combustion*, 103(1):55–91, 2019.

E. Goraki Fard. *A Cumulant LBM approach for Large Eddy Simulation of Dispersion Microsystems*. PhD Dissertation, Technische Universität Braunschweig, 2015.

N.C. Groves, T.T. Huang, and M.S. Chang. Geometrical characteristics of DARPA SUBOFF models (DTRC Model Nos. 5470 and 5471). Technical Report DTRC/SHD-1298-01, David Taylor Reseach Center, 1989.

Z. Guo, C. Zheng, and B. Shi. Discrete lattice effects on the forcing term in the lattice Boltzmann method. *Physical Review E*, 65(4):046308, 2002.

M. Han, R. Ooka, and H. Kikumoto. Lattice Boltzmann method-based large-eddy simulation of indoor isothermal airflow. *International Journal of Heat and Fluid Flow*, 130: 700–709, 2019.

M. Han, R. Ooka, and H. Kikumoto. A wall function approach in lattice Boltzmann method: algorithm and validation using turbulent channel flow. *Fluid Dynamics Research*, 53(4):045506, 2021a.

M. Han, R. Ooka, and H. Kikumoto. Effects of wall function model in lattice Boltzmann method-based large-eddy simulation on built environment flows. *Building and Environment*, 195:107764, 2021b.

F.J. Harris. On the use of windows for harmonic analysis with the discrete Fourier transform. *Proceedings of the IEEE*, 66(1):51–83, 1978.

Y. Hasegawa, T. Aoki, H. Kobayashi, and K. Shirasaki. Large-scale LES analysis for aerodynamics of a group of racing bicycles by lattice Boltzmann method. *Transactions of the JSME (in Japanese)*, 85(870):00441, 2019.

F. Haussmann, M .and Ries, J.B. Jeppener-Haltenhoff, Y. Li, M. Schmidt, C. Welch, L. Illmann, B. Böhm, H. Nirschl, M.J. Krause, and A. Sadiki. Evaluation of a Near-Wall-Modeled Large Eddy Lattice Boltzmann Method for the Analysis of Complex Flows Relevant to IC Engines. *Computation*, 8(2):43, 2020.

M. Haussmann, A. Claro Barreto, G. Lipeme Kouyi, N. Rivière, H. Nirschl, and M.J. Krause. Large-eddy simulation coupled with wall models for turbulent channel flows at high Reynolds numbers with a lattice Boltzmann method - Application to Coriolis mass flowmeter. *Computers & Mathematics with Applications*, 78(10):3285–3302, 2019.

X. He and L.-S. Luo. Theory of the lattice Boltzmann method: From the Boltzmann equation to the lattice Boltzmann equation. *Physical Review E*, 56:6811–6817, 1997.

X. He, Q. Zou, L.-S. Luo, and M. Dembo. Analytic Solutions of Simple Flows and Analysis of Nonslip Boundary Conditions for the Lattice Boltzmann BGK Model. *Journal of Statistical Physics*, 87:115–136, 1997.

S. Hickel, N.A. Adams, and J.A. Domaradzki. An adaptive local deconvolution method for implicit LES. *Journal of Computational Physics*, 213(1):413–436, 2006.

J.O. Hinze. *Turbulence*. McGraw-Hill New York, 1959.

Y. Hoarau, S.-H. Peng, D. Schwamborn, and A. Revell, editors. *Proceedings of the 6th Symposium on Hybrid RANS-LES Methods, 26–28 September 2016, Strasbourg, France*, volume 137 of *Notes on Numerical Fluid Mechanics and Multidisciplinary Design*, 2018. Springer Cham.

S. Hou, J.D. Sterling, S. Chen, and G.D. Doolen. A lattice Boltzmann subgrid model for high Reynolds number flows. In A.T. Lawniczak and Kapral R., editors, *Pattern Formation and Lattice Gas Automata*, volume 6 of *Fields Institute Communications*, pages 151–166. American Mathematical Society, 1996.

K. Jacobs. *Neuere Methoden und Ergebnisse der Ergodentheorie*. Ergebnisse der Mathematik und ihrer Grenzgebiete. 2. Folge. Springer Berlin Heidelberg, 1960.

L. Jahanshaloo, E. Pouryazdanpanah, and N.A. Che Sidik. A Review on the Application of the Lattice Boltzmann Method for Turbulent Flow Simulation. *Numerical Heat Transfer, Part A: Applications*, 64(11):938–953, 2013.

C.F. Janßen. *Kinetic approaches for the simulation of non-linear free surface flow problems in civil and environmental engineering*. PhD Dissertation, Technische Universität Braunschweig, 2010.

C.F. Janßen and M. Krafczyk. A lattice Boltzmann approach for free-surface-flow simulations on non-uniform block-structured grids. *Computers & Mathematics with Applications*, 59(7):2215–2235, 2010.

C.F. Janßen and M. Krafczyk. Free surface flow simulations on GPGPUs using the LBM. *Computers & Mathematics with Applications*, 61(12):3549–3563, 2011.

C.F. Janßen, S.T. Grilli, and M. Krafczyk. On enhanced non-linear free surface flow simulations with a hybrid LBM-VOF model. *Computers & Mathematics with Applications*, 65(2):211–229, 2013.

C.F. Janßen, D. Mierke, M. Überrück, S. Gralher, and T. Rung. Validation of the GPU-Accelerated CFD Solver ELBE for Free Surface Flow Problems in Civil and Environmental Engineering. *Computation*, 3(3):354–385, 2015.

C.F. Janßen, D. Mierke, and T. Rung. On the development of an efficient numerical ice tank for the simulation of fluid-ship-rigid-ice interactions on graphics processing units. *Computers & Fluids*, 155:22–32, 2017.

M. Junk. A finite difference interpretation of the lattice Boltzmann method. *Numerical Methods for Partial Differential Equations*, 17(4):383–402, 2001.

C.J. Kähler, S. Scharnowski, and C. Cierpka. Highly resolved experimental results of the separated flow in a channel with streamwise periodic constrictions. *Journal of Fluid Mechanics*, 796:257–284, 2016.

I.V. Karlin, A. Ferrante, and H.C. Öttinger. Perfect entropy functions of the Lattice Boltzmann method. *Europhysics Letters*, 47:182, 1999.

I.V. Karlin, F. Bösch, and S.S. Chikatamarla. Gibbs' principle for the lattice-kinetic theory of fluid dynamics. *Physical Review E*, 90(3):031302, 2014.

S. Kawai and J. Larsson. Wall-modeling in large eddy simulation: Length scales, grid resolution, and accuracy. *Physics of Fluids*, 24(1):015105, 2012.

A. Keating and U. Piomelli. A dynamic stochastic forcing method as a wall-layer model for large-eddy simulation. *Journal of Turbulence*, 7:N12, 2006.

J. Kim, P. Moin, and R.D. Moser. Turbulence statistics in fully developed channel flow at low Reynolds number. *Journal of Fluid Mechanics*, 177:133–166, 1987.

S.J. Kline, D.E Coles, and E.A. Hirst, editors. *Proceedings of the AFOSR-IFP conference, 19–24 August 1968, Stanford, California*, Computation of Turbulent Boundary Layers, 1969. Stanford University, Thermosciences Division.

A.N. Kolmogorov, V. Levin, J.C.R. Hunt, O.M. Phillips, and D. Williams. The local structure of turbulence in incompressible viscous fluid for very large reynolds numbers. *Proceedings of the Royal Society of London. Series A: Mathematical, Physical and Engineering Sciences*, 434(1890):9–13, 1991a.

A.N. Kolmogorov, V. Levin, J.C.R. Hunt, O.M. Phillips, and D. Williams. Dissipation of energy in the locally isotropic turbulence. *Proceedings of the Royal Society of London. Series A: Mathematical, Physical and Engineering Sciences*, 434(1890):15–17, 1991b.

R. Kotapati, A. Keatin, S. Kandasamy, B. Duncan, R. Shock, and H. Chen. The Lattice-Boltzmann-VLES Method for Automotive Fluid Dynamics Simulation, a Review. Technical Report 2009-26-0057, SAE International, 2009.

M. Krafczyk, J. Tölke, and L.-S. Luo. Large-eddy simulations with a multiple-relaxation-time LBE model. *International Journal of Modern Physics B*, 17(1&2):33–39, 2003.

M. Krafczyk, K. Kutscher, Y. Wang, and M. Geier. DNS/LES Studies of Turbulent Flows Based on the Cumulant Lattice Boltzmann Approach. In W.E. Nagel, D.H. Kröner, and M.M. Resch, editors, *High Performance Computing in Science and Engineering '14*, pages 519–531. Springer International Publishing, Cham, 2015.

P. Lallemand and L.-S. Luo. Theory of the lattice Boltzmann method: Dispersion, dissipation, isotropy, Galilean invariance, and stability. *Physical Review*, 61(6):6546–6562, 2000.

P. Lammers, K.N. Beronov, R. Volkert, G. Brenner, and F. Durst. Lattice BGK direct numerical simulation of fully developed turbulence in incompressible plane channel flow. *Computers & Fluids*, 35(10):1137–1153, 2006.

J. Latt and B. Chopard. Lattice Boltzmann method with regularized pre-collision distribution functions. *Mathematics and Computers in Simulation*, 72(2–6):165–168, 2006.

J. Latt, O. Malaspinas, D. Kontaxakis, A. Parmigiani, D. Lagrava, F. Brogi, M.B. Belgacem, Y. Thorimbert, S. Leclaire, S. Li, F. Marson, J. Lemus, C. Kotsalos, R. Conradin, C. Coreixas, R. Petkantchin, F. Raynaud, J. Beny, and B. Chopard. Palabos: Parallel Lattice Boltzmann Solver. *Computers & Mathematics with Applications*, 81:334–350, 2021.

B.E. Launder and D.B. Spalding. The numerical computation of turbulent flows. *Computer Methods in Applied Mechanics and Engineering*, 3:269–289, 1974.

M. Lee and R.D. Moser. Direct numerical simulation of turbulent channel flow up to $\mathrm{Re}_\tau \approx 5200$. *Journal of Fluid Mechanics*, 774:395–415, 2015.

S. Lenz, M. Schönherr, M. Geier, M. Krafczyk, A. Pasquali, A. Christen, and M. Giometto. Towards real-time simulation of turbulent air flow over a resolved urban canopy using the cumulant lattice Boltzmann method on a GPGPU. *Journal of Wind Engineering and Industrial Aerodynamics*, 189:151–162, 2019.

A. Leonard. Energy Cascade in Large-Eddy Simulations of Turbulent Fluid Flows. In F.N. Frenkiel and R.E. Munn, editors, *Turbulent Diffusion in Environmental Pollution*, volume 18 of *Advances in Geophysics*, pages 237–248. Elsevier, 1975.

S. Li, X. Yang, G. Jin, and G. He. Wall-resolved large-eddy simulation of turbulent channel flows with rough walls. *Theoretical and Applied Mechanics Letters*, 11(1):100228, 2021.

D.K. Lilly. On the Application of the Eddy Viscosity Concept in the Inertial Sub-range of Turbulence. Technical Report NCAR-123, National Center for Atmospheric Research, Boulder, Colorado, 1966.

J.L. Lumley and G.R. Newman. The return to isotropy of homogeneous turbulence. *Journal of Fluid Mechanics*, 82(1):161–178, 1977.

H. Maeyama, T. Imamura, J. Osaka, and N. Kurimoto. Unsteady turbulent flow simulation using lattice Boltzmann method with near-wall modeling. In *AIAA Aviation 2020 Forum, June 15–19, Virtual Event*. American Institute of Aeronautics and Astronautics, 2020.

H. Maeyama, T. Imamura, J. Osaka, and N. Kurimoto. Turbulent channel flow simulations using the lattice Boltzmann method with near-wall modeling on a non-body-fitted Cartesian grid. *Computers & Mathematics with Applications*, 93:20–31, 2021a.

H. Maeyama, T. Imamura, J. Osaka, and N. Kurimoto. Application of Wall-modeled Large-eddy Simulation based on Lattice Boltzmann Method to External Flow Analyses. In *AIAA Scitech 2021 Forum, January 11-21, Virtual Event*. American Institute of Aeronautics and Astronautics, 2021b.

O. Malaspinas and P. Sagaut. Consistent subgrid scale modelling for lattice Boltzmann methods. *Journal of Fluid Mechanics*, 700:514–542, 2012.

O. Malaspinas and P. Sagaut. Wall model for large-eddy simulation based on the lattice Boltzmann method. *Journal of Computational Physics*, 275:25–40, 2014.

M. Manhart, F. Tremblay, and R. Friedrich. MGLET: a parallel code for efficient DNS and LES of complex geometries. In C.B. Jenssen, H.I. Andersson, A. Ecer, N. Satofuka, T. Kvamsdal, B. Pettersen, J. Periaux, and P. Fox, editors, *Parallel Computational Fluid Dynamics 2000*, pages 449–456. North-Holland, Amsterdam, 2001.

S. Marié and X. Gloerfelt. Adaptive filtering for the lattice Boltzmann method. *Journal of Computational Physics*, 333:212–229, 2017.

B. Maronga, C. Knigge, and S. Raasch. An Improved Surface Boundary Condition for Large-Eddy Simulations Based on Monin–Obukhov Similarity Theory: Evaluation and Consequences for Grid Convergence in Neutral and Stable Conditions. *Boundary-Layer Meteorology*, 174(2):297–325, 2020.

C.P. Mellen, J. Fröhlich, and W. Rodi. Large eddy simulation of the flow over periodic hills. In M. Deville and R. Owens, editors, *16th IMACS World Congress on Scientific Computation, Applied Mathematics and Simulation, August 21–25, Lausanne, Switzerland*. École Polytechnique Fédérale de Lausanne, 2000.

F.R. Menter. Zonal two equation k-ω turbulence models for aerodynamic flows. In *23rd Fluid Dynamics, Plasmadynamics, and Lasers Conference, July 6–9, Orlando, Florida*, AIAA 1993–2906. American Institute of Aeronautics and Astronautics, 1993.

J. Meyers and P. Sagaut. On the model coefficients for the standard and the variational multi-scale Smagorinsky model. *Journal of Fluid Mechanics*, 569:287–319, 2006.

D. Mierke, C.F. Janßen, and T. Rung. GPU-Accelerated Large-Eddy Simulation of Ship-Ice Interactions. In F. Salvatore, R. Broglia, and R. Muscari, editors, *6th International Conference on Computational Methods in Marine Engineering, June 15–17, Rome, Italy*, pages 850–862. CIMNE, 2018.

D. Mierke, M. Gehrke, T. Rung, and Q. Hisette. Validation of a GPU-Accelerated Fully Viscous Numerical Ice Tank Using Lattice Boltzmann Method. In *8th International Conference on Computational Methods in Marine Engineering, May 13–15, Gothenburg, Sweden*, (Presentation), 2019.

D. Mierke, C.F. Janßen, and T. Rung. An efficient algorithm for the calculation of sub-grid distances for higher-order LBM boundary conditions in a GPU simulation environment. *Computers & Mathematics with Applications*, 79(1):66–87, 2020.

C.-H. Moeng. A Large-Eddy-Simulation Model for the Study of Planetary Boundary-Layer Turbulence. *Journal of the Atmospheric Sciences*, 41(13):2052–2062, 1984.

P. Moin and J. Kim. Numerical investigation of turbulent channel flow. *Journal of Fluid Mechanics*, 118:341–377, 1982.

R.D. Moser and P. Moin. Direct Numerical Simulation of Curved Turbulent Channel Flow. Technical Report TM-85974, NASA, 1984.

R.D. Moser, J. Kim, and N.N. Mansour. Direct numerical simulation of turbulent channel flow up to $\mathrm{Re}_\tau \approx 590$. *Physics of Fluids*, 11(4):943–945, 1999.

A.J. Musker. Explicit Expression for the Smooth Wall Velocity Distribution in a Turbulent Boundary Layer. *AIAA Journal*, 17(6):655–657, 1979.

P. Nathen, D. Gaudlitz, M.J. Krause, and N.A. Adams. On the Stability and Accuracy of the BGK, MRT and RLB Boltzmann Schemes for the Simulation of Turbulent Flows. *Communications in Computational Physics*, 23(3):846–876, 2018.

C.A. Niedermeier, C.F. Janßen, and T. Indinger. Massively-parallel multi-GPU simulations for fast and accurate automotive aerodynamics. In *7th European Conference on Computational Fluid Dynamics, June 11–15, Glasgow, Scotland, UK*, 2018.

N.V. Nikitin, F. Nicoud, B. Wasistho, K.D. Squires, and P.R. Spalart. An approach to wall modeling in large-eddy simulations. *Physics of Fluids*, 12(7):1629–1632, 2000.

S. Noelting and E. Fares. The Lattice-Boltzmann Method: An Alternative to LES for Complex Aerodynamic and Aeroacoustic Simulations in the Aerospace Industry. Technical Report 2015-01-2575, SAE International, 2015.

N. Onodera and T. Aoki. Large-eddy simulation of turbulent flow around a car body using lattice Boltzmann method on the TSUBAME supercomputer. In *11th World Congress on Computational Mechanics (WCCM XI), July 20–25, Barcelona, Spain*, 2014.

S.A. Orszag. Analytical theories of turbulence. *Journal of Fluid Mechanics*, 41(2):363–386, 1970.

A. Pasquali. *Enabling the cumulant lattice Boltzmann method for complex CFD engineering problems*. PhD Dissertation, Technische Universität Braunschweig, 2016.

A. Pasquali, M. Schönherr, M. Geier, and M. Krafczyk. Simulation of external aerodynamics of the DrivAer model with the LBM on GPGPUs. In G.R. Joubert, H. Leather, M. Parsons, F. Peters, and M. Sawyer, editors, *Parallel Computing: On the Road to Exascale*, volume 27 of *Advances in Parallel Computing*, pages 391–400. IOS Press, Amsterdam, 2016.

A. Pasquali, M. Geier, and M. Krafczyk. Near-wall treatment for the simulation of turbulent flow by the cumulant lattice Boltzmann method. *Computers & Mathematics with Applications*, 79(1):195–212, 2020.

U. Piomelli and E. Balaras. Wall-Layer Models for Large-Eddy Simulations. *Annual Review of Fluid Mechanics*, 34(1):349–374, 2002.

U. Piomelli and J.R. Chasnov. Large-Eddy Simulations: Theory and Applications. In M. Hallbäck, D.S. Henningson, A.V. Johansson, and P.H. Alfredsson, editors, *Turbulence and Transition Modelling. ERCOFTAC Series*, 2, pages 269–336. Springer, Dordrecht, 1996.

U. Piomelli and J. Liu. Large-eddy simulation of rotating channel flows using a localized dynamic model. *Physics of Fluids*, 7(4):839–848, 1995.

U. Piomelli, J. Ferziger, P. Moin, and J. Kim. New approximate boundary conditions for large eddy simulations of wall-bounded flows. *Physics of Fluids*, 1(6):1061–1068, 1989.

S.B. Pope. *Turbulent Flows*. Cambridge University Press, 2000.

M. Popovac and K. Hanjalic. Compound Wall Treatment for RANS Computation of Complex Turbulent Flows and Heat Transfer. *Flow, Turbulence and Combustion*, 78: 177–202, 2007.

L. Prandtl. 7. Bericht über Untersuchungen zur ausgebildeten Turbulenz. *ZAMM - Journal of Applied Mathematics and Mechanics / Zeitschrift für Angewandte Mathematik und Mechanik*, 5(2):136–139, 1925.

Y.H. Qian, D. d'Humières, and P. Lallemand. Lattice BGK Models for Navier Stokes Equation. *Europhysics Letters*, 17(6):479–484, 1992.

C. Rapp and M. Manhart. Experimental investigations on the turbulent flow over a periodic hill geometry. In R. Friedrich, N.A. Adams, J.K. Eaton, Humphrey. J.A.C., N. Kasagi, and M.A. Leschziner, editors, *TSFP*, 5th International Symposium on Turbulence and Shear Flow Phenomena, August 27–29, Munich, Germany, pages 649–654. Begell House Inc., Danbury, Connecticut, 2007.

C. Rapp and M. Manhart. Flow over periodic hills: an experimental study. *Experiments in Fluids*, 51(1):247–269, 2011.

C. Rapp, M. Breuer, M. Manhart, and N. Peller. *2D Periodic Hill Flow (UFR 3-30 Test Case), ERCOFTAC*, 2009. URL `https://www.kbwiki.ercoftac.org/w/index.php?title=UFR_3-30_Test_Case`. Accessed October 1, 2021.

O. Reynolds. XXIX. An experimental investigation of the circumstances which determine whether the motion of water shall be direct or sinuous, and of the law of resistance in parallel channels. *Proceedings of the Royal Society of London*, 174:935–982, 1883.

O. Reynolds. IV. On the dynamical theory of incompressible viscous fluids and the determination of the criterion. *Proceedings of the Royal Society of London. Series A: Mathematical, Physical and Engineering Sciences*, 186:123–164, 1895.

L.F. Richardson. *Weather prediction by numerical process*. Cambridge University Press, 1922.

D.P. Rizzetta and D.J. Garmann. Wall-Resolved Large-Eddy Simulation of Smooth-Body Separated Flow. *International Journal of Computational Fluid Dynamics*, 36(1):1–20, 2022.

W. Rodi, J.-C. Bonnin, and T. Buchal, editors. *Proceedings of the 4th ERCOFTAC/IAHR Workshop on Refined Flow Modelling - Revised test case descriptions and calculation results, April 3–7, Karlsruhe, Germany*, ERCOFTAC Workshop on Data Bases and Testing of Calculation Methods for Turbulent Flows, 1995. University of Karlsruhe.

J.C. Rotta. *Turbulente Strömungen: Eine Einfürung in die Theorie und ihre Anwendung*. B.G. Teubner Stuttgart, 1972.

T. Rung, H. Lübcke, and F. Thiele. Universal wall-boundary conditions for turbulence-transport models. *ZAMM - Journal of Applied Mathematics and Mechanics / Zeitschrift für Angewandte Mathematik und Mechanik*, 81(S3):481–482, 2001.

A. Ruprecht, T. Helmrich, and I. Buntic. Very Large Eddy Simulation for the Prediction of Unsteady Vortex Motion. In J. Vad, T. Lajos, and R. Schilling, editors, *Modelling Fluid Flow*, pages 229–246. Springer, Berlin Heidelberg, 2004.

P. Sagaut. *Large Eddy Simulation for Incompressible Flows*. Springer, Berlin Heidelberg, 3 edition, 2001.

P. Sagaut. Toward advanced subgrid models for Lattice-Boltzmann-based Large-eddy simulation: Theoretical formulations. *Computers & Mathematics with Applications*, 59 (7):2194–2199, 2010.

H. Schlichting, K. Gersten, K. Krause, and Oertel. H. *Boundary Layer Theory*. Springer, Berlin Heidelberg, 9 edition, 1955.

M. Schönherr. *Towards reliable LES-CFD computations based on advanced LBM models utilizing (Multi-) GPGPU hardware*. PhD Dissertation, Technische Universität Braunschweig, 2015.

F. Schornbaum and U. Rüde. Massively parallel algorithms for the Lattice Boltzmann Method on nonuniform grids. *SIAM Journal on Scientific Computing*, 38(2):96–126, 2016.

M.P. Schultz and K.A. Flack. Reynolds-number scaling of turbulent channel flow. *Physics of Fluids*, 25(2):025104, 2013.

U. Schumann. Subgrid scale model for finite difference simulations of turbulent flows in plane channels and annuli. *Journal of Computational Physics*, 18(4):376–404, 1975.

S. Seeger and K.H. Hoffmann. The cumulant method for computational kinetic theory. *Continuum Mechanics and Thermodynamics*, 12(6):403–421, 2000.

X. Shan, X.-F. Yuan, and H. Chen. Kinetic theory representation of hydrodynamics: a way beyond the Navier-Stokes equation. *Journal of Fluid Mechanics*, 550:413–441, 2006.

K.V. Sharma, R. Straka, and F.W. Tavares. Lattice Boltzmann Methods for Industrial Applications. *Industrial & Engineering Chemistry Research*, 58(36):16205–16234, 2019.

T.-H. Shih, L.A. Povinelli, N.-S. Liu, M.G. Potapczuk, and J.L. Lumley. A generalized wall function. Technical Report TM-1999-209398, NASA, 1999.

T.-H. Shih, L.A. Povinelli, and N.-S. Liu. Application of generalized wall function for complex turbulent flows. In W. Rodi and N. Fueyo, editors, *Engineering Turbulence Modelling and Experiments 5*, 5th International Symposium on Engineering Turbulence Modelling and Measurements, 16–18 September, Mallorca, Spain, pages 177–186. Elsevier Science Ltd, Oxford, 2002.

M.L. Shur, P.R. Spalart, M.K. Strelets, and A.K. Travin. A hybrid RANS-LES model with delayed DES and wall-modeled LES capabilities. *International Journal of Heat and Fluid Flow*, 29(6):1638–1649, 2008.

J. Smagorinsky. General Circulation Experiments with the Primitive Equations. *Monthly Weather Review*, 91(3):99–164, 1963.

P.R. Spalart and S.R. Allmaras. A one-equation turbulence model for aerodynamic flows. In *30th Aerospace Sciences Meeting and Exhibit, January 6–9, Reno, Nevada*, AIAA 1992–0493. American Institute of Aeronautics and Astronautics, 1992.

P.R. Spalart, W.-H. Jou, M. Strelets, S.R. Allmaras, C. Liu, Z. Liu, and L. Sakell. Comments on the Feasibility of LES for Wings, and on a Hybrid RANS/LES approach. In *1st Advances in DNS/LES: Direct numerical simulation and large eddy simulation*, pages 137–148. Greyden Press, 1997.

P.R. Spalart, S. Deck, M.L. Shur, K.D. Squires, M.K. Strelets, and A.K. Travin. A New Version of Detached-eddy Simulation, Resistant to Ambiguous Grid Densities. *Theoretical and Computational Fluid Dynamics*, 20(3):181, 2006.

D.B. Spalding. A single formula for the law of wall. *Journal of Applied Mechanics*, 28(3): 455–458, 1961.

C.G. Speziale. Turbulence Modeling for Time-Dependent RANS and VLES: A Review. *AIAA Journal*, 36(2):173–184, 1998.

J.D. Sterling and S. Chen. Stability Analysis of Lattice Boltzmann Methods. *Journal of Computational Physics*, 123(1):196–203, 1996.

M. Stiebler, M. Krafczyk, S. Freudiger, and M. Geier. Lattice Boltzmann large eddy simulation of subcritical flows around a sphere on non-uniform grids. *Computers & Mathematics with Applications*, 61(12):3475–3484, 2011.

G.G. Stokes. X. On the Effect of the Internal Friction of Fluids on the Motion of Pendulums. *Transactions of the Cambridge Philosophical Society*, 9:8–106, 1851.

K. Suga, Y. Kuwata, K. Takashima, and R. Chikasue. A D3Q27 multiple-relaxation-time lattice Boltzmann method for turbulent flows. *Computers & Mathematics with Applications*, 69(6):518–529, 2015.

G.I. Taylor. Statistical theory of turbulence. *Proceedings of the Royal Society of London. Series A: Mathematical, Physical and Engineering Sciences*, 151(873):421–444, 1935a.

G.I. Taylor. Statistical theory of turbulence-II. *Proceedings of the Royal Society of London. Series A: Mathematical, Physical and Engineering Sciences*, 151(873):444–454, 1935b.

G.I. Taylor and A.E. Green. Mechanism of the production of small eddies from large ones. *Proceedings of the Royal Society of London. Series A - Mathematical and Physical Sciences*, 158(895):499–521, 1937.

C.M. Teixeira. Incorporating Turbulence Models into the Lattice-Boltzmann Method. *International Journal of Modern Physics C*, 9(8):1159–1175, 1998.

L. Temmerman and M.A. Leschziner. Large eddy simulation of separated flow in a streamwise periodic channel constriction. In M.A. Leschziner, J. Eaton, Humphrey. J.A.C., A. Johansson, N. Kasagi, and M. Sommerfeld, editors, *TSFP*, 2nd International Symposium on Turbulence and Shear Flow Phenomena, June 27–29, Stockholm, Schweden, pages 399–404. Begell House Inc., Danbury, Connecticut, 2001.

H. Tennekes and J.L. Lumley. *A First Course in Turbulence*. The MIT Press, 1972.

J. Tölke. Implementation of a Lattice Boltzmann kernel using the Compute Unified Device Architecture developed by nVIDIA. *Computing and Visualization in Science*, 13(1):29–39, 2008.

J. Tölke and M. Krafczyk. TeraFLOP computing on a desktop PC with GPUs for 3D CFD. *International Journal of Computational Fluid Dynamics*, 22(7):443–456, 2008.

J. Tölke, S. Freudiger, and M. Krafczyk. An adaptive scheme using hierarchical grids for lattice Boltzmann multi-phase flow simulations. *Computers & Fluids*, 35(8–9):820–830, 2006.

D.J. Tritton. Some new correlation measurements in a turbulent boundary layer. *Journal of Fluid Mechanics*, 28(3):439–462, 1967.

S. Uphoff. *Development and validation of turbulence models for Lattice Boltzmann schemes*. PhD Dissertation, Technische Universität Braunschweig, 2013.

A. Uzun and M.R. Malik. Wall-Resolved Large-Eddy Simulation of Flow Separation Over NASA Wall-Mounted Hump. In *AIAA SciTech Forum and Exposition 2017, January 9–13, Grapevine, Texas*, NF1676L-24481. American Institute of Aeronautics and Astronautics, 2017.

E.R. van Driest. On Turbulent Flow Near a Wall. *Journal of the Aeronautical Sciences*, 23(11):1007–1011, 1956.

A.W. Vreman and J.G.M. Kuerten. Comparison of direct numerical simulation databases of turbulent channel flow at $\mathrm{Re}_\tau = 180$. *Physics of Fluids*, 26(1):015102, 2014.

X. Wang and T. Aoki. High Performance Computation by Multi-Node GPU Cluster-Tsubame2.0 on the Air Flow in an Urban City Using Lattice Boltzmann Method. *International Journal of Aerospace and Lightweight Structures*, 2(1):77–86, 2012.

X. Wang, Y. Shangguan, N. Onodera, H. Kobayashi, and T. Aoki. Direct Numerical Simulation and Large Eddy Simulation on a Turbulent Wall-Bounded Flow Using Lattice Boltzmann Method and Multiple GPUs. *Mathematical Problems in Engineering*, 2014: 742432, 2014.

Z.J. Wang, K. Fidkowski, R. Abgrall, F. Bassi, D. Caraeni, A. Cary, H. Deconinck, R. Hartmann, K. Hillewaert, H.T. Huynh, N. Kroll, G. May, P.-O. Persson, B. van Leer, and M. Visbal. High-order CFD methods: current status and perspective. *International Journal for Numerical Methods in Fluids*, 72(8):811–845, 2013.

S. Watanabe and T. Aoki. Large-scale flow simulations using lattice Boltzmann method with AMR following free-surface on multiple GPUs. *Computer Physics Communications*, 264:107871, 2021.

H. Werner and H. Wengle. Large-Eddy Simulation of Turbulent Flow Over and Around a Cube in a Plate Channel. In F. Durst, R. Friedrich, B.E. Launder, F.W. Schmidt, U. Schumann, and J.H. Whitelaw, editors, *Turbulent Shear Flows 8*, 8th International Symposium on Turbulent Shear Flows, September 9–11, Munich, Germany, pages 155–168. Springer Berlin Heidelberg, 1993.

D.C. Wilcox. *Turbulence Modeling for CFD*. DCW Industries, Inc, 1993.

S. Wilhelm, J. Jacob, and P. Sagaut. An explicit power-law-based wall model for lattice Boltzmann method-Reynolds-averaged numerical simulations of the flow around airfoils. *Physics of Fluids*, 30(6):065111, 2018.

D.A. Wolf-Gladrow. *Lattice-Gas Cellular Automata and Lattice Boltzmann Models*. Springer Berlin Heidelberg, 2000.

Z. Xia, Y. Shi, R. Hong, Z. Xiao, and S. Chen. Constrained large-eddy simulation of separated flow in a channel with streamwise-periodic constrictions. *Journal of Turbulence*, 14(1):1–21, 2013.

H. Xiao, J.-L. Wu, S. Laizet, and L. Duan. Flows over periodic hills of parameterized geometries: A dataset for data-driven turbulence modeling from direct simulations. *Computers & Fluids*, 200:104431, 2020.

X.I.A. Yang, G.I. Park, and P. Moin. Log-layer mismatch and modeling of the fluctuating wall stress in wall-modeled large-eddy simulations. *Physical Review Fluids*, 2(10):104601, 2017.

D. Yu, R. Mei, L.-S. Luo, and W. Shyy. Viscous flow computations with the method of lattice Boltzmann equation. *Progress in Aerospace Sciences*, 39(5):329–367, 2003a.

D. Yu, R. Mei, and W. Shyy. A Unified Boundary Treatment in Lattice Boltzmann Method. In *41st Aerospace Sciences Meeting and Exhibit, January 6–9, Reno, Nevada*, AIAA 2003–0953. American Institute of Aeronautics and Astronautics, 2003b.

H. Yu, L.-S. Luo, and S.S. Girimaji. LES of turbulent square jet flow using an MRT lattice Boltzmann model. *Compututers & Fluids*, 35(8-9):957–965, 2006.

E.-S. Zanoun, F. Durst, and H. Nagib. Evaluating the law of the wall in two-dimensional fully developed turbulent channel flows. *Physics of Fluids*, 15(10):3079–3089, 2003.

D.P. Ziegler. Boundary conditions for lattice Boltzmann simulations. *Journal of Statistical Physics*, 71(5/6):1171–1177, 1993.